ASTEROID GRAVITY FIELD ESTIMATION BY A SATELLITE CONSTELLATION

MSc Thesis

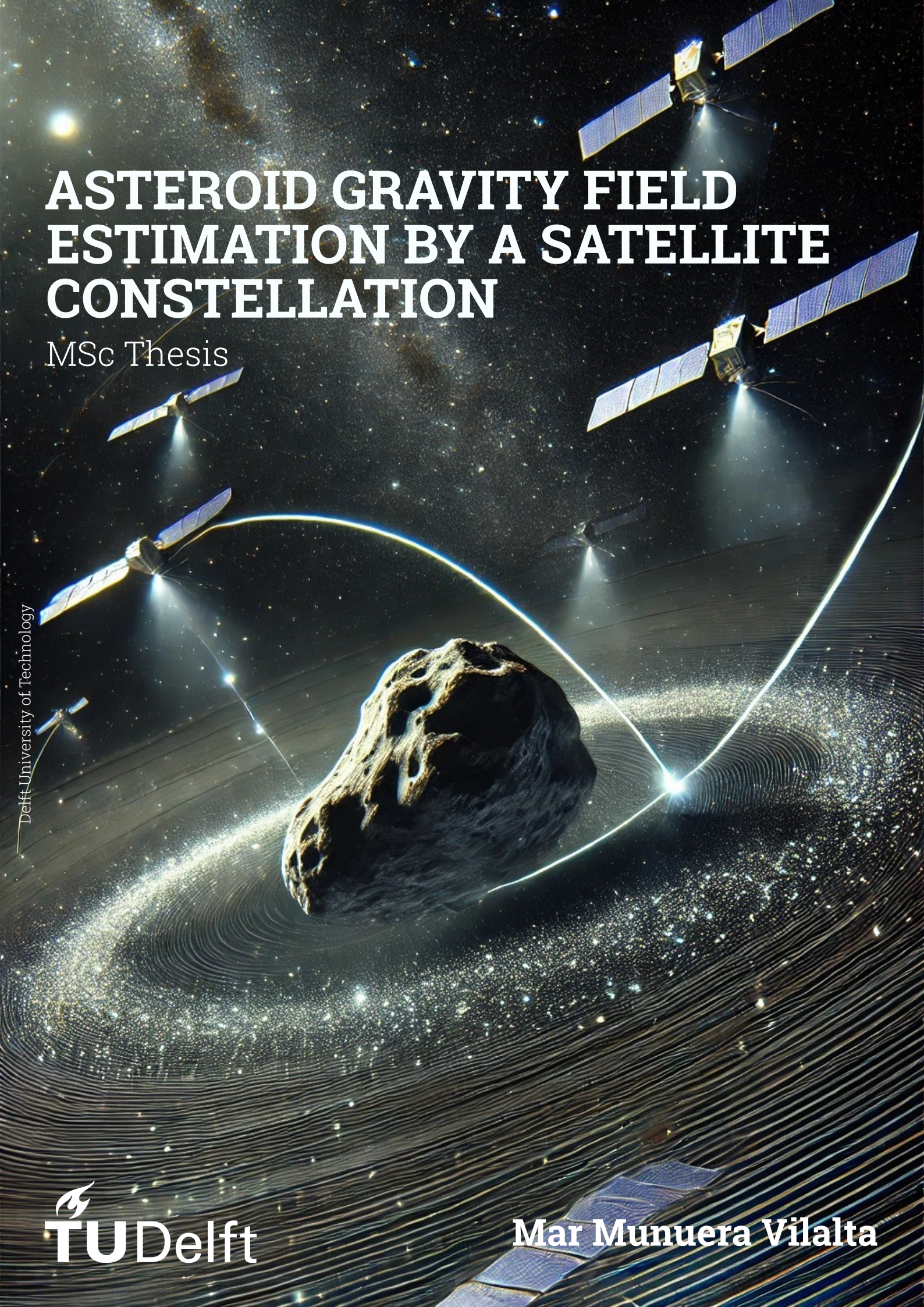

Delft University of Technology

TU Delft

Mar Munuera Vilalta

Asteroid Gravity Field Estimation by a Satellite Constellation

MSc Thesis

by

Mar Munuera Vilalta

to obtain the degree of Master of Science
at the Delft University of Technology,
to be defended publicly on Friday September 6, 2024 at 01:30 PM.

Student number:	5852552	
Project duration:	November, 2023 – July, 2024	
Thesis committee:	Dr. ir. E. Mooij,	TU Delft, supervisor
	Dr. ir. B. Root,	TU Delft, chair
	Dr. ir. J. De Teixeira da Encarnacao,	TU Delft, external examiner

Cover: AI-generated using DALL-E
Style: TU Delft Report Style, with modifications by Daan Zwaneveld

An electronic version of this thesis is available at http://repository.tudelft.nl/.

TU Delft

Abstract

Asteroid missions stand at the forefront of space exploration endeavours. The study of these rocky bodies has gained importance over the years and has been shown to have significant implications for science for a number of reasons. Asteroids contain leftovers from the process that led to the formation of planets and can thus provide invaluable scientific insight into the formation of the Solar System. In addition, they contain raw materials that could be used for the development of a number of technologies, which highlights the potential of these bodies for mining. Furthermore, having identified more than a thousand asteroids as potential threats to Earth, proper research of these bodies can improve the prediction of their motion and therefore aid in the prediction and avoidance of possible Earth impacts in the future.

Asteroid missions face a number of challenges, with safe navigation being one of the main issues. The irregular nature of these bodies creates highly perturbed gravity fields that, if modelled incorrectly, can be a danger to the safe navigation of the spacecraft. Therefore, improving the gravity field modelling of asteroids is of key importance.

This research aims to improve gravity field estimation of asteroids through the use of a satellite constellation consisting of a mothership and a set of CubeSats. In particular, it focuses on the modelling and estimation of the gravity field with spherical harmonics (SH), which makes the research only applicable to the navigation of the spacecraft outside of the Brillouin sphere.

The system design is based on a CubeSat constellation orbiting the asteroid that relays measurements back to a mothership that estimates its state and gravity field through an Unscented Kalman Filter (UKF). The research is centered around 433 Eros asteroid for the model implementation, being an irregular body with known characteristics from the Near-Shoemaker mission.

An end-to-end simulation environment is implemented for the system research. This allows for simulating the orbits of the satellites in a real-world environment considering SH gravity field up to degree and order 15, the perturbation effect of the Sun point mass, and the solar radiation pressure. Additionally, it includes a realistic polyhedral shape of the asteroid including its landmarks. The asteroid model is used together with the modelling of the satellite sensors to estimate the measurements that can be obtained in a realistic scenario including sensor errors, visibility, and communications constraints. Furthermore, the simulation environment contains a UKF filter capable of conducting the gravity-field estimates from the measured states of the constellation satellites.

The research conducts a thorough sensitivity analysis of the scenario evaluating how the constellation design impacts the estimates obtained. This highlights the importance of obtaining a full coverage of the asteroid to be able to model all the irregularities present. Moreover, it underlines the detrimental effect produced by visibility and communications constraints, which create the need for the filter to be restarted, decreasing its efficiency. This analysis evaluates a number of filter designs, and determines that better performance is achieved when the design models the dynamics of several satellites at the same time. This is followed by an analysis of variance, conducted to obtain a better understanding of the constellation characteristics' effects on the filter estimates.

From the results obtained, a design synthesis is conducted to test the system implemented with an optimised constellation design. Furthermore, the filter design is re-evaluated and improved through the addition of better covariance matrix tuning and the addition of a degree-by-degree estimation procedure that allows to reduce computational load, a main constraint of the system. The results obtained show that the model is capable of accurately estimating the gravity field spherical harmonic coefficients with an error lower than 15% when the filter is tuned properly for SH up to degree and order nine. Additional verification of its applicability has been conducted by testing the system with extreme case asteroids (Kleopatra, Itokawa, and Vesta), which show that the system requires a thruster and control system for the satellites to be capable of maintaining stable orbits around the asteroids when these have extremely irregular gravity fields.

Preface

I would like to express my deepest gratitude to Dr. Erwin Mooij for his invaluable guidance and support throughout this project. His insightful advice and encouragement have inspired me to explore new ideas and have greatly contributed to my growth as an engineer.

I also extend my heartfelt thanks to my family and friends, whose unwavering support and encouragement kept me motivated during this endeavour.

As Steven Hawking said, "*to confine our attention to terrestrial matters would be to limit the human spirit*". Conducting research at TU Delft in the field of Space has been a lifelong dream and a rewarding experience, and I will always cherish my time here as an MSc student.

Mar Munuera Vilalta
Delft, July 2024

Contents

Nomenclature

Abbreviations

ANOVA	Analysis of Variance
CPU	Central Processing Unit
DCM	Direction Cosine Matrix
DEM	Digital Elevation Model
DSE	Design Space Exploration
DSN	Deep Space Network
DoE	Design of Experiments
EOM	Equation of Motion
ESA	European Space Agency
EKF	Extended Kalman Filter
FD	Factorial Design
FOV	Field-of-View
GMOEA/D-DE	Multi-objective Evolutionary Algorithm by Decomposition Generational
GNC	Guidance, Navigation, and Control
GPS	Global Positioning System
IMU	Inertial Measurement Unit
ISAS	Institute of Space and Astronautical Science
JAXA	Japan Aerospace Exploration Agency
JPL	Jet Propulsion Laboratory
KF	Kalman Filter
LIDAR	Light Detection And Ranging
LOS	Line-Of-Sight
MOEA/D-DE	Multi-objective Evolutionary Algorithm by Decomposition
MSE	Mean Squared Error
NASA	National Aeronautics and Space Administration
NAVCAM	Navigation Cameras
NEA	Near Earth Asteroid
NEAR	Near Earth Asteroid Rendezvous
NEO	Near-Earth Object
NTF	Natural Tracking Feature
NLR	NEAR Laser Rangefinder
NSGA2	Non-dominated Sorting Genetic Algorithm 2
NSN	Near Space Network
OSIRIS-REx	Origins, Spectral Interpretation, Resource Identification, Security, Regolith Explorer
PDF	Probability Density Function
PF	Particle Filter
PyGMO	Python Parallel Global Multiobjective Optimizer
RK	Runge-Kutta
RKF	Runge-Kutta-Fehlberg
SH	Spherical Harmonics
SINS	Strapdown Inertial Navigation System
SRP	Solar Radiation Pressure
STR	Star-Tracker
TOF	Time-Of-Flight
TSI	Taylor Series Integration
UKF	Unscented Kalman Filter

UT	Unscented Transformation
USM	Unified State Model

Notation

a	Scalar parameters are represented in italic characters
$\mathbf{a}$	Vectors are represented in bold and lowercase characters
$\dot{\mathbf{a}}$	First time derivative of a vector
$\ddot{\mathbf{a}}$	Second time derivative of a vector
$\parallel \mathbf{a} \parallel$	Norm of a vector
$\hat{a}$	Estimate of a parameter
$\tilde{a}$	Noisy value of a vector
$\bar{\mathbf{a}}$	Normalised parameter
$\mathbf{A}$	Matrices are represented in bold and uppercase characters
$\mathbf{A^{-1}}$	Inverse matrix
$\mathbf{A^{T}}$	Transpose matrix
A_{ij}	Matrix element located at row i and column j

Latin Symbols

A	Area, [m^2]
$\mathbf{A}$	Jacobian system matrix, [-]
a	Semi-major axis, [m]
$\mathbf{a}$	Acceleration, [m/s^2]
$\hat{\mathbf{a}}$	Euler-axis, [-]
$\mathbf{C}$	Direction Cosine Matrix, [-]
$\mathbf{C}$	Radial vector, [-]
C_R	Reflectivity coefficient, [-]
$C_{n,m}$, $S_{n,m}$	Spherical harmonics coefficients of degree n and order m, [-]
$\bar{C}_{n,m}$, $\bar{S}_{n,m}$	Normalised spherical harmonics coefficients of degree n and order m, [-]
$\mathbf{e_{xk}^-}$	*a-priori* estimation error, [-]
$\mathbf{e_{xk}}$	*a-posteriori* estimation error, [-]
$\mathbf{e_{zk}^-}$	Measurement residual, [-]
e	Eccentricity, [-]
$\mathbf{F}$	Force vector, [N]
$\mathcal{F}_I$	Inertial reference frame, [-]
$\mathcal{F}_A$	Asteroid reference frame, [-]
$\mathcal{F}_B$	Body reference frame, [-]
f	Focal length, [m]
$f()$	Process function, [-]
$\mathbf{g}$	Gravity acceleration, [m/s^2]
G	Gravitational constant, [$m^2/(kg\ s^2)$]
$\tilde{\mathbf{h}}$	Measurement vector, [-]
i	Inclination, [°]
$\mathbf{K}$	Kalman gain, [-]
k	Number of ANOVA factors, [-]
L_e	Dimensionless per-edge factor, [-]
m_b	Mass of body b, [kg]
M	Mass, [kg]
m	Order, [-]
m	Number of ANOVA levels, [-]
N	Number of samples, [-]
n	Degree, [-]
$\hat{\mathbf{n}}$	Normal vector,[-]
$P_{n,m}$	Legendre polynomial of degree n and order m, [-]

$\bar{P}_{n,m}$	Normalized Legendre polynomial of degree n and order m, [-]
$P_\odot$	Solar radiation pressure, [N/m^2]
P_i	Vertex, [-]
P_i	Variance contribution percentage, [-]
p	Density, [kg/m^3]
$\mathbf{Q}$	Process noise covariance matrix, [-]
$\mathbf{q}$	Quaternion, [-]
$\mathbf{q_{A/B}}$	Attitude quaternion of frame B with respect to frame A, [-]
$\boldsymbol{R}$	Measurement device noise, [-]
R	Reference radius, [m]
R	Perturbing potential, [-]
$\mathbf{r}$	Position, [m]
r	Distance, [m]
S_i	Sum of squares for factor x_i, [-]
S_T	Total sum of squares, [-]
SF	Solar flux, [W/m^2]
T	Total sum of all responses, [variable]
t	Time, [s]
U	Gravitational Potential, [m^3/(kg $\cdot$ s^2)]
V_r	Radial velocity, [m/s]
V_s	Pseudo-transverse velocity, [m/s]
V_t	Transverse velocity, [m/s]
v	Velocity, [m/s]
$\boldsymbol{W}$	Weights matrix, [-]
$\boldsymbol{\omega}$	Weights, [-]
$\mathbf{x}$	State vector, [variable]
$\mathbf{X}$	State and parameters vector, [variable]
$\mathbf{x_0}$	Initial position vector, [m]
$\hat{\mathbf{x}}^-$	*a-priori* estimate, [variable]
$\hat{\mathbf{x}}$	*a-posteriori* estimate, [variable]
$\dot{\mathbf{x}}$	Velocity vector, [m/s]
$\ddot{\mathbf{x}}$	Acceleration vector, [m/s^2]
Y	Response value for an ANOVA observation, [variable]
y_i	Individual response value for observation i, [variable]
$y(x_i^+)$	Response value when factor x_i is at the +1 level, [variable]
$y(x_i^-)$	Response value when factor x_i is at the -1 level, [variable]
$\mathbf{z}$	Measurements vector, [-]
$(u,\ v)$	Pixel coordinates, [px]

Greek Symbols

α_i	Effect of an ANOVA factor (α) for level i, [-]
β_j	Effect of an ANOVA factor (β) for level j, [-]
$\boldsymbol{\chi}$	Sigma matrix, [-]
χ	Sigma points, [-]
ϵ	Reflectivity coefficient, [-]
ϵ	Error, [-]
ζ	Non-dimensional elements of Dromo, [-]
λ	Longitude, [rad]
μ	Gravitational parameter, [m^3/s^2]
ν	Process noise, [-]
ν	True anomaly, [°]
ϕ	Co-latitude, [rad]
Φ	Euler rotation angle, [rad]
ρ	Range, [m]

ρ	Density, [kg/m^3]
$\dot{\rho}$	Range rate, [m/s]
σ	Measurement noise [-]
θ	Latitude, [rad]
$\boldsymbol{\theta}$	Particle, [-]
$\boldsymbol{\omega}$	Rotational rate vector, [rad/s]

Subscripts

A	Asteroid reference frame
ast	Asteroid
AB	Adams-Bashforth
AM	Adams-Moulton
B	Body reference frame
$grav$	Gravitational
I	Inertial reference frame
L	Landmark
p	Point
$pert$	Perturbation
S	Sun
sat	Satellite
SRP	Solar Radiation Pressure
$trunc$	Truncation
$3rd$	Third body perturbation

1 Introduction

Asteroid autonomous navigation stands at the forefront of space exploration endeavours, presenting a unique set of challenges and opportunities that demand interdisciplinary research and innovative solutions. This chapter aims to present the field of the research done. An introduction to asteroids is presented in Section 1.1, which includes arguments supporting the importance of their study, an overview of past asteroid missions and insight into the challenges that asteroid missions present. This is followed by a brief insight into the thesis heritage in Section 1.2, which serves as a starting point for this research. Subsequently, Section 1.3 presents the focus of the thesis research, depicting the research objective and questions, some considerations to be had and assumptions made, and mission requirements. Finally, Section 1.4 highlights the structure of the report.

1.1. Asteroids

Also known as minor planets, asteroids are small rocky inactive bodies that orbit the Sun. Composed of rocks, metals, and gases, these bodies are believed to be remains that endured from the early development of our Solar System around 4.6 billion years ago. Over the last years, more interest has grown in their research and study, which has led to several missions being developed to increase our knowledge of them. This interest is due to a number of reasons. These are presented in the following subsection.

1.1.1. Significance of Asteroid Research

Firstly, asteroids can provide invaluable scientific insight into the formation of the Solar System, containing leftovers from the process that led to the formation of planets. Additionally, these bodies are also the source of a number of meteorites that have reached Earth and may have brought carbon-based molecules and other volatile materials that participated in the building blocks of life [1].

Secondly, asteroid collisions can pose a threat to Earth. Although the Earth is constantly struck with interplanetary bodies, these are mostly burnt off in its atmosphere. However, on average, Earth is expected to be threatened every 100 years by large asteroids that could cause global disasters if they impact the Earth's surface. Currently, 1,784 asteroids are identified as a potential hazard out of the more than 730,000 known asteroids [2]. While the probability of an asteroid having a devastating impact on Earth is remote, it is crucial to have a deep knowledge of their compositions, sizes, structures, and trajectories. Properly understanding the motion of the asteroid in the Solar System can help with the prediction and possibly avoidance of possible impacts in the future.

Thirdly, with the current overconsumption of resources on the Earth, asteroids have gained a great deal of importance in the last decades due to their potential use for mining (Hessel et al., 2020). They contain raw materials that could be used in the development of a number of technologies on Earth. It is estimated that the asteroid belt may contain a mineral wealth value of over 100 billion dollars for all

[1] D. K. Yeomans, "Why Study Asteroids?", Available at: https://ssd.jpl.nasa.gov/sb/why_asteroids.html, Accessed on 24-11-2023

[2] L. Tavernier, "How NASA Studies and Tracks Asteroids Near and Far", Available at https://www.jpl.nasa.gov/edu/news/2017/4/18/how-nasa-studies-and-tracks-asteroids-near-and-far/, Accessed on 24-11-2023

people on Earth[3]. As Azadmanesh et al. (2023) present, asteroids can have very different compositions, which can be classified into three main groups: 1) Type C asteroids, also known as chondrites, represent the most common asteroids, consisting of clay and silicate rocks that have a dark appearance. These contain large amounts of water, which could be used in exploration missions, as well as organic substances such as carbon and phosphorus. 2) S-type asteroids, also referred to as stony, are known to be conformed by silicate materials and nickel-iron. While these carry very low amounts of water, they contain abundant metals such as nickel, cobalt, platinum, gold and rhodium amongst others. 3) Type M asteroids are metallic asteroids, most commonly differentiated by the distance of the Sun at their formation. These can contain up to ten times the amount of metal contained in S-type asteroids, making them very attractive for mining.

1.1.2. Past Asteroid Missions: A Historical Perspective

Several missions have been carried out over the years to study asteroids in the Solar System. The most relevant are presented in this section.

NEAR Shoemaker Mission

The Near Earth Asteroid Rendezvous (NEAR) mission was the first mission of NASA's Discovery Programme and the first to orbit an asteroid and to produce scientific data on its surface composition, geology, physical properties, and internal structure (Prockter et al., 2002).

Launched in 1997, this was the first spacecraft to enter the orbit of the Near Earth Orbit (NEO) asteroid 433 Eros on February 14, 2000. Moreover, the spacecraft "NEAR Shoemaker" became as well the first one to land on an asteroid, touching down on Eros on February 12, 2001 (Cheng, 2002).

This mission faced many challenges. The spacecraft experienced a loss of control with the inertial guidance system for a period of time, requiring the orbit to be corrected with the rocket propulsion system. The significant fuel loss led to a considerable reduction in the spacecraft's propellant margin, which helped in the decision to land on Eros as an end-of-mission scenario (Antreasian et al., 2001). Additionally, the spacecraft encountered navigation challenges due to the irregularity of Eros' shape and its low gravity. The disturbances in the gravity field had not been anticipated and resulted in a very slow convergence of the model. This is common in asteroid missions, since there is only a basic *a priori* knowledge of the body, and the perturbations present in the environment cannot be predicted (Williams, 2002), which underlines the necessity of a high navigation accuracy of the spacecraft. In particular, the "NEAR Shoemaker" spacecraft was able to improve the irregular shape model of the asteroid through the use of landmark locations and a NEAR Laser Rangefinder (NLR).

Hayabusa Mission

The Hayabusa mission was planned by the Institute of Space and Astronautical Science (ISAS), which after the launch was unified into the Japan Aerospace Exploration Agency (JAXA). Launched on May 9, 2003, it had as its main purpose to obtain samples from an asteroid and return them to Earth.

This mission explored Itokawa, which was the first sub-kilometre-sized near-Earth asteroid to ever be explored (Yoshikawa et al., 2021).

Although this mission aimed to have autonomous navigation, the malfunction of the reaction wheels prevented the location of the asteroid's centre of mass, and a hybrid ground-based optical navigation system was used instead. Nevertheless, the spacecraft managed to collect 1500 grains of dust, despite the malfunction of the ion thrusters and the degradation experienced by the solar cells.

Rosetta Mission

The Rosetta mission was launched on March 2, 2004, by the European Space Agency, becoming the first mission to orbit and land on a comet. Carrying the Philae lander, this mission had originally as its main objective to analyse the cometary matter through a rendezvous with comet 46P/Wirtanen, but due to a launch delay, comet 67P/Churyumov-Gerasimenko was chosen as the spacecraft's destination.

On its path to the comet, Rosetta carried out two flybys on asteroids 2867 Šteins in 2008 and 21 Lutetia in 2010, obtaining valuable information, and finally arriving at 67P/Churyumov-Gerasimenko. The Philae lander made a detailed study for a 2 year period from November 2014 to September 2016,

[3]D. K. Yeomans, "Why Study Asteroids?", Available at: https://ssd.jpl.nasa.gov/sb/why_asteroids.html, Accessed on 24-11-2023

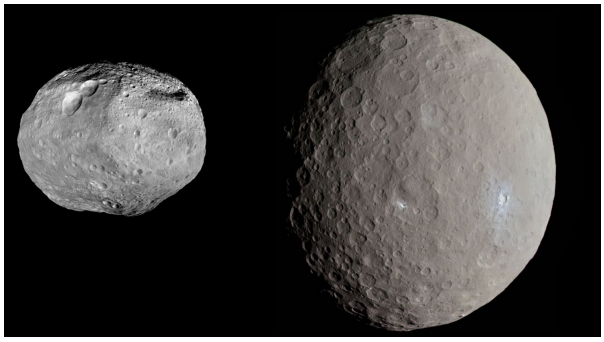

Figure 1.1: Celestial bodies orbited by the Dawn Mission with Vesta to the left and Ceres to the right [5]

when the mission finalised with a controlled impact on said comet, obtaining the most detailed study of a comet ever done[4].

This mission depicted weaknesses in its navigation system as a result of the star trackers being disturbed by the debris present around the comet. They were unable to properly function independently and the monitoring of the spacecraft's attitude deteriorated, consequently worsening communication with Earth. Nevertheless, this became one of ESA's most successful missions, having retrieved a large amount of data about the comet. The Rosetta spacecraft was able to detect the presence of water vapour and ice, molecular oxygen and nitrogen, glycine, and the DNA phosphorus component (Siddiqi, 2018), which supports the theory that both asteroids and comets contain the building blocks of life.

Dawn Mission

Launched in 2007, the Dawn mission was the ninth of NASA's Exploration Program. The main goal of the mission was to explore Ceres and Vesta[5], depicted in Figure 1.1, two of the most massive objects in the main asteroid belt and remnants of the planet formation epoch. Additionally, this mission was the first to carry out relative navigation through optical instruments, and absolute navigation through Doppler and radiometric data.

This mission successfully explored approximately 45% of the mass of the main asteroid belt, concluding in October 2018 after orbiting 1.1 years around Vesta and 3.7 years around Ceres. Dawn is expected to remain in its final orbit until November 2038 around this dwarf planet (Rayman, 2020).

This mission is considered to be very successful in spite of the fact that the spacecraft experienced multiple malfunctions, which resulted in the spacecraft having to go into safe mode and components becoming unstable in the course of the mission.

OSIRIS-REX Mission

The OSIRIS-REx mission, which stands for Origins, Spectral Interpretation, Resource Identification, Security, and Regolith Explorer is a NASA mission carried out in partnership with the University of Arizona and Lockheed Martin. Launched on September 8, 2016, this mission has as its main objective to obtain dust, soil and rock samples of the asteroid 101955 Bennu (March, 2021), a Near-Earth Asteroid. This mission used lidar (Laser Imaging Detection and Ranging) to navigate autonomously with the aid of Natural Tracking Feature (NTF). This system allowed to decrease the laser error range through the integration of captured images by optical systems with an existent on-board catalogue.

Having obtained the desired dust samples in September 2023, the spacecraft is currently on a path to the asteroid Apophis, where it is expected to arrive in 2029 [6].

Lucy Mission

The Lucy mission is part of NASA's Discovery Program and the first mission that aims to study the Jupiter Trojan asteroids. This spacecraft was launched in 2021 and is expected to have encounters with

[4]The European Space Agency, "Rosetta overview", Available at: https://www.esa.int/Science_Exploration/Space_Science/Rosetta_overview, Accessed on 20-11-2023

[5]Wikipedia, "File:Eros, Vesta and Ceres size comparison.jpg", Available at https://en.m.wikipedia.org/wiki/File:Eros,_Vesta_and_Ceres_size_comparison.jpg, Accessed on 08-12-2023

[6]N. Tillman, "OSIRIS-REx: A complete guide to the asteroid-sampling mission", Available at: https://www.space.com/33776-osiris-rex.html, Accessed on 20-11-2023

Figure 1.2: Celestial bodies orbited by the Lucy Mission [5]

the selected asteroids from 2025 to 2033, visiting 3548 Eurybates, Polymele, Leucus, Orus, and the Patroclus/Menoetius binary. These are illustrated in Figure 1.2[7].

To carry out the mission, Lucy will carry out a series of close flybys and utilise high-heritage remote sensing instruments to map the geology, the colour of the surface and its composition, and thermal properties, amongst others (Clark et al., 2018).

Psyche Mission

The Psyche mission, led by the Arizona State University and managed by NASA's JPL, was launched on October 13, 2023 [8] as the 14th mission of the Discovery Programme. It aims to reach the asteroid Psyche by 2029, which is the largest metallic asteroid known, and is believed to be by scientists the core of a planet that did not form (Witze, 2023).

Additionally, this mission also aims to test the NASA Deep Space Optical Communications technology[9].

1.1.3. Navigating the Unpredictable: Challenges in Asteroid Environments

The past missions on asteroids presented in Subsection 1.1.2 have shown a number of technical difficulties, thus highlighting the challenges present in navigating an asteroid's environment. Spacecraft in the vicinity of asteroids are affected by the asteroid's gravity field and interplanetary forces and perturbations due to the bodies in the vicinity and the Sun. While these perturbations can be estimated with good accuracy when knowing the spacecraft's distance to the bodies, the gravity field of the asteroid poses a bigger issue.

Asteroid shapes are a challenge to properly estimate due to their large distances from Earth, and since most asteroids have very irregular shapes, they also have significantly irregular gravity fields. The environment becomes significantly disturbed when the spacecraft enters the asteroid's sphere of influence, resulting in a highly complex dynamical environment (Hesar et al., 2016). Therefore, it is crucial to have a proper estimation of the gravity field of the asteroid for the successful completion of missions involving asteroids. Unexpected perturbations in the environment, even if small, can have considerable consequences on the success of a mission, causing collisions between the spacecraft and asteroid or even causing the spacecraft to escape.

An additional challenge faced when navigating an asteroid is the determination of the position and velocity of the spacecraft. Missions generally use the Deep Space Network (DSN), sending radiometric measurements to Earth and obtaining the estimated parameters back. Since the spacecraft is located at a very large distance from Earth, the communication requires a considerable time, which limits the update frequency of the estimations. Additionally, the DSN connection is not always available depending on the location of the spacecraft, which further highlights the need for autonomous navigation of the spacecraft.

Autonomous navigation does not use radiometric tracking from Earth ground stations, but relies on the use of other instruments to have optical navigation as well as ranging. Navigation systems are dependent on the knowledge given by the sensors for position estimation. Therefore, it is crucial that the navigation system contains the necessary sensors for the mission. A trade-off must be made between

[7]Space, "Meet the 10 asteroids NASA's Lucy spacecraft will visit", Available at https://www.space.com/nasa-lucy-asteroids-mission-targets, Accessed on 08-12-2023

[8]Jet Propulsion Laboratory, "Psyche", Available at: https://www.jpl.nasa.gov/missions/psyche, Accessed on 20-11-2023

[9]L. Gowran, "What you need to know about NASA's Psyche mission", Available at: https://www.siliconrepublic.com/innovation/psyche-asteroid-nasa-mission-what-you-need-to-know, Accessed on 20-11-2023

the accuracy desired and the computational costs and spacecraft physical restrictions associated. This is due to the fact that while having a large number of sensors can result in higher-accuracy estimation of the position, this also increases the weight and costs of the spacecraft. Additionally, the sensor measurements contain errors and do not directly provide the position of the spacecraft, but the use of navigation filters are required to produce a proper estimation of the spacecraft's state.

The development of autonomous navigation systems has further advantages in missions. Not only does the use of autonomous navigation result in lower operational costs of missions, but also in safer missions. A spacecraft carrying out operations close to an asteroid's surface has direct responses with autonomous navigation, whereas otherwise relies on communication with Earth, which has a much higher delay, reducing the spacecraft's safety. Autonomous navigation allows the spacecraft to fly at lower altitudes from the asteroids surface more safely due to the faster response times.

1.2. Thesis heritage

This thesis can be considered an extension to the work carried out by Razgus (2017), Bourgeaux (2020), and Spee (2022) on the topic of autonomous navigation in the vicinity of asteroids.

Razgus (2017) aimed to improve relative navigation techniques, increasing their robustness, and reliability and making them autonomous for asteroid missions. To research this, the dual-quaternion approach was researched and compared with a conventional one, which consists of the use of Cartesian coordinates for position and the use of quaternions for attitude. The simulations were carried out using the Kleopatra and Itokawa asteroids. It was concluded that both methodologies presented identical performances. Several reasons were presented as possible explanations for this. The identical performance could be explained by the fact that the models have similar measurement equations, which means that both models have a high dependency on the measurements. A number of recommendations were given, in particular, Razgus (2017) recommended the testing of the extended Kalman filter (EKF) navigation filters used with a gravity model of higher precision, and the implementation of real-time estimations.

Bourgeaux (2020) researched how to increase the safety of autonomous navigation for asteroid missions. This was done through the simulation of a spacecraft in 433 Eros environment, the gravity of which was modelled with spherical harmonics. The simulation was implemented with both extended and unscented Kalman navigation filters, which showed no significant performance differences. Several conclusions were made from the work. Firstly, autonomous navigation safety can be improved by increasing the accuracy of the measured forces and torques acting on the spacecraft. Furthermore, it was shown that neglecting the effect of the solar radiation pressure (SRP) and the Sun's third body perturbation in the navigation model led to considerable errors in the gravitational parameter estimation, and their inclusion in the model was therefore recommended. Finally, it was concluded that the estimation should include the gravity field of the asteroid. Additionally, it should be noted that the work done accomplished the estimation of the position and velocity with errors below 10 meters and 0.01 m/s, respectively. Furthermore, it was seen that the estimation of the spherical coefficients above order 8 had no considerable increase in accuracy, having achieved an estimation of the coefficients with an error below 10% (Mooij et al., 2024). Bourgeaux (2020) particularly recommended the consideration of a different gravity model for the scenarios where the spacecraft enters the Brillouin sphere.

Spee (2022) aimed to increase the safety of navigation close to asteroids through the improvement of the gravity-field estimation inside the Brillouin sphere. This was done through the implementation of a mascon (mass concentration) gravity model. A spacecraft was simulated close to 433 Eros having an EKF to carry out the state estimations. Through a number of simulations, it was determined that the filter was capable of estimating the state with the same accuracy for heterogeneous and homogeneous density distribution in asteroids. Furthermore, it demonstrated the benefits of using mascon models inside of the Brillouin sphere instead of a spherical harmonics model. Nevertheless, no conclusion was reached in the determination of the improvement of robustness in autonomous navigation. Several recommendations for future work in the field were given, the most relevant one being the consideration of a new model less computationally expensive than mascon, for instance through the combination of the mascon model with spherical harmonics.

In addition, the work carried out by Heijden (2022) has been considered for its relevance in autonomous navigation. The research aimed to investigate if and how accurate relative navigation around an asteroid could be achieved using learning-based algorithms. A convolutional neural network

based pose estimation pipeline was developed succesfully for autonomous navigation around asteroids. Furthermore, its applicability in producing estimates of instantaneous position was demonstrated, thus depicting the efficacy of using such systems for navigation around asteroids, which do not rely on the use of *a-priori* information of the asteroid and are proven to be more robust against factors such as illumination conditions and image noise.

1.3. Thesis focus and considerations

This chapter has highlighted the importance of asteroid missions and the challenges faced. In particular, this thesis focuses on enhancing the gravity-field estimation of asteroids using autonomous navigation strategies, increasing therefore the safety of asteroid missions. Building upon the studies done in the field introduced in this chapter, this research proposes the implementation of a satellite constellation as a methodology to improve the accuracy of said estimation.

This section delineates the scope of the thesis research. The research questions of the study and its objectives are presented in Subsection 1.3.1, followed by Subsection 1.3.2, which presents the considerations of the scenario and assumptions made for its implementation. Furthermore, Subsection 1.3.3 outlines the mission requirements.

1.3.1. Research Questions

Building upon the introductory context, this thesis is dedicated to fulfilling the following objective:

Increase the safety of autonomous navigation asteroid missions by improving gravity-field estimation.

To achieve this objective, this thesis explores the use of satellite constellations around asteroids as a beneficial model for gravity-field estimation. The research done aims to answer the following research question:

How can the integration of autonomous navigation strategies within a satellite constellation enhance the accuracy of gravity-field estimation for asteroids?

Additionally, the following sub-questions aim to be answered to get a proper understanding of the effect that the constellation design and hardware used have on the gravity-field estimation.

a) *What is the influence of the number of satellites in a constellation on the estimation accuracy?*

b) *How does the orbital distribution of the satellites in a constellation impact the estimation accuracy?*

c) *How do the communication constraints of the constellation impact the system?*

d) *How do the resolution and pointing error of the sensors used affect the position estimation of the satellite system?*

1.3.2. Scenario and considerations

In defining the mission and its scenario, several considerations and assumptions have been made. Furthermore the limitations of the research can be drawn. These are detailed in this section.

Orbiting region

As highlighted by Bourgeaux (2020) and Spee (2022), determining the orbiting region is crucial for selecting appropriate models for the scenario environment.

This research focuses on the autonomous navigation of a constellation of satellites along a complex dynamical system outside the Brillouin sphere. This is due to the fact that gravity-field estimation inside the Brillouin sphere requires very computationally intensive gravity-field models, which are considered and presented in Subsection 2.2.1. Given the high computational demands of the simulation and optimisation of a satellite constellation, a study of the gravity field inside of the Brillouin sphere would significantly increase the CPU load and complicate the research within the project's timeframe.

Nevertheless, it should be noted that this assumption impacts the results obtained, rendering them applicable only to mission phases conducted outside the Brillouin sphere. This approach is inadequate for mission scenarios that require a closer orbit of the satellite and landing. The simulation of a satellite constellation inside the Brillouin sphere is deferred for future investigation.

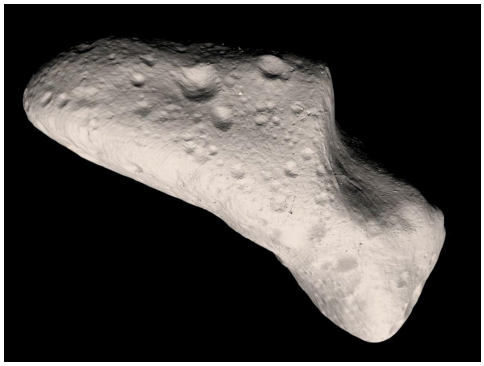

Figure 1.3: Image of 433 Eros asteroid taken by NEAR Shoemaker [10]

Target asteroid

To conduct this research, it is essential to select a target asteroid with a detailed shape model and available density measurements. There is a limited number of asteroids that have been properly researched and from which sufficient data is known. Potential candidates include 433 Eros, Vesta, Ceres, Bennu, Itokawa, Ryugu, and Kleopatra, among others. Out of these, asteroid 433 Eros has been chosen as the target. This selection is based on its irregular shape, as depicted in Figure 1.3[10], which makes it an intriguing study case. Additionally, Eros has been extensively researched, with crucial data obtained from the NEAR mission aiding in the asteroid's modelling and environmental understanding, as well as previous thesis work.

It should be noted, however, that while this thesis focuses on improving gravity-field estimation for asteroids in general, using a single target asteroid means that the results may not be universally representative. Ideally, this mission design should be applied to multiple asteroids to fully address the research question. However, because of the constraints of this research, the main focus is on one asteroid, although some other asteroids will be briefly assessed to gain more insight into the validity of the results.

With these considerations on the target asteroid, the following assumtions are made:

1. The asteroid's orbital period around the Sun is too large to have a significant effect on the simulation. Therefore, the asteroid's orbit around the Sun is not simulated.
2. The only forces acting on the environment are the gravitational force of the asteroid, the solar radiation pressure of the Sun, and the third body perturbation from the Sun.

Mission scenario

As previously introduced, the current research focuses on the effect that the use of a satellite constellation can have on the gravity-field estimation. The mission scenario involves a mothership launched from Earth, which navigates to 433 Eros and enters an orbit around the asteroid. During this phase, the mothership maps the asteroid's landmarks and releases the CubeSats it carries into orbit, creating a constellation around Eros. This thesis considers the starting point of the simulation to be when all satellites are already in orbit around the asteroid. Consequently, the trajectory of the mothership, landmark processing, and the release of CubeSats are not within the scope of this research, so the following assumptions are made:

3. The research considers a starting point in which the constellation satellites are in orbit around the asteroid. Therefore, the trajectory of the mothership from Earth to Eros and the release of the CubeSats into the desired orbits is not a part of the research and is assumed to be carried out successfully.
4. Following the previous assumption, this research will not consider propulsion systems in the satellites. However, these might be required for the orbital placement depending on the deployment method used and the orbital parameters of the constellation chosen. Furthermore, propulsion may

[10] A. Hale, "SPECIAL TOPIC: ASTEROID (433) EROS", Available at https://www.rocketstem.org/2020/01/18/ice-and-stone-special-topic-04/, Accessed on 08-12-2023

be necessary for maintaining the orbits within the desired parameters and correcting deviations. Nevertheless, the control-system design of the CubeSats is out of the scope of the research, but should be considered in future work.

5. The simulation does not include a guidance or control system and no attitude control is implemented. It is assumed that the satellite sensors point to the centre of mass of the asteroid at all times.
6. The shape of the asteroid is assumed to be mapped by the mothership in the previous phase before the release of the CubeSats into orbit. During this phase, the mothership is assumed to use navigation cameras to model the shape and map the landmarks. As a consequence, when the CubeSats are released into orbit, they are considered to have the data on the landmark positions that they will later require for their position estimation.
7. The asteroid rotates at a constant angular velocity along the Z-axis of the asteroid. This rotation rate is assumed to be estimated in the initial phases of the mission by the mothership before the deployment of the satellite constellation and is used to model the dynamics of the system.
8. The mothership will estimate the gravitational parameter of the asteroid before the release of the CubeSats and the CubeSats will later use the estimate on their dynamics model to estimate their position with time.

This research focuses on the simulation of the satellite constellation around 433 Eros. In it, each of the CubeSats continuously estimates its position and the gravity field in it, and transmits it to the mothership, which makes a better estimation with all the data received. It should be noted that to carry out the estimations, the measurements are collected at the frequency that the hardware sensors of the satellites can gather their corresponding data. This frequency will be thus dependent on the hardware and its effect on the estimates is studied. Several assumptions on the sensors have been made:

9. The sensors modelled are asssumed to be noisy and therefore are not properly aligned.
10. The simulation does not consider image processing in the NAVCAM for the detection of the landmarks. It is assumed that the landmarks in the field-of-view of the NAVCAM are detected and identified adequately, since image processing is out of the scope of this research.

This design is dependent on the communications between the CubeSats and the mothership. For the transmission of the data to be successful, there must be line-of-sight (LOS) between the CubeSat and the mothership, and the communication system can effectively transmit data with a range larger than the distance between both transmitter and receiver. Additionally, to facilitate the simulation of this system several assumptions are made:

11. All the CubeSats that are able to establish LOS with the mothership at a given time instant are assumed to transmit the data instantly. This is an assumption made due to the fact that the amount of data to be transmitted for each CubeSat is very low, which at the high-frequency bands such as S, X or Ka-band used for these applications, which have very high data rates, the transmission is extremely fast.
12. Additionally, the simulation works under the assumption that the mothership is able to receive signals from various CubeSats at the same time. This could be accomplished with a variety of methods such as the use of Frequency Division Multiplexing (FDM), in which the signals are transmitted on different frequency bands, thus allowing the receiver to separate the frequency bands with a filter to isolate and process each signal independently.

Overall, it should be noted that the considered communication system is not representative of a real one, and is only implemented as a constraint, and not as an instrument in the implementation. This is due to the fact that the proper simulation of a communication system is out of the scope of this research.

Software definition

The research requires the simulation of the scenario to answer the research questions. Python programming language has been chosen for the development of the simulation. This language allows to make use of the TU Delft Astrodynamics Toolbox (Tudat)[11] library. This is a well-implemented and

[11]TU Delft, "Tudat Space", Available at: https://docs.tudat.space/en/latest/index.html, Accessed on 24-11-2023

verified library that supports astrodynamics and space research. It contains a number of algorithms for the propagation of spacecraft and the integration of orbital trajectories that are required for this research. Moreover, it also presents implemented acceleration models to simulate the environment of the asteroid with, for instance, gravitational models such as spherical harmonics. Tudat's core functionalities are implemented in C++, which implies efficient and fast computation that can be used through the Tudatpy Python interface. Moreover, this library can be used together with PyGMO (the Python Parallel Global Multiobjective Optimiser)[12], a scientific library commonly used for optimisation in astrodynamics (Izzo, 2012). It contains a number of optimisation algorithms that are suitable for the optimisation of the Kalman filter parameters for the development of the research. The use of this library is crucial in the development of the research, considerably decreasing the implementation time by using developed and tested models. However, not all the necessary models are implemented, and algorithms such as those related to the navigation system have been directly implemented in Python.

Optimisation methodology

This research studies the effect of a satellite constellation on the gravity-field estimation. Initially, the design of the constellation was intended to be optimised by exploring various configuration parameters aiming to determine an optimal setup for an accurate gravity-field estimation.

There are a number of optimisation techniques available, which can be divided into two main groups: deterministic methods, which require physical knowledge of the problem, and stochastic methods, which do not.

Stochastic heuristic methodologies are known to be suitable for optimisations of trajectory problems due to the fact that the domain of the problem is too complex to be properly represented or explored by a mathematical formulation (Acciarini et al., 2020).

Several models were initially considered for the optimisation, including the Particle Swarm Optimisation (PSO) algorithm (Chuanjun et al., 2023) and differential evolution algorithms (Storn and Price, 1997). Literature commonly recommends the use of a Non-dominated Sorting GA2 (NSGA2), since it tends to exhibit a good spread of the particles and convergence (Savitri et al., 2017). NSGA2[13] was has therefore considered as a proper optimiser for the research.

The second and last optimiser that was considered for the development is the Multi-objective Evolutionary Algorithm by Decomposition (MOEA/D-DE). This is known to be a very successful algorithm, presenting good convergence properties [14].

However, upon further investigation and implementation, it became apparent that the computational load associated with using NSGA2, or MOEA/D-DE for this problem was prohibitively high. Given these constraints, the optimization process was restructured to focus on a Design of Experiments (DoE) approach combined with Analysis of Variance (ANOVA).

DoE is a field of applied statistics focused on the systematic planning, execution, analysis, and interpretation of controlled experiments[15]. DoE allows for a systematic exploration of the parameter space with the goal of understanding the effects that multiple factors of the constellation design have on the gravity-field estimates.

An ANOVA has been set to be done on a Factorial Design (FD). This method offers a systematic approach to explore the design space. It is based on the orthogonality of a design matrix that allows to obtain information efficiently without the need of conducting a large amount of simulations, such as required when using a Monte Carlo method. Through ANOVA, the significant factors and interactions that affect the system's performance can be identified.

The use of a DoE and ANOVA provides a more feasible and computationally efficient means of determining the optimal constellation configuration without the heavy computational burden of stochastic optimization algorithms.

[12]D. Izzo and F. Biscani, "PyGMO". Available at: https://esa.github.io/pygmo/index.html, Accessed on 24-11-2023

[13]Pagmo 2.19.0 documentation, "Non dominated sorting genetic algorithm (NSGA-II)". Available at: https://esa.github.io/pagmo2/docs/cpp/algorithms/nsga2.html, Last accessed on 27-11-2023

[14]Pagmo 2.19.0 documentation, "Multi-objective Evolutionary Algorithm by Decomposition (MOEA/D-DE)". Available at: https://esa.github.io/pagmo2/docs/cpp/algorithms/moead.html, Last accessed on 27-11-2023

[15]JMP Statistical Discovery, "Design of experiments". Available at: https://www.jmp.com/en_in/statistics-knowledge-portal/what-is-design-of-experiments.html, Last accessed on 02-03-2024

1.3.3. Mission requirements

Having explored the mission heritage, the requirements for the thesis can be drawn. These are as follows:

REQ-AST-01 The target asteroid of the mission is 433 Eros.

REQ-AST-02 The asteroid's physical shape shall be modelled from the information obtained in the NEAR mission.

REQ-AST-03 The asteroid's real-world gravity field shall be modelled with a spherical harmonics model obtained in the NEAR mission.

REQ-MIS-01 The mission shall be carried out with a constellation consisting of a mothership and a number of CubeSats larger to one.

REQ-MIS-02 The satellites conforming to the constellation shall remain outside of the Brillouin sphere at all times.

REQ-MIS-03 The satellites shall not collide with the asteroid nor with each other.

REQ-MIS-04 The satellites shall navigate autonomously.

REQ-MIS-05 The constellation design shall be optimised, in terms of number and orbit configuration.

REQ-SAT-01 The satellites shall be equipped with the necessary sensors to estimate their position.

REQ-NAV-01 The navigation system shall use a Kalman filter for producing its state estimates.

REQ-NAV-02 The navigation system shall estimate the position and velocity of the spacecraft.

REQ-NAV-03 The navigation system shall estimate the spherical harmonics coefficients.

REQ-SYS-01 The spherical harmonics coefficients of the gravity field shall be determined at least up to order and degree 8 with a 3-sigma accuracy of 15 % following Bourgeaux's (2020) work.

REQ-SYS-02 The position of the CubeSats shall be determined with a precision of 10 m with 3-sigma confidence following the results obtained by Bourgeaux (2020).

REQ-SYS-03 The velocity of the CubeSats shall be determined with a precision of 1 mm/s with 3-sigma confidence following the results obtained by Bourgeaux (2020).

1.4. Thesis outline

This thesis explores the research questions and answers them through the simulation of the scenario. The literature study done for the proper development of the research is presented in the following chapters:

Chapter 2 addresses the mission definition as well as the mechanics involved and its environment. It starts diving into the mission heritage and presents a proper definition of the mission scenario of the thesis. Then it introduces the spherical representation of the coordinates. Moreover, the main focus is the environment of the asteroid, and the spacecraft and CubeSats dynamics.

Chapter 3 presents the navigation system of the mission, presenting the sensors and their respective models to be used. Furthermore, it studies navigation filters that can produce a proper estimation of the state.

Chapter 4 discusses the architecture of the simulator and introduces the approaches used for the simulation of the dynamics and sensors in the system and validates the implementation.

Chapter 5 conducts a sensitivity analysis on the scenario researching how the constellation design affects the estimates of the gravity field.

Chapter 6 presents a design exploration using ANOVA to optimise the constellation design and further understand the effects and interactions between the orbital parameters of the satellites in the constellation.

Chapter 7 contains the synthesis of the design choices and methodologies developed throughout the study. This culminates in the identification of an "ideal" case constellation design. Additionally, the limitations of the filter are examined and innovative adaptations are presented to improve the efficiency of the model and thus the resulting gravity field estimates.

Chapter 8 concludes the report with the outcomes of the research discussing their validity and limitations, and presents recommendations for future work.

Furthermore, a number of appendices are present that contain further details of the research conducted. These are the following:

Appendix A presents the development plan of the research. It details the tasks that were initially intended with their corresponding Gantt chart, and the modifications and updates made to the planning to ensure the project's completion within the time limitations.

Appendix B provides further detail on the software designed for the research.

Appendix C contains the spherical harmonic coefficients data used in the research and presents an analysis of the contribution of the coefficients to the gravity field of the asteroid.

Appendix D acts as a support to Chapter 5 by presenting further details on the tests conducted in the sensitivity analysis of the system for a number of scenarios.

Appendix E presents further details on the ANOVA optimisation conducted in Chapter 6 and the results obtained.

Appendix F provides further detail on the settings and tests conducted in the final design synthesis presented in Chapter 7.

2

Orbital Mechanics and Asteroid Environment

This chapter presents the main mathematical and physical models required for the simulation of the mission. Firstly, Section 2.1 presents the basic models for the representation and transformation of coordinates. This is followed by a study of the asteroid's environment in Section 2.2, where the accelerations of the environment are presented and discussed. Finally, Section 2.3 presents the dynamics of the system and discusses the propagator and integrator models to be used in the simulation.

2.1. Spatial Representation

This section presents the reference frames that are used in the system in Subsection 2.1.1, followed by spherical coordinates in Subsection 2.1.2 and finally introduces methodologies for transformation between reference frames in Subsection 2.1.3.

2.1.1. Reference Frames

This environment can be studied from three different (right-handed) frames of reference, which can be seen in Fig. 2.1. These are the following:

Inertial Reference Frame

This frame of reference is assumed to have its origin in the asteroid's centre of gravity. Furthermore, its axes are inertially fixed and are thus assumed to be non-rotating and non-accelerating. The coordinates of this frame are denoted by (x_I, y_I, z_I).

Asteroid Reference Frame

This frame of reference is fixed in the asteroid and rotates with it, and is, therefore, a non-inertial reference frame. Fixed to the centre of gravity of the asteroid, its X-axis coincides with the prime meridian of the asteroid. Note that the prime meridian has been drawn through a crater at one end of Eros by the NEAR mission scientists. It should be noted that this reference has the same z-axis as the inertial reference frame during a rotation around the z-axis. The coordinates of this frame are denoted by (x_A, y_A, z_A).

Body Reference Frame

This frame of reference is fixed to the orbiting bodies, the CubeSats and the mothership. Its axes x, y and z are fixed with respect to the body of the spacecraft and are defined along the length, width, and height, respectively. Given that CubeSats typically have equal dimensions, a convention is adopted where the x-axis is aligned with the camera sensors, the y-axis with the communications antennas, and the z-axis is defined as perpendicular to both.

This is a reference frame useful for the computation of the pointing of the instruments and sensors of the body. The coordinates of this frame are denoted by (x_B, y_B, z_B).

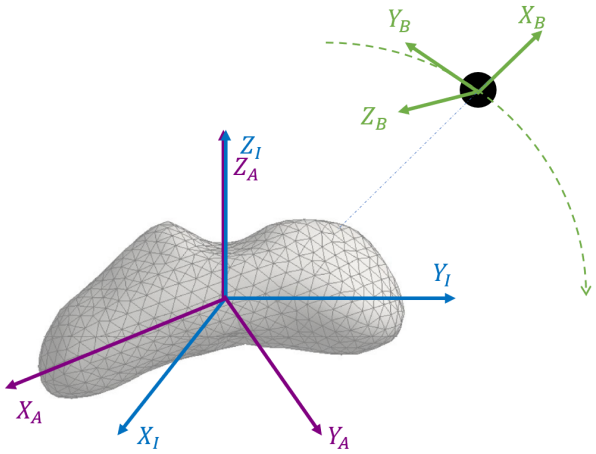

Figure 2.1: Reference frames of the scenario

2.1.2. Sphere-based Coordinates

The position of the bodies orbiting the asteroid can be expressed in spherical-based coordinates in addition to Cartesian coordinates within the reference frames presented. These representations are particularly useful for modelling sensors of the spacecraft.

Spherical Coordinates

This three-dimensional coordinate system is used in the spherical harmonics computation method of the gravity field, which is presented in Subsection 2.2.1, and consists of the following components, which are depicted in Figure 2.2:

- ρ: Distance from the centre to the body
- θ: The co-latitude, which depicts the angle between the position of the body and the Z-axis. It can take values from 0° to 180°.
- λ: The longitude, which depicts the angle between the position projection in the X-Y plane and the prime meridian. It can take values from 0° to 180°.

Spherical coordinates can be transformed into Cartesian coordinates through:

$$\begin{aligned} x &= \rho \sin\theta \cos\lambda \\ y &= \rho \sin\theta \sin\lambda \\ z &= \rho \cos\theta \end{aligned} \tag{2.1}$$

or the inverse conversion can be done with:

$$\begin{aligned} \rho &= \sqrt{x^2 + y^2 + z^2} \\ \theta &= \arctan\frac{y}{x} \\ \lambda &= \arccos\frac{z}{\rho} \end{aligned} \tag{2.2}$$

Geographical Coordinates

This two-dimensional coordinate system provides information on the relative location of a body on the asteroid surface. It uses latitude (θ) and longitude (λ) angles to express a surface coordinate. These angles are shown in Figure 2.2.

2.1.3. Reference Frame Transformations

The simulator must use several reference frames and switch from one to another. This requires rotational parameters, which can be described with a number of methods. This section presents the commonly used Direction Cosine Matrix, Euler angles, and attitude quaternions.

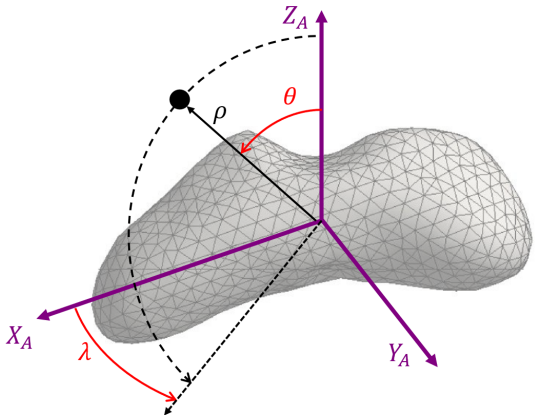

Figure 2.2: Coordinate system

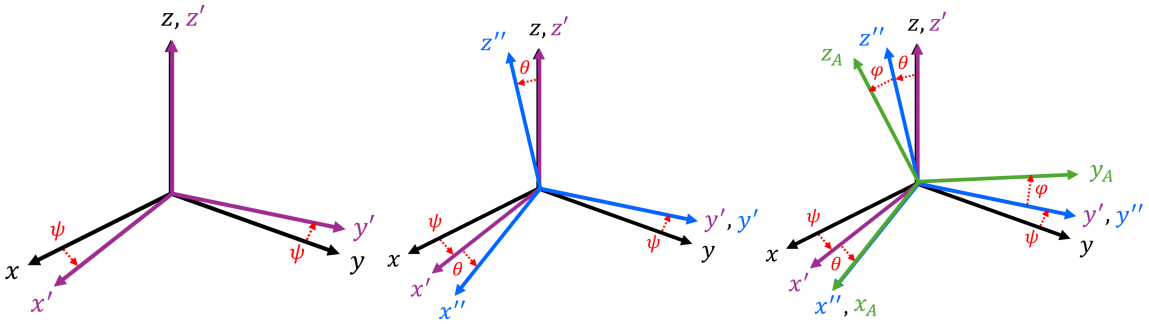

(a) Z-axis rotation **(b)** Y′-axis rotation **(c)** x″-axis rotation

Figure 2.3: Euler-angle rotations

Direction Cosine Matrix

The Direction Cosine Matrix (DCM) allows expressing of a given vector in a given reference frame (B) into another desired reference frame (A). The DCM is used to transform vectors from one frame to another as presented in the following equation, where a given vector $\mathbf{R}_B$ in frame B ($\mathcal{F}_B$) can be transformed into reference frame A ($\mathcal{F}_A$).

$$\mathbf{R}_A = \mathbf{C}_{A/B}\mathbf{R}_B \tag{2.3}$$

It should be noted that the DCM is an orthonormal matrix and thus presents the following properties:

$$\begin{aligned} &\det \mathbf{C}_{A/B} = 1 \\ &\mathbf{C}_{A/B}^{-1} = \mathbf{C}_{B/A} = \mathbf{C}_{A/B}^{T} \\ &\mathbf{C}_{A/B}^{-1}\mathbf{C}_{A/B}^{T} = \mathbf{I}_3 \end{aligned} \tag{2.4}$$

Euler Angles

The Euler angles are three attitude angles that can be used for the representation of the attitude of spacecraft. These are the roll angle φ, the pitch angle θ and the yaw angle ψ, which can range between the values presented in Eq. (2.5). Any rotation of two frames in 3D can be described with up to three successive rotations, as depicted in Figure 2.3; observe.

$$\begin{cases} -\pi \leq \varphi < \pi \\ -\frac{\pi}{2} \leq \theta \leq \frac{\pi}{2} \\ -\pi \leq \psi < \pi \end{cases} \tag{2.5}$$

The rotation around the X-axis, Y-axis, and about the Z-axis can be described with the equations:

$$\mathbf{C}_X = \begin{bmatrix} 1 & 0 & 0 \\ 0 & \cos\varphi & \sin\varphi \\ 0 & -\sin\varphi & \cos\varphi \end{bmatrix} \tag{2.6}$$

$$\mathbf{C}_Y = \begin{bmatrix} \cos\theta & 0 & -\sin\theta \\ 0 & 1 & 0 \\ \sin\theta & 0 & \cos\theta \end{bmatrix} \tag{2.7}$$

$$\mathbf{C}_Z = \begin{bmatrix} \cos\psi & \sin\psi & 0 \\ -\sin\psi & \cos\psi & 0 \\ 0 & 0 & 1 \end{bmatrix} \tag{2.8}$$

The DCM of a rotation sequence where the first rotation is around X, then Y and then Z, can be computed through the multiplication $\mathbf{C}_z\mathbf{C}_y\mathbf{C}_x$ (Diebel, 2006). The resulting DCM is presented in the following equation:

$$\mathbf{C}_{B/A} = \begin{bmatrix} \cos\theta\cos\psi & \cos\theta\sin\psi & -\sin\theta \\ \sin\varphi\sin\theta\cos\psi - \cos\varphi\sin\psi & \sin\varphi\sin\theta\sin\psi + \cos\varphi\cos\psi & \sin\varphi\cos\theta \\ \sin\varphi\sin\theta\cos\psi - \cos\varphi\sin\psi & \cos\varphi\sin\theta\sin\psi - \sin\varphi\cos\psi & \cos\varphi\cos\theta \end{bmatrix} \tag{2.9}$$

It should be noted that the rotation sequence defines the order of multiplication of the rotation matrices. Since matrix multiplications are not commutative, up to 12 different transformation matrices can be obtained to represent a given rotation, six symmetrical and six asymmetrical.

2.2. Asteroid Environment

As Capannolo et al. (2023) state, the mission constraints for all spacecraft in orbit are set by the space environment, which characterises the design of a mission, as well as the design of the guidance, navigation, and control (GNC) system.

Proper modelling of the environment is therefore crucial for the mission design, which consists of considering all the perturbation sources that the spacecraft can experience and choosing an adequate model for them that provides the necessary accuracy without having an excessive CPU load.

Working under the assumption that the scenario only considers the presence of the asteroid and the Sun, there are a number of sources that can give rise to perturbations in the environment. The most important for this scenario is the gravity-field acceleration from the asteroid, which can be computed with several models that are introduced in Subsection 2.2.1. Another gravitational force that must be taken into account is that of the Sun, and therefore the third body perturbations are presented in Subsection 2.2.2. Additionally, the Solar Radiation Pressure (SRP), which in some scenarios can produce a disturbance more significant than that of the third body perturbation (Bourgeaux, 2020) is also considered in the environment and introduced in Subsection 2.2.3.

In addition to the presented perturbations, other considerations can be had, such as the effect of the asteroid's albedo on the bodies, thermal re-radiation, or antenna thrust. In particular, the thrust of the antenna must be taken into consideration given the communications via radio from the CubeSats to the mothership for the transmission of the measurements taken. Nevertheless, all these perturbances can be neglected when compared to the effect of the SRP, as depicted in Table 2.1, which shows the accelerations of these forces on Galileo satellites, which would present higher values of antenna thrust, thermal effects and albedo than for the current scenario. Furthermore, this is further confirmed by Bury et al. (2020), who determined that the impact of the antenna thrust of a 100 W power transmission is approximately a total of 1 cm on a Galileo satellite. Considering that orbits are expected to be determined with a level of precision not higher than metres, as in the research done by Scheeres et al. (2012), and that the CubeSats in the scenario will have a much lower transmission power, the antenna thrust perturbation can be neglected.

This can additionally be confirmed by the research done on 433 Eros through simulations by Bourgeaux (2020) and Spee (2022), amongst others, who only considered the effects of Eros' gravity field, SRP and the Sun's third body perturbations.

2.2.1. Gravity Field

To design the constellation orbit around an asteroid it is critical that the gravitational field is modeled adequately. 433 Eros is an irregularly shaped asteroid and therefore presents a complex source of gravitational disturbances in its surroundings, which can increase the risk of collisions with the surface if incorrectly modeled.

This section depicts the most commonly used models for gravity-field estimation and concludes with the most adequate one to use on 433 Eros for the purposes of this thesis.

Point Mass Approximation

A simple way to estimate the gravity field of a body is through the point mass estimation method. This consists in Newton's law of gravitation, which states that two bodies attract each other with a force that is proportional to their masses and inversely proportional to their distance (Wakker, 2015) as:

$$F = G\frac{m_1 m_2}{r^2} \tag{2.10}$$

where r is the distance between the two bodies, m_1 and m_2 are the mass of bodies 1 and 2, respectively, and G is the universal gravitational constant.

Since the mass of the spacecraft in orbit is considered to be negligible in comparison with the mass of the asteroid, following Newton's second law, the gravitation exerted by the asteroid can be expressed with

$$\mathbf{g} = -G\frac{m_{ast}}{\| \mathbf{x}_s - \mathbf{x}_{ast} \|^3}(\mathbf{x}_s - \mathbf{x}_{ast}) \tag{2.11}$$

where $\mathbf{g}$ represents the gravity acceleration, m_{ast} the asteroid's mass, and $\mathbf{x}_s$ and $\mathbf{x}_{ast}$ the position vectors of the spacecraft and asteroid, respectively.

While this model is a good option for approximations, it does not adequately capture the dynamics of the asteroid considered and is therefore not an appropriate option (Pearl and Hitt, 2022).

Spherical Harmonics

The Spherical Harmonics (SH) model is commonly used to represent geopotential models (Lin et al., 2014). This model consists of the expansion of the gravitational potential U into a series of harmonics as:

$$U(r,\phi,\lambda) = -\frac{\mu}{r}\left[1 + \sum_{n=2}^{\infty}\sum_{m=0}^{n}\left(\frac{R}{r}\right)^n P_{n,m}(\sin\phi)\left\{C_{n,m}\cos(m\lambda) + S_{n,m}\sin(m\lambda)\right\}\right] \tag{2.12}$$

The coefficient series of the harmonics can be estimated from spacecraft tracking data or evaluated as integrals (Werner and Scheeres, 1996). Equation (2.12) depicts the gravity field (Wakker, 2015) where r represents the distance between the centre of the spherical body considered and the spacecraft, R is the reference radius of the spherical body also known as the Brillouin sphere, and λ and ϕ the longitude and latitude of the spacecraft, respectively. Note that the colatitude (θ) is the complementary angle of the latitude (ϕ). Furthermore, the spherical harmonics coefficients are represented by $C_{n,m}$ and $S_{n,m}$, where n represents the degree and m the order, and $P_{n,m}$ is the Legendre function presented in the following equation:

$$P_{nm}(t) = \frac{1}{2^n n!}\left(1-t^2\right)^{m/2}\frac{\mathrm{d}^{n+m}}{\mathrm{d}t^{n+m}}\left(t^2-1\right)^n \tag{2.13}$$

where t denotes time. Finally, μ represents the body's gravitational parameter that can be computed with the product of the gravitational constant G and the mass m of the body.

Table 2.1: Perturbing accelerations on Galileo satellites (Bury et al., 2020)

Source	Acceleration (nm/s^2)
Direct solar radiation pressure (maximum)	122.0
Albedo (maximum)	1.0
Antenna thrust (for 200 W antenna)	1.0
Thermal effects (D2S variability)	0.7

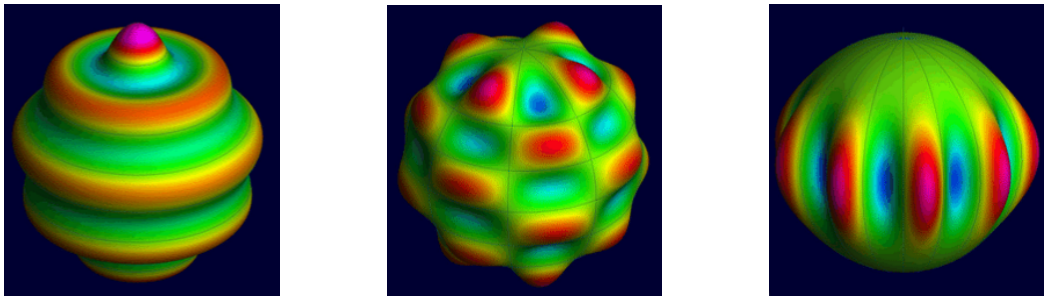

(a) Zonal harmonics **(b)** Tesseral harmonics **(c)** Sectorial harmonics

Figure 2.4: Spherical harmonic types (Ince et al., 2019)

The spherical harmonic coefficients presented can take values ranging from zero to infinite. The higher the order and degree values, the more complex the modelling of the gravity field can be obtained.

Figure 2.4 depicts the geometrical representation of the types of spherical harmonics depending on the order and degree values. As Hofmann-Wellenhof and Moritz (2005) presents, zonal harmonics correspond to null orders ($m = 0$), describing variations with the latitude of the body, changing their sign n times in the interval from $0 \leq \phi \leq \pi$. Sectorial harmonics, on the other hand, occur when the degree and order are the same ($m = n$), describing variations with the longitude of the body. Finally, tesseral harmonics describe the cases in which degree and order have different values ($m \neq n$). Their associated Legendre functions have a sign change $n - m$ times from $0 \leq \phi \leq \pi$ and have a total of $2m$ zero values from $0 \leq \lambda \leq 2\pi$, dividing the sphere into a series of compartments.

Furthermore, as Hofmann-Wellenhof and Moritz (2005) explains, the gravity field is expressed with normalised spherical coefficients ($\bar{C}_{nm}$, $\bar{S}_{nm}$) and normalised Legendre polynomials ($\bar{P}_{nm}$), transforming Eq. (2.12) into:

$$U(r,\phi,\lambda) = \frac{GM}{R}\sum_{n=0}^{\infty}\left(\frac{R}{r}\right)^{n+1}\sum_{m=0}^{n}\bar{P}_{nm}(\sin\phi)\times\left[\bar{C}_{nm}\cos(m\lambda)+\bar{S}_{nm}\sin(m\lambda)\right] \tag{2.14}$$

The normalised polynomials and coefficients used are computed with:

$$\left.\begin{aligned}\bar{P}_{nm} &= P_{nm}\sqrt{2(2n+1)\tfrac{(n-m)!}{(n+m)!}}\\ \bar{C}_{nm} &= C_{nm}\sqrt{\tfrac{1}{2(2n+1)}\tfrac{(n+m)!}{(n-m)!}}\\ \bar{S}_{nm} &= S_{nm}\sqrt{\tfrac{1}{2(2n+1)}\tfrac{(n+m)!}{(n-m)!}}\end{aligned}\right\}\quad (m \neq 0). \tag{2.15}$$

The acceleration of gravity on a spacecraft can be obtained from the presented gravity field potential using a local northeast-down (NED) coordinate system. The components of the gravitational acceleration in the vertical frame in this system (in north, east, and down direction) are given by:

$$\mathbf{g}_v = \begin{pmatrix} g_n & g_e & g_d \end{pmatrix}^{\mathrm{T}} = \begin{pmatrix} -\frac{1}{r}\frac{\partial U}{\partial \lambda} & -\frac{1}{r\cos\lambda}\frac{\partial U}{\partial \phi} & -\frac{\partial U}{\partial r} \end{pmatrix}^{\mathrm{T}} \tag{2.16}$$

Having presented the gravity computation, the characteristics of this method can be evaluated. Firstly, this model is guaranteed to converge to the adequate gravity outside of the Brillouin Sphere (Werner and Scheeres, 1996) and can be truncated to the desired accuracy for the model. Therefore, this method should not be used for surface gravity studies for irregularly shaped bodies, but only for modelling the gravity field outside of the Brillouin sphere.

In the NEAR-Shoemaker mission, several data of the 433 Eros asteroid were collected that allowed to obtain the spherical harmonics coefficients depicted in Table 2.2, making this model a suitable option for the implementation.

Polyhedron Model

This approach consists of modelling the asteroid as a polyhedron of constant density. A polyhedron is a three-dimensional solid body with a surface composed of planar faces that intersect along straight edges

Table 2.2: Properties of 433 Eros asteroid obtained from the NEAR-Shoemaker data (Yeomans et al., 2000): cosine and sine coefficients for degree and order four.

Normalised SH coefficients	True gravity model	Constant density shape model
C_{10}	0	0.000630
C_{11}	0	−0.000202
S_{11}	0	−0.000211
C_{20}	−0.052484(0.000032)	−0.052056
C_{21}	0	0.000317
S_{21}	0	−0.000101
C_{22}	0.082533(0.000046)	0.082671
S_{22}	−0.027739(0.000053)	−0.027107
C_{30}	−0.001159(0.000094)	−0.001701
C_{31}	0.004232(0.000045)	0.004053
S_{31}	0.003348(0.000048)	0.003369
C_{32}	0.001834(0.000101)	0.002004
S_{32}	−0.000689(0.000108)	−0.000810
C_{33}	−0.010308(0.000153)	−0.010435
S_{33}	−0.012218(0.000149)	−0.012145
C_{40}	0.012509(0.000299)	0.012762
C_{41}	−0.000105(0.000077)	−0.000258
S_{41}	−0.000050(0.000076)	0.000198
C_{42}	−0.017488(0.000249)	−0.017288
S_{42}	0.004872(0.000243)	0.004389
C_{43}	0.000056(0.000387)	−0.000223
S_{43}	−0.000332(0.000376)	−0.000273
C_{44}	0.017534(0.000486)	0.017571
S_{44}	−0.008993(0.000490)	−0.008667

or isolated points known as vertices. The modelling resolution of the body does not have to be constant and can be increased in more detailed parts. This approach provides an exact gravity modelling for a specific shape, thus having the errors of the model be a direct result of the accuracy of the shape determination and the assumption of a density distribution. Additionally, this model ensures that the gravity field converges and through the use of the Laplacian of the potential it can be determined if a particular point is located inside or outside of the body (Werner and Scheeres, 1996).

The gravity potential can be computed as presented in:

$$U = \frac{1}{2} G\rho \sum_{e \in \text{ edges}} \mathbf{r}_e^T \mathbf{E}_e \mathbf{r}_e \cdot L_e - \frac{1}{2} G\rho \sum_{f \in \text{ faces}} \mathbf{r}_f^T \mathbf{F}_f \mathbf{r}_f \cdot \omega_f \tag{2.17}$$

where G is the gravitational constant, ρ is the density, which can vary along the polyhedron volume, and $\mathbf{r}$ is the position at which the gravity field is evaluated. Additionally, the suffixes f and e present stand for face and edge respectively.

It should be noted that the dyadic products $\mathbf{E}$ and $\mathbf{F}$ for each of the faces can be described with:

$$\begin{aligned} \mathbf{E}_e &= \hat{\mathbf{n}}_A \left(\hat{\mathbf{n}}_{12}^A\right)^T + \hat{\mathbf{n}}_B \left(\hat{\mathbf{n}}_{21}^B\right)^T \\ \mathbf{F}_f &= \hat{\mathbf{n}}_f \hat{\mathbf{n}}_f^T \end{aligned} \tag{2.18}$$

where $\hat{\mathbf{n}}$ is the normal vector that points outwards of each of the faces. Furthermore, the dimensionless per-edge factor L_e is defined in Eq. (2.19), where $\mathbf{r}_i$, $\mathbf{r}_j$ are the vectors from the origin to the vertices P_i and P_j, respectively.

$$L_e = \ln \frac{\mathbf{r}_i + \mathbf{r}_j + e_{ij}}{\mathbf{r}_i + \mathbf{r}_j - e_{ij}}, \tag{2.19}$$

Similarly to the per-edge factor, the per-face factor ω_f is defined by:

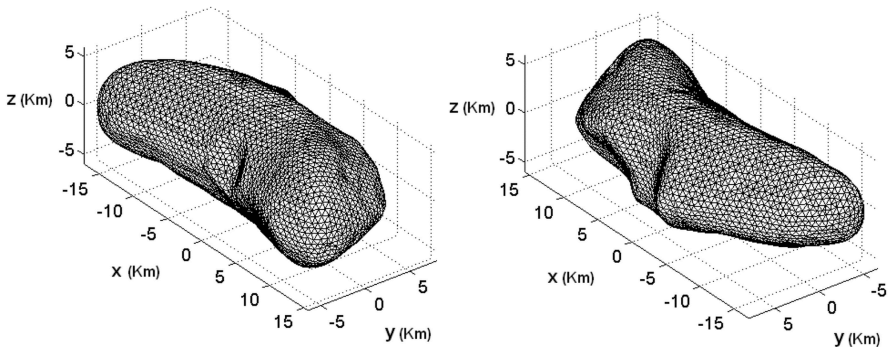

Figure 2.5: 433 Eros representation using the Polyhedron model with 7790 faces (Chanut et al., 2014)

$$\omega_f = 2 \arctan \left[\frac{\mathbf{r}_i \cdot \mathbf{r}_j \times \mathbf{r}_k}{\mathbf{r}_i \mathbf{r}_j \mathbf{r}_k + \mathbf{r}_i \left(\mathbf{r}_j \cdot \mathbf{r}_k \right) + r_j \left(\mathbf{r}_k \cdot \mathbf{r}_i \right) + r_k \left(\mathbf{r}_i \cdot \mathbf{r}_j \right)} \right] \tag{2.20}$$

Having described the computation of the gravitational potential, the following equation defines the gravitational acceleration at a given location.

$$\mathbf{g}(\mathbf{r}) = \frac{\partial U(\mathbf{r})}{\partial \mathbf{r}} = -G\rho \sum_{e \in e \text{ edges}} \mathbf{E}_e \mathbf{r}_e \cdot L_e + G\rho \sum_{f \in \text{ faces}} \mathbf{F}_f \mathbf{r}_f \cdot \omega_f \tag{2.21}$$

In regards to utilising this model for 433 Eros, Yeomans et al. (2000) state that the asteroid's gravity field can be obtained by assuming a constant density and using the polyhedron shape model of Eros. This shape model is depicted in Figure 2.5. It should be noted nevertheless that the assumption of a constant density for this model is controversial, and that it can be used to discover heterogenerity within the asteroid.

Mass Concentration Model

Also known as MASCONS, this model was first used in satellite geodesy applications in the 1970s, consisting of the use of a finite number of localized masses distributed over an evenly spaced grid in a volume to represent its mass (Russell and Arora, 2012). Note that the summation of the individual masses used is equal to the total mass of the body in question.

Figure 2.6 depicts the representation of different approaches of the MASCON model used for the gravity-field model of 433 Eros asteroid.

This method allows us to model the gravity field of irregularly shaped and heterogeneous density asteroids. However, it has a number of shortcomings. This model does not provide data indicative of if a point is inside or outside of the body. Furthermore, it is known to be less accurate than a SH model for a given computational effort. Additionally, this approach converges to the true gravity field with limitations on the number of mascons used (Werner and Scheeres, 1996). As Russell and Arora (2012) noted, this model has an ill-conditioned summation problem resulting from the point-mass terms taking both positive and negative values. This leads to summation errors giving in a precision loss of approximately three digits.

Discussion

Having examined the most commonly used methodologies for gravity-field estimation, a decision has been made to use the spherical harmonics method for this thesis. This is a result of several considerations.

Firstly, the point-mass approximation has been discarded due to the fact that while it provides an adequate approximation for far fields, it is not sufficient for navigation in the vicinity of an irregularly shaped asteroid. However, this model is used for testing and verification of the UKF filter in Subsection 4.6.2.

The MASCON model, while allowing navigation inside the Brillouin sphere, has also been discarded given its extensive computational requirements and the fact that, for the same computational load, spherical harmonics offer higher accuracy results. The same reasoning has been followed for the use

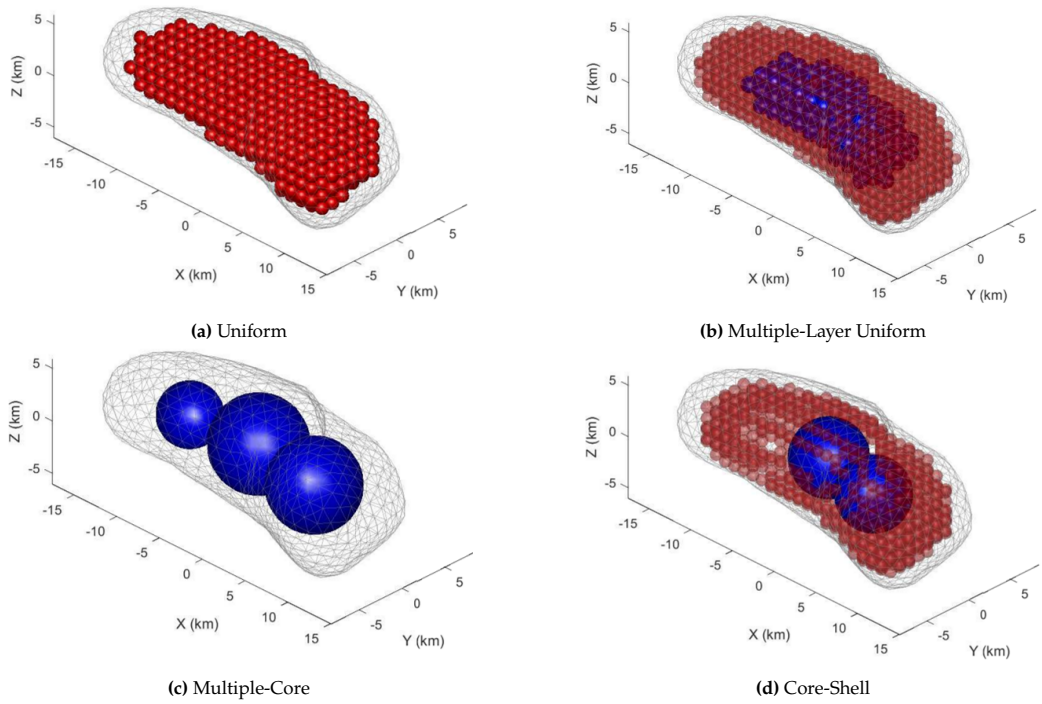

(a) Uniform

(b) Multiple-Layer Uniform

(c) Multiple-Core

(d) Core-Shell

Figure 2.6: MASCON model applied to 433 Eros asteroid (Russell and Wittick, 2017)

of polyhedron models. While this model converges inside the sphere and is suitable for both regions, it was demonstrated by Chanut et al.(2015) that its use requires an even higher computational load than the MASCON model, thus making it an unsuitable choice for implementation for this research. Nevertheless, the polyhedron models have been used for modeling the shape of the asteroid, which is necessary for the definition of the landmarks and for the simulation of the satellite sensors, as well as for the simulation of the communications line-of-sight constraints. This is implemented in Section 4.5, and in particular, the per-edge-factor introduced is used for the detection of the landmarks inside of the NAVCAM field-of-view presented in Subsection 4.5.3.

The spherical harmonics model is suitable for computing the gravity field of this scenario outside of the Brillouin sphere, which is the region determined for the research. This model is chosen as the better suited for the simulation due to computational constraints. For the same resolution, the MASCOn and polyhedron model require higher computational loads. Using SH therefore reduces substantially the computation time of a very heavy simulation, which is a considerable advantage for the simulation.

2.2.2. Third-body Perturbation

The dynamics of the satellites around the asteroid can be affected by other bodies in the Solar System. This thesis is done under the assumption that only the Sun, located at a distance of approximately 1.45 AU from Eros, is considered a perturbing body in the environment. Note that other large bodies in the solar system have not been considered due to their considerably smaller effect. For instance, Jupiter has a mass of three orders of magnitudes lower than the Sun and has thus a much smaller effect at similar distances than the Sun from Eros. This can be considered negligible for the purposes of this research.

The region where the third-body perturbation should not be considered is defined within the Hill Sphere. This sphere provides an approximation of the region where in a 3-body system, the gravitational field of a secondary body (the asteroid) dominates over the influence of a third body. It can be computed with Eq. (2.22), where R_h represents the radius of the Hill Sphere, and M_{ast} and M_S represent the mass of the asteroid and the Sun respectively. Furthermore, a represents the semi-major axis of the body's orbit around the Sun and e the orbit's eccentricity.

$$R_h \approx a(1-e) \times \left(\frac{M_{ast}}{M_S}\right)^{\frac{1}{3}} \tag{2.22}$$

This results in a first approximation of around 1752 km, defining therefore this region as non-dominantly perturbed by the Sun. The perturbation of the Sun shall be considered outside of this region. Equation (2.23) presents the computation of the acceleration perturbation $\mathbf{a}_{3rd}$ exerted by the Sun on the satellites, where M_{ast} and M_S represent the mass of the asteroid and the mass of the Sun respectively, and where $\mathbf{r}_{sat}$ and $\mathbf{r}_S$ are the position of the satellite and the Sun respectively.

$$\mathbf{a}_{3rd} = -GM_{ast}\frac{\mathbf{r}_{sat}}{\| \mathbf{r}_{sat} \|^3} + GM_S\left(\frac{\mathbf{r}_{sat}-\mathbf{r}_S}{\| \mathbf{r}_{sat}-\mathbf{r}_S \|^3} - \frac{\mathbf{r}_S}{\| \mathbf{r}_S \|^3}\right) \tag{2.23}$$

In the work of Bourgeaux (2020), it was demonstrated that when Ero's Sphere of Hill is crossed, the bodies orbiting the asteroid shall do so with a stable orbit, and when entering the Sphere of Influence (SOI), the gravitational effect of 3rd bodies can be neglected. It should be noted nevertheless that this has yet to be proven by implementation and simulation. Furthermore, it is shown that the estimation of this perturbation is better done when the 3rd perturbation model is included in the navigation filter model.

2.2.3. Solar Radiation Pressure

Solar Radiation Pressure (SRP) is a non-conservative force that acts on satellites and spacecraft, affecting their orbits. As Markley and Crassidis (2014) states, this force acts on the bodies through a momentum exchange between the spacecraft and the incident photons. Consequently, this is only present when the spacecraft is in direct sunlight.

This is considered to be one of the most relevant sources of perturbation for spacecraft in deep space that are located far from an attractor (Capannolo et al., 2023). This perturbation depends on both the solar and spacecraft properties.

There are a number of models to estimate the SRP effect with different accuracy. The model presented by Markley and Crassidis (2014) consists of dividing the spacecraft into illuminated and shadowed surfaces. The resulting force of the summation of all the N number of illuminated surfaces is presented in the following equation:

$$\mathbf{a}_{SRP} = -P_\odot \sum_{i=1}^{N} \cos\theta_i A_i \left((1-c_R)\,\mathbf{e}_{S/B,i} + 2c_R \cos\theta_i \hat{\mathbf{n}}_i\right) \tag{2.24}$$

In it, $P_\odot$ represents the solar radiation pressure, θ_i depicts the angle of incidence of the photons in a given plane i, and A_i symbolises the area of a plane i. Additionally, c_R represents the reflectivity factor and $\mathbf{e}_{S/B,i}$ describes the unit vector directed towards the Sun and $\hat{\mathbf{n}}_i$ the normal vector of the spacecraft surface.

The simplest model, and the one whose implementation is available in Tudat is the cannonball model. This considers the spacecraft as a sphere and therefore does not consider the attitude of the spacecraft (Capannolo et al., 2023) and is computed as:

$$\mathbf{a}_{SRP,A} = -\frac{P_{SRP}c_R A}{m}\hat{\mathbf{r}}_{Sun,A} \tag{2.25}$$

In it, m depicts the spacecraft mass, A its area, and $\hat{\mathbf{r}}_{Sun}$ the direction of the Sun with respect to the spacecraft. Additionally, P_{SRP} corresponds to the radiation pressure, which can be obtained through:

$$P_{SRP} = \frac{SF}{c} \tag{2.26}$$

Note that c represents the speed of light and SF the solar flux.

For the purposes of this research, the cannonball model has been chosen for the SRP computation of the orbiting bodies. This simplifies the implementation at the expense of decreasing the accuracy and reliability of the results. Therefore, to be conservative, an error of 5 % will be considered in the implementation. Additionally, it should be noted the use of the cannonball model implies that the CubeSats and mothership are simulated as spheres.

2.3. Spacecraft and CubeSats dynamics

The simulator will have to model accurately the dynamics of the spacecraft and CubeSats in the scenario. Therefore, it is crucial that the forces acting on these bodies are accurately modelled as well as their attitude. Furthermore, it is of utmost importance that adequate propagator and integrator models are chosen for the simulation.

2.3.1. Equations of Motion

The basic equations of motion that describe the orbit of bodies around the asteroid are given by:

$$\begin{aligned} \frac{\mathrm{d}\mathbf{x}}{\mathrm{d}t} &= \mathbf{v} \\ \frac{\mathrm{d}\mathbf{v}}{\mathrm{d}t} &= \mathbf{a} \end{aligned} \tag{2.27}$$

The acceleration is defined as the force acting on the body $\mathbf{f}$ divided by the mass ($\mathbf{a} = \mathbf{f}/m$). As Section 2.2 has presented, there are three accelerations to be considered in the asteroid environment. The total force exerted on the body composed by the sum of the gravitational force from the asteroid ($\mathbf{f}_{grav}$), the solar radiation pressure force ($\mathbf{f}_{SRP}$) and the 3rd body perturbation ($\mathbf{f}_{3rd}$) force exerted by the Sun. With this consideration, the acceleration of the bodies in the inertial frame ($\mathbf{a}_I$) is calculated as:

$$\mathbf{a}_I = \mathbf{C}_{I/A}\mathbf{a}_{g,A} + \mathbf{a}_{SRP,I} + \mathbf{a}_{3rd,I} \tag{2.28}$$

It should be noted that the gravity-field acceleration is expressed in the asteroid reference frame, and therefore requires a transformation from the asteroid frame to the inertial reference frame.

2.3.2. Orbit Propagation Models

Propagation methods are indispensable tools in orbital mechanics for the prediction and simulation of the trajectories of bodies in space. Several propagator methodologies have been considered for implementation in this research to ensure that an adequate propagator is used.

The Cowell propagator model, as presented by Pascual (2019), is the simplest methodology available and the first to be considered for this implementation. This model is able to propagate the equations of motions with as many perturbations, which makes it appropriate for this scenario considering the perturbations from the Sun considered. Furthermore, another advantage is its simple implementation and use of Cartesian coordinates. Nevertheless, this model has been shown to be the least computationally efficient of all.

Another propagator considered is the Encke model. This model is able to improve Cowell's method efficiency by integrating the difference between the real perturbed orbit and the unperturbed orbit (Pascual, 2019), thus increasing the complexity of its implementation. Additionally, this method also uses Cartesian coordinates for the state representation, which facilitates the interpretation of the results obtained. However, it should be noted that for this method to present a good accuracy, it must be used in a scenario where the effect of the perturbation effects is considerably lower than the effect of the main acceleration, in this case, the gravity field of the asteroid. Since this is the case, this propagator model is better suited than the Cowell model, since it offers better accuracy and a simple implementation.

The USM model propagators are adequate for the propagation of perturbed orbits, being competitors of the Cowell and Encke models (Vittaldev et al., 2012). USM uses quaternions and velocity-hodograph parameters to represent orbits (Altman, 1972), which allows this model to have better numerical stability than Cowell and Encke. This is due to the fact that whereas the Cartesian coordinates vary at each time step, describing the state with USM results in having three slowly varying and four relatively fast varying elements (Vittaldev et al., 2012). Additionally, the USM propagators have shown a considerable increase in computational efficiency with respect to Cowell and Encke. In particular, out of these, the USM method with exponential map (USM-EM) has been found to have better performance in terms of both accuracy and CPU load (Vittaldev et al., 2012). This comes at the expense of an increase of difficulty in the interpretation of the propagation results. Nevertheless, a conversion from the USM-EM can be easily carried out into Cartesian coordinates.

Additionally, the Dromo regularisation method has been considered. While regularised methods have not been widely adopted for orbital propagation problems, these have been shown to offer a significant reduction in the steps to obtain the same accuracy as Cowell or Encke methods (Geul

et al., 2021). Possible reasons for this can be attributed to the fact that they present a more difficult implementation than other methods or that they require additional transformations to obtain the time variable of the propagation. This method has shown promising efficiency results for the same accuracy as the previous methods at the expense of an increase in the difficulty of its implementation.

With these methods' characteristics in mind, a proper decision can be made. Although, ideally, the methodologies that provide lower computational loads are better suited for the thesis, this is not the driver for the proper choice of propagator method. For a proper representation of the model, the constellation of satellites will have to be evaluated at the refresh frequency of its sensors. Therefore, while the models presented have been shown to have improved efficiency by maintaining reliable measurements using large time steps in the propagation, the time steps that must be used are small and determined by the sensors, making, therefore, these models' main advantage null for the thesis. With this consideration, the models that best fit the requirements for this scenario are Cowell and Encke.

Discussion

Both Cowell and Encke methods have an easy implementation and interpretability of the results, through the use of Cartesian coordinates.

On the on hand, the Cowell method is not dependent on any *a priori* assumptions on the behaviour of the spacecraft, and that it presents simple equations of motion that ease its implementation. Furthermore, this propagation method has three main disadvantages. Firstly, it can present large values for its state derivative, which can result in larger numerical errors. Additionally, it also can present large variations in its state derivative, increasing the difficulty of setting an adequate time step. Furthermore, it is a slow propagator, which is due to the fact that it has to perform the numerical computations over a large number of small time steps to maintain the desired accuracy (Rollock, 1994).

On the other hand, the main advantage of the Encke model is its small state derivatives and small state derivatives variations. However, this comes at the cost of the states' accumulation over time, which results in $\Delta\mathbf{r}$ and $\mathbf{r}$ presenting similar magnitudes. Furthermore, there is an increase in the complexity of the differential equation with respect to the Cowell method and it can additionally present faster variations in the state elements. In contrast, this model has one main disadvantage. For the Encke model to be more efficient than Cowell, the main gravity perturbation must be considerably higher than the effect of all the perturbations. Otherwise, as stated by Pascual, 2019 (Pascual), the method requires a number of extra digits of computer precision to maintain a reasonable accuracy.

Cowell has been seen to be the propagation method that requires smaller time steps to maintain a high level of accuracy, while Encke can be used with larger time steps (Wakker, 2015). This is however not a determinant factor for the best performing method in this scenario, since small time steps will be used as required by the simulation of the hardware components of the satellites in the constellation. In particular, for the same time step, Wakker (2015) states that Encke's method involves more computation time per step than Cowell's.

With these considerations, the main determining factor between both is the fact that Encke has limitations when the perturbing forces are large and accumulate over time, which requires the reference orbit to be rectified. This can be avoided by using Cowell, and thus this method has been chosen as better suited for the research. This method is presented in more detail in the following section.

Cowell

Developed by P. H. Cowell at the beginning of the 20th century, this is the simplest method available for the computation of a perturbed orbit (Wakker, 2015). As Rollock (1994) states, this is also a high-fidelity propagator, since it solves complete unsimplified differential equations. Additionally, this method uses Cartesian coordinates to represent the state of the spacecraft.

Its common formulation is presented in the following equation:

$$\ddot{\mathbf{r}} + \frac{\mu}{r^3}\mathbf{r} = \frac{\sum \mathbf{f}_{\text{pert}}}{m} \tag{2.29}$$

Moreover, the states are presented as:

$$\mathbf{x} = \begin{pmatrix} \mathbf{r} \\ \dot{\mathbf{r}} \end{pmatrix} \quad \dot{\mathbf{x}} = \begin{pmatrix} \dot{\mathbf{r}} \\ \ddot{\mathbf{r}} \end{pmatrix} \quad \ddot{\mathbf{r}} = \frac{\sum \mathbf{f}}{m} \quad s = t \tag{2.30}$$

where m stands for the mass, μ for the standard gravitational parameter, and $\mathbf{f}_{\text{pert}}$ for the perturbation forces. Additionally, $\mathbf{x}$ represents the state of the spacecraft in Cartesian coordinates, where $\mathbf{r}$ depicts the position, $\dot{\mathbf{r}}$ the velocity, and $\ddot{\mathbf{r}}$ the acceleration.

2.3.3. Orbit Integration Methods

The use of an adequate integrator method is important to ensure the accuracy, stability, and efficiency of the propagation. There are a number of integration models that can be used with the chosen propagation method. The most basic methodology that can be used is the Euler integration method (Rosłoniec, 2008), however, there are better methodologies that can provide an improvement in both computational efficiency and accuracy of the results.

The Runge-Kutta method is widely used. This technique is known for being a reliable method with a relatively easy implementation. Additionally, the Runge-Kutta method allows for propagation with fixed time steps and with variable time steps (Runge-Kutta-Fehlberg), which increases the efficiency of the method, maintaining a given level of error tolerance. With these considerations, this method is considered as a good option for use in the simulation.

Another known methodology is the Richardson extrapolation and in particular its implementation as the Bulirsch-Stoer integrator. This method is particularly popular for its adequacy for long integration periods, being able to provide adequate quality solutions with a good computational efficiency [1]. Given that the time steps that will be used in the simulation will be small, as presented earlier, this integrator is not studied further and discarded as it is not the most efficient for the scenario considered.

Another well-known integrator method is the Adams-Basforth-Moulton. This is a multistep method, which improves its efficiency by using the information from previous steps for the computation of the current time step[2]. This integrator presents good CPU efficiency. Furthermore, it is well suited for smooth solutions, which is the case of this scenario. Therefore is considered and further studied as an adequate choice.

Additionally, there are less common integration methodologies that could also be used in this scenario such as DVODE, Gauss-Jackson Integration (Berry and Healy, 2004), Strömer-Cowell (Ramos and Vigo-Aguiar, 2005), Shampine and Gordon, and Taylor Series Integration. In particular, Taylor Series Integration seems to present a considerable advantage in the integration. Taylor Series Integration has been shown to have good outcomes in orbital propagation for high order and large time steps, outperforming other commonly used integrators in terms of CPU computational load. However, this does not offer an advantage in this particular scenario, where small time steps will be used.

With these considerations, both Runge-Kutta-Fehlberg and the Adams-Bashforth-Moulton are adequate options for this scenario, providing reliable accurate results. Considering that the system uses a small and fixed time step, the main consideration for the determination of the integrator is that it can provide a reliable value with a low CPU computational cost. While the use of a simple RK4 method requires four evaluations, the fourth-order Adams-Bashforth-Moulton predictor-corrector method requires only two evaluations per time step, thus presenting an advantage in terms of computational efficiency. This was further confirmed by Gebregiorgis and Gonfa (2021), who compared the computation times with the use of both methodologies and found the ABM to be considerably faster. Moreover, this was additionally confirmed through simulations of the propagation of a three-satellite constellation, which showed significantly low differences in the trajectory obtained for a time step of two seconds between RK4 and Adams-Bashforth-Moulton, while having considerably faster results with the use of the second integrator. Additionally, both methods are implemented in Tudat and therefore their implementation in the simulation is not a differentiating trait. With these considerations, it is determined that the best choice for the scenario is the use of the Adams-Bashforth-Moulton integration method with a fixed time step.

The Adams-Basforth-Moulton integrator uses two integration methods: the Adams-Bashforth, which is an explicit, linear and multi-step technique as presented by Bashforth and Adams (1883), and the Adams-Moulton integration method, which is an implicit methodology as presented by Moulton (1926). These are presented in this subsection following Hayes (2011).

[1] Tudat, "Integration Setup", Available at https://docs.tudat.space/en/0.0.3/_src_user_guide/state_propagation/integration_setup.html, Accessed on 24-12-2023

[2] University of Connecticut, "Multistep methods", Available at https://www.phys.uconn.edu/~rozman/Courses/m3510_17f/downloads/multistep-methods.pdf, Accessed on 24-12-2023

Adams-Basforth

Following Hayes (2011) work, to depict this method functioning a given function $y(x)$ and their respective derivative $y'(x)$ are considered. These can be quantized with the initial conditions as $y_0 = y(x_0)$ with the following equation:

$$y_{i+1} \equiv y\left(x_{i+1}\right) = y\left(x_i\right) + \int_{x_i}^{x_{i+1}} y'(x, y)\mathrm{d}x \tag{2.31}$$

This method is based on the use of the Lagrange polynomial approximations of the derivative. Each step requires a new polynomial ($P_{\mathrm{AB}i}$), which for a convergence of order N, can be expressed as:

$$P_{\mathrm{AB}i}(\mathbf{x}) \equiv \sum_{j=i-N+1}^{i} y'_j \prod_{k=i-N+1, k\neq j}^{i} \frac{(\mathbf{x} - x_k)}{(x_j - x_k)} \tag{2.32}$$

where $y'_j = y'(x_j, y_j)$ and $\mathbf{x} = x - x_i$. This equation can be simplified by defining $\psi_{\mathrm{AB}ij}$ as:

$$\psi_{\mathrm{AB}ij}(\mathbf{x}) \equiv \prod_{k=i-N+1, k\neq j}^{i} \frac{(\mathbf{x} - x_k)}{(x_j - x_k)} \tag{2.33}$$

which results in the following equation:

$$P_{\mathrm{AB}i}(\mathbf{x}) = \sum_{j=i-N+1}^{i} y'_j \psi_{\mathrm{AB}ij}(\mathbf{x}) \tag{2.34}$$

The application of the Adams-Bashford approximation to the computation of y_{i+1} from a given origin of P_{AB} is presented in the following equation:

$$\begin{aligned} y_{\mathrm{AB}i+1} &\approx y_{\mathrm{AB}}\left(x_i\right) + \int_0^{\Delta x_i} P_{\mathrm{AB}i}(\mathbf{x})\mathrm{d}\mathbf{x} \\ &= y_{\mathrm{AB}}\left(x_i\right) + \int_0^{\Delta x_i} \sum_{j=i-N+1}^{i} y'_j \psi_{\mathrm{AB}ij}(\mathbf{x})\mathrm{d}\mathbf{x} \\ &= y_{\mathrm{AB}}\left(x_i\right) + \sum_{j=i-N+1}^{i} \left(\int_0^{\Delta x_i} \psi_{\mathrm{AB}ij}(\mathbf{x})\mathrm{d}\mathbf{x} \right) y'_j \end{aligned} \tag{2.35}$$

It should be noted that $\psi_{\mathrm{AB}ij}(\mathbf{x})$ represents a polynomial that can be integrated analytically through:

$$\psi_{\mathrm{AB}ij}(\mathbf{x}) = \frac{\phi_{\mathrm{AB}ij}(\mathbf{x})}{\phi_{\mathrm{AB}ij}\left(x_j\right)} \tag{2.36}$$

Note that $\Phi_{\mathrm{AB}ij}(\mathbf{x})$ is computed with:

$$\phi_{\mathrm{AB}ij}(\mathbf{x}) \equiv \prod_{k=i-N+1, k\neq j}^{i} (\mathbf{x} - x_k) = \frac{\Phi_{\mathrm{AB}i}(\mathbf{x})}{(\mathbf{x} - x_j)} \tag{2.37}$$

where $\Phi_{\mathrm{AB}i}(\mathbf{x})$ is computed as:

$$\Phi_{\mathrm{AB}i}(\mathbf{x}) \equiv \prod_{k=i-N+1}^{i} (\mathbf{x} - x_k) \tag{2.38}$$

Adams-Moulton

The Adams-Moulton methodology can be derived very similarly to the Adams-Bashford method (Hayes, 2011) and is computed as:

$$P_{\mathrm{AM}i}(\mathbf{x}) \equiv \sum_{j=i-N+1}^{i+1} y'_j \prod_{k=i-N+1,k\neq j}^{i+1} \frac{(\mathbf{x}-x_k)}{(x_j-x_k)} \tag{2.39}$$

As depicted, the upper limit is $i+1$ as opposed to the limit of i in the Adams-Bashford method. This equation can be transformed into the following:

$$P_{\mathrm{AM}i}(\mathbf{x}) \equiv \sum_{j=i-N+1}^{i+1} y'_j \psi_{\mathrm{AM}ij}(\mathbf{x}) \tag{2.40}$$

using $\psi_{\mathrm{AM}ij}(\mathbf{x})$, which can be defined as:

$$\psi_{\mathrm{AM}ij}(\mathbf{x}) \equiv \prod_{k=i-N+1,k\neq j}^{i+1} \frac{(\mathbf{x}-x_k)}{(x_j-x_k)} \tag{2.41}$$

The application of the Adams-Moulton approximation of y_{i+1} is described by:

$$\begin{aligned} y_{\mathrm{AM}}(x_{i+1}) &\approx y_{\mathrm{AM}}(x_i) + \int_0^{\Delta x_i} P_{\mathrm{AM}i}(\mathbf{x})\mathrm{d}\mathbf{x} \\ &= y_{\mathrm{AM}}(x_i) + \int_0^{\Delta x_i} \sum_{j=i-N+1}^{i+1} y'_j \psi_{\mathrm{AM}ij}(\mathbf{x})\mathrm{d}\mathbf{x} \\ &= y_{\mathrm{AM}}(x_i) + \sum_{j=i-N+1}^{i+1} \left(\int_0^{\Delta x_i} \psi_{\mathrm{AM}ij}(\mathbf{x})\mathrm{d}\mathbf{x} \right) y'_j \end{aligned} \tag{2.42}$$

Note that the polynomial $\psi_{\mathrm{AM}ij}(\mathbf{x})$ used can be integrated analytically with:

$$\psi_{\mathrm{AM}ij}(\mathbf{x}) = \frac{\phi_{\mathrm{AM}ij}(\mathbf{x})}{\phi_{\mathrm{AM}ij}(x_j)} \tag{2.43}$$

Additionally, $\phi_{\mathrm{AM}ij}(\mathbf{x})$ is defined in:

$$\phi_{\mathrm{AM}ij}(\mathbf{x}) \equiv \prod_{k=i-N+1,k\neq j}^{i+1} (\mathbf{x}-x_k) = \frac{\Phi_{\mathrm{AM}i}(\mathbf{x})}{(\mathbf{x}-x_j)} \tag{2.44}$$

where $\Phi_{\mathrm{AM}i}(\mathbf{x})$ is:

$$\Phi_{\mathrm{AM}i}(\mathbf{x}) \equiv \prod_{k=i-N+1}^{i+1} (\mathbf{x}-x_k) \tag{2.45}$$

Adams-Basforth-Moulton

The Adams-Basforth-Moulton is the desired integration method for the simulation, which is a combined predictor-corrector method. It follows the steps depicted below (Rozman, 2017):

1. **Prediction**: The Adams-Bashforth method is used to compute the initial approximation of y_{n+1}, which is expressed with $\hat{y}_{n+1}$.
2. **Evaluation**: The function $f(t_{n+1}, \hat{y}_{n+1})$ is evaluated.
3. **Correction**: The Adams-Moulton method is used to compute y_{n+1}, using $f(t_{n+1}, \hat{y}_{n+1})$.
4. **Evaluation**: The function $f(t_{n+1}, y_{n+1})$ is evaluated for use in the following step.

It must be considered that these methods require another methodology used for their initialisation. This is commonly done with RK. Additionally, it should be noted that as introduced by Rozman (2017), this method can maintain a constant level of precision, which is an additional advantage to its implementation.

2.4. Rotational Motion

It is crucial to consider the attitude of the bodies in the scenario to be able to properly model the environment and transform the force from one body to another accurately with the use of frame transformations, as presented in Section 2.1. This section presents the asteroid and spacecraft kinematics.

2.4.1. Asteroid Kinematics

The asteroid 433 Eros orbits the Sun with a period of 1.76 Earth years[3] with a period of rotation of 5.27 Earth hours[3], revolving around the Z-axis. The angular velocity of the asteroid will be assumed to be constant in both direction and magnitude, as presented in the following equation:

$$\boldsymbol{\omega}_{A/I}^{A} = (0, 0, \omega_z)^T \tag{2.46}$$

Additionally, the attitude will be considered in the simulation. This can be directly computed through the use of the direction cosine matrix of the asteroid's attitude with respect to the inertial frame ($\mathbf{C}_{A/I}$):

$$\dot{\mathbf{C}}_{A/I} = -\boldsymbol{\omega}_{A/I} \times \mathbf{C}_{A/I} \tag{2.47}$$

where $\boldsymbol{\omega}_{A/I}$ is the vector depicting the rate of rotation of the asteroid with respect to the inertial frame. This equation must satisfy the six constraint equations on the nine elements.

2.4.2. Spacecraft and CubeSats Kinematics

A proper attitude representation of the spacecraft and CubeSats is crucial for the mission to ensure that the instruments used are pointed correctly and provide the desired measurements.

To accurately model the attitude of the orbiting bodies, the torque effects of the asteroid's gravity-field force, the Solar radiation pressure and the third body perturbations must be considered. Nevertheless, this thesis is carried out under the assumption that the attitude control of the CubeSats and motherships is not simulated and that the instruments are pointing where they should be. An adequate attitude control system would use instruments such as reaction wheels to correct the effect of the torques and point the body adequately. Since this control is not simulated, the inclusion of the torques in the model is not necessary.

[3]The National Aeronautics and Space Administration, "Eros", Available at: https://science.nasa.gov/solar-system/asteroids/433-eros/, Accessed on 24-12-2023

3

Navigation system

To properly design a mission around an asteroid, it is essential to have a working navigation system. Navigation aims to answer the basic question "where is the spacecraft?". This requires knowledge of the surroundings and the state in which the spacecraft is and possibly was. The navigation system aims to estimate as accurately as possible the state of the spacecraft. This estimation is done through a navigation filter, which uses the measurement data of the environment to estimate the state variables.

This chapter presents the mission vehicles and their respective sensors which are to be used in the navigation system in Section 3.1, and then presents in Section 3.2 the estimator filter models for the navigation.

3.1. Mission vehicles and sensors

As presented in Chapter 1, the mission researched requires the use of a mother-ship and a number of CubeSats, all of which will orbit around the asteroid. This section will introduce their characteristics and the sensors that they carry to take the measurements for the navigation system.

Mothership

The mothership physical characteristics are not properly known due to the fact that the number of CubeSats that it must carry is unknown until the optimisation of the CubeSat constellation is carried out, and its design is out of the scope of this thesis. However, this spacecraft must be modelled for simulation purposes. This is done following the work of Razgus (2017) and Spee (2022), which carried out their thesis simulations modelling the spacecraft after the Rosetta mission spacecraft[1], which is depicted in Figure 3.1.

The main characteristics are depicted in Table 3.1, having been obtained directly from ESA. In particular, it is important for the model to consider that the Rosetta spacecraft had a mass of 2100 kg at rendezvous with the target body. It should be noted that if attitude control was done in the spacecraft, it would be crucial to model the shape of the spacecraft with its inertia tensors. However, as stated in the previous chapters, the thesis simulates the spacecraft with no attitude control, assuming that the

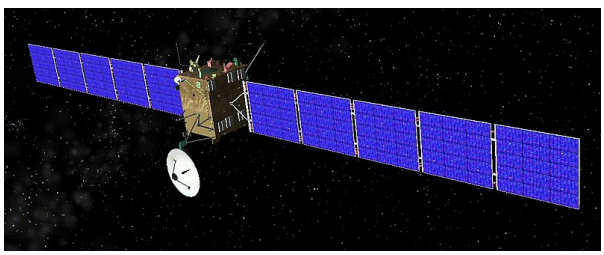

Figure 3.1: Rosetta spacecraft [1]

[1]Wikipedia, "Rosetta", Available at: https://es.wikipedia.org/wiki/Rosetta_%28sonda_espacial%29, Accessed on 07-12-2023

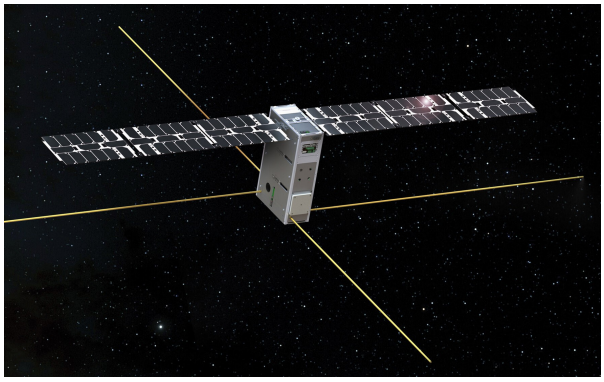

Figure 3.2: Juventas spacecraft[3]

mothership has a control system that points the camera and lidar towards the centre of the asteroid at all times. Furthermore, given that the cannonball model has been chosen to model the SRP, a model of the surfaces of the mothership is not required. The reflectivity of this sphere can be assumed to be C_r =0.5 (Spee, 2022).

Additionally, while the Rosetta spacecraft carried a number of instruments for the mission, this thesis considers only the sensors used in the navigation system, which are modelled in the simulation to carry out the estimations. This spacecraft will carry a lidar and a navigation camera (NAVCAM). Additionally, it should be noted that if this research considered attitude control, the addition of sensors for attitude determination, such as Sun sensors, star trackers and, gyroscopes, would be required.

CubeSats

Similarly to the mothership, a proper model for the CubeSats is not known, and its design is out of the scope of the thesis. Therefore, the CubeSats are modelled after an average CubeSat used in a deep space mission for the geophysical characterisation of the Dimorphos asteroid known as Juventus[3], which is shown on Figure 3.2.

The main characteristics of the CubeSat are depicted in Table 3.2. Similarly to the mothership, the CubeSats are simulated with no attitude control and as a sphere due to the use of the cannonball model, with a reflectivity (C_r) of 0.5.

Similarly to the mothership, sensors for the navigation system are modelled. While the use of an altimeter, presented in Subsection 3.1.3 was initially considered for the modelling of CubeSats due to it being less computationally demanding and power-consuming, and thus, better suited for smaller satellites, the use of a single altimeter is insufficient for the estimation of the position from the

Table 3.1: Mothership characteristics[2]

Characteristics	Value
Volume	2.1 x 2.0 x 2.8 m
Solar array diameter	32 m
Total Solar array surface	64 m^2
Total launch mass	3000 kg (approx.)
Propellant mass	1670 kg (approx.)
Science payload mass	165 kg

Table 3.2: CubeSat characteristics [3]

Characteristics	Value
Volume	10 x 20 x 30 cm (6U-XL)
Mass	12 kg

[2]European Space Agency, "The Rosetta orbiter" Available at: https://www.esa.int/Science_Exploration/Space_Science/Rosetta/The_Rosetta_orbiter, Accessed on: 07-12-2023

[3]ESA, "Juventas Cubesat", Available at: https://www.heramission.space/hera-mission-juventas-cubesat, Accessed on 30-12-2023

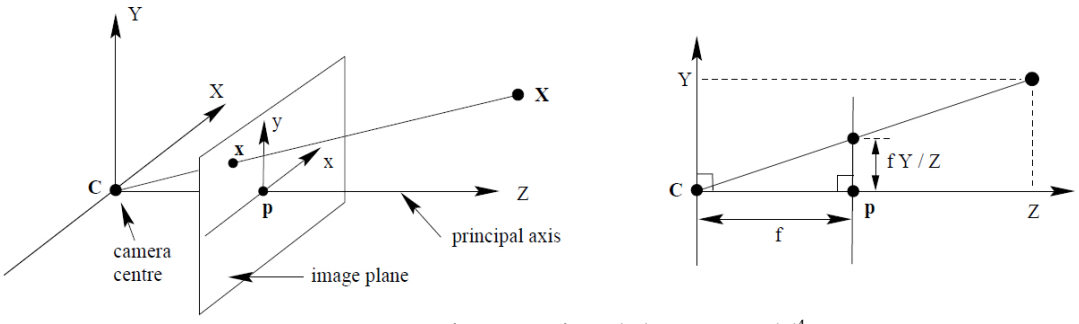

Figure 3.3: Image formation of a pinhole camera model[4]

landmarks, and therefore, the software models lidars to properly obtain the position of the satellite from the landmarks.

It should be noted that these missions commonly require the use of star trackers (STT) and Sun sensors for the determination of the attitude of the spacecraft orbiting the asteroid. Nevertheless, these are not required in this simulation since no attitude control is simulated on the vehicles. Furthermore, it should be additionally considered that since the research does not focus on the hardware design and therefore a proper design of the satellites with additional sensors has not been considered.

3.1.1. Navigation cameras

Navigation cameras (NAVCAM) are a key instrument for the localization of recognisable features, in this case, on the surface of an asteroid. These can be used for modelling the shape of the asteroid and to determine the relative position of the spacecraft when the coordinates of the recognisable features are known. This is known as Landmark Tracking, which was studied for autonomous navigation for landings by Gaskell (2005).

This technology consists of using images taken through the optical cameras that are then processed onboard to be used for autonomous navigation. This requires complex algorithms that are out of the scope of this thesis. It will therefore be assumed that this instrument directly outputs the coordinates of the landmarks inside of its field of view.

Additionally, the implementation of this NAVCAM model requires a previous generation of the landmark map of 433 Eros, the determination of which of those landmarks are visible, and the transformation of the landmarks coordinates in the asteroid frame into the field of view plane of the camera. This transformation is described in the following paragraphs.

Using a simple pinhole camera model[4], which is depicted in Figure 3.3, the reference frame of the camera is located in its optical centre and is assumed to be aligned with the body.

Given a point "p", its coordinates $\begin{pmatrix} X_p & Y_p & Z_p \end{pmatrix}^T$ in the image plane can be described as

$$\begin{aligned} X_p &= f\frac{X}{Z} \\ Y_p &= f\frac{Y}{Z} \end{aligned} \tag{3.1}$$

where f is the focal length of the optic lens of the camera and coordinates (X, Y, Z) are expressed from the camera centre as illustrated in Figure 3.3.

Given that the image plane is a discretised matrix with a given number of pixels, the non-dimensional pixel coordinates u and v of "p" can be computed with:

$$\begin{aligned} u &= \frac{f}{p_{size}}\frac{X}{Z} \\ v &= \frac{f}{p_{size}}\frac{Y}{Z} \end{aligned} \tag{3.2}$$

where the pixel size is represented by p_{size}.

[4]HediVision, "Pinhole Camera Model", Available at: https://hedivision.github.io/Pinhole.html, Accessed on 14-12-2023

Considering that the landmark algorithm recognition is not implemented in the thesis, additional noise and errors are added to the coordinates as depicted by the following equation :

$$\begin{pmatrix} \tilde{u} \\ \tilde{v} \end{pmatrix} = \begin{pmatrix} u \\ v \end{pmatrix} + \begin{pmatrix} N(0, \delta u) \\ N(0, \delta v) \end{pmatrix} \tag{3.3}$$

where δu and δv are white Gaussian noise with zero mean. Additionally, in some cases, it might be useful to express the measurements as unit vectors as:

$$\tilde{\boldsymbol{b}} = \frac{1}{\sqrt{(p_{size}\tilde{u})^2 + (p_{size}\tilde{v})^2 + f^2}} \begin{pmatrix} p_{size}\tilde{u} \\ p_{size}\tilde{v} \\ f \end{pmatrix} \tag{3.4}$$

Table 3.3 presents the technical characteristics of the NAVCAMs of both types of spacecraft in the mission. The technical characteristics of the mothership have been taken as a reference from Rosetta's navigation cameras (Herfort and Casas, 2015), and the technical specifications for the CubeSats from Ferrari et al. (2021).

As introduced previously, all the satellites in the constellation require NAVCAMS for the landmark detection to estimate their position. The implementation of this sensor in the algorithm is presented in Subsection 4.5.3.

3.1.2. Lidar

A lidar is an instrument used for autonomous navigation. As Colagrossi et al. (2023) depict, this electro-optical sensor directs a laser beam in the desired direction and is able to measure the reflected light, analyse the beam of light properties and its arrival time.

This instrument carries out its measurements through the computation of the laser beam return times and its wavelength (λ). Additionally, 3D measurements can be obtained through the use of these laser scanners independently of the illumination of the body studied, in this case, the asteroid. Nevertheless, this comes at the expense of a bulkier and less power efficient and more computationally expensive instrument.

The principle behind this technology relies on the reflection of light. This instrument sends a laser light onto a target and measures the time of arrival and wavelength of the reflected beam (Mehendale and Neoge, 2020). The distance between the orbiting spacecraft and the asteroid landmarks can be computed through the following equation:

$$\rho = c\frac{t}{2} \tag{3.5}$$

where ρ is the range of the spacecraft, c is the speed of light, and t is the time from when the beam has been sent to when it has been received.

The simulation model will work under the assumption that the spacecraft will have a map of the asteroids' landmarks and the lidar will send pulses directed to the known landmarks with the aid of the NAVCAM. The combined use of the NAVCAM and lidar sensors for the relative position estimation of a spacecraft with respect to the asteroid is implemented in Subsection 4.5.5. This instrument selection has been made considering the research conducted by Woicke (2019) presenting the multiple sensor options that are available for landmark detection. In it, Woicke highlights that the digital elevation model (DEM) of the terrain can be obtained through single or multiple cameras (using stereo vision) or through the use of a lidar. The use of cameras is constrained by light conditions but can generate a DEM faster than when using a lidar, which is generally heavy and requires a substantial amount of power to function.

This scenario is represented in Figure 3.4, where $(x_s,\ y_s,\ z_s)$ represent the coordinates of the spacecraft and $(x_L,\ y_L,\ z_L)$ those of the landmark expressed in $\mathcal{F}_A$. Equation (3.6) presents the range computation through these coordinates.

Table 3.3: NAVCAM characteristics for the mothership and CubeSat

Characteristics	NAVCAM mothership	NAVCAM CubeSat
FOV	5x5 deg x deg	21x16 deg x deg
Sensor	1024x1024 pix x pix	2048×1536 pix x pix

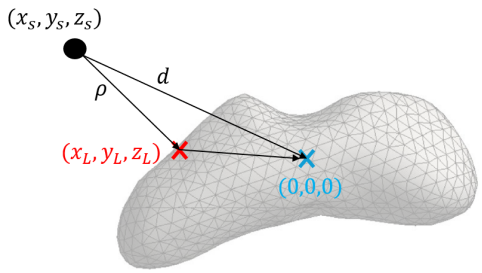

Figure 3.4: Range of the spacecraft to the asteroid landmark representation

$$\rho = \sqrt{(x_s - x_L)^2 + (y_s - y_L)^2 + (z_s - z_L)^2} \tag{3.6}$$

The simulator must take into consideration the resolution errors that the instrument can present. On the one hand, the measured range resolution is directly proportional to the resolution of the time measurements of the instrument, the range with its resolution errors $\tilde{\rho}$ is presented in the following equation:

$$\tilde{\rho} = c\frac{\tilde{t}}{2} \tag{3.7}$$

where the time with errors $\tilde{t}$ is computed as:

$$\tilde{t} = t + \sigma_t + \sigma_r \tag{3.8}$$

where σ_t and σ_r represent the error due to white Gaussian noise in nanoseconds and the resolution error, respectively. The sum of both of these parameters results in the noise covariance of the measurement errors as:

$$\sigma_l = \sigma_t + \sigma_r \tag{3.9}$$

Additionally, the lidar might present pointing errors and bias.

This instrument provides information on both the spacecraft's location in spherical coordinates and the relative velocity of the orbiting spacecraft. The measurement vector ($\mathbf{h}_i$) of the lidar for a i landmark is calculated as:

$$\tilde{\mathbf{h}}_i = \begin{pmatrix} \rho_i \\ \dot{\rho}_i \\ \theta_i \\ \psi i \end{pmatrix} + \boldsymbol{\sigma}_{l,i} \tag{3.10}$$

Note that ρ represents the range between the landmark and the sensor, $\dot{\rho}$ the rate of change of the range, and θ and ψ represent the position in spherical coordinates with azimuth and elevation angles, respectively. The angles including pointing errors are:

$$\begin{aligned} \tilde{\theta} &= \theta + N(0, \delta_\theta) \\ \tilde{\psi} &= \psi + N(0, \delta_\psi) \end{aligned} \tag{3.11}$$

These angles can be computed with the following equations:

$$\begin{aligned} \theta &= \arctan\frac{y_{L,b}}{x_{L,b}} \\ \psi &= \arctan 2\frac{z_{L,b}}{\sqrt{x_{L,b}^2 + y_{L,b}^2}} \end{aligned} \tag{3.12}$$

where the Cartesian coordinates are presented in the body's reference frame, as shown in Figure 3.5.

The lidar simulation implementation in the software is presented in Subsection 4.5.4, used for the estimation of the range between the satellites and the landmarks.

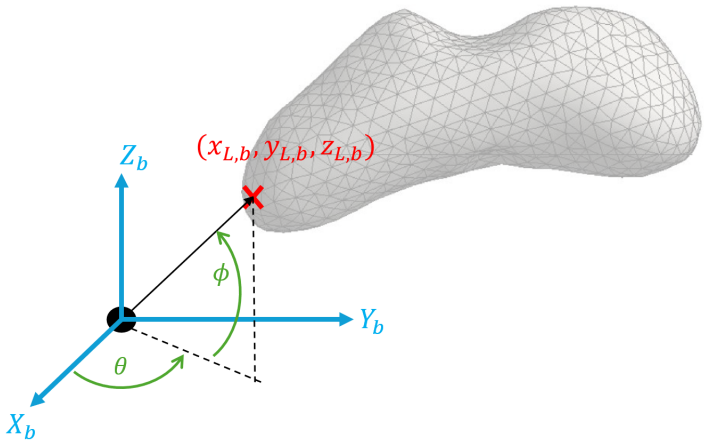

Figure 3.5: Position of the landmark in spherical coordinates

3.1.3. Altimeter

First developed in the early 1960s, satellite altimetry has been used to obtain accurate measurements of the surface shape of planets. These instruments are based on the measurement of the time that an electromagnetic signal takes from its transmission to its reception after bouncing back on the surface of the asteroid (Colagrossi et al., 2023). This principle is followed by all altimeters, which can have a variety of properties. In particular, a differentiation worth making in this thesis is between those using a radar and a laser.

The altimeter to be simulated in the CubeSats is an instrument used to obtain the distance of the satellite to a given point of the asteroid. The instrument sends a signal that bounces back from the surface of the asteroid and is received by a transponder. Measuring the time between the transmission and reception, the instrument is able to compute the distance of the CubeSat to the asteroid.

The altimeter's crucial parameter is the antenna footprint, which represents the area of the surface in which the range measurement is done. This area is defined by the beam width. The narrower the beams used, the better accuracy that is provided, but the larger the antennas must be. This can be improved through the use of a pulse-limited configuration, for which a smaller diameter antenna can be used.

The main distinction between the use of radar and laser altimeters remains in the working frequency used. Radar altimeters have a larger footprint and therefore have a worse horizontal resolution. Nevertheless, the vertical accuracy remains comparable to that of a laser altimeter. Additionally, radar altimeters are heavier than laser altimeters, but require a lower power, which is a crucial parameter to account for in a CubeSat power budget. Additional distinctions can be made in the presence of an atmosphere, but these shall not be considered, since the asteroid does not have an atmosphere.

The model of the altimeter in the simulation will be assumed to point directly to a landmark of a known position and obtain the range from the CubeSat. This technology contains small errors due to the wave dispersion and pointing of the wave. These must be included when modelling the sensor in the software. The resulting sensor measurement ($\mathbf{h}_i$) of a landmark i is presented in the following equation:

$$\mathbf{h}_i = \rho_i + N(0, \sigma_{l,i}) \tag{3.13}$$

An example of the characteristics of laser altimeters instruments is presented in Table 3.4, with the FLARE [5] altimeter. Peral et al. (2018) present common radar altimeter used in CubeSats characteristics stating that they might require up to 22 W of power, and in the case of the RainCube, a NASA InVEST mission that demonstrated the first radar payload on a CubeSat, consume 10 W for receiving and 3 W for being on standby, weigh 5.5 kg, and use Ka-band.

3.1.4. Hardware constraints for the mission

The presented sensors will provide the necessary measurements for the estimation of the gravity field of the asteroid. However, there are additional hardware considerations to be made for the scenario at

[5] SatSearch, "FLARE - Full-wave Laser RangEfinder", Available at: https://satsearch.co/products/mda-flare-full-wave-laser-rangefinder, Accessed on 07-12-2023

hand. In particular, one of the constraints that this thesis will consider is that of the communication between CubeSats and mothership for the transmission of the computed measurements. It should be noted that this hardware is not simulated, but only considered as a constraint of the scenario.

Two main considerations are to be had with satellite communications: the bit rate, to consider the time that a CubeSat requires of LOS for the transmission of the data, and the slant range, to ensure that the distance between the CubeSat and the mothership is adequate for the transmission.

This communication can be done through radio or laser. Satellite communications have commonly used radio. In particular, the bands UHF (300 to 1000 MHz), S (2 to 4 GHz), X (8 to 12 GHz) and Ka (27 to 40 GHz) are commonly used. In recent years, the S, X, and Ka bands have been used more extensively, offering higher transmission rates. Furthermore, these are the frequencies used in the NASA Near Space Network (NSN)[6]. While operation at such high frequencies may present issues when having atmospheres, this is not a consideration to be had in this scenario and therefore not a disadvantage.

The Integrated Solar Array and Reflectarray Antenna (ISARA) mission[6], carried out at JPL, used a Ka-band communications system in a CubeSat and successfully demonstrated its functioning with a downlink rate of 100 Mbps, from an orbital altitude of 600 km[7]. This serves as a confirmation of suitability for the research scenario. Furthermore, it can be considered that given the high rate of transmission available, the data information is done instantly when LOS is achieved between CubeSat and mothership.

Additionally, it should be noted that laser communications could also be an option for the communications scenario. However, while this technology presents better performance in terms of bit rate and higher slant range, these require higher power, which might be an issue in CubeSats. In both cases, it can be determined that the transmission capabilities of the system are sufficient for the transmission of the measurements from CubeSats to the mothership and therefore the communication system will not be restricted by the distance between the satellites at the mothership since the ranges of semi-major axis that the constellation will have around the asteroid will be much lower than the maximum transmission distance of the communications system. Furthermore, as has been presented in Chapter 1, the system is modelled under the assumption that the communications are instantaneous. While this is not a true representation of the real system, given that the rate of transmission is quite high and that there is very little data to be transmitted, assuming an instantaneous transmission will still fairly represent the system and not have an effect on the conclusions obtained with the research.

3.2. Estimators

Navigation aims to provide an accurate estimation of the state of a spacecraft. This is a challenging task due to the discrepancies between the models used to estimate the trajectory and position of a spacecraft and the actual values of trajectory and position. As a consequence, several methodologies have been developed to provide high-accuracy estimations of the spacecraft's state. Recursive filtering techniques stand out for their efficiency in using a number of sensor measurements and estimating the desired variables. This section aims to determine which filter is better suited for the research scenario.

The first filters considered are Kalman filters, which are very effective estimators used in a wide range of applications. The Linear Kalman Filter (LKF) is the original Kalman Filter and the most simple of the family. This is known to be effective in the estimation of the state of a linear system from noisy

Table 3.4: Laser altimeter characteristics [5]

Characteristics	Laser altimeter
Measurement rate	1,5 Hz
Mass	900 g
Average power	8 W
Input voltage	28 V
Minimum range	50 m
Maximum range	5 km

[6]The National Aeronautics and Space Administration, "State-of-the-Art of Small Spacecraft Technology - Communications", Available at: https://www.nasa.gov/smallsat-institute/sst-soa/soa-communications/, Accessed on 23-12-2023

[7]eoPortal, "ISARA (Integrated Solar Array and Reflectarray Antenna)", Available at: https://www.eoportal.org/satellite-missions/isara#spacecraft, Accessed on 23-12-2023

measurements (Welch and Bishop, 2006). The LKF can be discarded as an adequate option for the dynamical scenario of the thesis, given that it aims to produce the estimation of a linear system.

The extended and the unscented Kalman filters present a considerable improvement from the LKF, being able to produce estimations of non-linear systems such as the orbital dynamics of a satellite, and are therefore better suited for this scenario. To make an appropriate choice between both, literature has been considered together with the specific scenario of the thesis.

The EKF is widely used in state estimation, presenting a faster convergence than other estimators available and producing highly accurate estimations. The UKF also presents a good performance for non-linear systems and can be a better choice than the EKF when its estimation efficiency is insufficient, presenting an improvement by the use of the Unscented Transformation method.

The UKF algorithm was preferred over the EKF by Bourgeaux (2020) for the estimation of the spherical harmonics coefficients of the gravity field. This decision was a result of the easier implementation of the UKF algorithm, which does not require the Jacobian matrix as the EKF does, requiring the analytical expressions or tuned numerical derivatives of each state parameter. Furthermore, it was seen that the UKF had a better performance when estimating the μ parameter.

The opposite choice was made by Spee (2022), preferring the use of an EKF over that of a UKF. This was due to the fact that the use of the UKF would result more computationally costly for the modelled scenario, using a polyhedron gravity field, requiring the system to carry out the computation of a large number of sigma points for each time step. In contrast, their gravity model has an easier analytical derivation, which confirms the preference for the use of the EKF.

In regards to computational load for both filters, literature presents several discrepancies. Wan and Merwe (2000) state that both filters have a comparable level of complexity and computational load when used in non-linear control applications requiring full-state feedback. However, Jose (2009), who studied the comparison between both filters when applied to an INS-GPS integration, showed that the EKF had considerably lower CPU times. This was confirmed by Wei et al. (2018) when applied to a SINS/GPS integrated navigation system, as shown in Table 3.6.

Another filter that has been considered, as opposed to the Kalman filter, is the Particle Filter (PF), which is known to be an effective method for estimating full state probability density function (PDF) of non-linear models and non-Gaussian PDFs (Mashiku et al., 2012). Furthermore, it is known to be fit for solving highly dimensional non-linear problems (Rigatos, 2012). The PF, similarly to the UKF does not require the Jacobian matrix, which is necessary in the EKF. Furthermore, it presents a performance improvement from the non-linear Kalman filter approach, since it is well-suited for the estimation of non-Gaussian measurements. Rigatos (2012) studied the performance of a non-linear Kalman filter and a particle filter for the case of integrated navigation of unmanned vehicles. It showed that while both UKF and PF provide reliable non-linear estimations, the computational speed of the UKF is faster than when using a PF since fewer samples are necessary for the proper approximation of the state as well as for the EKF, as shown in Table 3.5.

With these considerations, the PF has been discarded, since it requires a large set of weighted state vector estimates to carry out a proper estimation and presents higher computational loads than the non-linear Kalman filters. In regards to the non-linear Kalman filters, considering the small performance differences between UKF and EKF presented by (Bourgeaux, 2020), the main consideration to be had is in the ease of implementation. Given that the scenario models the gravity field with spherical harmonics, the use of EKF requires the derivation of the analytical expressions or tuned numerical derivatives of each state parameter to be extensive, whereas the UKF does not (Hong-de et al., 2012), easing, therefore,

Table 3.5: Computational load comparison using EKF and PF (Rigatos, 2012)

	EKF	**PF**
Total runtime (s)	104.39	623.92
Cycle time (s)	0.0209	0.1248

Table 3.6: Computational load comparison using EKF, UKF and PF for a dynamic navigation scenario (Wei et al., 2018)

	EKF	**UKF**	**PF**
Running time (s)	0.202	0.958	2.411
Normalised running time (s)	0.0505	0.2395	0.6028

the implementation considerably. Consequently, the UKF model is preferred for this implementation and is further studied in this section.

3.2.1. Unscented Kalman Filter

The Unscented Kalman Filter (UKF) presents good performance for non-linear models. This filter presents an improvement on the EKF through the use of an unscented transformation (UT) (Wan and Merew, 2000). This, proposed by J. Uhlmann, works under the premise that the approximation of an arbitrary density after a non-linear transformation is harder than that of a Gaussian distribution[8]. This transform consists of the computation of a subset of points, known as sigma points, which are later propagated through a non-linear map and estimated through a Gaussian distribution. Requiring only a number of sigma points of twice the dimensions plus one, this transform presents a good escalation with respect to the number of dimensions of the data as opposed to other more computationally demanding methods such as Monte Carlo sampling.

This method uses a deterministic sampling approach to obtain better precision in the results. Additionally, a collection of points is used to describe a state. When used with a non-linear EOM, this filter can estimate up to third-order uncertainties.

Equation (3.14) depicts the steps for computing the statistics of a variable after a non-linear transformation. This is done assuming a variable or random nature $\mathbf{x}$ with dimension $\mathbf{L}$ that is used in a nonlinear function to produce $\mathbf{y}$ as $\mathbf{y} = g(\mathbf{x})$. Note that variable $\mathbf{x}$ has a mean value represented by $\overline{\mathbf{x}}$ and a covariance represented by $\mathbf{P}_x$. The following equations depict the computation of $\mathbf{y}$ using a matrix χ containing a number of $2L + 1$ sigma vectors. Note that λ is a scaling parameter that can be computed as $\lambda = \alpha^2(L + \kappa) - L$, where α determines the sigma points spread around the mean value of $\mathbf{x}$. Furthermore, κ is a scaling parameter commonly set to a null value and β introduces prior information on the variable $\mathbf{x}$ distribution. The standard values that are used for these parameters are as follows: $\alpha = 0.1$, $\beta = 2.0$ and $\kappa = 0.0$.

$$\begin{aligned}
\chi_{0,k} &= \overline{\mathbf{x}}_k \\
\chi_{i,k} &= \overline{\mathbf{x}_k} + \sqrt{(L+\lambda)\mathbf{P}_{\mathbf{x},k} + \mathbf{Q}_{\mathbf{x},k+1}}\Big|_i \qquad i = 1, \ldots, L \\
\chi_{i,k} &= \overline{\mathbf{x}_k} - \sqrt{(L+\lambda)\mathbf{P}_{\mathbf{x},k} + \mathbf{Q}_{\mathbf{x},k}}\Big|_{i-L} \qquad i = L+1, \ldots, 2L
\end{aligned} \tag{3.14}$$

The weights that are associated to their corresponding sigma are defined as:

$$\begin{aligned}
W_0^{(m)} &= \lambda/(L+\lambda) \\
W_0^{(c)} &= \lambda/(L+\lambda) + \left(1 - \alpha^2 + \beta\right) \\
W_i^{(m)} &= W_i^{(c)} = 1/\{2(L+\lambda)\} \qquad i = 1, \ldots, 2L
\end{aligned} \tag{3.15}$$

The computation of the mean covariance for $\mathbf{y}$ with the use of weighted samples and the covariance of the posterior sigma points can be carried out with the following equation:

$$\overline{\mathbf{y}}_k \approx \sum_{i=0}^{2L} W_i^{(m)} \boldsymbol{\mathcal{Y}}_{i,k} \tag{3.16}$$

$$\mathbf{P}_{\mathbf{y},k} \approx \sum_{i=0}^{2L} W_i^{(c)} \left\{\boldsymbol{\mathcal{Y}}_{i,k} - \overline{\mathbf{y}}\right\} \left\{\boldsymbol{\mathcal{Y}}_{i,k} - \overline{\mathbf{y}}_k\right\}^T \tag{3.17}$$

This filter updates the state at each time step, similarly to the EKF, but adds the sigma point computation. The non-linear equation for the computation of the sigma matrix is as follows:

$$\boldsymbol{\chi}_{k+1|k} = f(\boldsymbol{\chi}_k, \mathbf{u}_k, \mathbf{v}_k) \tag{3.18}$$

[8]G. Gundersen, "The Unscented Transform", Available at: https://gregorygundersen.com/blog/2020/11/19/unscented-transform/, Accessed on 13-12-2023

As Julier and Uhlmann (2004) explain, the current *a-priori* state vector estimate ($\hat{\mathbf{x}}_{k+1}^{-}$) and the covariance matrix ($\mathbf{P}_{k+1}^{-}$) can be computed with the following equations, respectively;

$$\hat{\mathbf{x}}_{k+1}^{-} = \sum_{i=1}^{2L+1} W_i^{(m)} \boldsymbol{\chi}_{i,k+1|k} \tag{3.19}$$

$$\mathbf{P}_{k+1}^{-} = \sum_{i=1}^{2L+1} W_i^{(m)} \left(\boldsymbol{\chi}_{k+1|k}^{-} \hat{\mathbf{x}}_{k+1}^{-}\right) \left(\boldsymbol{\chi}_{k+1|k}^{-} \hat{\mathbf{x}}_{k+1}^{-}\right)^T \tag{3.20}$$

The *a-priori* measurements and covariance matrix can be found by applying the unscented transform to the measurement equations with:

$$\boldsymbol{\zeta}_{i,k+1|k} = f(\boldsymbol{\chi}_{i,k+1|k}, \mathbf{w}_k) \tag{3.21}$$

$$\hat{\mathbf{z}}_k = \sum_{i=1}^{2L+1} \mathbf{W}_i^{(m)} \boldsymbol{\zeta}_{i,k+1|k} \tag{3.22}$$

$$\mathbf{P}_{\bar{\mathbf{z}}k+1}^{-} = \sum_{i=1}^{2L+1} \mathbf{W}_i^{(m)} \left(\boldsymbol{\zeta}_{k+1|k}^{-} \hat{\mathbf{z}}_{k+1}^{-}\right) \left(\boldsymbol{\zeta}_{k+1|k}^{-} \hat{\mathbf{z}}_{k+1}^{-}\right)^T \tag{3.23}$$

Note that $\boldsymbol{\zeta}_{i,k+1|k}$ depicts a set of $M \times 2L + 1$ sigma measurement points for a total of M measurements. The *a-posterior* state can be computed with:

$$\hat{\mathbf{x}}_k = \hat{\mathbf{x}}_k^{-} + \mathbf{K}\left(\mathbf{z}_k - \hat{\mathbf{z}}_k^{-}\right) \tag{3.24}$$

The Kalman gain $\mathbf{K}_k$ is computed as:

$$\mathbf{K}_k = \mathbf{P}_{\mathbf{xz},k} \mathbf{P}_{\tilde{\mathbf{z}},k}^{-1} \tag{3.25}$$

where the covariance propagation is presented in the following equation:

$$\mathbf{P}_{\mathbf{x},k}^{-} = \mathbf{P}_{\mathbf{x},k} + \mathbf{K}_k \mathbf{P}_{\mathbf{z},k}^{-} \mathbf{K}_k^T \tag{3.26}$$

Additionally, the cross-covariance matrix can be found with:

$$\mathbf{P}_{\mathbf{xz},k+1} = \mathbf{W}_i^{(m)} \left(\boldsymbol{\chi}_{k+1|k} - \hat{\mathbf{x}}_{k+1}^{-}\right) \left(\boldsymbol{\zeta}_{k+1|k} - \hat{\mathbf{z}}_{k+1}^{-}\right)^T \tag{3.27}$$

3.2.2. UKF tuning

The performance of the UKF is strongly dependent on the measurement noise covariance matrix $\mathbf{R}$ and the process noise covariance matrix $\mathbf{Q}$ (Horváth and Kuslits, 2017). Additionally, the estimation performance of this methodology is also dependent on the three scalar parameters of the UT (α, β, λ) (Scardua and Cruz, 2017). Scardua and Cruz (2017) confirmed the improvement of the estimation with proper tuning of the UKF.

There are a number of methodologies that can be used for tuning the filter. The simplest one is through trial and error. However, this technique can be extremely time-consuming and is neither optimal nor efficient.

Optimisation methods are better suited to tune the UKF. While a number of optimisation methods have been designed particularly for this filter, as summarised by Horváth and Kuslits (2017), general optimisation algorithms are also used. Common approaches for tuning use Genetic Algorithms (GA) (Ludwig, 2018) and Particle Swarm Optimisation (PSO) (Ramakoti et al., 2009).

Genetic algorithms are suitable for complex non-linear optimisation problems, being able to search a large solution space. However, this algorithm can have large convergence times. Furthermore, it can be set with a number of parameters, which have an impact on its performance, thus increasing the implementation difficulty.

The use of PSO has a number of benefits compared to GA. In particular, it has a faster convergence and is less sensitive to the initial conditions set. Furthermore, it is significantly simpler to implement,

having fewer parameters. Nevertheless, this algorithm is more likely to find a local optima in complex and multimodal search spaces and has a more limited exploration of the search space than GA.

Although both algorithms are adequate for this implementation, PSO (Gad, 2022) is preferred for this optimisation given its faster convergence and ease of implementation. It has been implemented with a population size of 20 individuals for 20 evolutions.

Following the research of Bourgeaux (2020), the tunning considers the covariance matrix decomposed into a vector as:

$$\boldsymbol{Q} = \begin{pmatrix} q_1 & q_2 & q_3 \end{pmatrix} \begin{bmatrix} 1 & 0 & 0 \\ 0 & 1 & 0 \\ 0 & 0 & 1 \end{bmatrix} \tag{3.28}$$

where the values are constrained between 10^{-20} and 10^{-2} as recommended by Bourgeaux. Moreover, the fitness function that the optimiser aims to minimise is the mean-square error:

$$MSE = \frac{1}{N} \sum_{k=1}^{N} (y_k - \hat{y}_k)^2 \tag{3.29}$$

It should be noted that, ideally, the filter should be tuned for each scenario tested to obtain the most efficient results. This tuning process has been conducted for the UKF implementation verification. Nevertheless, a PSO optimisation of the UKF for the full system considering the satellite measurements and the estimation of the SH coefficients has not been conducted due to computational load constraints, for which conducting an optimisation is unfeasible. Therefore, a trial and error approach has been used for the UKF tuning. Furthermore, it has been seen that the addition of noise to the measurements of the filter affects the estimates and therefore requires re-tuning for each case to improve the efficiency. Nevertheless, given the number of tests that are computed in the following sections, it is unrealistic for all the cases to undergo a filter tuning optimisation, and thus, the filter tuning is done only for general scenarios.

4

Simulator design

The design of the software used for the autonomous navigation of the constellation satellites around an asteroid is presented in this chapter. This simulator has been designed for the purpose of estimating the gravity field of the asteroid accurately, thus allowing for the autonomous and safe navigation of the satellites orbiting an asteroid.

The chapter initially introduces the top-level architecture of the software in Section 4.1. Then, further detail is presented of the main implementation modules designed for the implementation. The configuration module is introduced in Section 4.2. Furthermore, the environment module is illustrated in Section 4.3, followed by the propagation module in Section 4.4, the hardware module in Section 4.5, and finally the estimation module in Section 4.6.

4.1. Top-level architecture

The architecture of the software has been modelled after the real-life scenario where the CubeSats orbit in a constellation, each of them taking measurements and estimating their positions and relaying these back to the mothership for continuous estimation of the gravity field.

For the simulation to be carried out in the most efficient manner, the software will first propagate the trajectories of the satellites in orbit around the asteroid, then simulate and obtain the measurements taken by the sensors and simulate the data transmission between the CubeSats and carry out the estimations of the spherical harmonic coefficients.

To carry out this simulation, the software has been organised into five main blocks:

1. **Configuration module:** This defines the settings for the simulation defining the environment and propagation characteristics.
2. **Environment module:** This sets the environment of the system, creating the bodies present in the scenario with their specific properties set in the configuration as well as the asteroid's physical characteristics.
3. **Propagation module:** This module propagates all spacecraft present in the scenario with the characteristics of the configuration.
4. **Measurements module:** This simulates the sensors of the spacecraft as they orbit the asteroid and generate measurements.
5. **Estimation module:** This contains the UKF and carries out the state and gravity field spherical harmonic coefficients estimates from the measurements.

Further details of the simulator software architecture can be found in Appendix B. This appendix details the code modules and their respective classes summarising their functionalities.

A simple flow of the simulation program is presented in Figure 4.1, depicting the flow of use between the classes and blocks of the code for the simulation of the real conditions of the system.

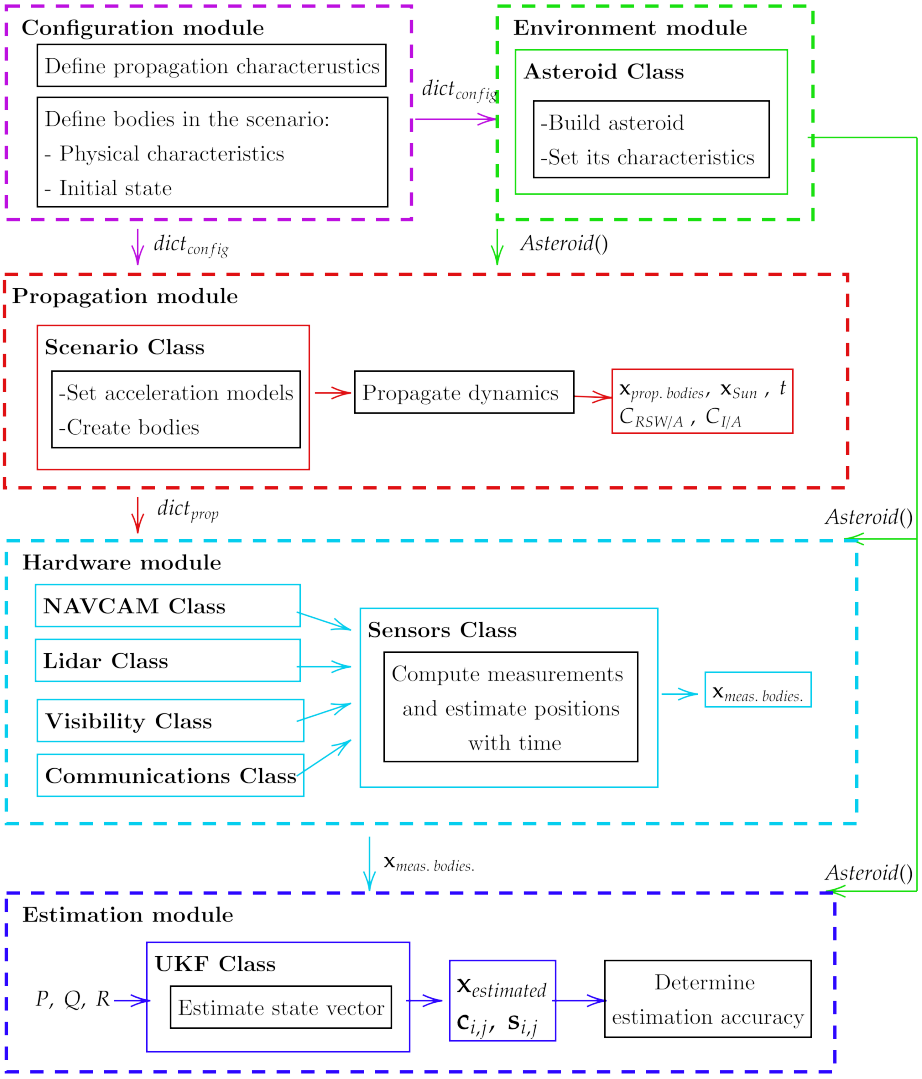

Figure 4.1: Top-level architecture flow for the simulation of the scenario in real conditions

Considerations for optimisation

While ideally the optimisation of the constellation characteristics should be done following the steps depicted in Figure 4.1 and using all the blocks (configuration, environment, propagation, measurements and estimation). This would require a very high computational workload that the available computers for the research cannot handle within the time constraints of the research. Therefore, the optimisation of the system is done by bypassing the "measurements block" and directly adding a noisy error to the propagated positions of the spacecraft.

4.2. Configuration Module

This module has been designed to allow the user to define all the characteristics of the system using configuration files. The software transforms the configuration files into a configuration dictionary containing all the specifications for the system simulation that is used to customise the scenario simulated. All the modules of the code use the configuration dictionary defined.

The configuration files allow the definition of the propagation characteristics such as the initial start epoch and final epoch and the propagation time step. Furthermore, it allows the definition of the forces in the environment, as well as the constellation bodies to be simulated in the constellation defining all their initial orbit Kepler parameters as well as their physical characteristics.

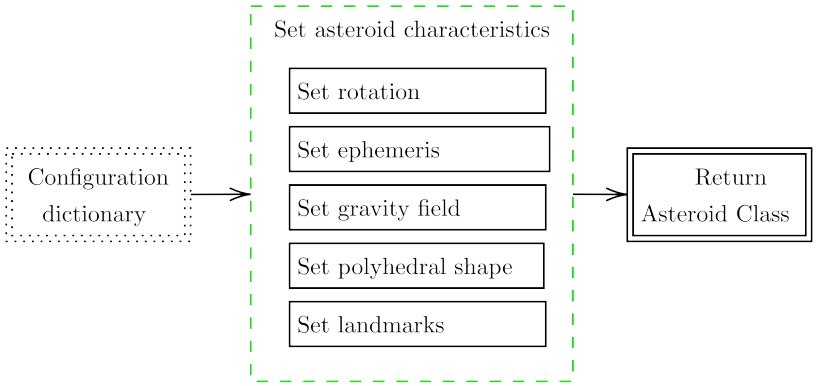

Figure 4.2: Architecture diagram of the environment module

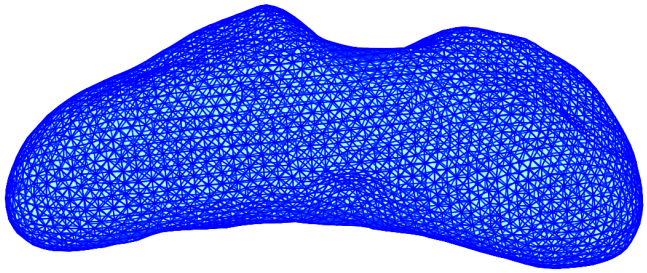

Figure 4.3: Polyhedron shape of 433 Eros

4.3. Environment Module

This module contains all the models necessary for the definition of Eros and its environment, Figure 4.2 presents the flow of this module. It should be noted that while the characteristics and information of the Sun are contained in Tudat spice, the 433 Eros asteroid has to be modelled specifically with all its characteristics. In particular, its rotation, ephemeris, gravity field, and a basic spherical shape.

It should be noted that the modelling of the rotation of the asteroid on its Z-axis with a period of 5.27 h (Miller et al., 2002). Additionally, the gravity field of Eros has been modelled with spherical harmonic coefficients taken from the NEAR mission. These can be found in Section C.1.

In addition, spacecraft orbiting the asteroid must also be defined. In this case, the mothership has been modelled with a weight of 1330 kg, a reference area radiation of 64 m^2 and a reflectivity coefficient of 0.5. Additionally, the CubeSats are modelled with a weight of 12 kg, an estimated reference area radiation of 22 m^2 with a reflectivity coefficient of 0.5.

This section presents the implementation both in terms of its shape modelling, depicted in Subsection 4.3.1 and its landmarks as detailed in Subsection 4.3.2 and in the gravity-field definition as presented in Subsection 4.3.3.

4.3.1. Polyhedron shape of the asteroid

Correct modelling of the physical shape of the asteroid is necessary for the simulation, since it is required for the simulation of the sensor measurements through the hardware simulated as well as for the determination of LOS between CubeSats and mothership. Shape modelling has been implemented using polyhedron models with face data present in [1], with a total of 7790 facets. The simulated model shape is presented in Figure 4.3.

4.3.2. Landmarks of the asteroid

For an adequate determination of the position of the spacecraft when orbiting the asteroid, the sensors require the identification of specific locations on the asteroid or, in other words, landmarks. These are distinguishable features on the surface, such as rocks or craters, that can be identified.

The NEAR spacecraft identified a total of 1555 landmark positions on Eros[1], which have been modelled in the simulation and are illustrated in Figure 4.4.

It must be considered that the gravity-field estimation accuracy is dependent on the number of

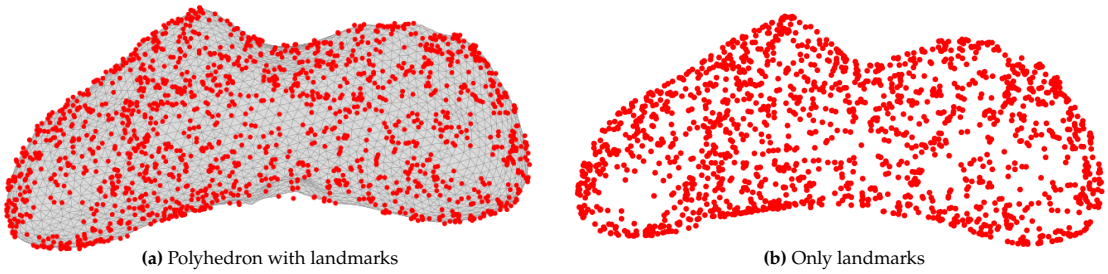

(a) Polyhedron with landmarks **(b)** Only landmarks

Figure 4.4: Eros model with landmarks

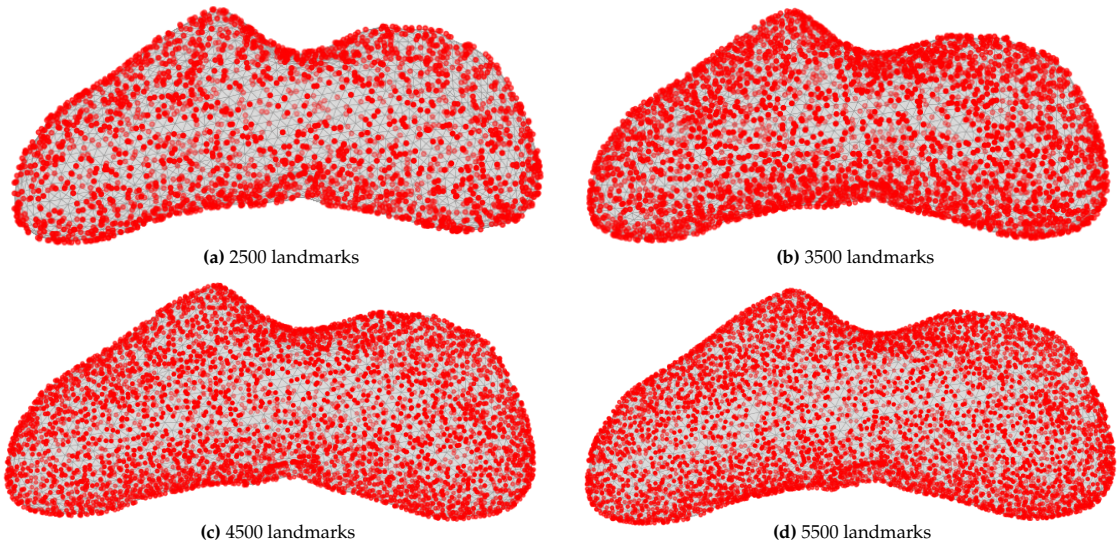

(a) 2500 landmarks **(b)** 3500 landmarks

(c) 4500 landmarks **(d)** 5500 landmarks

Figure 4.5: Landmark disposition in Eros 433 asteroid

landmarks of the asteroid. Razgus (2017) used a total of 4900 landmarks in the Itokawa asteroid, which has a surface of 1125 km^2. This is a much higher (approximately 4 times larger) density of landmarks per surface area than a total of 1555 landmarks in approximately 4473 km^2 of 433 Eros. Therefore, the modelling of additional landmarks is considered, to properly study their effect on the SH coefficient estimation in this scenario. To do so, additional higher-density landmark distributions have been defined. The modelling of the landmarks can be done through a random distribution following the model presented by Osada et al. (2002) with:

$$\mathbf{P} = (1 - \sqrt{r_1})\mathbf{A} + \sqrt{r_1}(1 - r_2)\mathbf{B} + \sqrt{r_1}r_2\mathbf{C} \tag{4.1}$$

where **A**, **B** and **C** represent the vertices of the polyhedron triangles and r_1 and r_2 are random numbers uniformly distributed taking values from 0 to 1.

Figure 4.5 depicts the Eros asteroid polyhedron model covered with the computed landmark distributions using the described methodology for a different set of total landmark numbers.

Additionally, it should be considered that while this research considers relative navigation through the use of landmarks, there are other methods available for position estimation that make use of machine learning which do not rely on the number of landmarks visible by the spacecraft to produce an accurate estimation. For instance, Heijden (2022) researched the use of keypoint-based convolutional neural network-based methods for position estimation and demonstrated successful results in close proximity operations around asteroids.

4.3.3. Gravity field of the asteroid

The gravity field of the asteroid is simulated with the spherical harmonics model introduced in Subsection 2.2.1. This model is simulated in two different manners. Initially, with the use of TUdatpy for the acceleration computation for the simulation of the real gravity field of the scenario, and then with a python-coded model used in the filters for the estimation of the coefficients.

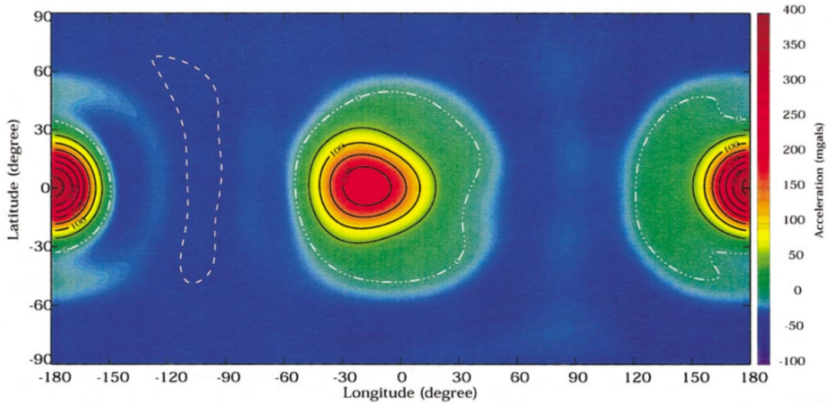

Figure 4.6: Radial acceleration of Eros gravity field up to degree and order 8 on a sphere of 16km radius (Miller et al., 2002)

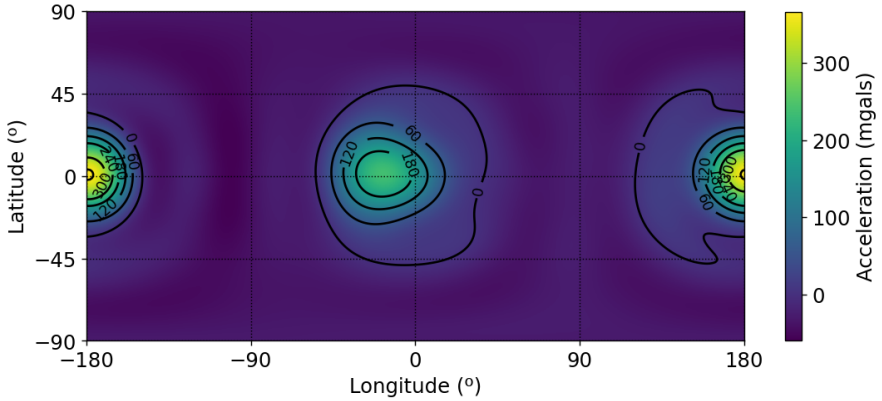

Figure 4.7: Radial acceleration of Eros gravity field up to degree and order eight on a sphere of 16 km radius without the point mass gravity field

It should be noted that the spherical harmonics in both cases have been implemented with the coefficients taken from the NEAR mission available in website[1] up to degree and order 15. These coefficients can be found in Appendix C, Section C.1.

Following Eq. (2.16) (presented in Subsection 2.2.1) depicting the potential of the gravity field and considering the gravity-field acceleration in NED coordinates, the derivatives of the potential can be computed as:

$$\begin{aligned}
\frac{\partial U}{\partial \lambda} &= \frac{\mu}{r}\sum_{n=1}^{n_{\max}}\left(\frac{R_e}{r}\right)^n\sum_{m=0}^{n}\left(\bar{C}_{n,m}\cos m\phi + \bar{S}_{n,m}\sin m\phi\right)\frac{\partial \bar{P}_{n,m}}{\partial \lambda} \\
\frac{\partial U}{\partial \phi} &= \frac{\mu}{r}\sum_{n=1}^{n_{\max}}\left(\frac{R_e}{r}\right)^n\sum_{m=0}^{n} m\left(\bar{S}_{n,m}\cos m\phi - \bar{C}_{n,m}\sin m\phi\right)\bar{P}_{n,m} \\
\frac{\partial U}{\partial r} &= \frac{\mu}{r^2}\left\{1+\sum_{n=1}^{n_{\max}}\left[\left(\frac{R_e}{r}\right)^n\sum_{m=0}^{n}\left(\bar{C}_{n,m}\cos m\phi + \bar{S}_{n,m}\sin m\phi\right)(n+1)\bar{P}_{n,m}\right]\right\}
\end{aligned} \tag{4.2}$$

The accuracy of the implemented gravity-field model has been verified by comparing the radial acceleration of Eros' gravity field as estimated by Miller (shown in Figure 4.6) with the same estimation using the developed model (shown in Figure 4.7). Both figures exhibit identical gravity-field patterns, confirming the correctness of the model. Notably, the gravity field reveals two prominent spots with high accelerations centred at 180° and -10° longitude, corresponding to the two tips of the asteroid.

Furthermore, an analysis of the effect of the model's degree has been conducted. As shown in Figure 4.8, increasing the degree of the coefficients used results in more irregularities in the gravity

[1]Planetary Science Institute, "NEAR Collected Shape and Gravity Models" Available at: https://sbn.psi.edu/pds/resource/nearbrowse.html, Accessed on: 15-01-2024

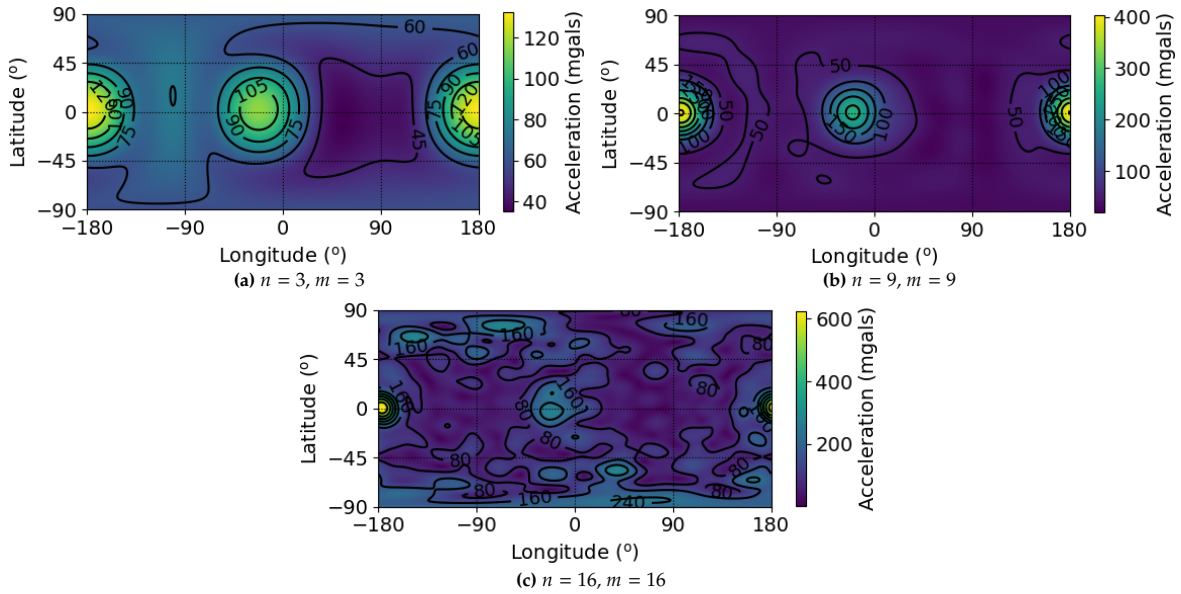

(a) $n = 3, m = 3$ **(b)** $n = 9, m = 9$

(c) $n = 16, m = 16$

Figure 4.8: Gravity-field norm of Eros for a range of degrees and order

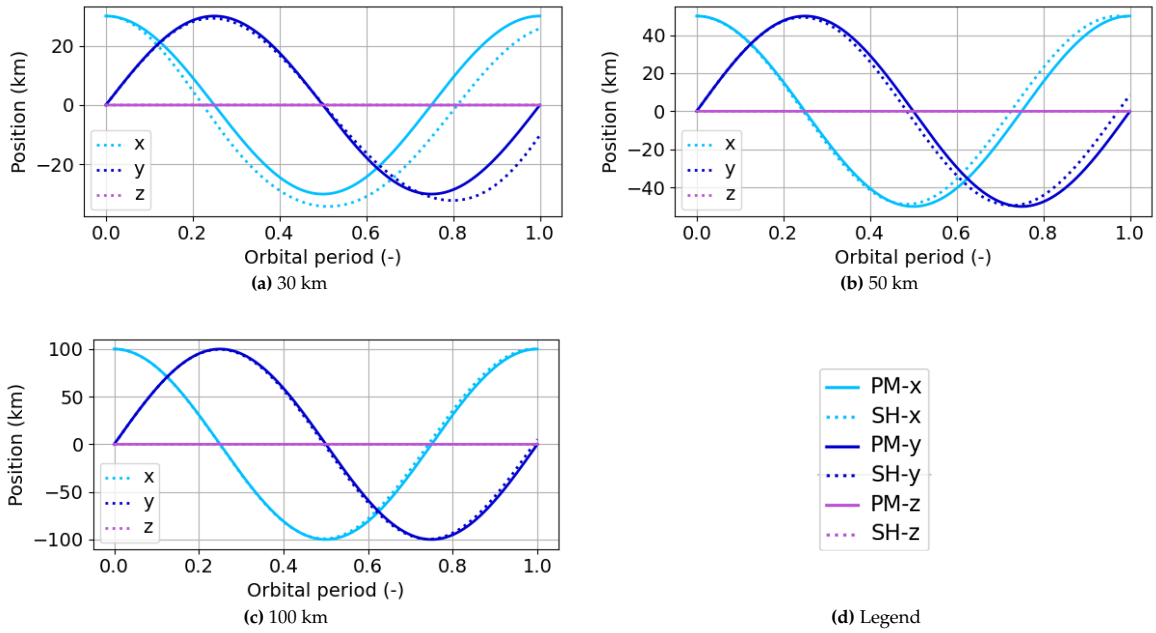

(a) 30 km **(b)** 50 km

(c) 100 km **(d)** Legend

Figure 4.9: Position of a satellite in a 0-degree inclination orbit for a series of semi-major axes depicting the position computed with point mass (PM) and spherical harmonics (SH) gravity field.

field, as can be expected.

In addition, it should be noted that the effect of the spherical harmonics gravity field decreases with larger semi-major axis of the orbit. This is confirmed in Figure 4.9, where it can be seen that the difference between the position computed using the point mass gravity-field model and the spherical harmonics decreases as the semi-major axis increases. Moreover, this is further confirmed with Figure 4.10, which depicts the gravity field on different semi-major axes, thus showing the impact of the altitude of the spacecraft on the proper estimation of the gravity field. Note, that while the force is as high as 600 mgals on the surface of Eros, this value decreases to 12 mgals for a 30 km orbit, to 1.2 mgals for a 50 km orbit, and even as low as 0.007 mgals for a 100 km orbit.

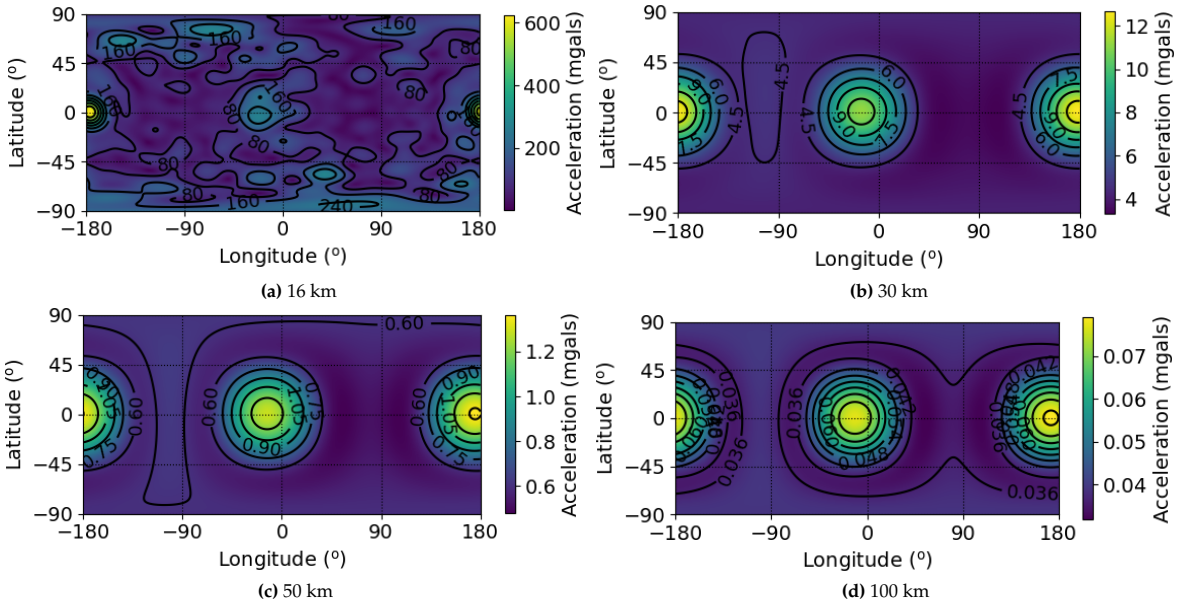

(a) 16 km **(b)** 30 km **(c)** 50 km **(d)** 100 km

Figure 4.10: gravity-field norm of 16 degree and order spherical harmonics of Eros for a range of altitudes

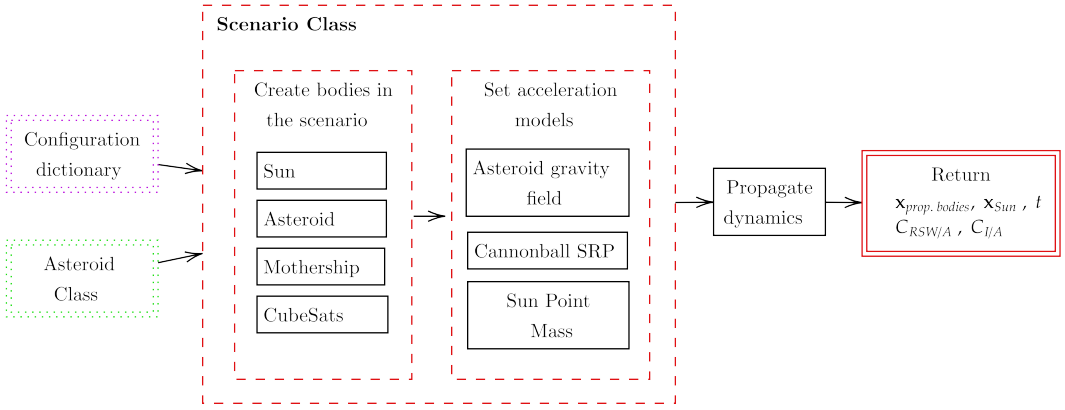

Figure 4.11: Architecture diagram of the propagation module

4.4. Propagation Module

The propagation module is used for the definition of the scenario and the propagation of the bodies with time following the literature study findings and the configuration dictionary provided. The block computes the trajectories of the constellation satellites and returns a dictionary with the states of the satellites in the inertial and asteroid reference frame. Additionally, the dictionary contains the rotation matrices for each time instant and satellite from the inertial reference frame to the satellite reference frame that is required for the simulation of the hardware presented in the following section.

A simple top-level architecture of the flow of this module is presented in Figure 4.11.

4.5. Hardware Module

The hardware module of the simulation contains a measurement block that activates all the steps to obtain the measurements once the scenario has been propagated. The steps followed to obtain them are shown in Figure 4.12. It should be noted that the order of the steps to be taken has been devised to ensure maximum efficiency, having to rotate the asteroid only once for each time step and the visible landmarks, which can be reused for all the vehicles in orbit. Additionally, the communication constraints are considered before the measurements are simulated to reduce the computational load, avoiding the computation of measurements that cannot be transmitted.

To carry out these functionalities, the hardware module contains a number of classes. It has a visibility

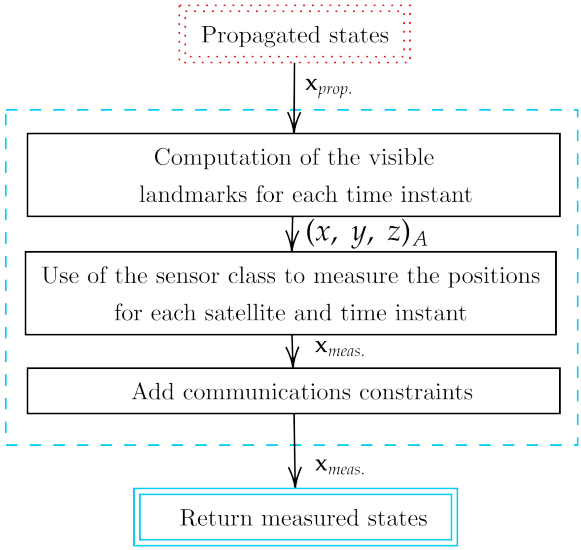

Figure 4.12: Architecture diagram of the measurements block

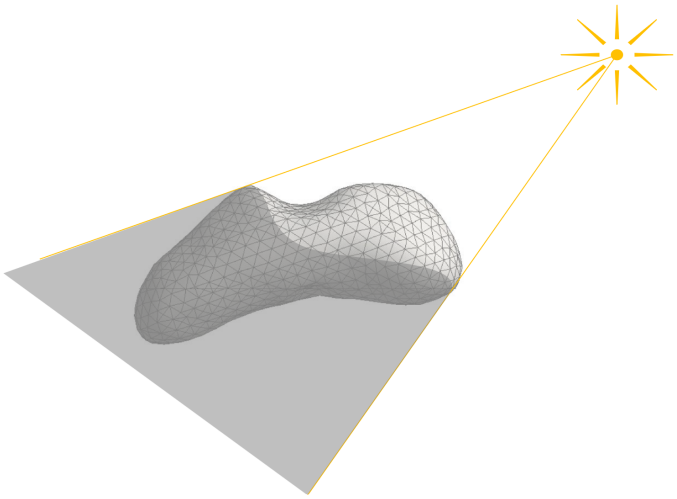

Figure 4.13: Sun effect on the asteroid

class that deals with the lighting conditions of the asteroid, which is presented in Subsection 4.5.1. In addition, a communication class is used for the determination of the communications link feasibility between CubeSats and mothership, the implementation of which is depicted in Subsection 4.5.2. Finally, a NAVCAM class is also contained in the module for the simulation of the instrument as detailed in Subsection 4.5.3.

4.5.1. Visibility restrictions of the hardware

The hardware can only operate correctly under adequate light conditions. As depicted in Figure 4.13, there is a considerable part of the asteroid where the landmarks are not visible, and therefore measurements cannot be taken. An algorithm has been devised to compute the landmarks that are visible, depending on sunlight conditions.

Verification

A simple verification of the correct functioning of the code can be done by simulating a scenario with several locations of the Sun. As can be seen in Figure 4.14, the simulation is able to distinguish between the landmarks that are in direct Sunlight and the ones that are in the shade.

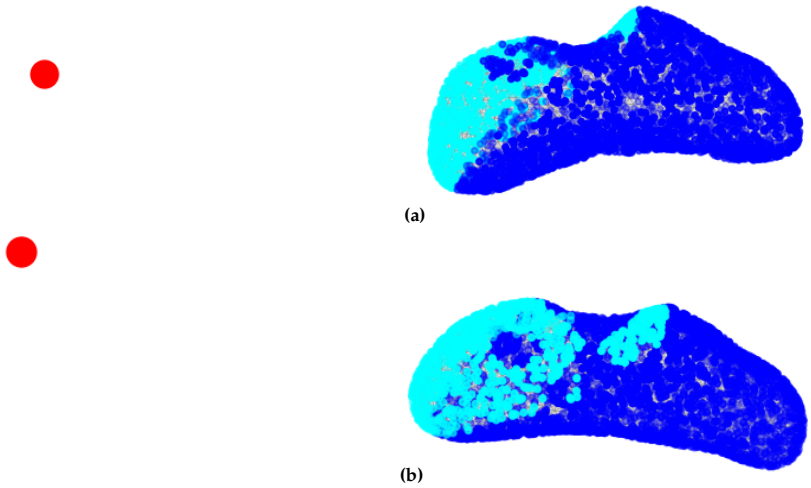

Figure 4.14: Determination of landmarks with direct light from the Sun with different perspectives

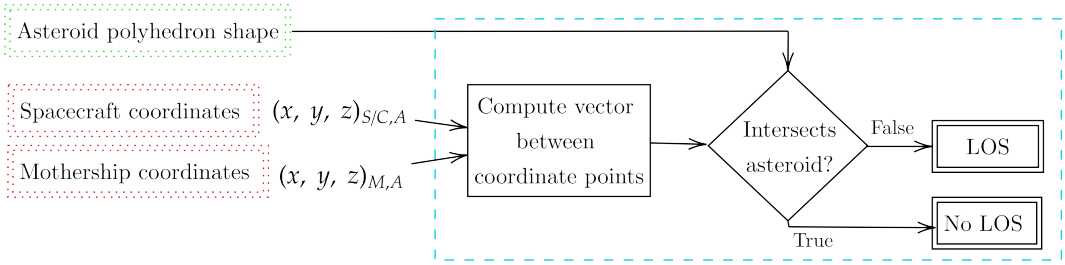

Figure 4.15: LOS algorithm

4.5.2. Communication hardware restrictions

The scenario being considered relies on the position estimation of each CubeSat being transmitted to the mothership. Thus, the simulation must take into consideration the communication constraints. The algorithm presented in Figure 4.15, has been designed to verify whether the direct vector between the CubeSat at hand and the mothership intersects with the asteroid's shape or not. This is carried out using a ray tracing algorithm to check for line segment intersections with the asteroid's polyhedron.

In addition, the communication's range must also be considered according to the hardware used in the satellites. Considering the use of S-band communications as introduced in the previous chapter, the range of such a technology is thousands of kilometres and therefore it is not a restriction for the orbits being considered of the semi-major axis of up to 50 km.

Verification

The correct functioning of this algorithm has been verified by visualising several scenarios, where LOS is established and it is not. Figure 4.16 depicts a case where LOS cannot be established between two coordinates due to the intersection with the asteroid and another, where the communications can be established and there is no intersection with the asteroid.

4.5.3. NAVCAM sensor

The NAVCAM sensor enables the detection of a landmark in a given field of view and the determination of its position. The NAVCAM sensor algorithm simulates the FOV of the camera, its characteristics dependent on the spacecraft, detects the visible landmarks of the asteroid, and computes its positions in pixel coordinates.

Landmark detection

The algorithm for landmark detection is presented in Figure 4.18 and depicts the computation of the landmarks that are visible in the field of view of a given sensor. It should be noted that the determination of whether a landmark is contained within the NAVCAM FOV or not can be done using the properties of

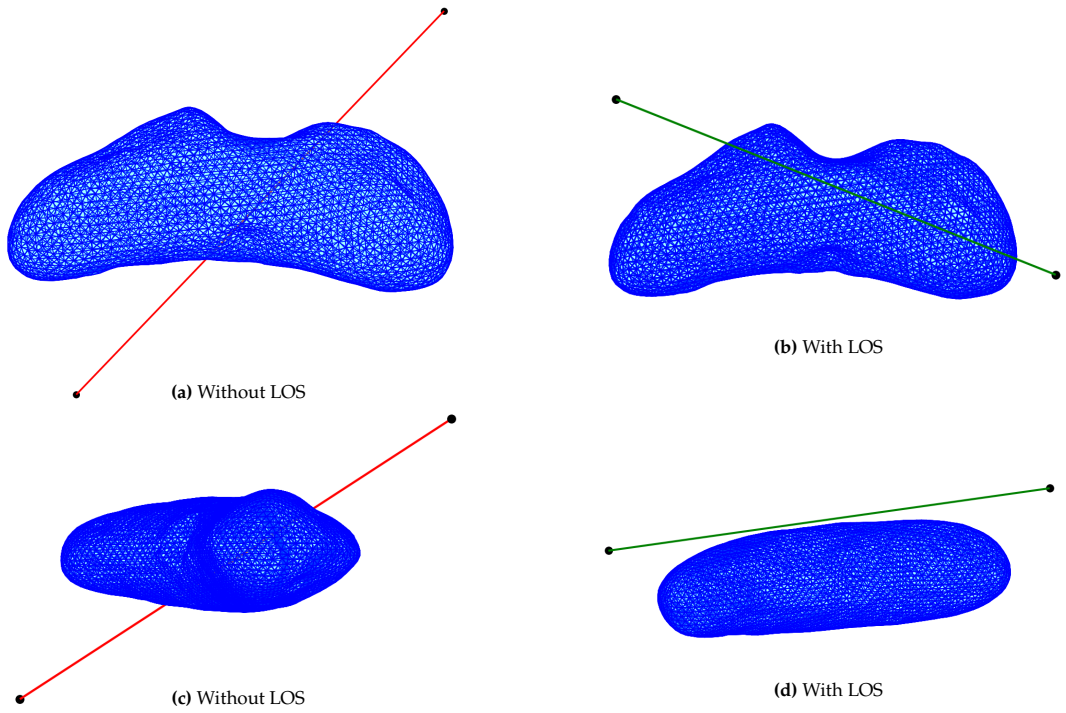

(a) Without LOS

(b) With LOS

(c) Without LOS

(d) With LOS

Figure 4.16: Scenario representing the direct vector between two coordinate points around the 433 Eros asteroid. It should be noted that the coordinates are represented in black spheres and that the LOS is presented in red when it cannot be established and in green when it can.

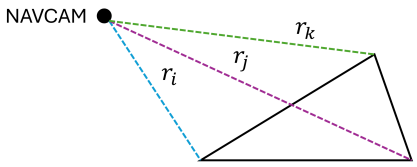

Figure 4.17: NAVCAM landmark detection algorithm

polyhedrons, in particular through the use of the dimensionless factor ω_f. This factor can be computed with Eq. (4.3), where the vectors $\mathbf{r}_i$, $\mathbf{r}_j$ and $\mathbf{r}_k$ are depicted in Figure 4.17.

$$\omega_f = 2\arctan\left[\frac{\mathbf{r}_i \cdot \mathbf{r}_j \times \mathbf{r}_k}{r_i r_j r_k + r_i(\mathbf{r}_j \cdot \mathbf{r}_k) + r_j(\mathbf{r}_i \cdot \mathbf{r}_k) + r_k(\mathbf{r}_i \cdot \mathbf{r}_j)}\right] \tag{4.3}$$

The solid angle can be computed through the summation of the dimensionless per-face factor of all faces, following. If this sum ($\sum \omega_f$) returns a value of 4π, it is indicative that the landmark is within the FOV of the camera. It should be noted that since this formula requires the use of triangles, the rectangular field of view of the camera will be represented by two triangles inside the pyramidal polyhedron.

The proper functioning of this model has been verified through the simulation of a rectangle containing 13 landmarks as depicted in Figure 4.19. The algorithm must be able to detect which out of the 21 landmarks are contained inside of the sensor's FOV and which are not. Figure 4.19a depicts the FOV of the camera and all the landmarks located in the test scenario. The proper functioning of the algorithm is verified with Figure 4.19a, where the nine coordinates contained inside the rectangle have been detected by the NAVCAM and plotted in green, and the landmarks outside have been discarded correctly. It should be noted that the scenario tested considers a FOV of five degrees and a height of 230 m between the sensor and the plane containing the landmarks.

In addition to being able to detect which landmarks are inside of the polyhedron FOV created for simulating the camera, it is crucial that only those landmarks in direct line of sight with the camera are detected. In order to satisfy this a ray tracing algorithm has been implemented and tested in a similar

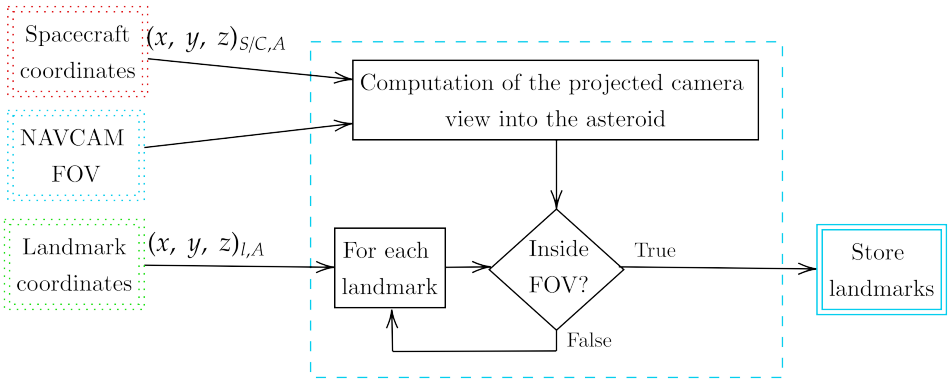

Figure 4.18: NAVCAM landmark detection algorithm

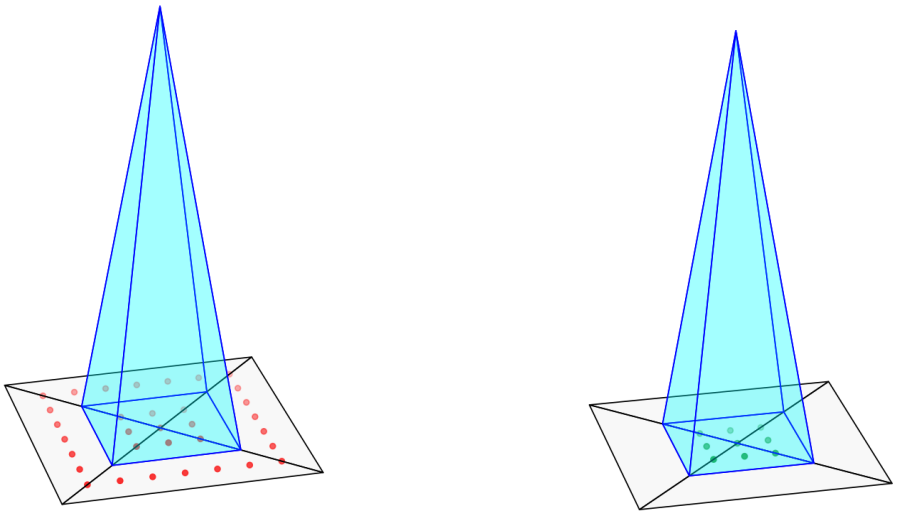

(a) Landmark disposition before NAVCAM detection

(b) Landmarks detected by NAVCAM

Figure 4.19: Landmark disposition

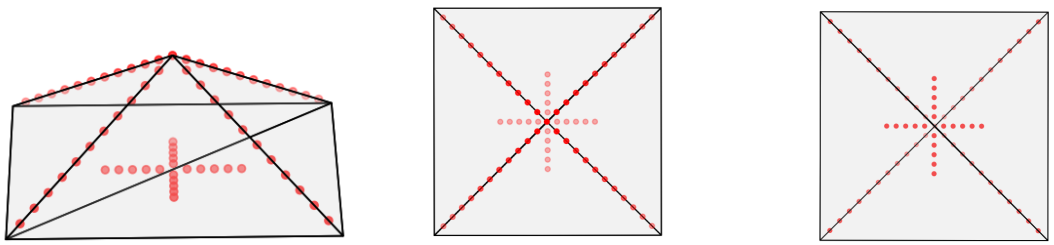

(a) Frontal view

(b) Top view

(c) Bottom view

Figure 4.20: Landmark disposition in the test polyhedron

scenario, now with a pyramid polyhedron containing landmarks in the top and bottom faces as depicted in Figure 4.20. For the algorithm to be considered successful, only the landmarks that are within the FOV of the camera located in the top faces of the pyramid should be detected. This is demonstrated with Figure 4.21, where it can be seen that only the landmarks with direct line-of-sight with the camera are detected and presented in green.

NAVCAM measurements

In addition to being able to detect landmarks in the FOV of the camera, this sensor must estimate the landmark coordinates. An algorithm has been devised to carry out the computation of a given landmark in the camera's pixel coordinates. The algorithm is depicted in Figure 4.22.

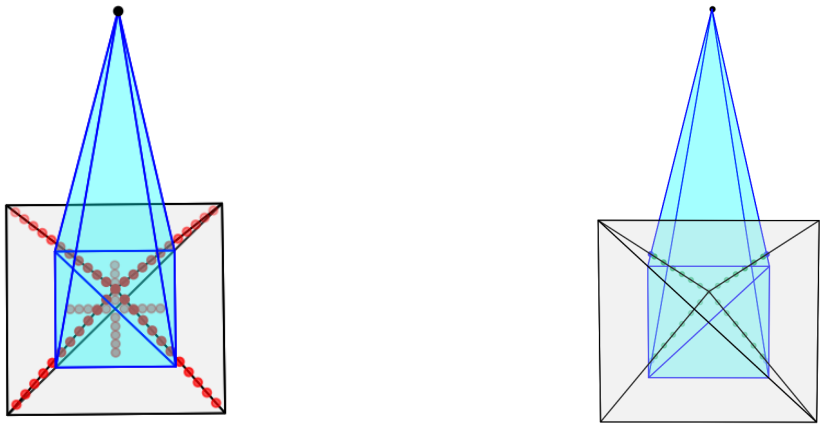

(a) Landmark disposition before NAVCAM detection

(b) Landmarks detected by NAVCAM

Figure 4.21: Landmark disposition

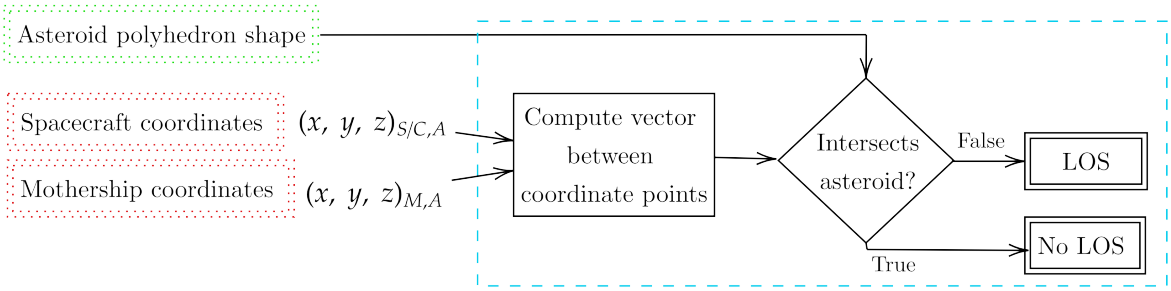

Figure 4.22: NAVCAM landmark coordinate computation algorithm

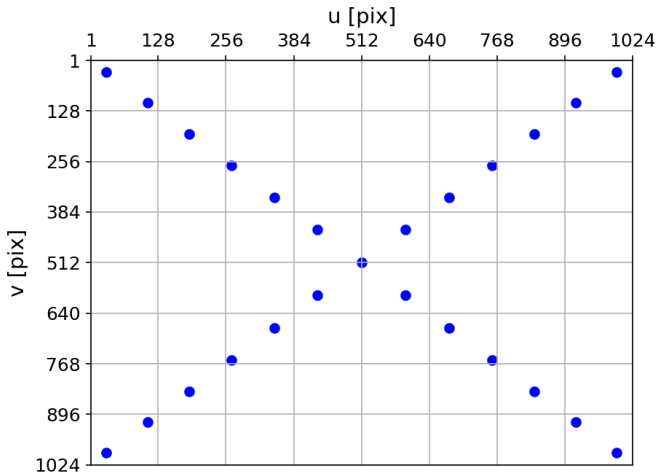

Figure 4.23: NAVCAM landmark coordinate detection in pixel coordinates

The verification of the algorithm can be tested using the previous scenario. Since the landmarks are distributed in a clear pattern, it can be easily verified that the coordinates computed by the simulation and shown in Figure 4.23 are correct.

NAVCAM capacity for landmark detection

The NAVCAM instrument has a limitation for the detection of landmarks depending on their size. This is due to the fact that if a landmark is smaller than a pixel size it will not be detected, therefore, this consideration must be had in the model implementation. This has been analysed and as shown in Figure 4.24, for distances between the NAVCAM and the landmark lower than 100 km, the landmark

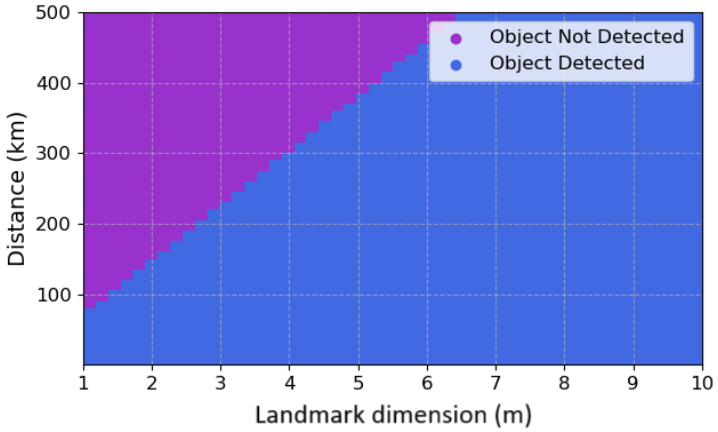

Figure 4.24: Detection of landmarks depending on its dimensions for a NAVCAM of focal length 152.5 mm, 1024x1024 pixels and 5x5° of FOV.

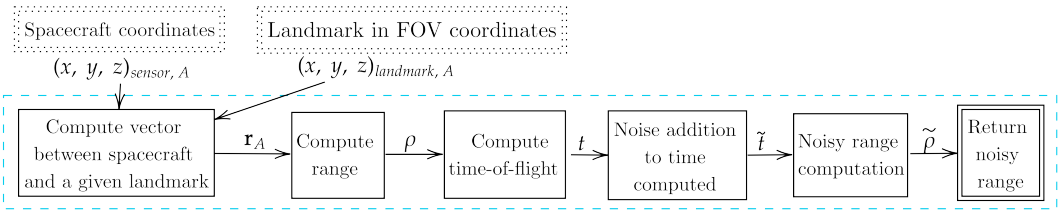

Figure 4.25: Lidar algorithm architecture for the range computation

will be detected as long as it is larger than a meter, thus confirming that this condition does not have to be checked during the simulations of the constellation, since the semi-major axis will have lower values than 100 km. Additionally, this plot also verifies the fact that the satellites can start taking measurements and making preliminary estimations from higher orbits, as long as the landmarks are larger than 7 m in size. Additionally, it should be considered that the landmark dimensions have an effect on the resolution of the position determination. If a landmark occupies a number of pixels, the determination of its position will have a lower accuracy. Although this consideration is noted, it is not included in the simulation scenario, and the code will work under the assumption that the determination of the position is done without errors resulting from the dimensions of the landmark. It is recommended that further research is done on the effect of landmark dimensions on the position estimation of the satellites.

4.5.4. Lidar and Altimeter sensor

These sensors allow the estimation of the range between a given position and the spacecraft. This is done by sending a pulse and computing the time it takes to reach the target and bounce back to the sensor. Figure 4.25 presents the algorithm developed to simulate the sensor and obtain the range from the sensor to a given landmark, and Figure 4.26 present. It should be noted that the accuracy of the estimations is dependent on the resolution of the sensor used. In particular, the error present due to the timing device in the altimeter will be set to $1 \cdot 10^{-12}$ s, following the current data presented in the International Laser Ranging Service on timing devices[2]. In addition, the pointing accuracy is set to $8.5 \cdot 10^{-5}$ rad for the mothership and to $1.78 \cdot 10^{-4}$ rad for CubeSats, considering the restrictions of the NAVCAM specifications.

Verification

A simple verification of the correct functioning of the sensor can be done through the simulation of a given set of landmarks and a satellite in space. Having checked that with a null noise in the computation of the range and the control angles, the position of the satellite is computed adequately, and an analysis of the behaviour of the position error in different scenarios has been done.

Figure 4.27 shows how the position error of the satellite increases with the pointing error of the

[2]International Laser Ranging Service, "Timing Devices" Available at: https://ilrs.gsfc.nasa.gov/technology/groundSegment/timing_devices.html, Accessed on: 10-02-2024

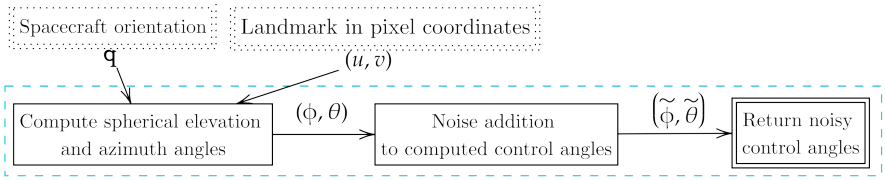

Figure 4.26: Lidar algorithm architecture for the control angles computation

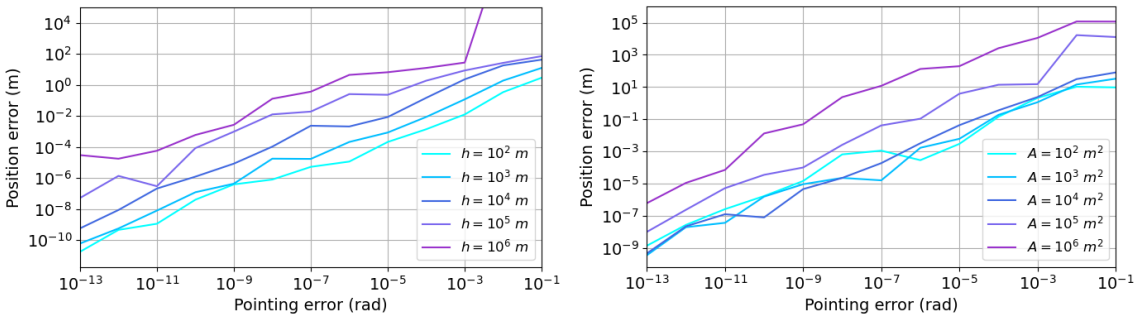

(a) Scenario with various altitudes (h) **(b)** Scenario with various landmark distribution dimensions (A)

Figure 4.27: Effect of the pointing error of the altimeter sensor on the spacecraft estimated position error

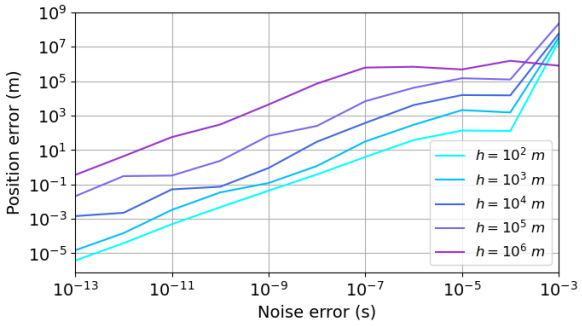

Figure 4.28: Effect of the noise error of the altimeter sensor on the spacecraft estimated position error for various altitudes (h)

sensor. The scenario simulated is a simple square with 60 landmarks randomly distributed and a satellite.

Figure 4.27a presents the effect of the altitude of the satellite on the position error. In particular, this scenario has been simulated with the landmarks spread along a square of 200 m per side and the satellite located at a range of distances, centred in the square. As can be seen, the lower the altitude is, the lower the position error is. This is due to the fact that for the same angular error, following basic geometry with Pythagoras's law, the larger the altitude the larger the deviation in the landmark position estimation and thus the larger the range computation and consecutively the satellite's position error. Another parameter in the scenario with a considerable effect on the position error is the distribution of the landmarks. Figure 4.27b presents the effect of the square size on the position error for a set altitude. Logically, it can be expected that the further the landmarks are spread from one another, the better the position estimation is. Nevertheless, this is not directly represented in the plot. As can be seen, larger position estimation errors can be found for landmarks spread in dimensions of 10^5 by 10^5 m^2 and 10^6 by 10^6 m^2. This is due to the fact that for a fixed attitude of 10^4 m, the pointing errors have a higher effect on the landmark position estimation. In the cases where the attitude is larger than the landmarks dispersion area, the dispersion has no relevant effect on the position error.

Figure 4.28 shows the effect of the noise error in the range computation on the computed position for different altitudes. While the noise error has only a proportional effect on the range computation, one would expect that the altitude of the orbit would not make a difference in the position error. Nevertheless, the error increases with the altitude due to the fact that the estimation of the satellite's position for the same additional error in the range is worse the less dispersed the landmarks are.

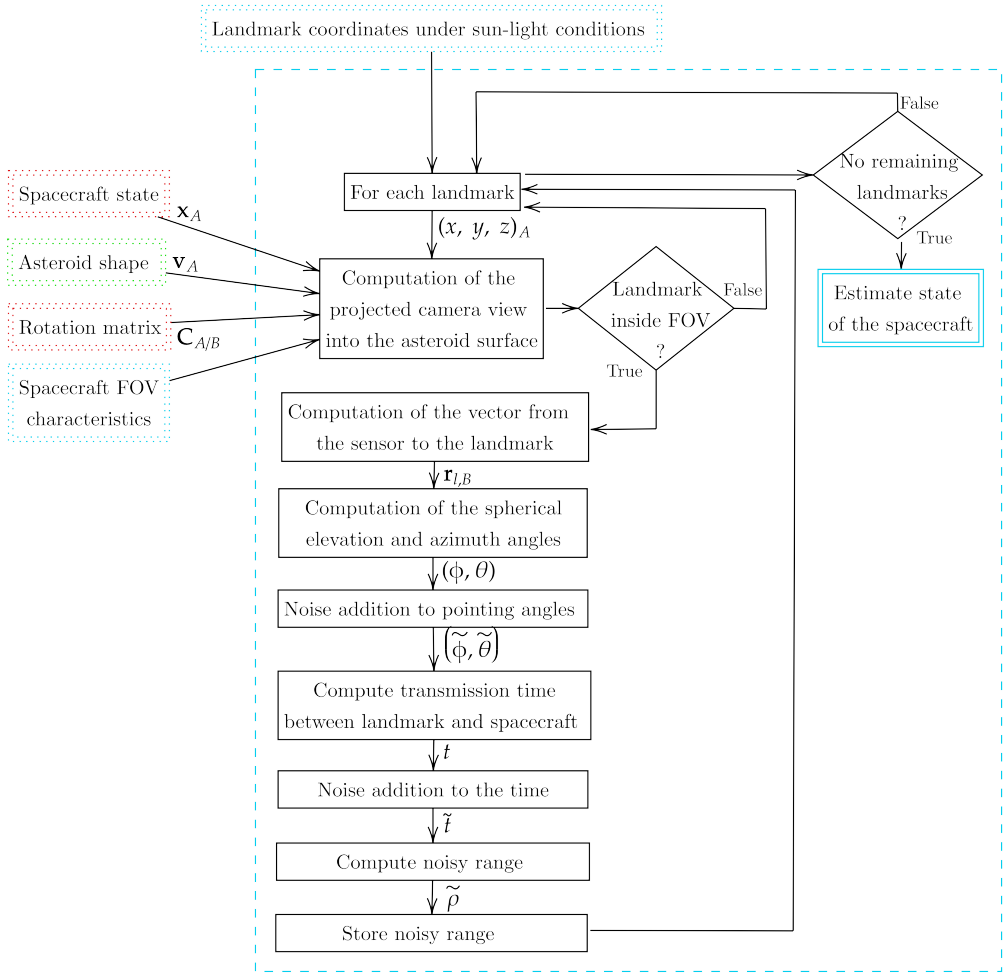

Figure 4.29: Architecture diagram of the measurement computation block

4.5.5. Measurement estimation through the sensors

As presented in Section 3.1, the satellites have been simulated with a NAVCAM and a lidar to estimate their position with respect to the asteroid reference frame from the landmarks detected. Its implementation is presented in this section. The measurement computation is done using the NAVCAM and lidar sensors to obtain the range and control angles of the space vehicle for a given landmark. From the measurements for all the landmarks visible by the NAVCAM, the state of the spacecraft carrying the sensor is then estimated. This process is carried out following the steps depicted in Figure 4.29.

It should be noted that to properly use the sensors, the RSW reference frame is used, and therefore transformations between the asteroid reference frame and the RSW must be done.

Verification

The correct functioning of this block can be verified through a simulation of all the sensors together and an estimation of the state of the vehicle through them. The scenario in hand is presented in Figure 4.30, depicting a satellite orbiting the asteroid with a semi-major axis of 25 km, and the NAVCAM'S field of view amongst the asteroid's landmarks.

The complete system has been used to calculate the error in the position estimates derived from the measurements obtained from the satellites considering the visibility constraints of landmarks and the characteristics of the sensors for a set of conditions. Figure 4.31a shows how as expected, the number of detected landmarks is highly dependent on the total number of landmarks distributed along the asteroid. Note that during sun-lit areas, the number detected is variable because of the irregular distribution of the landmarks along the surface. This irregularity is more prone to lead to insufficient landmark detections in specific areas for low-density landmark distribution. Furthermore, it can be observed that, as expected, the satellites do not detect any landmarks when they are located in shadow regions. The

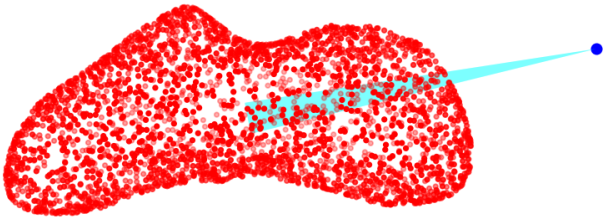

Figure 4.30: Spacecraft (presented in blue) field of view on the asteroid's landmarks (presented in red)

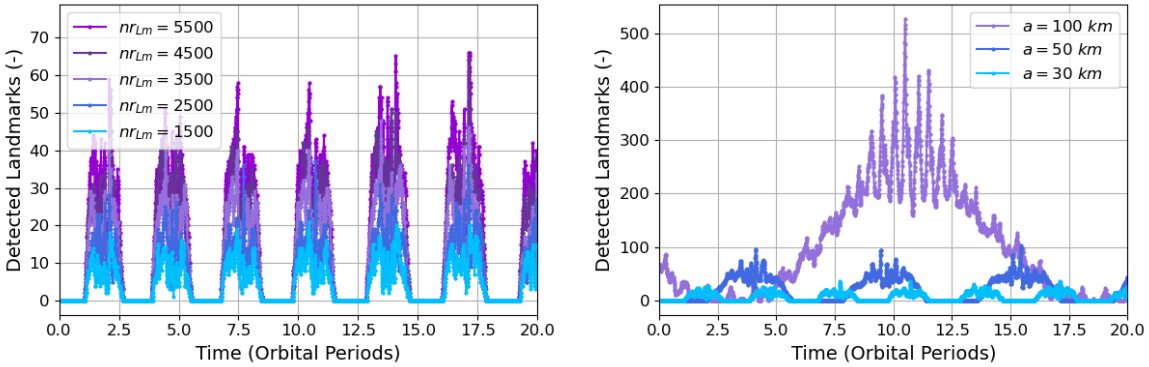

(a) Varying number of total landmarks and $a = 30$ km

(b) 2500 total landmarks with varying a

Figure 4.31: Total detected landmarks as a function of time

shadow effect is particularly noticeable in Figure 4.31b, which shows the landmarks detected for a range of semi-major axes. Since the velocity of the satellites orbiting the asteroid varies depending on the semi-major axis, the shadow areas where no landmarks are detected are located at different times on the plot. The lower the altitude, the higher the number of orbits around the asteroid that the satellites do in the same amount of time, and therefore, the larger the number of shadow regions encountered. This can be observed in the figure, depicting a larger number of sun-lit regions of shorter duration for lower altitude orbits. Additionally, this figure also highlights how the larger the altitude, the higher the number of detected landmarks is, which can be directly linked to a larger FOV of the NAVCAM.

Further testing has been done with the Eros polyhedron model considering a total of 1500 landmarks. The sensor algorithm has been used to estimate the position of a satellite orbiting Eros for a set of semi-major axis values as a function of time. This test has considered a fixed value of pointing and noise error of $1.0 \cdot 10^{-5}$ and $1.0 \cdot 10^{-9}$ respectively. As depicted in Figure 4.32, the position error remains very similar as the semi-major axis of the orbit increases. While this might seem counterintuitive, since the lower the altitude the more spread out the landmarks are with respect to the satellite's position, and thus the better the trilateration algorithm for the position estimation should perform. However, having higher altitudes allows the NAVCAM the detection of a higher number of landmarks, which compensates for this fact and leads to a similar position error estimation. Furthermore, it can be noted that as the altitude increases, so does the orbital period, leading to a smaller number of measurement blocks of longer length. This can be seen in the blank spaces between the estimates that indicate the shadow periods of time when the satellites cannot make measurements.

Moreover, Figure 4.33 shows the position error computed from the measurements of a mothership orbiting the satellite. In particular, Figure 4.33a illustrates the effect that the number of landmarks on the asteroid's surface has. It has been seen that there is a slight effect where the larger the landmark density, the lower the error. However, this is not as significant as one would expect. Furthermore, Figure 4.33b depicts the effect of the pointing error on the position estimation error. As can be seen, the position error is maintained below 1 m for pointing errors of 10^{-6} rad, below 10 m for pointing errors of 10^{-5} rad, 100 m for pointing errors of 10^{-4} rad, and 1000 m for pointing errors of 10^{-3} rad. This highlights the relevance of having an accurate sensor for improved behaviour of the system. Moreover, it should be noted that since the noise error in the range estimation is commonly of the order of 10^{-12}, which is included in the results presented, it is not dominant and thus has no effect on the position error. It

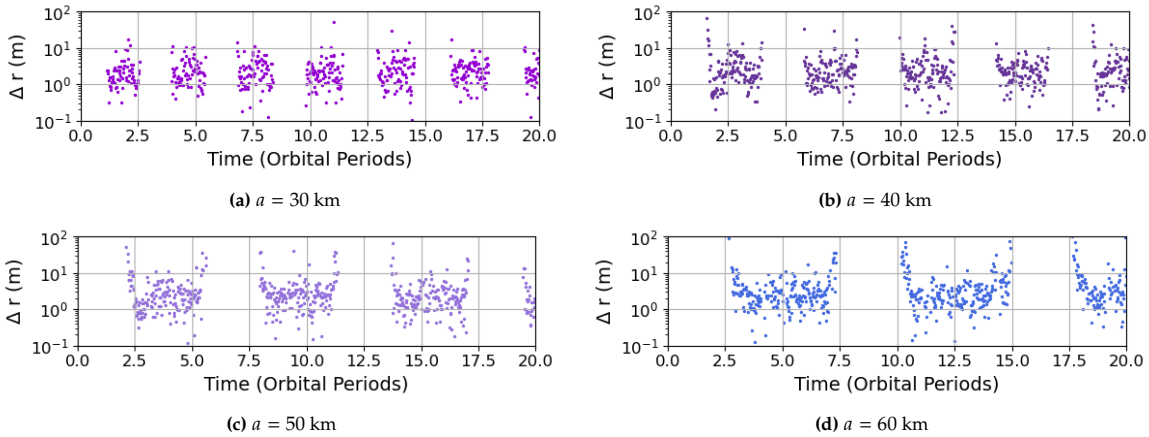

(a) a = 30 km

(b) a = 40 km

(c) a = 50 km

(d) a = 60 km

Figure 4.32: Error in position estimation considering a total of 1500 landmarks for a range of semi-major axis values.

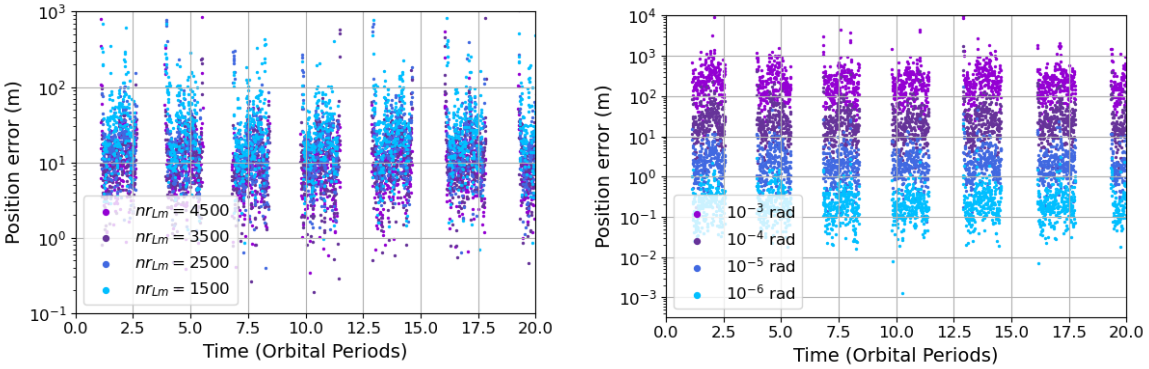

(a) For a range of landmarks with a mothership field of view and a $8.5 \cdot 10^{-5}$ rad pointing error.

(b) For 1500 landmarks with a mothership field of view and a range of pointing errors.

Figure 4.33: Position error as a function of time for the mothership for a semi-major axis of 30 km and an inclination of 90°.

should be noted that these plots have regions without position error values. These are indicative of shadow regions where the satellites cannot obtain measurements and therefore no position estimates are made.

In addition, mothership characteristics have been compared with CubeSats. Since the CubeSats FOV is larger, as the characteristics of the commercial-off-the-shelf NAVCAM presented in Section 3.1 presents, having an additionally larger pointing error than the mothership, their effect on the position error is compensated and both result in very similar results.

4.6. Estimation Module

The estimation block consists of the use of an unscented Kalman filter to estimate the state of the spacecraft and the spherical harmonics of the gravity field. The specific design of the filter within the constellation is further developed in Chapter 5 to ensure an efficient design and use of the measurements.

4.6.1. UKF algorithm

Figure 4.34 presents the UKF algorithm introduced in Section 3.2 to be used in the estimation of the Spherical Harmonic coefficients.

Verification

The proper implementation of this algorithm must be verified. To do so, the algorithm is implemented for the scenario presented by Zarchan and Musoff (2009), and the results obtained are compared to those presented in the book.

The problem investigated consists of the estimation of the altitude of a falling object tracked by a radar. This is depicted in Figure 4.35, showing that the falling object has an initial altitude of 200,000

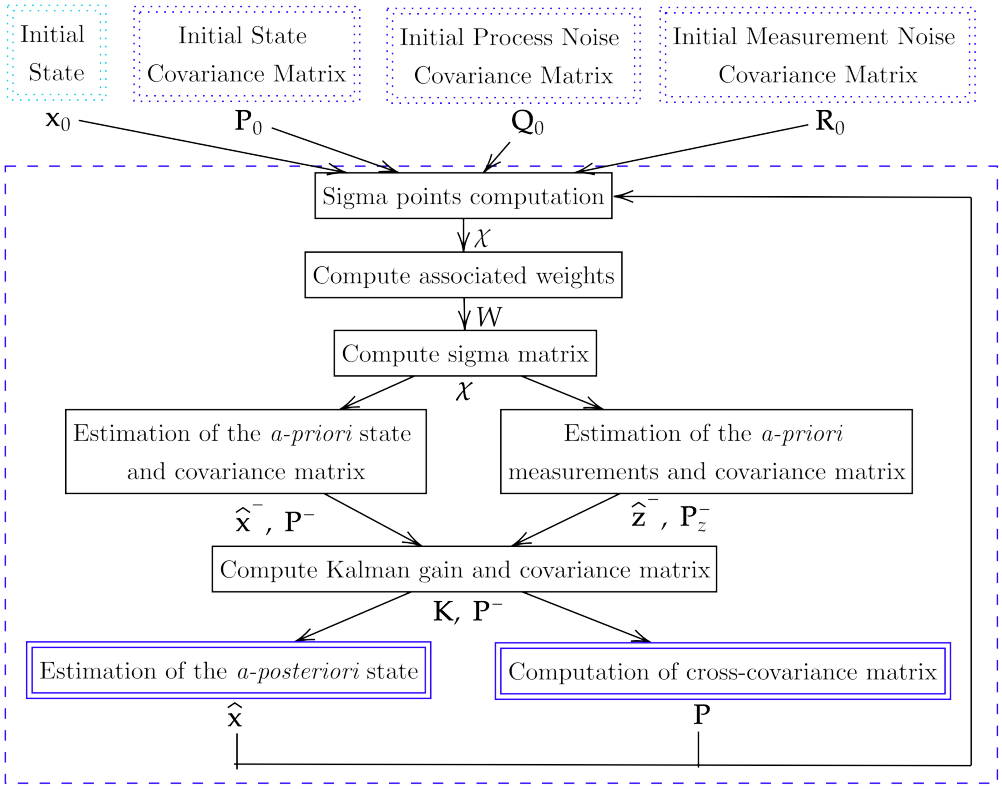

Figure 4.34: UKF algorithm

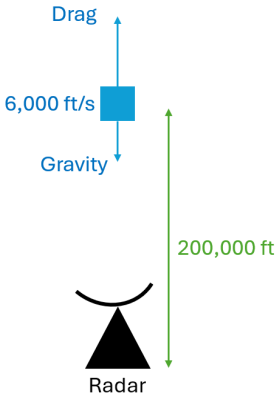

Figure 4.35: Kalman filter algorithm testing scenario

ft and an initial velocity of 6000 ft/s. It should be noted that the only forces that act on the body are gravity and drag.

To verify the functioning of the UKF, an EKF filter has been implemented to corroborate the Zarchan results can be correctly replicated. The scenario aims to estimate the altitude and velocity of the object through given measurements. Therefore, the state vector is defined as follows:

$$X = \begin{pmatrix} x \\ \dot{x} \end{pmatrix} \tag{4.4}$$

where x is the altitude and $\dot{x}$ is the velocity of the object. Furthermore, it should be noted that the dynamics of the scenario can be modelled with the following second-order differential equation depicting the acceleration of the object:

$$\ddot{x} = \frac{0.0034 g e^{-x/22000} \dot{x}^2}{2\beta} - g \tag{4.5}$$

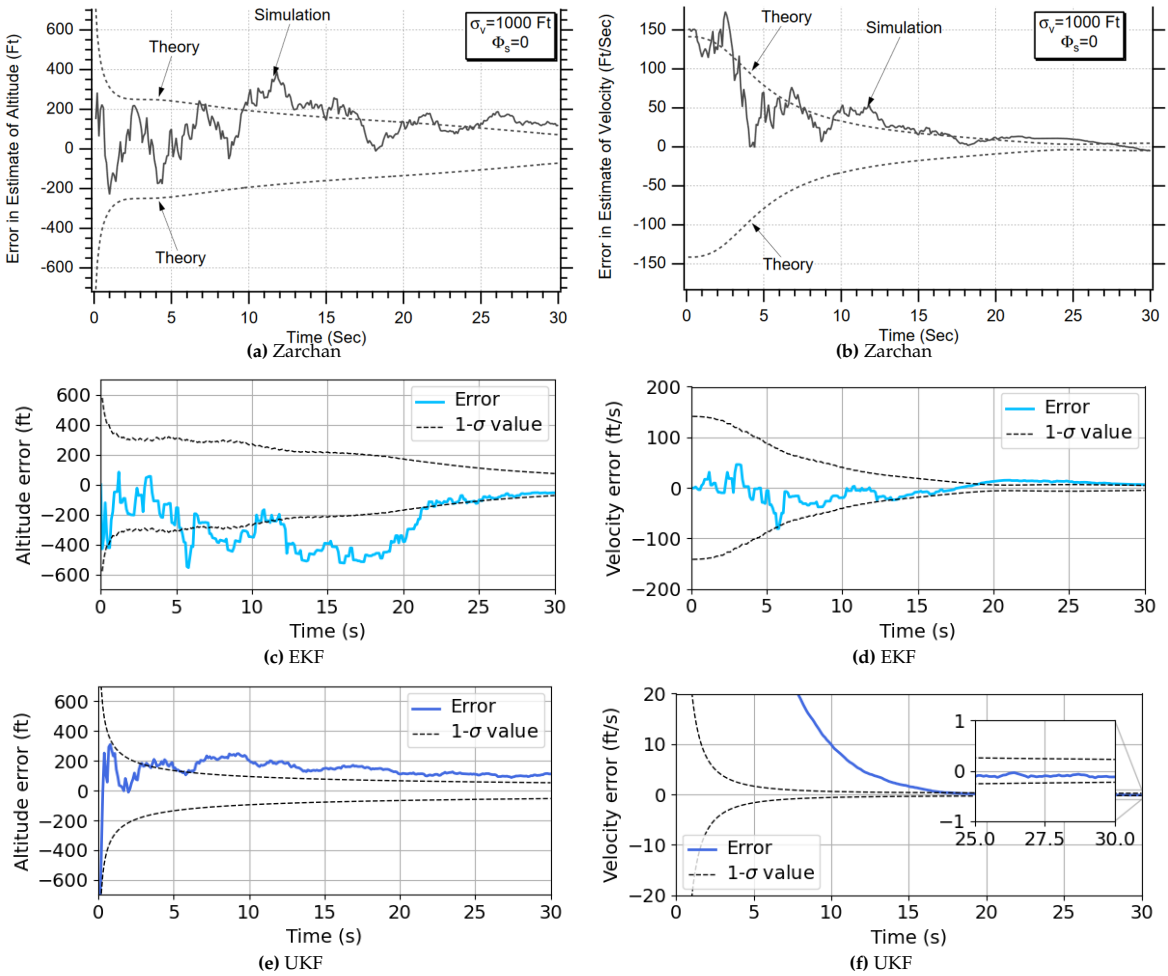

(a) Zarchan **(b)** Zarchan **(c)** EKF **(d)** EKF **(e)** UKF **(f)** UKF

Figure 4.36: Scenario considering 1000 ft of noise standard deviation and null process noise.

where β is the ballistic coefficient and g the gravity field, which has a constant value of 32.2 ft/s^2 (Zarchan and Musoff, 2009).

The filters have been set using only altitude measurements. The UKF filter measurement vector is as follows:

$$\mathbf{z}_k = x + \sigma_p \tag{4.6}$$

where σ_p is the measurement noise. Furthermore, the **P** and **Q** matrices used in the UKF are:

$$\mathbf{P} = \begin{bmatrix} p_x & 0 \\ 0 & p_v \end{bmatrix}, \quad \mathbf{Q} = \begin{bmatrix} q_x & 0 \\ 0 & q_v \end{bmatrix} \tag{4.7}$$

This scenario particularly shows the effect of the parameter tuning on the behaviour of the filter. Figure 4.36 presents the behaviour estimates of the filters when the process noise is set to zero and the measurement noise to 1000 ft. As it can be seen, in this case, the Zarchan EKF and the implemented EKF perform similarly, with the small differences caused by the use of different random seeds, while the UKF filter shows a considerably worse performance for both altitude and velocity estimates, since the estimates are outside of the 1-σ estimate, thus indicating that the filter believes it is performing better than it really is. This highlights the importance of proper filter tunning in both filters particularly in the UKF for an adequate implementation.

In addition, Figure 4.37 shows the effect of reducing the standard noise deviation from 1000 ft to 25 ft, which results in an unstable estimation of the velocity in all scenarios. Nevertheless, it can be seen that the UKF performs better than the EKF in this case. Furthermore, this figure also presents another test has been conducted considering a measurement error of 25 ft and a process noise of 100.

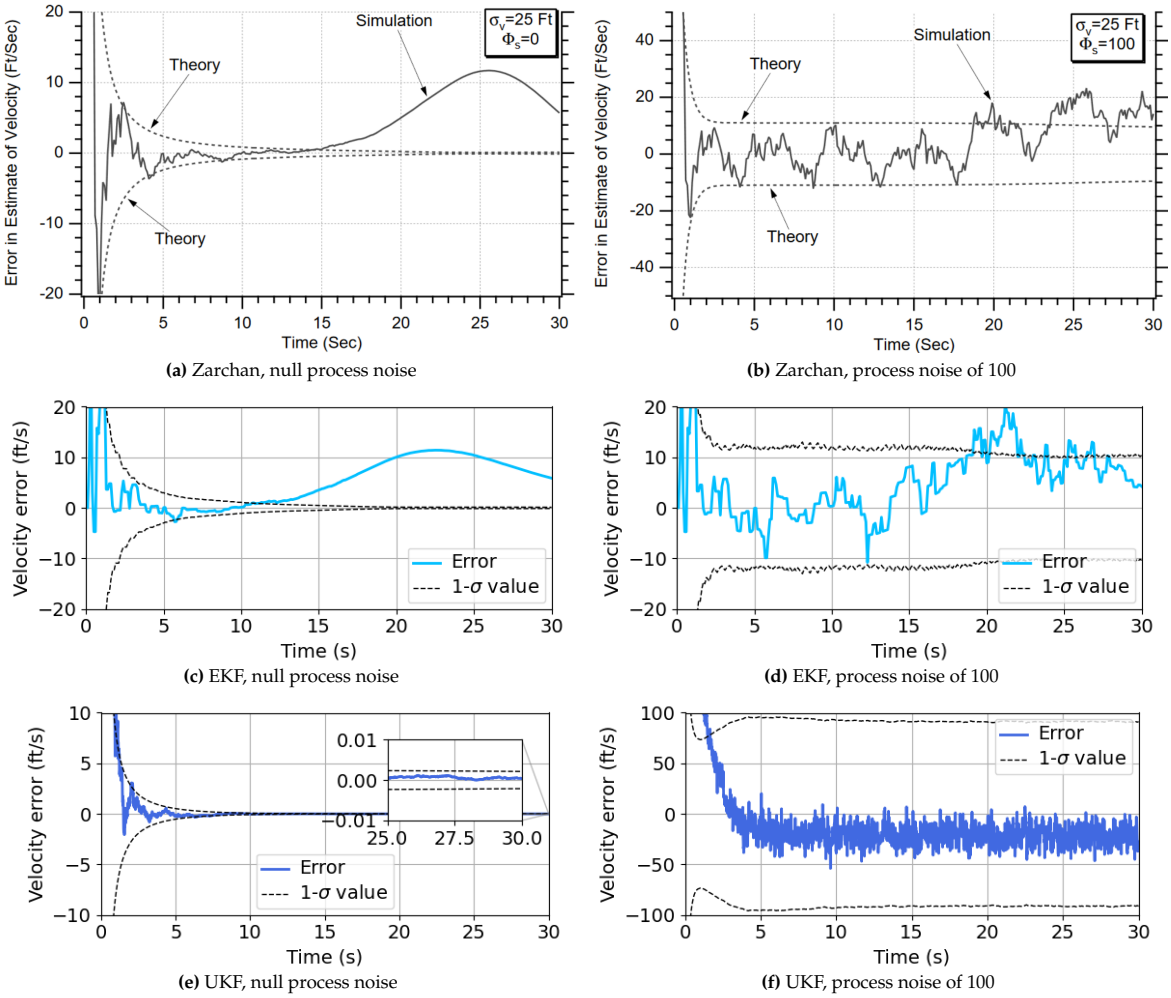

(a) Zarchan, null process noise

(b) Zarchan, process noise of 100

(c) EKF, null process noise

(d) EKF, process noise of 100

(e) UKF, null process noise

(f) UKF, process noise of 100

Figure 4.37: Scenario considering 25 ft of noise standard deviation for various process noise values.

The results are now more variable within the bounds of the filter's covariance, thus demonstrating the relevance of adequately tuning the process noise of the system.

4.6.2. UKF algorithm for the scenario

Having verified the correct implementation of the UKF algorithm, the filter has been applied to a simple scenario concerning the estimation of the estate of a spacecraft orbiting a non-rotating Eros.

Dynamics modelling using point mass gravity field in the environment and the filter dynamics

A number of simple tests have been conducted to analyse the filter's behaviour and validate it. The simplest scenario with which the algorithm has been tested is modelling both the Eros gravity field and the filter's dynamics with a point mass gravity-field model. For this implementation, the state vector has been set to:

$$X = \begin{pmatrix} \mathbf{x}_I \\ \dot{\mathbf{x}}_I \\ \mu \end{pmatrix} \tag{4.8}$$

The dynamics function for velocity (acceleration) is given as:

$$\dot{\mathbf{v}}_I = -\frac{\mu}{r_I^3}\mathbf{r}_I \tag{4.9}$$

Additionally, the measurement vector contains only the positions of the satellite, with an additional measurement noise σ_p as follows:

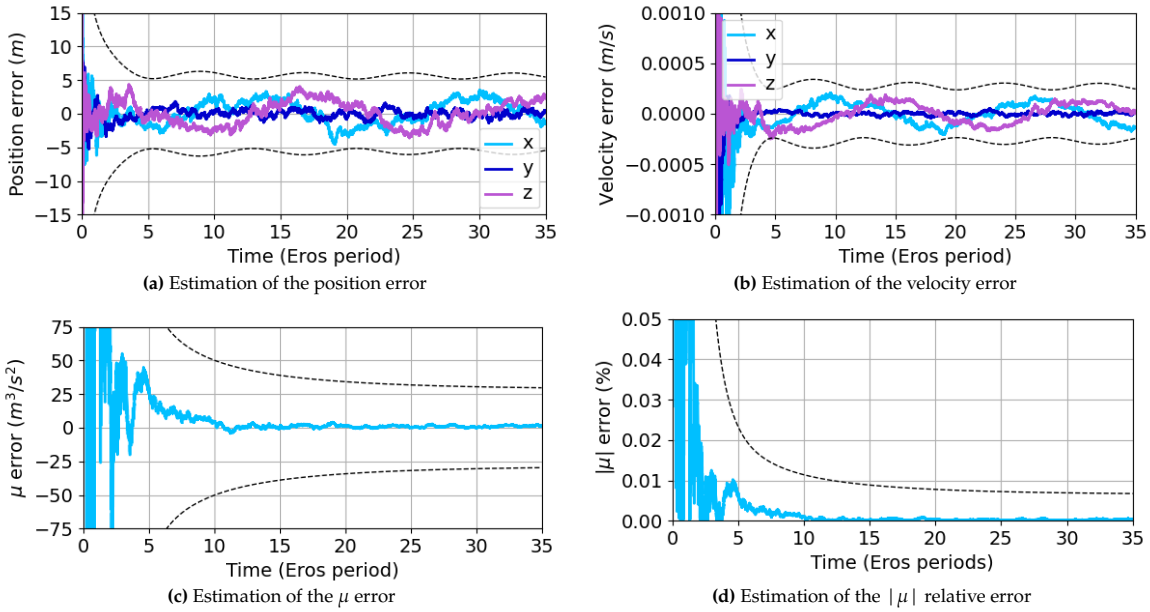

(a) Estimation of the position error

(b) Estimation of the velocity error

(c) Estimation of the μ error

(d) Estimation of the $|\mu|$ relative error

Figure 4.38: Estimation errors for the estimation of Eros asteroid with point mass gravity filed for an orbit of 100 km of semi-major axis and 90° inclination

$$\mathbf{z}_k = \left(\mathbf{x}_A\right) + \begin{pmatrix} \sigma_p \\ \sigma_p \\ \sigma_p \end{pmatrix} \tag{4.10}$$

The ideal scenario has been tested simulating a spacecraft orbiting the asteroid with a 100 km semi-major axis and 90° inclination. The simulation has considered measurement noise σ_p of 100 m.

The UKF algorithm has been tuned with a covariance matrix of $\sigma = 200$ m, a process noise matrix of:

$$\mathbf{Q} = \begin{bmatrix} \mathbf{I}_{3\times3} \cdot q_p & \mathbf{0}_{3\times3} & \mathbf{0}_{3\times1} \\ \mathbf{0}_{3\times3} & \mathbf{I}_{3\times3} \cdot q_v & \mathbf{0}_{3\times1} \\ \mathbf{0}_{1\times3} & \mathbf{0}_{1\times3} & q_\mu \end{bmatrix} \tag{4.11}$$

where after a filter optimisation, the parameters have been set to $q_p = 10^{-7}$, $q_v = 10^{-10}$ and $q_\mu = 10^{-15}$. Additionally, the filter has been set with $\alpha = 0.1$, $\beta = 2.0$ and $\kappa = 0.0$, which are the recommended values. It should be noted that the effect of the values selected for α, β and κ has been done and has shown no significant effects on the filter performance, thus confirming the adequacy of using the recommended values.

The results obtained with this scenario are illustrated in Figure 4.38. These show how the filter can reduce the position error from 100 m to 5 m and estimate the velocity, with a 1 m/s error in the initial state, with an error lower to 0.5 mm/s. Furthermore, the gravitational parameter estimated has an error lower than 0.01%, thus confirming that the UKF can successfully estimate the state of the satellite. These excellent results are to be expected since the same models are used for both the environment simulation and the filter dynamics.

Dynamics modelling using spherical harmonics gravity field in the environment and a point mass model in the filter dynamics

The same filter has been tested, but this time simulating Eros's gravity field with the spherical harmonics model up to degree and order 15 for two orbits of 100 km and 200 km. The estimates obtained are presented in Figure 4.39. Note that the filter has been updated with the following process noise matrix values: $q_p = 10^{-10}$, $q_v = 10^{-8}$ and $q_\mu = 10^4$ for the 100 km scenario and with $q_p = 10^{-14}$, $q_v = 10^{-10}$ and $q_\mu = 10^3$ for the 200 km.

As can be observed, both cases present now worse estimates than the previous case, as can be expected. In particular, the gravitational parameter estimate now includes perturbations. This is due to the fact that the dynamics of the filter only consider the point mass model while the real environment is

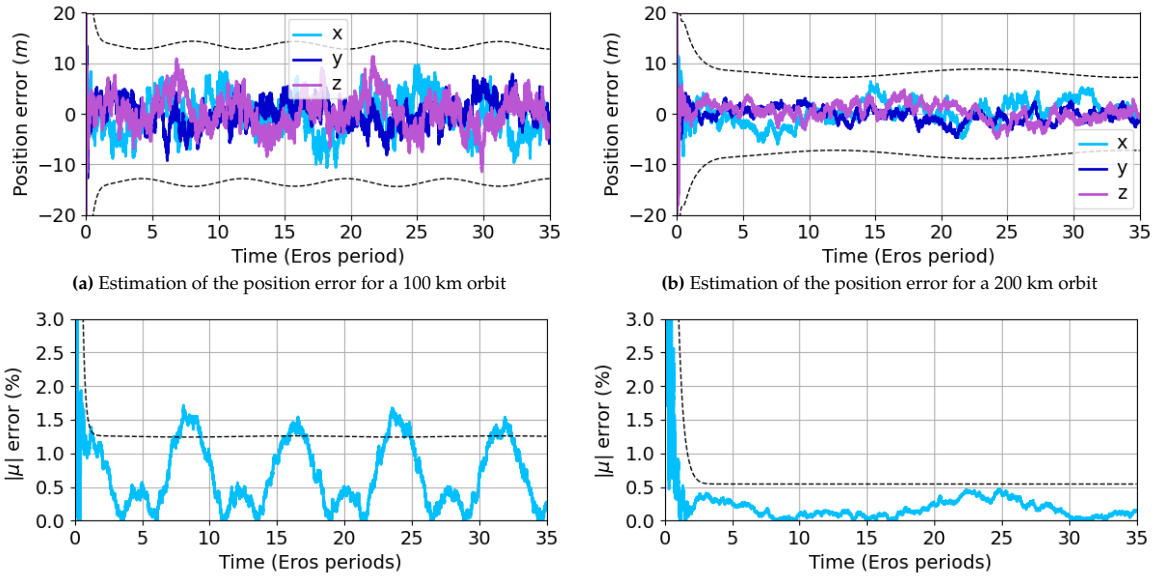

(a) Estimation of the position error for a 100 km orbit

(b) Estimation of the position error for a 200 km orbit

(c) Estimation of the $|\mu|$ relative error for a 100 km orbit

(d) Estimation of the $|\mu|$ relative error for a 200 km orbit

Figure 4.39: Estimation errors for the estimation of Eros asteroid with a complete spherical harmonics gravity filed

considerably disturbed by the irregularity of the asteroid, and thus, the perturbations of the environment cannot be fully modelled by the point mass dynamics considered in the filter.

The tests show how larger altitudes are able to provide better estimates. For instance, with the same measurement error, the higher orbit is able to estimate position with an error of 10 m and a velocity error of 1 mm/s, whereas the lower orbit does so with a 15 m position error and a 5 mm/s velocity error. These estimation errors are due to the difficulty in the estimation of the gravity field parameter. As depicted in the figure, for a 200 km orbit, the error is maintained within the bounds of a 0.5% error while for a 100 km altitude, the irregularity effects of the asteroid felt by the spacecraft are larger and this translates to the estimate reaching errors of 1.5%. It is interesting to point out that the distribution of the peaks in error can be attributed to the two bulges of the asteroid, which have the highest gravity field pull. This also explains why the distribution of the errors with time is different for both orbits since the lower orbit has higher velocity and therefore experiences the two bulges of the asteroid's effect, while the higher-altitude orbiting asteroid has a slower velocity and therefore only shows one main error perturbation. This highlights the importance of properly modelling the system environment and demonstrates the correct functioning of the system. Moreover, it should be noted that the filter is only capable of estimating adequately the μ, because the spacecraft orbits at large altitudes. The closer the asteroid is, the larger the perturbations in the environment, and the larger the estimation errors are. Therefore, the estimation of μ should be done at large attitudes when using point mass dynamics to obtain better accuracy in the estimation. Then, after proper convergence, $\tilde{\mu}$ can be removed from the filter estimates and hardcoded into the filter dynamics.

Dynamics modelling using spherical harmonics gravity field in the environment and in the filter dynamics

To further verify the previously obtained results the filter dynamics have now been modeled with the spherical harmonics model. As a verification scenario, the filter uses the SH coefficients of the asteroid and only estimates the gravitational parameter of the asteroid.

The estimates obtained for the scenario considering a 100 km orbit are presented in Figure 4.40. The estimates show how the filter is now able to estimate the μ very accurately with a percentage error lower than 0.04% as opposed to the 1.5% obtained when modelling the system with PM. Additionally, it can be seen that the estimation does not contain any peaks, thus demonstrating that by using the SH model in the filters' dynamics, the main perturbations are now modelled in the filter and the estimate is produced more accurately. Furthermore, this consequently results in an improvement of the position and velocity estimates and verifies the correct implementation of the model and filter performance.

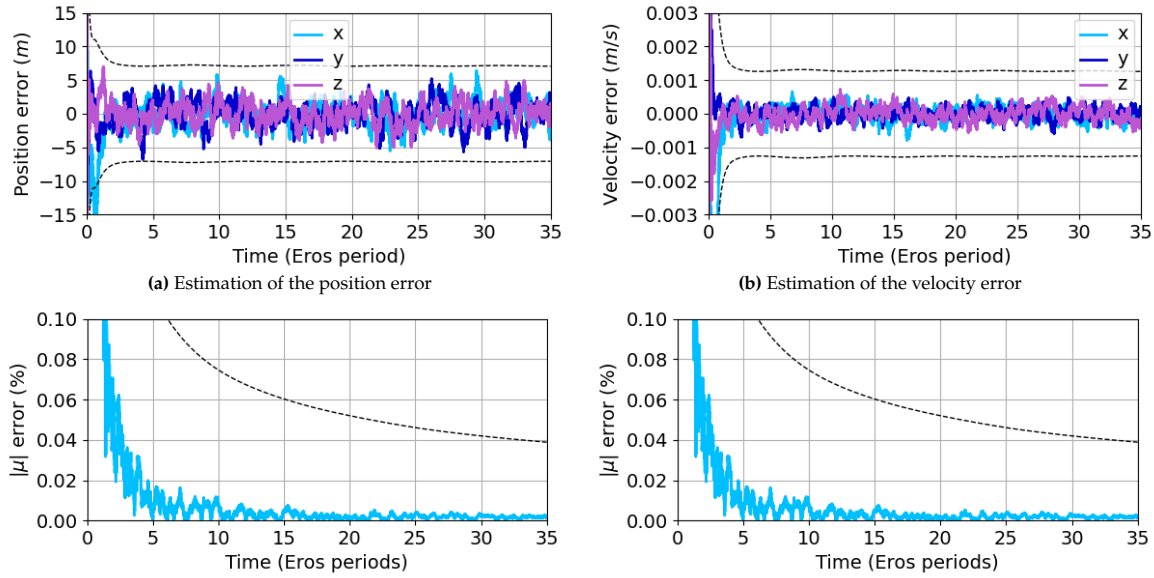

(a) Estimation of the position error

(b) Estimation of the velocity error

(c) Estimation of the μ error

(d) Estimation of the $|\mu|$ relative error

Figure 4.40: Estimation errors for the estimation of Eros asteroid with SH filed for an orbit of 100 km of semi-major axis and 90° inclination

4.7. Summary

1. The simulator is composed of the following main modules: configuration, environment, propagation, measurements, and estimation. Each containing all the functionalities necessary to simulate the entire system, and a variety of mission scenarios.
2. The environment module is necessary for the definition of the asteroid tested and its environment, containing the following main tasks:

   (a) The asteroid shape is modelled using a polyhedron model, with a set of landmarks randomly distributed along the surface with several spatial densities.
   (b) The gravity field of the asteroid is modelled using spherical harmonics with the coefficients estimated in the NEAR mission which are up to degree and order 15. The gravity field simulated has been verified with results obtained by Miller et al. (2002).

3. The hardware module is used for the simulation of the satellite hardware and measurement simulation. A number of functionalities have been implemented, the main being as follows:

   (a) Visibility constraints have been implemented within the code to detect which parts of the asteroid are in the shade and which are sun-lit, and therefore define at a given time instant, which landmarks can be detected by the satellite sensors.
   (b) Communications constraints have been implemented to simulate the data transmission necessary between CubeSats and mothership and determine when it is feasible and both transmitter and receiver can establish direct line-of-sight.
   (c) NAVCAM and Lidar sensors have been implemented and tested for the detection of landmarks and estimation of the range between the visible and detectable landmarks in the FOV of the satellite.
   (d) Using all the sensors for position estimation, several tendencies have been observed. The higher the density of landmarks within the asteroid, and therefore, the larger the number of landmarks detected by the sensors at each instant, the lower the position error overall. Nevertheless, the position error has shown which averages along the order of 10 m, has been shown to be very variable due to the irregular dispersion of the landmarks. Furthermore, the pointing error in the sensor has been shown to be the dominant error in the system, having very significant effects on the position error measured.

4. The estimation module has implemented a UKF algorithm to estimate the states of the satellites. The UKF implementation has been verified using a simple scenario considering a spacecraft

orbit around Eros. This has demonstrated the adequate performance of the filter being capable of estimating adequately the gravitational parameter of the asteroid with different models and highlighting the perturbations of the asteroids' gravity field in the environment.

5. The following chapter conducts a sensitivity analysis of the scenario. This considers a real-world simulation of the system and analyses how the parameters of the design affect the estimation obtained.

5

Sensitivity Analysis of the Scenario

Understanding and optimising the performance of the constellation of satellites requires a comprehensive sensitivity analysis. This identifies how variations in different parameters impact the estimates produced by the system. By examining these factors, the design of the constellation can be improved to enhance the performance of the system.

This chapter presents the considerations taken in the design and tuning of the scenario. To do so, an initial analysis of the spherical harmonic coefficients of the gravity field that the system aims to estimate is conducted to obtain a better understanding of the system behaviour and its results in Section 5.1. This is followed by the analysis of the system in a number of scenarios.

Firstly, a sensitivity analysis on the scenario design for a single satellite is then conducted in Section 5.2. This analysis aims to explore how different aspects of the system design affect the state estimates produced. The scenario analysis is divided into the following sections:

- Subsection 5.2.1 contains an analysis of the orbital coverage and its effect on the estimates.
- Subsection 5.2.2 presents an analysis of the effect that the errors in the states and measurements have on the estimates.
- Subsection 5.2.3 depicts an analysis of the frequency update of the measurement on the estimates.
- Subsection 5.2.4 includes an analysis of the forces considered in the scenario.

Secondly, an analysis of the system is conducted considering a scenario with a constellation of satellites in Section 5.3. This analysis is divided into the following sections:

- Subsection 5.3.1 analyzes the distribution of the satellites.
- Subsection 5.3.2 examines the effect of the number of satellites on the estimates.
- Subsection 5.3.3 investigates the impact of measurement update frequency and propagation time on the estimates.

Thirdly, an analysis of the constellation distribution sensitivity on the estimates is conducted when visibility and communication constraints are considered in Section 5.4. This analysis is divided into the following sections:

- Subsection 5.4.1 analyzes the effects of visibility constraints on the system.
- Subsection 5.4.2 examines the effect of communication constraints on the estimates.
- Subsection 5.4.3 investigates the impact of satellite distribution when both visibility and communication constraints are considered on the estimates.

It should be noted that Appendix D is referenced along the chapter. This appendix acts as a support containing detailed descriptions of the filters used, as well as the configuration parameters used in the tests presented and further results obtained.

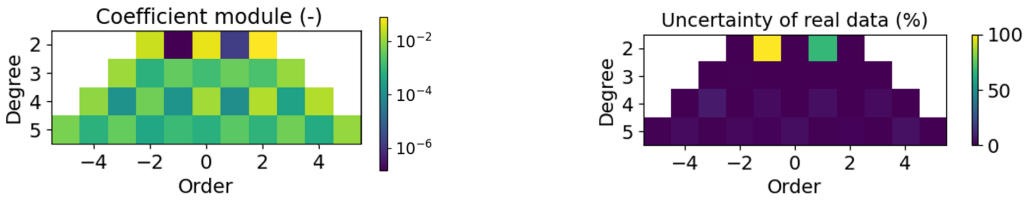

(a) Module **(b)** Uncertainty

Figure 5.1: Gravity field coefficients obtained in the NEAR mission

5.1. Coefficient Estimates Analysis

A proper understanding of the patterns of the spherical harmonic gravity-field coefficients that the filter aims to estimate is necessary to better comprehend the estimates produced by the UKF. This section presents the considerations from the coefficients that represent the true gravity-field scenario that have been had for the proper design of the UKF.

Detailed information on the spherical harmonics coefficients used can be found in Appendix C, depicting the normalised spherical harmonic coefficients used in this simulation and an analysis of their contribution to the gravity field of the asteroid. With the conducted analysis, it has been determined that the filter shall not aim to estimate all the coefficients. Two considerations have been made:

- Coefficient $C_{0,0}$ is set to 1, which indicates that the point mass gravity field to be used is the μ value that has been determined for the asteroid. Therefore, with this consideration, this coefficient will not be included in the estimation and a value of 1 is assumed for all cases.
- The coefficients $C_{1,0}$, $C_{1,1}$ and $S_{1,1}$ are related to the geocentric coordinates. This scenario works under the assumption that the origin of the asteroid coincides with the geocentre and thus, the filter will not aim to estimate these coefficients. Their null value can be additionally seen in the gravity-field plots, which present a regular distribution due to the lack of forces.

With these considerations noted, the coefficients are briefly analysed for a proper understanding of the results that are presented in the estimations made in this chapter that are presented in the following sections.

Figure 5.1a shows the absolute values of the coefficients that the UKF filter intends to estimate, conforming to the gravity field of the scenario. As can be seen, there are several patterns that can be noted from the distribution shown in this plot. These are as follows:

- The $C_{2,1}$ and $S_{2,1}$ are two coefficients that present considerably lower values than the rest, therefore it is to be expected that the filter has difficulty in their estimation.
- A tendency can be identified in which the absolute value decreases as the degree increases, which is indicative of the fact that high-degree coefficients might be more challenging to estimate than those with lower degrees.
- The coefficients' absolute values depict a checker pattern, which shows how the gravity-field force considerably changes with the coefficient's degree and order.

The $C_{2,1}$ and $S_{2,1}$ coefficients

Figure 5.1a has shown considerably lower values for the $C_{2,1}$ and $S_{2,1}$ coefficients than for the rest. These coefficients are connected to the mean rotational pole position, and therefore, its low value can be directly linked to the fact that this rotation is almost negligent.

Additionally, Figure 5.1b depicts the uncertainties present in the coefficients used to represent the gravity field of the scenario. As can be seen, these coefficients present considerable uncertainties, much larger than the rest, and presenting even a larger uncertainty than the estimated value itself. This can be directly related to the considerable small value of these coefficients, which being almost negligible is very challenging to estimate with a high accuracy. Therefore, it can be expected that the filter will also have difficulty with their estimation, and large errors can be expected.

This has been additionally tested with two scenarios, which aim to only estimate the effect of these coefficients by nulling the rest of the gravity field. The results obtained are depicted in Table 5.1, which presents the estimated coefficients and their true values. As can be seen, even when the filter is only used for these coefficients, it is unable to produce an accurate estimate.

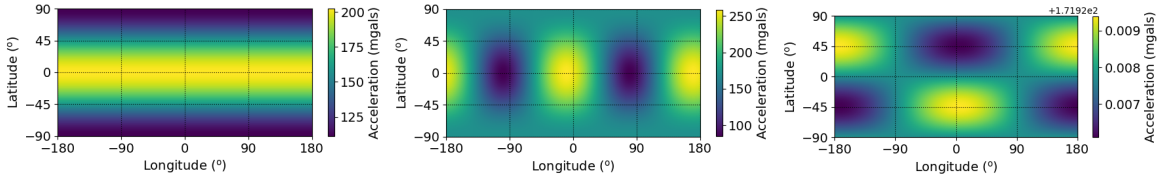

(a) $m = 2, n = 0$ **(b)** $m = 2, n = 2$ **(c)** $m = 2, n = 1$

Figure 5.2: gravity-field norm for the contribution of single cosine and sine coefficients

Additionally, Figure 5.2 presents the module of the gravity field contribution for these coefficients. As can be seen, the contribution of the SH coefficient for the first order is four orders of magnitude lower than that of the others, thus confirming its negligible effect on the gravity field. This can directly explain the difficulty that the filter has in estimating this coefficient.

5.2. Sensitivity Analysis: Single Satellite

This section presents an analysis of how the scenario parameters affect the spherical harmonic coefficient estimation for a simple scenario in which a single satellite is modelled. This simplified analysis aims to provide a more in-depth understanding of the sensitivity of the filter, since the effects derived from only considering one satellite allow to explore some effects in more detail and the results are applicable to the constellation of satellites.

Subsection 5.2.1 presents the effects that the orbital coverage has on the gravity filed estimates, Subsection 5.2.2 the effect of the state and measurements errors, Subsection 5.2.3 the effect of the frequency update of the measurements, and Subsection 5.2.4 the effect of the forces considered in the scenario.

It should be noted that this first set of sensitivity analysis models a simple environment, considering by default an environment with no external perturbations and the only force being the gravity field of the satellite modelled with up to degree and order five. Additionally, the filter in the tests aims to estimate only up to degree and order five since considering a lower order model decreases the computational time of the tests while still maintaining the behaviour of the system and therefore producing representative results. The design of the filter is presented in Subsection D.1.1 of Appendix D, detailing the state vector, the measurements used as well as the **P**, **Q**, and **R** matrices.

5.2.1. Orbit Coverage analysis

Given the irregularity of the gravity field, it is essential to have sufficient satellite coverage of the entire asteroid to accurately estimate the spherical harmonics coefficients. An initial analysis has been conducted to assess how orbit coverage influences the results. This analysis focuses on the main orbital parameters affecting coverage: inclination, semimajor axis, and propagation time, examined through test "ORB-1" and the impact of eccentricity is evaluated in the test "ORB-2". Details on the parameter settings used for the scenario simulation of these tests and the results obtained can be found in Subsection D.1.2 of Appendix D.

To accurately determine the effect of asteroid coverage on the gravity-field estimation, the contribution of each coefficient to the gravity field has been computed. Detailed plots in Section C.2 illustrate the contributions of each degree and order, highlighting the significance of orbital coverage for accurate coefficient estimation. From the gravity-field distributions, it is evident that coefficients with a zero order predominantly influence the field horizontally, significantly affecting the asteroid's poles. Therefore, their accurate estimation benefits from polar orbits. Conversely, coefficients with matching degrees and orders exhibit field variations along longitudes, indicating that their estimation is more accurate

Table 5.1: Estimation of the coefficients of degree 2 and order 1

Test	C_{21}	Tolerance C_{21}	S_{21}	Tolerance S_{21}
Real	$-1.637912 \cdot 10^{-6}$	$1.090773 \cdot 10^{-6}$	$-1.400038 \cdot 10^{-7}$	$1.100873 \cdot 10^{-6}$
1	$-3.290747 \cdot 10^{-6}$	$5.812358 \cdot 10^{-5}$	$2.633638 \cdot 10^{-6}$	$5.713275 \cdot 10^{-5}$
2	$-7.071760 \cdot 10^{-7}$	$3.354634 \cdot 10^{-5}$	$1.524818 \cdot 10^{-6}$	$3.299256 \cdot 10^{-5}$

with equatorial orbits. The remaining coefficients, which exhibit a grid-like distribution, require comprehensive longitudinal and latitudinal coverage for precise estimation.

Test ORB-1

This test aims to analyse the effect of the orbital semi-major axis and the inclination on the coverage of the asteroid and its impact on the estimation of SH coefficients.

An initial coverage analysis has been conducted to study the effects of the semi-major axis and inclination parameters over a propagation of 1 million seconds. The coverage obtained for different inclinations with a range of fixed semi-major axes shown in Figure 5.3.

The inclination determines the latitude range covered by the satellite. Higher inclinations generally provide better coverage, enhancing the estimation accuracy of SH coefficients. Furthermore, altitude significantly affects the coverage pattern. At lower altitudes (30 km), the coverage is more irregular due to the stronger influence of gravitational irregularities; note that Eros has its two main bulges in central latitudes which produce large variations in the gravity field. As altitude increases, the distribution becomes more regular as the perturbating effects decrease.

The altitude's impact on orbital radius is shown in Figure 5.4. Smaller semi-major axes result in higher perturbation effects, leading to larger variations in orbital radius. Furthermore, the inclination has also a considerable effect on the radius due to the effect of the irregularities of Eros. While the altitude might not appear to have relevance in terms of coverage, it has a considerable contribution to the estimation of the SH coefficients of the system due to several factors:

- **Measurement Errors:** The distance from the satellite to Eros's surface influences measurement errors. Greater distances increase the impact of pointing errors, thereby affecting estimation accuracy.
- **Orbital Velocity:** Higher altitudes result in lower orbital velocities, allowing for more accurate position estimations by the filter.

The orbit with a semi-major axis of 30 km and 30° inclination shows how the trajectory of the satellite diverges over time due to the strong gravitational irregularities, as depicted in Figure 5.3g. This results in an irregular coverage, with more frequent passes at latitudes near 15° and gaps in other regions. This divergence is further illustrated by the increasing radius of the orbit shown in Figure 5.4c, indicating the satellite's escape from Eros's orbit and significantly affecting the coverage distribution.

Figure 5.5 presents the SH coefficients estimation up to degree and order five for each studied orbit. Several direct relations can be identified:

- **Semi-Major Axis:** Larger semi-major axes result in larger estimation errors due to weaker gravitational field effects at greater distances. Therefore, orbits at 30 km and 50 km are more suitable for SH coefficient estimation compared to 100 km orbits. Note that for a fixed inclination of 60°, the majority of the coefficient estimates have an estimation error higher to 100% for a 100 km orbit, while this is significantly reduced in a 50 km orbit and further even in a 30 km orbit, having the majority of the errors lower to 15%.
- **Inclination:** Inclination affects coverage, and consequently, the estimation errors. Generally, higher inclinations provide better estimations due to more comprehensive coverage.

For a 30 km semi-major axis, higher inclinations improve coverage and estimation accuracy. For instance, the 30° inclination orbit shows significant deficiencies in estimating $C_{4,1}$ and $C_{5,0}$ due to inadequate coverage of specific latitudinal regions, as shown in Figure C.4b and Figure C.5a.

Conversely, for a 50 km semi-major axis, a 30° inclination provides better estimations than higher inclinations. This could be due to specific coverage patterns and the distribution of gravitational effects as well as the slower orbital velocity, which improves the filter performance.

Several tendencies can additionally be identified from the previous plots, these include:

- **Zero-Order Coefficients:** Higher inclination orbits estimate zero-order coefficients more accurately due to better polar coverage. This is illustrated by the presence of estimation errors larger than 100% for a 30 km orbit and 75% for 30° orbits, that are reduced to errors lower than 10% when using 60° and 90° inclination orbits.

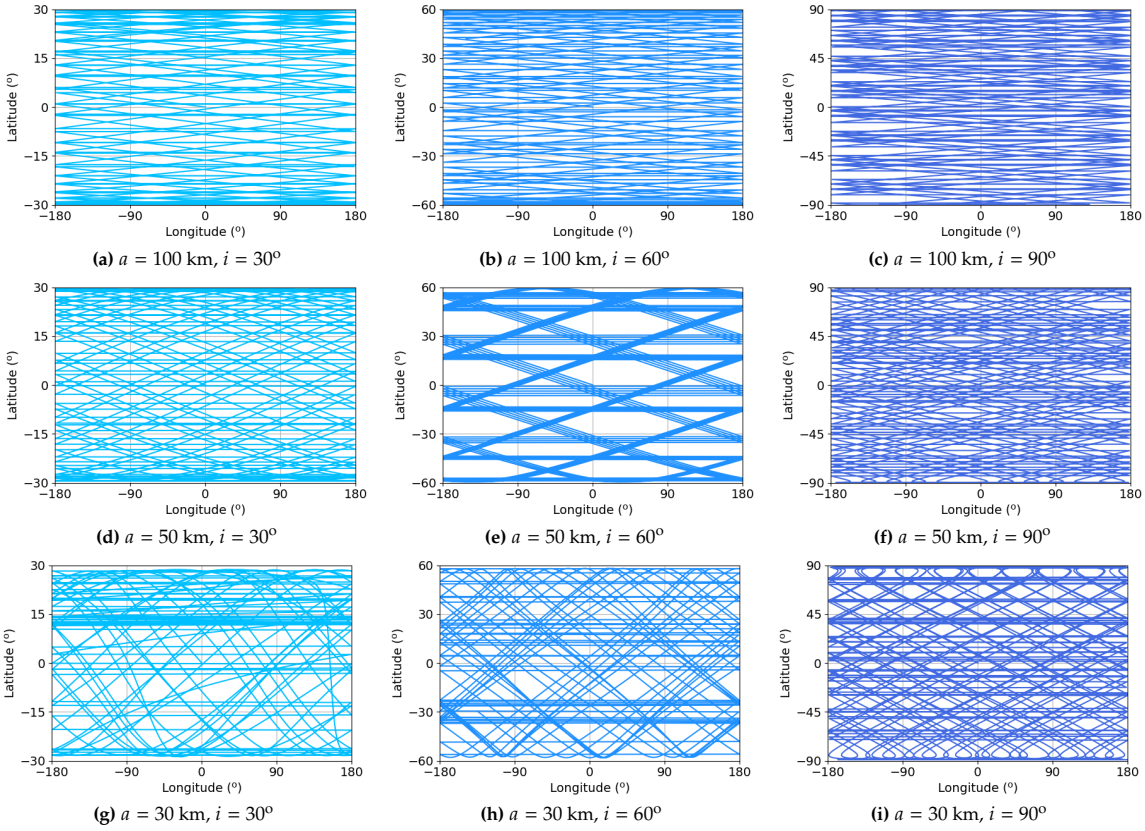

(a) $a = 100$ km, $i = 30^o$ **(b)** $a = 100$ km, $i = 60^o$ **(c)** $a = 100$ km, $i = 90^o$

(d) $a = 50$ km, $i = 30^o$ **(e)** $a = 50$ km, $i = 60^o$ **(f)** $a = 50$ km, $i = 90^o$

(g) $a = 30$ km, $i = 30^o$ **(h)** $a = 30$ km, $i = 60^o$ **(i)** $a = 30$ km, $i = 90^o$

Figure 5.3: ORB-1 Test: Coverage for a total propagation time of 1 million seconds

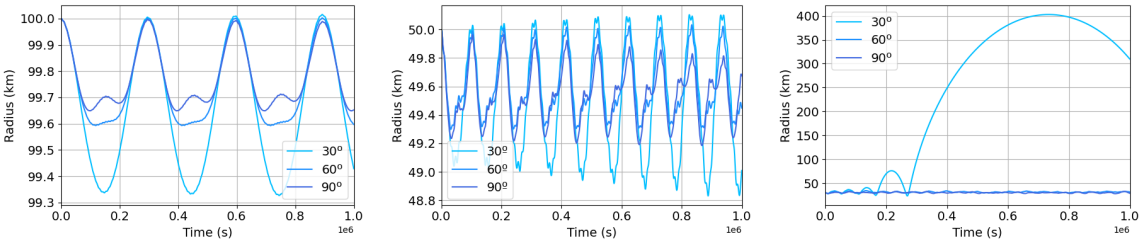

(a) $a = 100$ km **(b)** $a = 50$ km **(c)** $a = 30$ km

Figure 5.4: ORB-1 Test: Radius for a total propagation time of 1 million seconds

- **Equatorial Coefficients:** Coefficients with the same degree and order are well-estimated by all inclinations for 30 km and 50 km semi-major axes due to adequate equatorial coverage.
- **Intermediate Coefficients:** For coefficients with orders larger than zero but smaller than the degree, the estimation accuracy is sensitive to coverage gaps, explaining why the 30° inclination orbit at 30 km shows the worst estimations for these coefficients.

Additionally, the coverage for a 60° inclination orbit for a set of semi-major axis has been plotted above the gravity field of the asteroid in Figure 5.6. As can be seen, the larger the altitude, the lower the magnitude of the gravity field and therefore the harder that the estimation is for the filter, thus further confirming the results obtained. Moreover, the importance of adequate coverage is further shown in these figures, since it can be seen how restricted coverage limits the coverage of the regions of the asteroid that have gravity-field variations, thus worsening the filter estimates. It should be additionally considered that this is a simplified case and that when higher orders of SH coefficients are considered, not only are there more irregularities distributed along the environment, but also, the higher the altitude, the less effect that higher order coefficients have in the gravity field, making it more challenging to estimate the SH coefficients accurately and thus magnifying this effects.

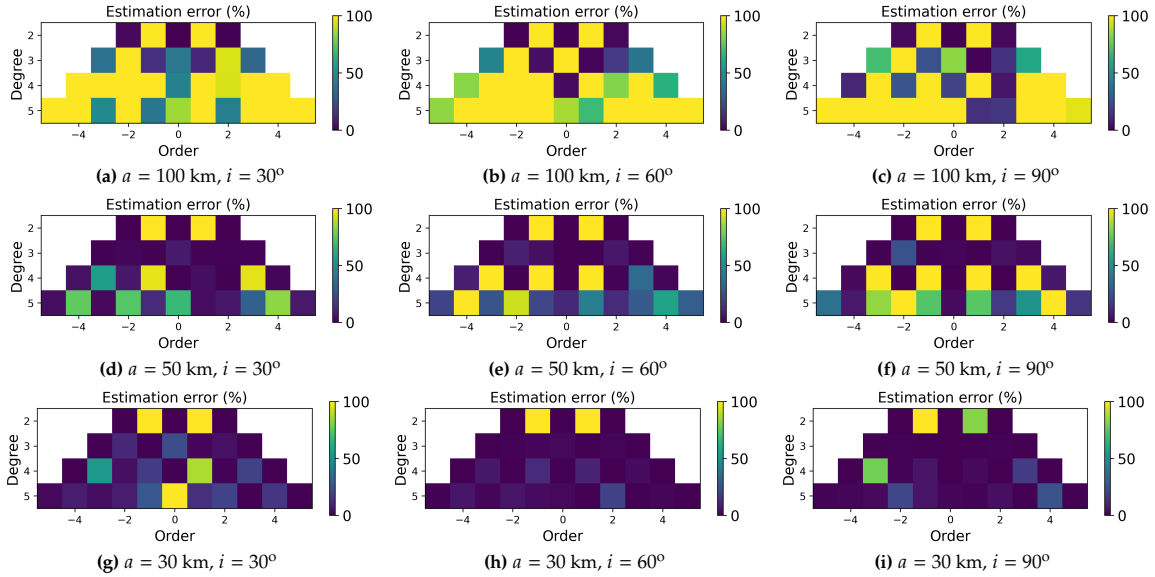

(a) $a = 100$ km, $i = 30^o$ **(b)** $a = 100$ km, $i = 60^o$ **(c)** $a = 100$ km, $i = 90^o$

(d) $a = 50$ km, $i = 30^o$ **(e)** $a = 50$ km, $i = 60^o$ **(f)** $a = 50$ km, $i = 90^o$

(g) $a = 30$ km, $i = 30^o$ **(h)** $a = 30$ km, $i = 60^o$ **(i)** $a = 30$ km, $i = 90^o$

Figure 5.5: ORB-1 Test: Estimation error of the SH coefficients degree and order 5

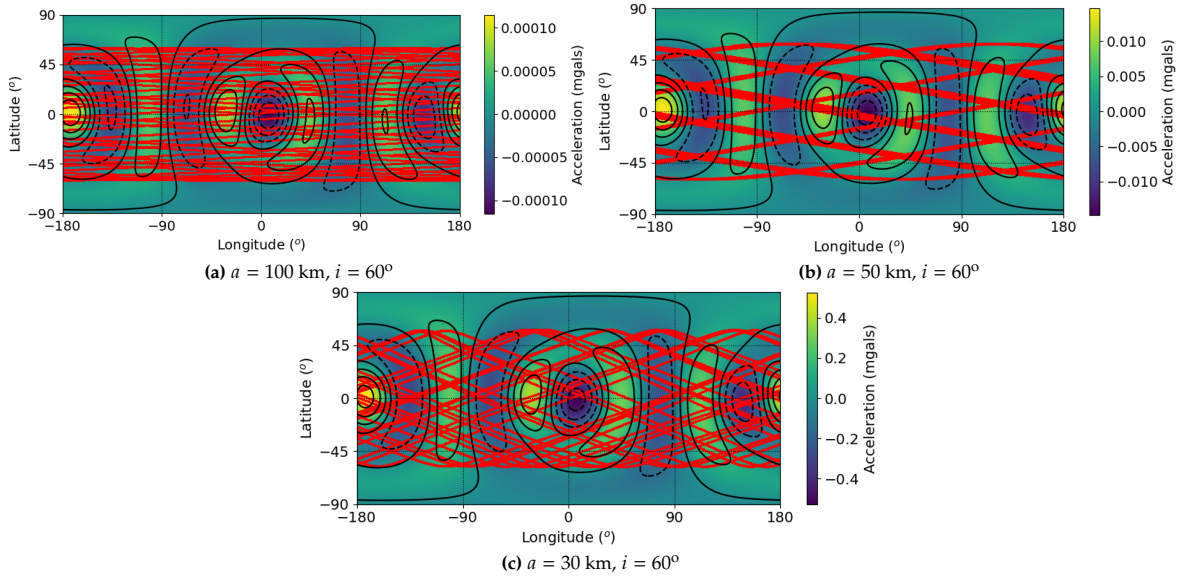

(a) $a = 100$ km, $i = 60^o$ **(b)** $a = 50$ km, $i = 60^o$

(c) $a = 30$ km, $i = 60^o$

Figure 5.6: ORB-1 Test: Coverage for a 1 million seconds propagation time shown above the SH gravity field of the asteroid up to degree and order 5. Contour lines are drawn in black, these represent regions where the gravity field has the same magnitude, illustrating the variations of the gravity field.

Increase of the propagation time

The coverage is not only influenced by the inclination and semi-major axis, but also by the propagation time of the satellite. Therefore, this scenario has been simulated again with an increased propagation time of 2.5 million seconds.

All scenarios have shown an improvement in coverage compared to the 1 million seconds propagation, but the improvement is not uniform. As noted in the previous analysis, certain configurations, such as the combination of a 50 km semi-major axis and 60° inclination, produce significant gaps in coverage. Although the overall coverage has increased, the pattern remains the same, and the gaps are still prominent in these scenarios. Conversely, patterns with a more diverse distribution, such as the 50 km semi-major axis and 30° inclination, show considerable improvement. The gaps previously observed at latitudes of -30° and 30° in Figure 5.5d have been filled. This result can be found in Figure D.2b. Similar improvements are observed for orbits with a 30 km semi-major axis at 60° or 90° inclinations, and for all cases with a 100 km semi-major axis.

In regards to the estimation errors of the SH coefficients, while one might expect that the longer the

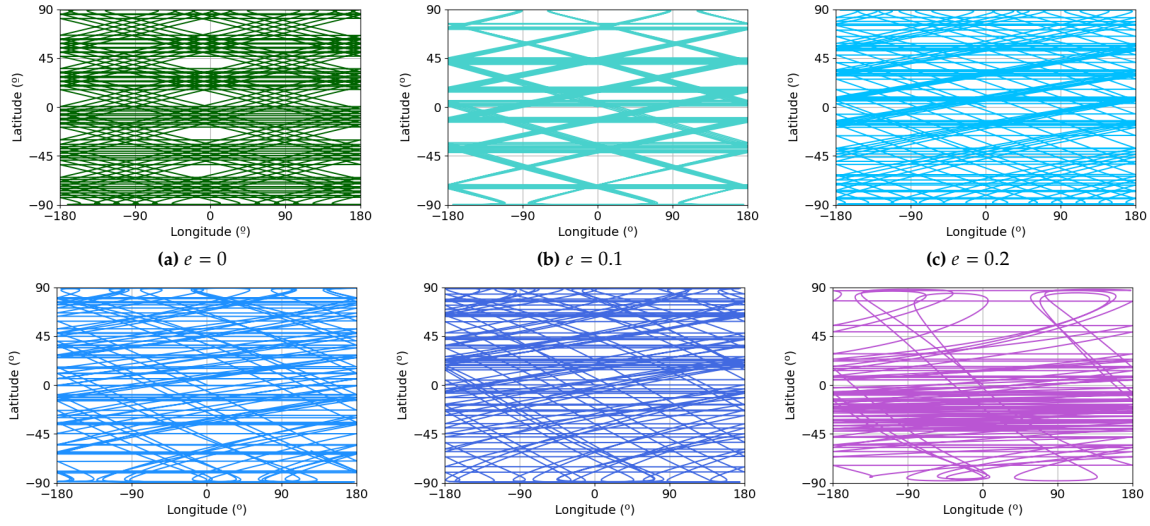

(a) $e = 0$ **(b)** $e = 0.1$ **(c)** $e = 0.2$

(d) $e = 0.3$ **(e)** $e = 0.4$ **(f)** $e = 0.5$

Figure 5.7: ORB-2 Test: Coverage for a total propagation time of 1 million seconds for an orbit with $a = 50$ km and $i = 90^o$

propagation time is, the better the estimation, having seen the improvement in the coverage obtained for each orbit, this is not the case for all scenarios. Orbits with a semi-major axis of 100 km remain unsuitable for SH coefficient estimation, and increased propagation time does not improve these estimations.

For orbits with semi-major axes of 30 km and 50 km, although coverage has improved, not all have shown a corresponding improvement in the spherical harmonic field coefficients. Notably, orbits with 60° and 90° inclinations do not exhibit significant estimation improvement. This can be attributed to the fact that while coverage has increased, the same coverage pattern is followed, leaving certain gaps unaddressed. This is particularly evident in the case of a 50 km semi-major axis and 60° inclination, where substantial gaps remain, albeit slightly reduced.

On the other hand, orbits with a 30° inclination show a visible improvement. The additional propagation time has significantly increased coverage between latitudes 30° and -30°, leading to better estimation of the coefficients. The improved coverage in these mid-latitudes allows for better estimation of coefficients affecting the gravity field in these regions, demonstrating the importance of comprehensive coverage for accurate SH coefficient estimation.

Test ORB-2

This test aims to analyse the effect of orbital eccentricity on the estimation of spherical harmonic coefficients. Two cases are considered: a highly inclined orbit and a low-inclination orbit.

1) Polar Orbit Analysis:

The first case examines a polar orbit with a 50 km semi-major axis and 90°, with eccentricity values ranging from 0 to 0.5. Figure 5.7 presents the coverage plots for the various eccentricities. As expected, the coverage pattern is most regular with zero eccentricity. Increasing eccentricity results in more irregular coverage, leading to uneven distribution of data over Eros's surface. Higher eccentricities cause certain regions to be more frequently observed than others, reducing overall coverage uniformity. Additionally, eccentricity impacts the satellite's orbital radius, as shown in Figure 5.8a. Larger eccentricity causes larger radius variations within the orbit, and at an eccentricity of 0.5, the satellite deviates significantly from its initial orbit, potentially escaping into a higher eccentricity orbit.

Generally, coefficient estimation has been shown to improve with higher eccentricity. For instance, the 5^{th} degree coefficients estimates for a null eccentricity orbit have approximately five estimates with errors larger than 50% whereas this value is reduced to one for an orbit of 0.5 eccentricity. This is likely due to the larger radius variations. Larger radii slow the satellite, benefiting the UKF estimator and enhancing filter performance. Moreover, as the satellite approaches the asteroid, it experiences stronger gravitational effects, allowing it to gather more representative data and improve coefficient estimations.

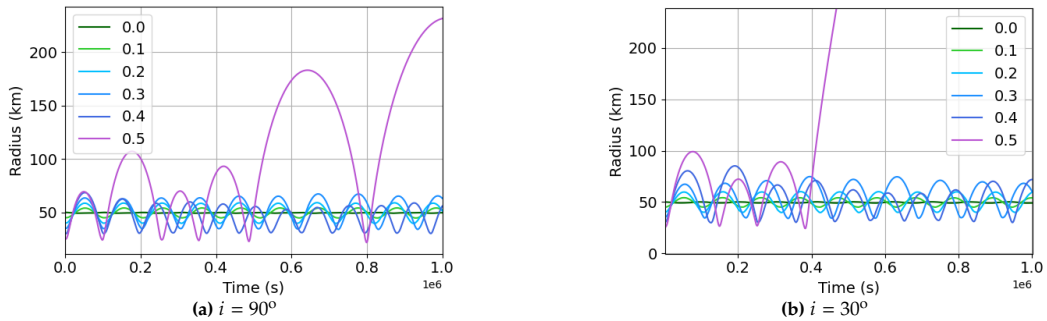

(a) $i = 90^o$ **(b)** $i = 30^o$

Figure 5.8: ORB-2 Test: Radius for a total propagation time of 1 million seconds for an orbit with $a = 50$ km

2) Low Inclination Orbit Analysis:

The second scenario involves a low-inclination orbit with an inclination of 30°. Similar to the polar orbit, higher eccentricities result in more irregular coverage patterns and greater altitude variations (Figure 5.8b). In particular, lower inclination orbits result in larger radius values as the eccentricity increases due to the higher gravity effects that the bulges of the asteroid have on the field, which are located in null latitudes. Notably, the satellite fails to achieve uniform coverage along the 30° and -30° latitudes, leading to significant coverage gaps. Note that the coverage obtained for this scenario can be found in Figure D.4.

Unlike the highly inclined orbit, higher eccentricities result in worse estimations due to significant coverage gaps. The null eccentricity orbit yields the best estimations. Increasing eccentricity leads to coverage deviations towards negative latitudes, reducing positive latitude coverage and degrading estimation accuracy. Eccentricities of 0.3 and 0.4 show substantial gaps from -15° to 25° latitude, increasing estimation errors for coefficients affecting gravity fields in mid-positive and negative latitudes. At an eccentricity of 0.5 (Figure D.4f), the orbit is highly disturbed, concentrating coverage along the equator. Consequently, coefficients of higher order have accurate estimations, whereas order 0 coefficients show higher errors due to insufficient coverage at the poles.

Conclusions

The analysis of orbital parameters and their effect on the estimation of spherical harmonic coefficients has highlighted several key findings related to the coverage areas of the asteroid:

5.2.1.1. The accurate estimation of the coefficients with the same degree and order requires the orbits to cover the equatorial region of the asteroid, which can be accomplished with any inclination as long as the eccentricity does not diverge the coverage from the area.

5.2.1.2. The accurate estimation of the null order coefficients requires the orbits to cover the polar regions of the asteroid, which can be best accomplished with polar orbits.

5.2.1.3. The accurate estimation of the rest of the coefficients requires the orbits to cover the mid-latitude regions of the asteroid, which can be best accomplished with polar orbits.

Additionally, several conclusions have been determined from the general estimation of the coefficients related to the orbital parameters:

5.2.1.4. The lower the semi-major axis, the higher the effects of the gravity field and therefore the better the estimation of the coefficients.

5.2.1.5. The larger the inclination of the orbit, the better distributed the coverage along the latitudes and thus the better overall estimation of the coefficients barring specific cases where the combination of inclination and semi-major axis result in a coverage pattern with gaps.

5.2.1.6. The eccentricity effect on the estimation is highly dependent on the inclination of the orbit. Higher eccentricities improve the estimation in polar orbits, but have negative effects in equatorial orbits. This is due to the stronger irregularities that the asteroid has on null latitudes. This leads to equatorial orbits obtaining larger radius values, thus having a negative impact on the coefficient estimates.

Overall, it can be determined that a proper design of the orbit is crucial for the best estimation of the SH coefficients. Furthermore, it must be noted that an increase in the propagation time is beneficial until a point is reached of sufficient coverage, from which the increased time does not provide more accurate estimations.

5.2.2. Analysis of the State and Measurements Errors

Errors in the initial state of the satellite and in the measurements significantly affect the performance of the filter. This section examines the impact of these errors on the estimation of spherical harmonic coefficients through tests ERR-1 and ERR-2. Details on the parameters used for the simulation of these tests and their results can be found in Subsection D.1.3.

Test ERR-1

Test ERR-1 investigates how initial state and measurement errors influence the estimation of spherical harmonic coefficients. The scenario involves a satellite in a 30 km semi-major axis orbit with a 90° inclination, incorporating various error conditions.

The filter's performance was evaluated under three conditions: zero errors in both initial state and measurements, zero errors in the initial state combined with position errors, and errors in both initial state and position measurements.

The filter has shown an excellent performance when a null error is considered in both the states and measurements. This case has been tested for sigma values of 1, 10 and 100 m. As can be seen in Figure 5.9, zero errors used with a σ_p = 1 m in the filter produce excellent results as presented in Figure 5.9a. It should be noted that as is to be expected, the larger the σ_p used in the filter, the worse the performance of the filter is since more uncertainty is introduced in the measurements and therefore the filter does not rely as much on them.

A similar trend has been observed when considering position measurements with errors. Figures 5.9d to 5.9f present the estimations obtained for the scenarios where the position measurements contain errors of 1, 10, and 100 m, respectively. Note that the σ_p value has been adjusted accordingly for each filter. As is to be expected, the lower the error is in the measurements, the better the filter is able to estimate the spherical harmonic coefficients. Particularly, the estimates produced depict how for large measurement errors such as the case of 100 m, the filter is able to estimate correctly some of the lower degree coefficients, whereas it presents much larger errors for higher-order coefficients. This is due to the fact that the higher-order coefficients have smaller gravity-field contributions than the lower-order, thus requiring more accuracy in the measurements for proper estimation.

When both measurement errors and initial state errors are present, the filter's performance does not significantly differ from the case with measurement errors alone, as long as initial state errors remain within the measurement error bounds. This indicates minimal impact of initial state errors on coefficient estimation.

Impact of velocity measurements

Additional tests have been conducted to assess the impact of including velocity measurements in the UKF. The settings for this test scenario are further specified in Table D.6.

Results, shown in Figure 5.9, indicate that incorporating velocity measurements considerably enhances filter precision. This improvement compensates for errors in position measurements and enhances the overall estimation accuracy. For instance, for a 1 m position error the estimates of the 5^{th} degree present a coefficient with estimation errors of a 100% and another with errors larger to 50%, while when considering velocity measurements with an error of 10 mm/s, the 5^{th} degree coefficients are estimated with errors below 5%. This effect is even more notable as the position error used increases, such as for the case of a 10 m position error, three coefficients present estimation errors of a 100% and six coefficients with errors larger to 30% approximately, which are reduced to errors lower to 5% when velocity measurement errors of 0.1 m/s are considered.

Test ERR-2

As has been noted previously, this filter operates under the assumption that, in the early stages of the mission, the mothership accurately estimates the gravitational parameter and rotational rate of the asteroid. This test examines how errors in these initial estimations affect the gravity-field coefficients estimation.

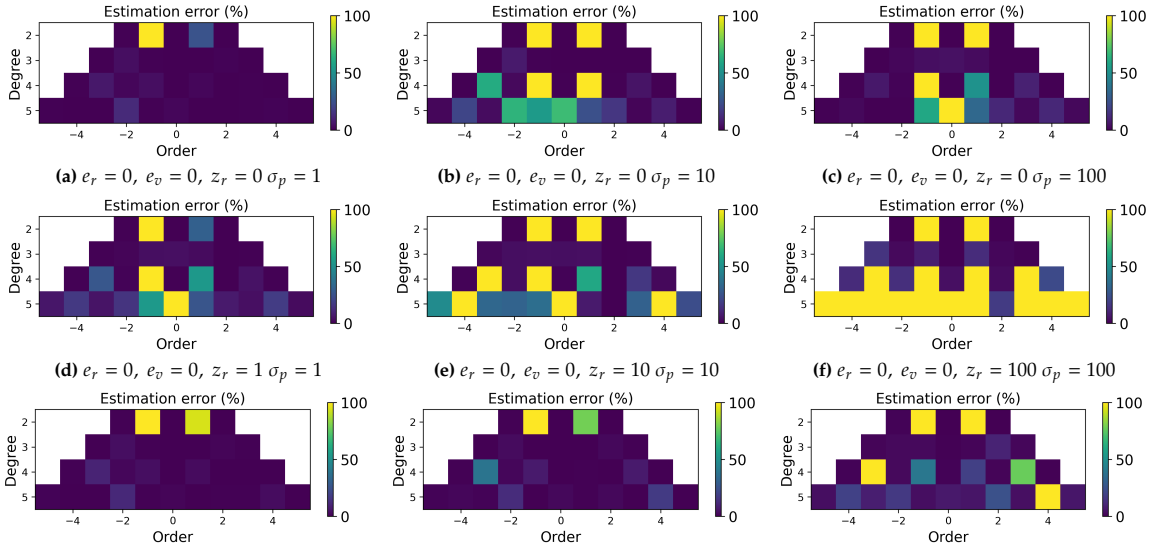

(a) $e_r = 0,\ e_v = 0,\ z_r = 0\ \sigma_p = 1$ **(b)** $e_r = 0,\ e_v = 0,\ z_r = 0\ \sigma_p = 10$ **(c)** $e_r = 0,\ e_v = 0,\ z_r = 0\ \sigma_p = 100$

(d) $e_r = 0,\ e_v = 0,\ z_r = 1\ \sigma_p = 1$ **(e)** $e_r = 0,\ e_v = 0,\ z_r = 10\ \sigma_p = 10$ **(f)** $e_r = 0,\ e_v = 0,\ z_r = 100\ \sigma_p = 100$

(g) $e_r = 0,\ e_v = 0,\ z_r = 1,\ z_v = 0.01,\ \sigma_r = 1,\ \sigma_v = 0.1$ **(h)** $e_r = 0,\ e_v = 0,\ z_r = 10,\ z_v = 0.1,\ \sigma_p = 10\ \sigma_v = 0.1$ **(i)** $e_r = 0,\ e_v = 0,\ z_r = 100,\ z_v = 1,\ \sigma_p = 100\ \sigma_v = 1$

Figure 5.9: ERR-1 Test: Estimation error of the SH coefficients degree and order 5 for 2.5 million seconds

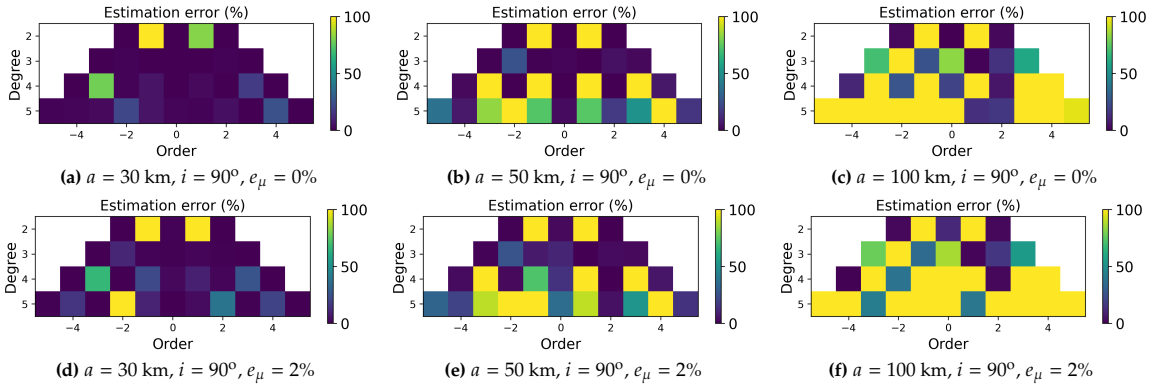

(a) $a = 30$ km, $i = 90^o$, $e_\mu = 0\%$ **(b)** $a = 50$ km, $i = 90^o$, $e_\mu = 0\%$ **(c)** $a = 100$ km, $i = 90^o$, $e_\mu = 0\%$

(d) $a = 30$ km, $i = 90^o$, $e_\mu = 2\%$ **(e)** $a = 50$ km, $i = 90^o$, $e_\mu = 2\%$ **(f)** $a = 100$ km, $i = 90^o$, $e_\mu = 2\%$

Figure 5.10: ERR-2 Test: Estimation error of the SH coefficients degree and order 5 for 1 million seconds including an error in the estimation of the gravitational parameter.

Figure 5.10 illustrates the impact of a 2% error in the gravitational parameter estimation on the coefficients for orbits with various semi-major axes. As shown, this 2% error significantly affects the coefficient estimations. Given that the gravitational pull is weaker at larger semi-major axes, errors in the gravity-field coefficients are expected to have a lesser impact on the model at these distances. This trend is evident in the results: for the smallest semi-major axis of 30 km, there is a noticeable divergence in the coefficient estimations (Figure 5.10d). As the distance between the satellite and Eros increases, this effect diminishes, as shown for a 50 km semi-major axis (Figure 5.10e). However, for the 100 km case, the coefficients estimation error presents a different pattern. This discrepancy is linked to the fact that this orbit is not suitable for accurate coefficient estimation and thus does not well represent the estimation errors related to the central gravity-field error.

Figure 5.11 presents the effects that the addition of a 2% error in the estimation of the rotational rate of the asteroid along its z-axis has on the estimation of the coefficients. This analysis has been conducted for different semi-major axes and two orbital inclinations

The first row of Figure 5.11 shows the coefficient estimations for various semi-major axes with a fixed inclination of 90^o. In all cases, the error in the rotational rate significantly affects the coefficient estimations. This outcome is expected since the rotation of Eros impacts the gravity-field estimation model regardless of the distance between the asteroid and the satellite. However, the inclination of the orbit plays a crucial role, as seen in the second row of plots. These plots, representing orbits with a 30^o inclination, exhibit significantly larger errors in coefficient estimation. For instance, in the 30 km orbital scenario, the estimates for zero-order coefficients are very accurate for the polar orbit, with errors

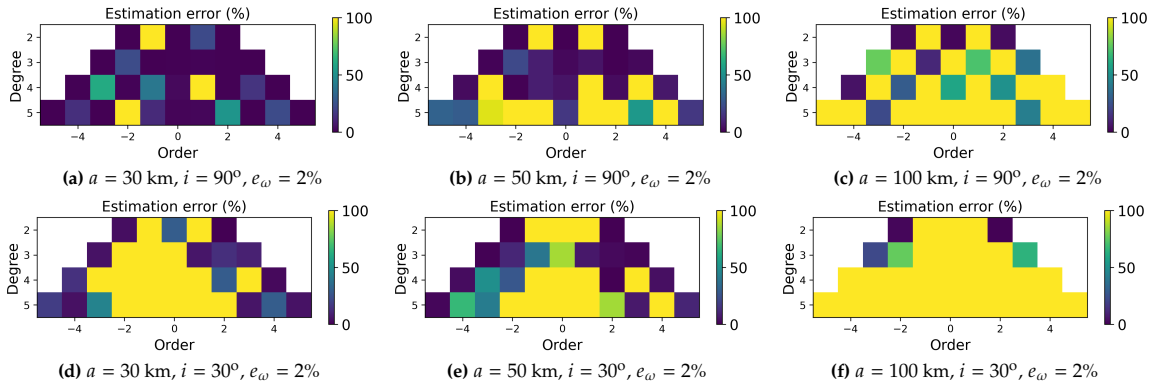

(a) $a = 30$ km, $i = 90^o$, $e_\omega = 2\%$ **(b)** $a = 50$ km, $i = 90^o$, $e_\omega = 2\%$ **(c)** $a = 100$ km, $i = 90^o$, $e_\omega = 2\%$

(d) $a = 30$ km, $i = 30^o$, $e_\omega = 2\%$ **(e)** $a = 50$ km, $i = 30^o$, $e_\omega = 2\%$ **(f)** $a = 100$ km, $i = 30^o$, $e_\omega = 2\%$

Figure 5.11: ERR-2 Test: Estimation error of the SH coefficients degree and order 5 for 1 million seconds including an error in the rotational rate of the asteroid

lower than 5%. In contrast, for the equatorial orbit, most of the coefficients present errors larger than 100%. This can be attributed to the fact that lower inclinations align more closely with the asteroid's rotation along the z-axis, whereas polar orbits experience the asteroid's rotation tangentially, resulting in a smaller effect on the model.

Conclusions

After analysing the impact of errors introduced to the filter, the following conclusions can be drawn:

5.2.2.1. Larger errors in position measurements significantly degrade the accuracy of coefficient estimations. High-order coefficients, in particular, require very low position measurement errors (on the order of 10 meters or less) for precise estimation (under 15% error).

5.2.2.2. Proper adjustment of the uncertainty associated with measurements is essential for the filter to perform optimally and produce the best possible estimations.

5.2.2.3. Errors in the initial state, when of the same magnitude as the measurement errors, do not significantly affect the estimation of the coefficients.

5.2.2.4. The addition of velocity measurements in the filter can be beneficial for the estimation of the coefficients, since they provide additional information with a different error source, thus decreasing the effect of the position measurement errors.

5.2.2.5. Incorporating velocity measurements into the filter can improve coefficient estimations by providing additional information with a different error source, thereby mitigating the impact of position measurement errors.

5.2.2.6. A small error in the gravitational parameter of 2% does not have a significant impact on the estimates, and only slightly degrades them.

5.2.2.7. Accurate estimation of the asteroid's rotation rate is essential. Even small errors can cause significant inaccuracies in the coefficient estimations, with up to a 100% estimation errors. This effect is reduced while being in polar orbits, as the orbital plane is more parallel to the asteroid's rotation axis, resulting in a smaller impact from rotational rate errors.

5.2.3. Analysis of the Frequency Update of the Measurements

The frequency at which measurements are updated significantly impacts the performance of the UKF algorithm. Higher update frequencies result in larger datasets, which generally enhance the algorithm's performance by providing more data for estimation. However, larger datasets also increase computational demands, leading to longer processing times. This section examines the effects of measurement update frequency on the estimates generated by the filter through the analysis conducted in test STEP-1. Details on the specific configuration parameters used in the simulation of the test scenario can be found in Table D.1.4.

Test STEP-1

The hardware considered for this study has an update frequency of down to 1 second. With this consideration, the test has analysed the effect that decreasing the update frequency has on the filter

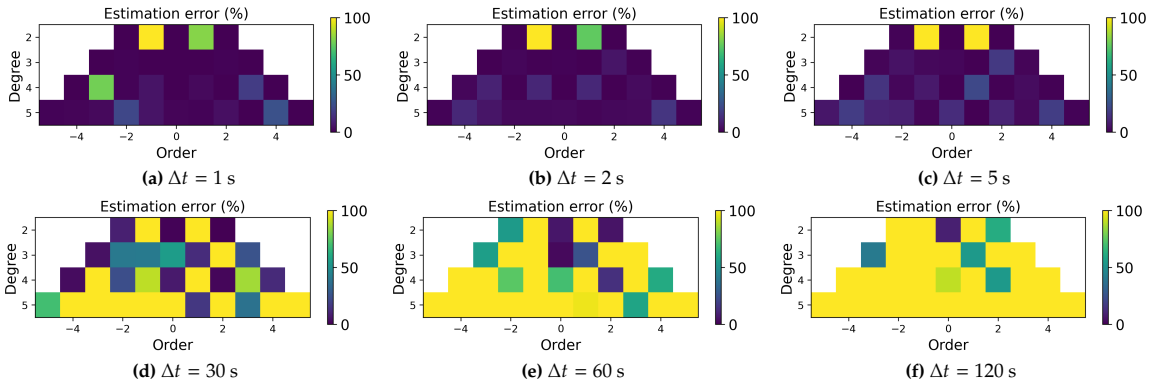

(a) $\Delta t = 1$ s **(b)** $\Delta t = 2$ s **(c)** $\Delta t = 5$ s

(d) $\Delta t = 30$ s **(e)** $\Delta t = 60$ s **(f)** $\Delta t = 120$ s

Figure 5.12: STEP-1 Test: Estimation error of the SH coefficients degree and order 5 for 1 million seconds with a=30 km for a range of time steps

estimates. A scenario has been devised with a single satellite orbit around Eros considering measurement update values of 1, 2, 5, 30 and 60 seconds. Additionally, the effects of increasing the time step have been tested for different satellite altitudes.

The estimated coefficients for a low-altitude orbit are shown in Figure 5.12. As illustrated, increasing the step size results in larger estimation errors. This can be attributed to several factors. Smaller step sizes enable the filter to better propagate state estimates of the satellite in the presence of nonlinear dynamics, thereby providing more accurate coefficient estimations. By using smaller time steps, the UKF can better capture the model's nonlinearities, reducing errors associated with linearisation. Secondly, smaller time steps decrease the distance between consecutive predicted states, minimising prediction errors. Lastly, smaller time steps enhance the filter's stability, preventing large deviations between predicted and measured states and ensuring accurate estimations over time.

A similar trend is observed for satellites at higher altitudes. As the update frequency decreases, the estimation error of the coefficients increases. However, the impact of the time step on the error is more pronounced at higher altitudes. This is due to the larger dynamic range in distances covered per orbital revolution at higher altitudes, making the errors introduced by larger time steps more significant compared to orbits with smaller semi-major axes. The estimation results for a higher altitude orbit can be found in Figure D.6.

Conclusions

The measurement update frequency significantly affects the estimation of spherical harmonic coefficients. Smaller update intervals improve filter performance, although they increase the computational load. The ideal time step for the filter depends on the satellite's orbit semi-major axis, with smaller steps providing better accuracy by capturing the system's nonlinearities and enhancing filter stability.

5.2.4. Analysis of the Real Scenario Forces

The forces considered in the system modelling significantly influence the estimation of the SH coefficients. To determine their impact, two tests were conducted: Test FOR-1, which examines the effects of the Sun's third-body perturbation and SRP, and Test FOR-2, which investigates the impact of the degree and order of the coefficients used in the system modelling. Details on the scenario configuration parameters and results can be found in Table D.12.

Test FOR-1

This test evaluates the filter's capability to estimate spherical harmonic coefficients when additional forces are present in a real-world scenario. Specifically, it compares estimations for three different orbits with semi-major axes of 50 km, 100 km, and 500 km. The comparisons are made between a scenario with only the SH gravity field up to degree and order five, one with the Sun's point mass gravity, and one with solar radiation pressure.

The results indicate that the Sun's third-body perturbation has no significant effect on the estimations. This is because the orbits in all three cases lie within the sphere of influence, rendering external forces non-dominant. Furthermore, since this effect is constant, the filter is able to deal with its effects adequately. However, SRP does have a slight impact on the estimations for the 100 km semi-major axis

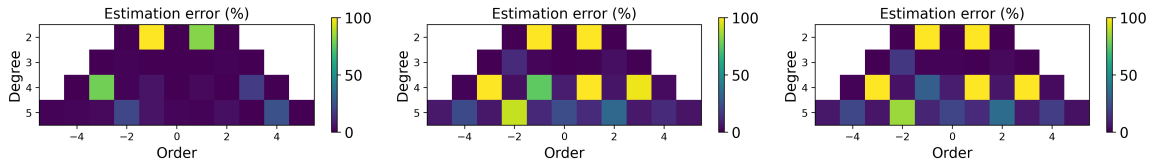

(a) $a = 30$ km, $n = 5$, $m = 5$ **(b)** $a = 30$ km, $n = 9$, $m = 9$ **(c)** $a = 30$ km, $n = 15$, $m = 15$

Figure 5.13: FOR-2 Test: Estimation error of the SH coefficients degree and order 5 for 1 million seconds considering different degrees and order of SH for the simulation of the true gravity field.

orbit, but not for orbits with smaller semi-major axes. This suggests that while it is possible to simulate the scenario with all acting forces, the filter does not need to include them in its state estimation to produce optimal results. These conclusions are supported by the estimations for a 30 km orbit with different forces considered, which have shown very similar results in all cases. Additional estimations for higher altitude orbits can be found in Figure D.7.

Test FOR-2

This test examines the impact of the degree and order of the spherical harmonic coefficients considered in the real scenario simulation on the estimation of coefficients up to degree and order five. To achieve this, the test estimated coefficients for orbits with semi-major axes of 30 km, 40 km, and 50 km, using coefficients of degree and order 5, 9, and 15.

This test has revealed that increasing the order of the coefficients in the real simulation scenario has a detrimental effect on the estimation of the coefficients, as can be seen in Figure 5.13. This is due to the fact that more gravity field irregularities must be accounted for by the model. The estimates produced for all the tested orbits can be found in Figure D.8.

Notably, the effect of increasing the degree and order of the coefficients is much stronger for the 30 km orbit compared to the 40 km orbit. Additionally, the 50 km orbit shows no significant changes in coefficient estimation. These findings suggest that for the most efficient estimation of the coefficients, lower orbits are preferable, and with proper tuning, the filter should accurately estimate the coefficients. However, higher orbits may not adequately model these effects.

Conclusions

The analysis of the perturbations in the system has shown the following:

5.2.4.1. The third-body perturbation of the Sun has no effect on coefficient estimation for orbits with semi-major axes within the Brillouin Sphere, as considered in this research.

5.2.4.2. The Solar Radiation Pressure does not present a significant contribution in the coefficient estimation for orbits with semi-major axis smaller than 100 km.

5.2.4.3. It has been confirmed that as concluded in previous tests, accurate estimation of high degree and order coefficients requires low semi-major axis orbits.

5.3. Sensitivity Analysis: Satellite Constellation

This section studies the best design of the UKF algorithm for the estimation of the spherical harmonic coefficients. Three designs for the UKF of the mothership have been considered for the estimation of the coefficients:

Configuration 1 (C1): This design works under the premise that the CubeSats in the constellation send their positions to the mothership as they update their measurements. Then, the mothership uses a large UKF algorithm that makes use of all the position measurements including its own. The mothership UKF estimates the positions of the satellites with time and the SH coefficients of Eros's gravity field.

Configuration 2 (C2): This design works under the premise that each of the CubeSats in the constellation has its own UKF that estimates its trajectory and the SH coefficients of Eros's gravity field. And that each of the CubeSats sends its SH estimates to the mothership continuously. The mothership uses its own position measurements and the mean value of the SH coefficient estimates received from the CubeSats to obtain the final coefficient estimates of the gravity field.

Configuration 3 (C3): This design works under the premise that each of the CubeSats in the constellation has its own UKF that estimates its trajectory and the SH coefficients of Eros's gravity field. And that each of the CubeSats sends its SH estimates to the mothership continuously. The mothership uses its own position measurements and all of the SH coefficients received from the CubeSats to obtain the final coefficient estimates of the gravity field.

Further details on the filter designs can be found in Subsection D.2.1, containing the state vectors, measurements and **P**, **Q**, and **R** matrices. It should be noted that these filters have been designed and implemented to be able to work for any number of CubeSats.

The designed filters are tested in a number of scenarios to analyse the effect of the constellation and scenario characteristics on the estimates produced by the UKF. An analysis of the distribution of the satellites can be found in Subsection 5.3.1, followed by an analysis of the effect of the number of satellites conforming to the constellation in Subsection 5.3.2. Furthermore, the effect of the measurements frequency update and orbital propagation time is presented in Subsection 5.3.2. It should be considered that all scenarios tested are simulated with all the environment perturbations produced by the Sun, as well as the asteroid's gravity field with spherical harmonics up to degree and order 15.

5.3.1. Analysis of the Distribution of the Satellites

This section analyses the impact of satellite distribution within the constellation orbiting Eros on the coefficient estimates for various proposed UKF designs. Three tests have been defined to evaluate this impact:

- Test DIST-1: Distribution of satellites along different true anomalies.
- Test DIST-2: Distribution of satellites at different inclinations.
- Test DIST-3: Distribution of satellites at different semi-major axes.

Details on the configuration parameters used for the tests can be found in Subsection D.2.2.

Additionally, the effect of the mothership's placement within the constellation on each UKF design is examined. The distribution of satellites within the constellation is critical for accurate estimation results. Subsequent sections provide a detailed analysis of satellite positions and their impact, particularly considering communication limitations that depend on maintaining a direct line-of-sight between the CubeSats and the mothership, as well as solar restrictions that limit the measurements taken by the satellites. These constraints are however not considered in these tests.

Test DIST-1

This test analyses the impact of satellite distribution along the true anomaly for three UKF designs. It is divided into two scenarios: one with satellites evenly distributed along 360° and another with satellites clustered closely together.

Scenario 1: Even Distribution

In this scenario, CubeSats orbit the asteroid with a semi-major axis of 30 km and a 90° inclination, evenly spread at true anomalies of 0º, 120º, and 240º.

To analyse the effect of the distribution accurately, the estimates produced by each satellite individually have been computed beforehand. The results can be found in Figure D.9. These have shown that although the satellites are placed on the same semi-major axis and with the same eccentricity, the true anomaly has a considerable effect on their trajectory and thus they present different levels of precision in their estimations. In particular, it can be seen that for this case, a true anomaly of 240° offers better estimates than the others, followed by 0° and 120° values.

Having these estimates, the constellation has been simulated for the three UKF designs. Figure 5.14 presents the estimates obtained for each filter design when placing the mothership at 0º true anomaly. As can be seen, there is a clear distinction in the errors presented by each of the configurations. For instance, C1 is able to estimate the fourth-degree coefficients with only one value with an error of 100%, maintaining the others below an error of 15%. C2 and C3 coefficients present a higher amount of errors, C2 having two coefficients with errors larger than 100% and C3 additionally to those errors, having two other coefficients with errors larger than 50%. Configuration C1, which uses the position measurements of the three satellites and propagates their position at the same time to produce the estimates of the

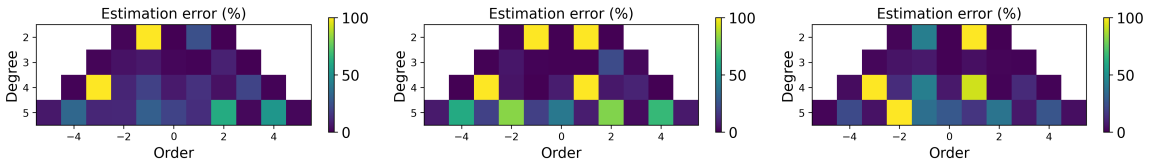

(a) C1, mothership with $\nu = 0^o$ **(b)** C2, mothership with $\nu = 0^o$ **(c)** C3, mothership with $\nu = 0^o$

Figure 5.14: DIST-1 Test: Estimation error of the SH coefficients degree and order 5 for 1 million seconds for the constellation.

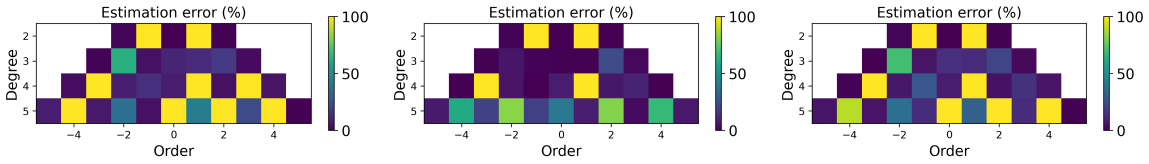

(a) C1, mothership with $\nu = 0^o$ **(b)** C2, mothership with $\nu = 0^o$ **(c)** C3, mothership with $\nu = 0^o$

Figure 5.15: DIST-1.2 Test: Estimation error of the SH coefficients degree and order 5 for 1 million seconds for the constellation.

coefficients provides the best estimates, followed by C2 and C3. This shows that using all position measurements of the satellites offers an advantage in the estimation, having more coverage and more data to compensate for the errors present in the measurements.

Further testing has been conducted to analyse the effect that the mothership's orbit has on the estimates produced. From the estimates obtained, it has been seen that, as expected, the mothership placement does not affect the results obtained, since the design uses the position measurements of all the satellites of the constellation, making no difference between the measurements taken by the CubeSat and those produced by the mothership. Nevertheless, it has been seen that the UKF C2 and C3 designs are affected considerably by the placement of the mothership within the constellation. Configuration C2 presents considerably larger errors when placing the mothership in the $\nu = 120^o$ orbit, which can be directly linked to that orbit having a worse coverage and therefore a larger error in the coefficient estimation. Therefore, by relying on the position measurements of that orbit for the estimation and assisting the estimations with the other satellites' coefficient estimations, the estimations of the mothership contain larger errors. This is improved when the mothership is placed in the $\nu = 240^o$ orbit, which having a better-suited orbit for the estimation, presents a better estimation of the coefficients when using the constellation. Configuration C3 shows better results in both cases than C2, having better measurements of the spherical harmonic coefficients and relying more on them. Furthermore, the final constellation estimation improves as well when placing the mothership in the best-suited orbit.

Scenario 2: Close Distribution

In this scenario, CubeSats orbit with the same parameters but are closely spaced at true anomalies of 0^o, 10^o and 20^o. Similarly to the previous scenario, the coefficient estimates have been computed for each individual satellite following the orbits used in the constellation. The results obtained can be found in Figure D.11. Opposed to the previous scenario, the best estimate is now produced by the null true anomaly orbit. Therefore it can be expected that the configurations estimates will produce worse results than in the previous scenario, which has been proven to be the case. The coefficient estimates produced by the constellation for the three UKF designs are presented in Figure 5.15. Further testing done to analyse the effects of the mothership placement can be found in Figure D.12.

The constellation estimates for each UKF design are presented in Figure 5.15. Configuration C1 shows that using all satellite positions is detrimental when one satellite has poor coverage (e.g., $\nu = 20^o$). However, combining all three positions still offers better estimates than relying solely on a poorly placed satellite.

Configuration C2 performs better than C1, with errors increasing as the mothership's orbit worsens (e.g., $\nu = 10^o$ and $\nu = 20^o$). This highlights the configuration's reliance on the mothership's orbit.

Configuration C3 generally provides the best estimates. For the mothership at $\nu = 0^o$, C3's estimates are slightly worse than C2's due to reliance on less accurate SH estimations from other orbits. However, when the mothership is at $\nu = 20^o$, C3 performs best, relying more on the better-placed satellites.

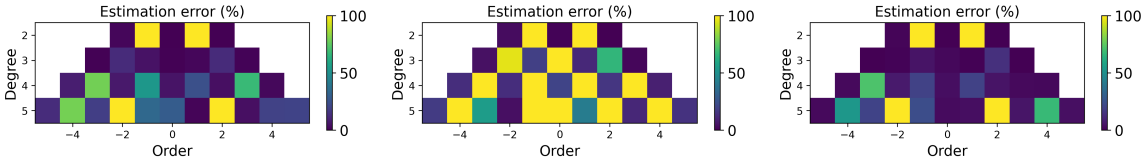

(a) C1, mothership with $i = 30^o$ **(b)** C2, mothership with $i = 30^o$ **(c)** C3, mothership with $i = 30^o$

Figure 5.16: DIST-2 Test: Estimation error of the SH coefficients degree and order 5 for 1 million seconds for the constellation for satellites distributed along different inclinations.

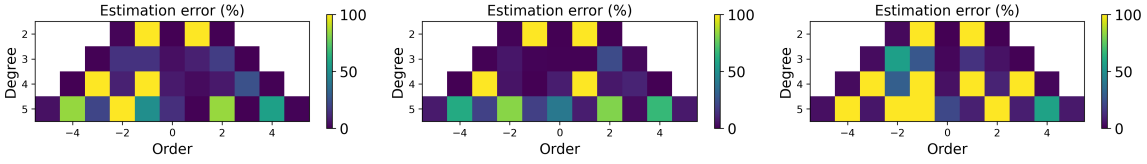

(a) C1, mothership with $a = 30$ km **(b)** C2, mothership with $a = 30$ km **(c)** C3, mothership with $a = 30$ km

Figure 5.17: DIST-3 Test: Estimation error of the SH coefficients degree and order 5 for 1 million seconds for the constellation.

Test DIST-2

This test aims to compare the behaviour of two models with an orbit of 30 km of semi-major axis with satellites depicting orbits of 30º, 60º and 90º of inclination.

An initial analysis of the individual satellite estimations, which can be found in Figure D.14, indicates that the satellite with a 30º inclination orbit exhibits significantly higher error rates compared to those with higher inclinations. This discrepancy is expected to impact the overall constellation estimates.

Figure 5.16 presents the estimates produced by each of the filter designs when the mothership is placed in a 30° inclination orbit. Despite the high inaccuracies in spherical harmonic estimations for the 30° inclination, as shown in Figure D.13a, Configuration C1 still produces excellent estimates. Note that all the scenarios studied estimates can be found in Figure D.14.

For Configuration C2, adequate estimates are achieved when the mothership is not in a 30° inclination orbit. In these cases, the filter relies more on the position measurements of the satellites than on the SH estimations from the 30° inclined orbit. This model performs significantly better when the mothership is in either of the other two orbital inclinations.

Configuration C3 shows the opposite trend to C2, with high estimation errors when SH estimates include data from a 30° inclined satellite. However, it achieves excellent results when the mothership is in a 30° inclination orbit and utilises SH coefficient estimates from the other two satellites.

Test DIST-3

This test aims to compare the behaviour of the two models with different semi-major axis orbits of 30, 35, and 40 km and a fixed inclination of 90°. The specific parameters used for this testing scenario can be found in Table D.18.

Individual satellite SH estimates show that larger semi-major axes lead to greater estimation errors, as expected. These results can be found in Figure D.15.

When analysing the constellation estimates, it is evident that Configuration C1 performs worse than individual satellites in 30 km and 35 km orbits due to the significant inaccuracies introduced by the 40 km orbit. This observation is confirmed in Figure 5.17.

Moreover, when the C2 configuration is used, the UKF is able to maintain a low error rate when using the mothership in an optimal 30 km orbit. However, estimation errors increase with the semi-major axis of the mothership. This is because C2 relies more on mothership position measurements than on SH coefficient estimates from other satellites. Conversely, Configuration C3 provides better estimates when the mothership is in a 40 km orbit, as it relies more on the SH estimates from other satellites than on the mothership's positional data.

Conclusions

Having analysed the previous test results a number of conclusions can be derived:

5.3.1.1. No single UKF configuration design performs best in all scenarios. The effectiveness of each design depends on the specific orbital characteristics of the CubeSats and the mothership.

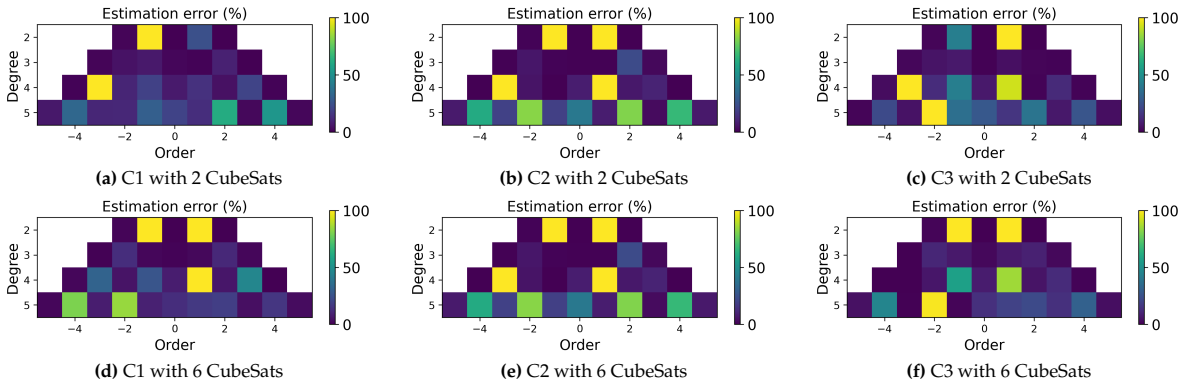

(a) C1 with 2 CubeSats **(b)** C2 with 2 CubeSats **(c)** C3 with 2 CubeSats

(d) C1 with 6 CubeSats **(e)** C2 with 6 CubeSats **(f)** C3 with 6 CubeSats

Figure 5.18: NUM-1 Test: Estimation error of the SH coefficients degree and order 5 for 1 million seconds for a constellation of a mothership and several CubeSats.

5.3.1.2. The C1 configuration is reliable, being able to combine the position measurements of all the satellites equally. This leads to very accurate estimates when all the orbits are adequate. However, if one or more of the orbits have poor coverage, the overall estimation accuracy suffers. Furthermore, the orbit of the mothership does not affect the performance when using this UKF design.

5.3.1.3. Configuration C2 is highly dependent on the mothership's orbit. This UFK design performs well when the orbit of the mothership has good coverage, leading to accurate estimates. The SH coefficient estimates of the other orbits improve the estimations of the filter. However, if these estimates are inaccurate, the overall estimation quality decreases slightly. Conversely, if the SH estimates are accurate but the mothership's orbit is inadequate, the final constellation estimation becomes unreliable. This is because the filter relies more on the mothership's position measurements than on SH coefficient estimates from other satellites.

5.3.1.4. Configuration C3 excels when the spherical harmonic measurements from the CubeSats have low error rates. In such cases, even if the mothership's position measurements are inadequate, the filter can still produce good estimates by relying on data from other satellites. Therefore, this design is highly dependent on the accuracy of the CubeSats' SH estimates.

5.3.2. Analysis of the Number of Satellites

This section examines the impact of the number of satellites on the estimation performance for different UKF configurations. Two test scenarios were designed for this analysis. Details on the configuration parameters for the test scenarios and their results can be found in Subsection D.2.3.

Test NUM-1

This test aims to compare the behaviour of the three models with varying numbers of satellites (two, four, six, and eight) in the constellation. All satellites use the same orbits, evenly spaced along the true anomaly, with the mothership positioned at $\nu = 0°$.

The results indicate that increasing the number of CubeSats does not necessarily improve the estimation of the coefficients as one might expect. This is because not all CubeSat orbits are equally suitable for accurate coefficient estimation. Specifically, configurations of two and six satellite constellations, as shown in Figure 5.18, illustrate this point. The key takeaway is that the quality of the trajectories followed by the CubeSats significantly influences the accuracy of the estimates, rather than merely the number of satellites in the constellation.

Figure 5.19 illustrates how the computation time per step increases with the number of satellites for each filter design. Design C1 shows the highest increase in computation time due to the additional six state parameters for each CubeSat, significantly increasing the computational load. Design C3 also exhibits an increase in computational time, although to a lesser extent, as it only increases the number of measurements without altering the state vector. Design C2 presents the least increase in computational time, as it neither increases the state nor the measurement vector, maintaining a feasible computation rate.

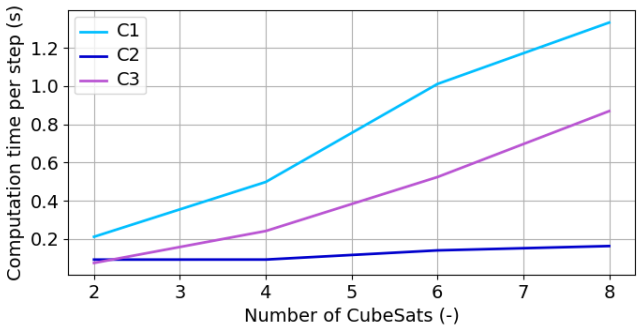

Figure 5.19: NUM-1 Test: Computational times per step

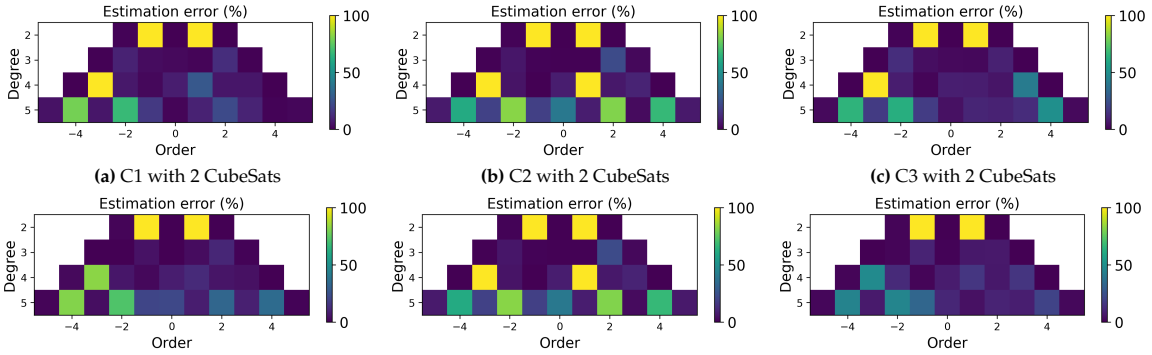

(a) C1 with 2 CubeSats **(b)** C2 with 2 CubeSats **(c)** C3 with 2 CubeSats

(d) C1 with 4 CubeSats **(e)** C2 with 4 CubeSats **(f)** C3 with 4 CubeSats

Figure 5.20: NUM-2 Test: Estimation error of the SH coefficients degree and order 5 for 1 million seconds for a constellation of a mothership and several CubeSats.

Test NUM-2

The previous test demonstrated that the accuracy of the estimates is highly dependent on the specific orbits of the satellites in the constellation. This test is designed to evaluate how the number of satellites, following optimal orbits for coefficient estimation, affects each of the UKF configurations. Various orbits were tested, and those providing the most accurate coefficient estimates were selected.

The results for two and four satellite constellations are shown in Figure 5.20, which indicates that increasing the number of satellites in the constellation improves the accuracy of the estimates. Furthermore, the different UKF designs produced varying estimates in all cases.

Configuration C1 has been shown to provide excellent results, decreasing the error in the estimates when increasing the number of trajectories considered in the states and measurements data, which can be directly related to the fact that the use of several adequate satellite data improves the estimates produced by only one, compensating for errors in the measurements used.

Configuration C3 has shown even better performance with a larger number of satellites, as it utilizes the best coefficient estimates from all CubeSats in the constellation. Since all selected orbits produce good estimates, this model achieves superior accuracy.

In contrast, Configuration C2 does not show a significant improvement with the addition of more satellites. This can be attributed to the fact that this filter design uses the average of the SH coefficients estimated by the CubeSats. Since all the CubeSats considered in this scenario have adequate orbits that produce similar SH coefficients, the average value does not change significantly with the addition of CubeSats, thus not presenting an advantage for this particular UKF design.

Conclusions

The analysis of the effect of the number of CubeSats in the constellation has led to the following conclusions:

5.3.2.1. Simply increasing the number of CubeSats in the constellation does not guarantee better estimates. The accuracy of the estimates heavily depends on the quality of the CubeSats' trajectories. When a constellation includes satellites with inadequate trajectories, having more

satellites can improve the overall estimates by reducing the reliance on any single poor-quality trajectory.

5.3.2.2. Configuration C1 performs well across various numbers of constellation satellites. However, as the number of satellites increases, the state of the filter grows, since each satellite adds three position values and three velocity values to the state. Consequently, the computational time required for coefficient estimation also increases, which can become a limiting factor for this filter.

5.3.2.3. Configuration C2 has shown minimal improvement with additional satellites. It relies primarily on the mothership's orbit and uses the average coefficient estimates from other satellites. Adjustments to the **R** matrix could potentially optimize this, but relying on average estimates is not ideal. If even one CubeSat has an inadequate trajectory, it significantly impacts the average and degrades the estimates. However, this design does not require additional computational time with more satellites, which is an advantage.

5.3.2.4. Configuration C3 has shown to perform well. Similarly to C1, this filter design provides improved estimates as the number of satellites in the constellation increases when they have adequate trajectories. When some trajectories are inadequate, the filter still maintains acceptable error levels by leveraging estimates from other CubeSats. The computational time for this filter increases with the number of CubeSats due to the additional measurements for each satellite's coefficients, but it remains lower than the computational time required by the C1 design.

5.3.3. Analysis of the Measurements Frequency and Orbital Propagation Duration

This section examines the impact of measurement update frequency and orbital propagation time on the UKF coefficient estimation for the three configurations. Detailed parameter settings used in the scenarios and their results can be found in Subsection D.2.4.

Test CSTEP-1

This test aims to analyse the effect of varying measurement update rates on the constellation filter design. The results have shown that there is a clear tendency for the estimation errors to increase with the update frequency. This is to be expected, as the higher the frequency updates, the better the filter can perform.

However, it can be seen that the effect is different for the tested configurations. In particular, the estimations considerably worsen with an increase of the time step for C3. In particular, this filter presents all the coefficient estimates of degree four and five below a 50% error when using a two seconds time step, three of the coefficient estimates present errors of 100% when a five seconds time step is used, and this number is increased to five coefficients for a 10 seconds time step. This can be explained by the fact that the filter is very reliant on the final SH estimation of the CubeSats, and as it has been observed in the previous section, the lower the frequency update in a single satellite, the worse the estimations. Configurations C1 and C2, on the other hand, do not show an increase in the estimation errors from $\Delta t = 2$ s to $\Delta t = 5$ s. This can be directly linked to the new constellation UKF designs, which might benefit from a longer time step reducing numerical instabilities or divergence issues. On the other hand, a larger increase in time to 10 s leads to considerably worse results.

Test CPROP-1

This test has been carried out to analyse the effect of propagation length on constellation filter design.

The C1 constellation has shown an improvement in the SH estimations from 0.5 million seconds to 1 million seconds of propagation time. However, doubling that time results in an increase of the estimation error. While this might seem counterintuitive, this can be directly linked to the CubeSat orbiting with a $\nu = 240°$ depicted in Figure D.21. As can be seen, a propagation time of 0.5 million seconds is insufficient for proper coverage of the asteroid and thus estimation of the coefficients. This is improved by doubling the propagation time. However, setting t_{prop} to 2 million seconds is unproductive, presenting higher errors in the estimation of the coefficients due to the divergence of the orbit. Configuration 3 presents a similar behaviour, presenting larger errors for the highest propagation orbit due to its high reliance on the estimation of the coefficients.

On the other hand, the C2 configuration presents an improvement with larger propagation times, being more dependent on the position measurements of the mothership than on the estimations of the CubeSat. This is illustrated by the estimates having five coefficients of degree four and five with estimate errors of 100% for a $t_{prop} = 5 \cdot 10^5$ s, only two coefficients for a $t_{prop} = 1 \cdot 10^6$ s, none for a $t_{prop} = 2 \cdot 10^6$ s.

Conclusions
Having analysed the previous test results a number of conclusions can be derived:

5.3.3.1. The frequency measurement update has a considerable impact on the estimations. While one might expect the higher the frequency update, the better the results, this has been shown not to be the case. In particular, the use of a five-second time step has been shown to provide overall the best results.

5.3.3.2. The propagation time of the satellites in the constellation has been shown to have a relevant impact on the estimations. However, this has been directly linked to the orbits adequate for coefficient estimation. Low values of propagation time can lead to insufficient coverage and therefore worse estimations, whereas propagation values that are too large might lead to orbital instabilities and be detrimental to the SH coefficient estimations. Furthermore, large propagation times can also saturate the filter, having a detrimental impact on the estimates produced.

5.4. Sensitivity Analysis: Satellite Constellation with Constraints

The functioning of the system is directly dependent on the visibility constraints and communications restrictions between satellites. This section aims to analyse how the filter behaves in these situations and presents adaptations to improve the efficiency of the system. In particular, Subsection 5.4.1 analyses the visibility restriction effects between satellites, followed by an analysis of the communications restrictions in Subsection 5.4.2. Finally, the satellite distribution effect is further studied considering both constraints in Subsection 5.4.3.

5.4.1. Analysis of the Visibility Restrictions between the Satellites

This subsection analyses the behaviour of filter estimations considering the visibility restrictions due to sunlight exposure. Since the NAVCAM of the satellites requires the asteroid to be visible, measurements cannot be produced when satellites are in the asteroid's shadow.

This section considers a simplified scenario where half of the three-dimensional space in inertial coordinates is in shadow, and the other half is sunlit. In this scenario, satellites having negative X coordinates cannot produce measurements. Detailed parameter settings used in the scenarios and their results can be found in Subsection D.3.1.

Test VIS-SAT-1
This "VIS-SAT-1" has been carried out to analyse the effect of adding visibility constraints to the constellation. Three single satellites have been propagated following an orbit of 30 km semi-major axis and a 90° inclination and with three different angles of true anomaly: 0°, 120°, and 240°. It should be noted that the measurements have been obtained with an update frequency of five seconds and propagation times of $1 \cdot 10^6$ s. Additionally, it should be considered that during periods of shadow where the satellites are unable to gather position measurements, the filter estimates the position of the satellite using the spherical harmonics model with null degree and order.

The coefficient estimates obtained are presented in Figure 5.22, which as can be seen, have considerable errors, much larger than the estimates obtained before adding the visibility constraint. Figure 5.21 shows the coverage of the satellites for different orbits, depicting how half of the coverage that was previously had is now fully reliant on the trajectory estimation using the PM gravity field. The inability of the filter to accurately estimate the coefficients can be directly linked to the fact that both real and estimated position measurements affect the SH coefficients estimation, leading to large errors. Furthermore, increasing the propagation time does not directly improve the estimations. On the contrary, larger propagation times involve larger blocks of estimated measurements, which can worsen the SH coefficients estimation.

These results highlight the significant impact of visibility constraints on the accuracy of filter estimations and underscore the need for careful consideration of sunlight exposure when designing satellite constellations for asteroid missions.

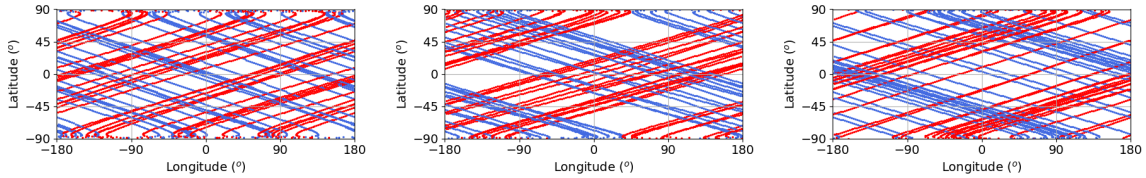

(a) $\nu = 0^o$ **(b)** $\nu = 120^o$ **(c)** $\nu = 240^o$

Figure 5.21: VIS-SAT-1 Test: Coverage for single satellites depicting in blue the times when the asteroid is visible and in red when it is in the shade for a propagation time of $t_{prop} = 1 \cdot 10^6$ s.

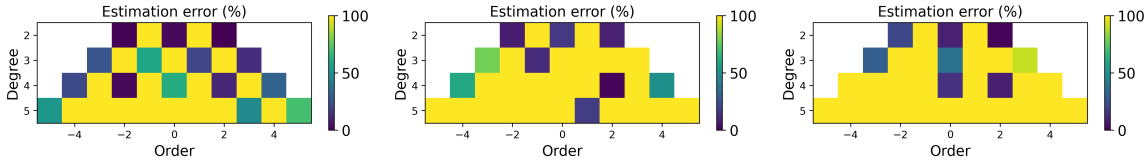

(a) $\nu = 0^o$ **(b)** $\nu = 120^o$ **(c)** $\nu = 240^o$

Figure 5.22: VIS-SAT-1 Test: Estimation error of the SH coefficients degree and order five for single satellites for a propagation time of $t_{prop} = 1 \cdot 10^6$ s and a time step of $\Delta t = 5$ s.

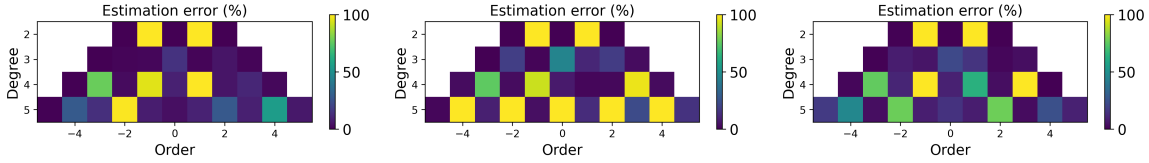

(a) $\nu = 0^o$, $\Delta t = 1$s **(b)** $\nu = 120^o$, $\Delta t = 1$s **(c)** $\nu = 240^o$, $\Delta t = 1$s

Figure 5.23: VIS-SAT-2 Test: Estimation error of the SH coefficients degree and order 5 for single satellites for $t_{prop} = 2.5 \cdot 10^6$ s.

Test VIS-SAT-2

In the previous test, it has been determined that the filter design is inadequate for coefficient estimation under visibility constraints. To address this, a new test scenario has been devised with an updated filter design. This new design pauses the filter when measurements are lost and restarts it when the satellite meets the visibility requirements again. Additionally, it should be noted that by restarting the filter, saturation is prevented, thus improving its performance.

The results of this updated design are presented in Figure 5.23. As seen, this filter design is able to estimate much more accurately the coefficients than the previous case, presenting a considerable reduction of the number of coefficients estimated with a 100% error. This is to be expected since in this scenario the filter only uses measurements obtained when visibility constraints are fulfilled, thus producing a more representative trajectory than in the previous scenario, when estimates of positions in shadow areas were used. Nevertheless, it still presents considerable errors, due to the fact that not only does the filter have to restart, which produces a small jump in the estimation, but also because the filter has half of the position measurements as it did before. The test has included doubling the propagation time up to $5 \cdot 10^6$ seconds, but no substantial change has been observed.

A more detailed study has been carried out to analyse the effect of the measurement update frequency and the propagation time. All the results obtained can be found in Table D.3.1 as well as further details on the scenario parameters. These tests have determined that a reduction of the time step from five seconds to one second yields better estimates. Nevertheless, doubling the propagation time does not improve the coefficient estimates. This can be attributed to the fact that the filter may be over-saturated.

In addition, these tests have been carried out considering velocity measurements in addition to the position measurements used, the results of which can be found in Figure D.25. Nevertheless, this has not shown an improvement in the measurements, which can be directly linked to the fact that the velocity measurements are directly linked to the position measurements, and therefore no new information on the dynamics is added to the filter. While the measurements can help the filter by bringing the same information with different errors, the errors of the position measurements overpower those of the velocity.

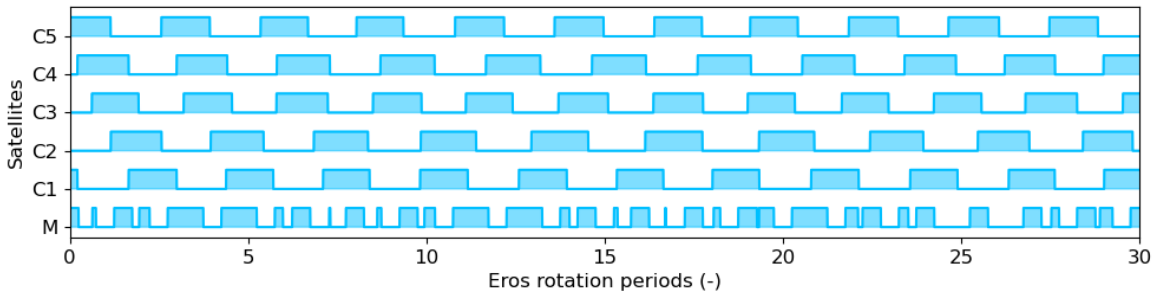

Figure 5.24: Satellites in the constellation with visibility conditions

Redesign of the filter

Having determined the effect that the visibility restrictions have on the SH coefficients estimation, the constellation filter design has been reevaluated and updated for better results. The three new filters designed are as follows:

Constrained Configuration 1 (CC1): This design follows that of Constellation 1, but in this case, this does not rely on all of the satellite measurements but only on two satellites that have adequate visibility. Furthermore, the filter is restarted every time a different satellite data is used.

Constrained Configuration 2 (CC2): This design is based on the Constellation 2 design. It works under the premise that each of the CubeSats in the constellation has its own UKF algorithm that estimates the SH coefficients from its position measurements and sends these estimates to the mothership. The mothership uses its own position measurements and the SH coefficient estimates from the CubeSats, computing a weighted average to obtain the best coefficient estimations. When a CubeSat is in the shaded area of the asteroid, the mothership uses the last SH coefficients produced by said CubeSat.

Constrained Configuration 3 (CC3): This design is very similar to that of CC2, but instead of considering the SH coefficient estimation from all the satellites independently of their visibility conditions, it only uses the estimates of the satellites that have visibility conditions.

Test VIS-CONST-1

This subsection aims to analyse the behaviour of the refined filters with a constellation of satellites considering visibility restrictions. To do so, this test considers a constellation with six satellites in total: the mothership located at $\nu = 0^o$, and five CubeSats spread out in $\nu = 60^o$, $\nu = 120^o$, $\nu = 180^o$, $\nu = 240^o$ and $\nu = 300^o$. Note that the estimates produced by these satellites individually can be found in Figure D.26. Further details on the configuration of the simulated scenario can be found in Table D.31.

Figure 5.25 presents the number of satellites of the constellation that have visibility conditions to obtain measurements and therefore position estimations. This is presented as a function of time for the first 30 Eros rotation period. As can be seen, the majority of the time there are from two to four satellites out of the six of the constellation with position estimates that can be used by the filter. Therefore, it is to be expected that having a considerable number of satellites with valid measurements the filters will be able to perform correctly and produce adequate coefficient estimates.

Figure 5.24 depicts the satellites' visibility conditions along the first 30 Eros rotation periods. As can be seen, these conditions are highly dependent on the orbit followed by each satellite. For example, the mothership has more irregular visibility conditions than the other cases. The number of satellites with visibility at each time instant is depicted in Figure 5.25, showing how for most time instances, the number of satellites with measurements varies from two to four, out of the six satellites in the constellation.

Some of the estimates produced by the redesigned constellation filters are presented in Figure 5.26, showing the results for a variety of propagation and frequency updates. Note that the full set of tests and their results can be found in Figure D.3.1.

Several observations can be made from the results. Firstly, it can be seen that the results obtained with the CC2 and CC3 designs are very similar. It should be noted that when exploring the values presented graphically, these present differences, although these are two minimal for the visual differentiation of the results. This is due to the settings of the filters, attributing more relevance to the position measurements

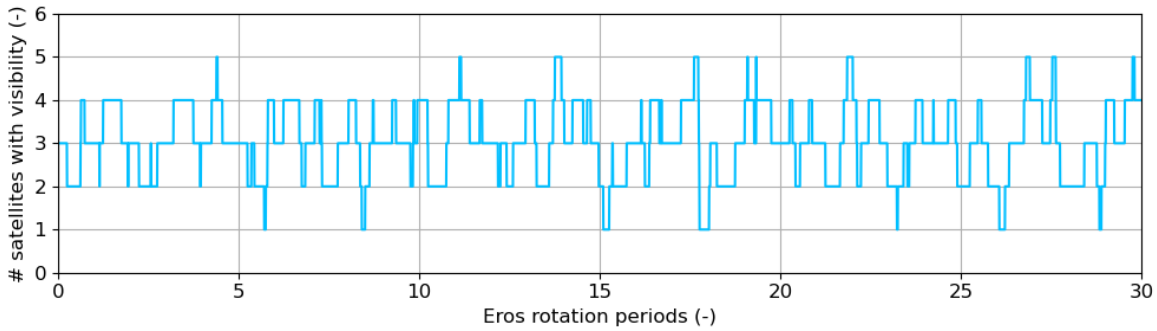

Figure 5.25: Satellites in the constellation with visibility conditions

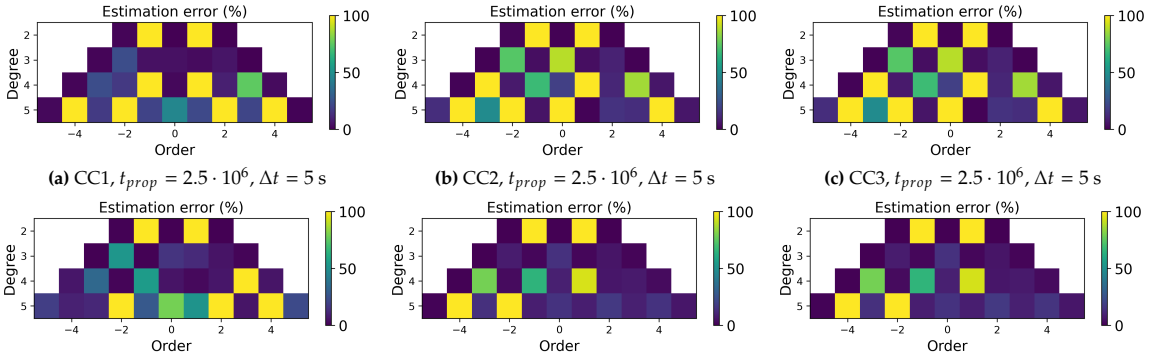

(a) CC1, $t_{prop} = 2.5 \cdot 10^6$, $\Delta t = 5$ s **(b)** CC2, $t_{prop} = 2.5 \cdot 10^6$, $\Delta t = 5$ s **(c)** CC3, $t_{prop} = 2.5 \cdot 10^6$, $\Delta t = 5$ s

(d) CC1, $t_{prop} = 2.5 \cdot 10^6$, $\Delta t = 1$ s **(e)** CC2, $t_{prop} = 2.5 \cdot 10^6$, $\Delta t = 1$ s **(f)** CC3, $t_{prop} = 2.5 \cdot 10^6$, $\Delta t = 1$ s

Figure 5.26: VIS-CONST-1 Test: Estimation error of the SH coefficients degree and order 5 for the new constellation designs for a time step of 5 seconds.

of the mothership than those of the SH coefficients obtained from the other satellites of the constellation. This has been further analysed by changing the uncertainty parameters of the coefficient measurements, the results of which are presented in Figure D.28. It has been seen that, as the value of σ is decreased and the filter trusts more the SH measurements, the estimates produced by both filters differ, and the CC2 design is shown to perform better. Furthermore, it should be noted that as the reliance on the SH measurements increases, the estimations become worse. This is due to the fact that the filter uses the estimates produced by satellites with poor orbits such as the case of $\nu = 180^o$, which has worse estimates than that of the mothership.

The effect of the mothership's orbit has also been analysed by placing the mothership in the orbit with a $\nu = 120^o$ and a CubeSat at $\nu = 0°$, thus maintaining the same orbits considered in the scenario. This change involves the use of a slightly worse performing orbit than that of the mothership and therefore negatively impacts the estimates of CC2 and CC3, which rely more on the mothership's estimates than CC1. The coefficients-estimate results for this scenario can be found in Figure D.29.

Additionally, it has been observed that there is a considerable improvement in estimation results when using a one-second time step as opposed to five seconds, which is to be expected, as the same tendency has been identified for the single satellite estimation scenarios. Furthermore, an increase in the propagation time has not necessarily led to an improvement in estimation measurements. This can be a result of the filter getting unstable, over longer intervals, nonlinear effects can become more significant, and the UKF's approximations may become less accurate, leading to a degraded performance.

Conclusions

This section has analysed the effect that the visibility restrictions have on the filter's coefficients estimate. It has been seen that for the filter to be able to estimate the coefficients effectively, it has to be restarted every time position measurements are lost due to visibility constraints. While this method has allowed the filter to estimate the coefficients, the estimations have shown a decrease in accuracy. Furthermore, with the new filter design that requires it to re-start, having lower time steps has shown to be crucial to improve the accuracy of the estimates, which is due to the fact that the filter is now split into smaller time periods, and having smaller time steps allows the filter more data to produce the estimates.

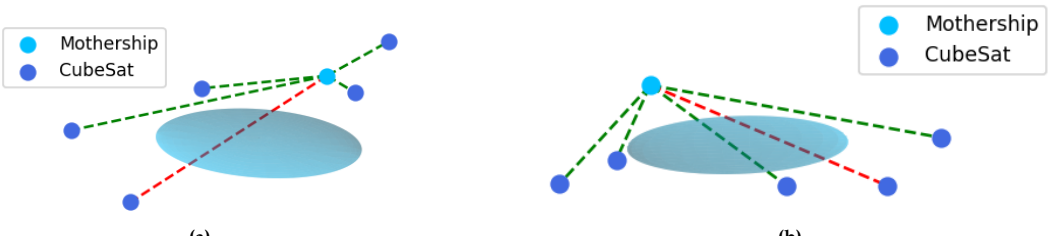

(a) (b)

Figure 5.27: Constellation scenario with a mothership and five CubeSats orbiting the asteroid depicting the line-of-sight constraints shown from different angles

After having analysed the effects resulting from the visibility restrictions, three new redesigns of the filters have been presented and studied. Each filter design has its own advantages and disadvantages:

5.4.1.1. The CC1 design uses the desired number of CubeSats that are visible in the constellation, which for this testing purpose has been set to two. This has the advantage that the filter uses measurements from all the satellites. This is an advantage since in the case that some of the trajectories of the CubeSats are inadequate, the filter can rely on the others, and therefore it ensures that the estimates will not be overpowered by incorrect trajectories. Nevertheless, this design is also the most computationally expensive, in particular the more satellite measurements that are considered at the same time.

5.4.1.2. The CC2 design has been shown to perform adequately using the weighted average of the coefficients estimations produced by the CubeSats. However, the accuracy obtained is highly dependent on the mothership trajectory id a high value is given to the R matrix, so it is crucial that this matrix is adjusted adequately for the scenario.

5.4.1.3. The CC3 design has shown similar results to the CC2 design, producing slightly worse results and requiring larger computation times.

With the aforementioned conclusions on the different designs tested, it has been determined that the CC1 design is the most appropriate for the estimation of the spherical harmonic gravity-field coefficients of the asteroid. Although this is the most computationally expensive filter design, it is the best equipped to produce the estimates of asteroids that are not well known. The CC2 and CC3 filters rely on the estimates produced individually by each satellite, which are then used by the mothership. If the mothership's trajectory is not adequate for the position estimation, the estimates produced are considerably worsened. This is a considerable disadvantage in the design. If the constellation design could be optimised to the asteroid, the best trajectories could be selected and these filter designs could be ideal choices. Nevertheless, this research is done under the premise that the mission is designed without previous knowledge of the gravity field of the asteroid, and therefore, the mothership trajectory cannot be designed to be optimal.

With this consideration, the CC1 filter is the most reliable, since it uses the measurements obtained from various satellites. Whereas an inadequate orbit will have a detrimental effect on the estimates, this will not be as severe, since the filter will equally rely on the other satellites of the constellation.

5.4.2. Analysis of the Communications Restrictions between the Satellites

This subsection examines the impact of communication constraints on the estimation of coefficients in the UKF filter when using a constellation of satellites. For the purposes of this simulation and in order to ease computational time, the asteroid has been modelled as an ellipsoid with the dimensions of 33 by 13 by 13 km [1] for the communications constraints computation.

A simple test scenario involving a mothership and five CubeSats orbiting the asteroid has been devised to validate the detection algorithm. Figure 5.27 shows the scenario at a specific time instant from different perspectives. The software successfully detects when the line-of-sight is established and when it is obstructed by the asteroid.

Several scenarios have been defined to assess the impact of communication constraints on the UKF and its coefficient estimation.

[1] https://nssdc.gsfc.nasa.gov/planetary/text/eros.txt#:~:text=Perihelion%20distance%20is%201.13%20AU,miles%2F218%20million%20kilometers

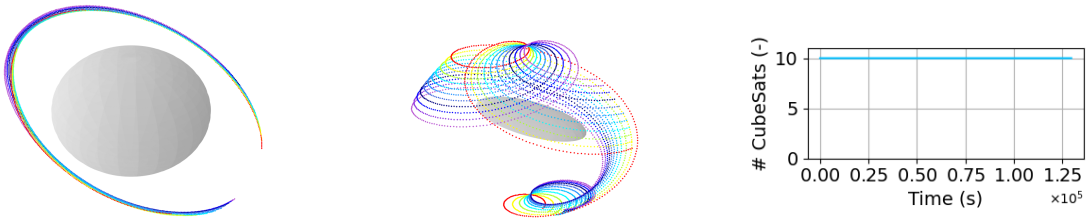

(a) Inertial frame **(b)** Asteroid frame **(c)** CubeSats with LOS

Figure 5.28: COMMS-1 Test: Trajectory plot of the constellation satellites of Scenario 1 and representation of the number of CubeSats with direct LOS with the mothership.

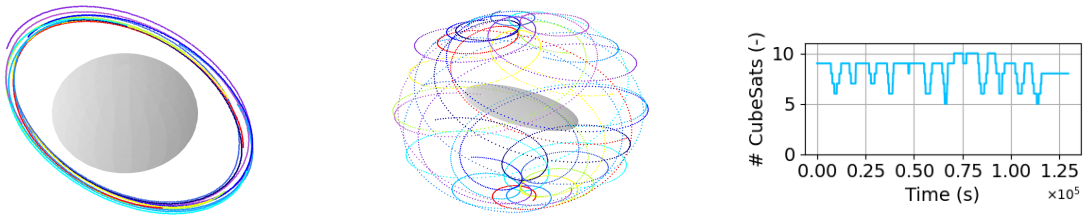

(a) Inertial frame **(b)** Asteroid frame **(c)** CubeSats with LOS

Figure 5.29: COMMS-1 Test: Trajectory plot of the constellation satellites of Scenario 2 and representation of the number of CubeSats with direct LOS with the mothership.

Test COMMS-1

This test evaluates a constellation of satellites with the same semi-major axis and inclination but different true anomalies to analyze how this distribution affects communication constraints between the mothership, positioned at $\nu = 0°$, and the CubeSats. Two scenarios with different satellite distributions have been considered.

Scenario 1 examines communication constraints when satellites are closely distributed along an orbit with a 30 km semi-major axis and 90° inclination. The mothership is at 0° true anomaly, and 10 CubeSats are positioned at 5° intervals from 5° to 50°. Figure 5.28 illustrates the satellites' trajectories over a short period. The closely spaced satellites maintain constant LOS with the mothership, indicating no impact on the filter's estimates.

Scenario 2 explores the effect of evenly distributing satellites along the true anomaly at 30°, 60°, 90°, 120°, 150°, 185°, 210°, 240°, 270°, and 300°. Figure 5.29 shows that satellites in this wider distribution experience greater LOS variability with the mothership, as illustrated in Figure 5.29c.

The availability of the satellites has been studied further, the results of which can be found in Subsection D.3.2 (in Figure D.30). Results indicate that LOS can be established with no issues for true anomalies ranging from 30° to 120° and 300°. On the other hand, the CubeSats that are located in opposite directions of the mothership have larger time periods of loss of contact given that the asteroid gets in the middle of both satellites. In addition, this plot depicts how the behaviour of the satellites changes with time, this is due to the fact that the asteroid rotates, which has an effect on the blockages that the satellites experience in their communications. Furthermore, the rotating asteroid and irregular gravity field contribute to the changing LOS conditions over time, further affecting communication constraints and filter performance.

Test COMMS-2

This test considers a constellation of satellites orbiting with the same semi-major axis with different values of inclination and aims to analyse the effect this distribution has on the communications constraint between the mothership, positioned at $i = 90^o$ and the Cubesats. Two scenarios have been considered: Scenarios 3 and 4.

Scenario 3 is presented in Figure 5.30. This considers the communications restrictions when an orbit of 30 km of semi-major axis is followed with 10 CubeSats distributed amongst the inclinations of 85°, 80°, 75°, 70°, 65°, 60°, 55°, 50°, 45° and 40°. As can be seen, the satellites depict very close trajectories and therefore, as is to be expected, they maintain constant LOS with the mothership. The communications constraints have been analysed further for this scenario. The results of this analysis can be found in

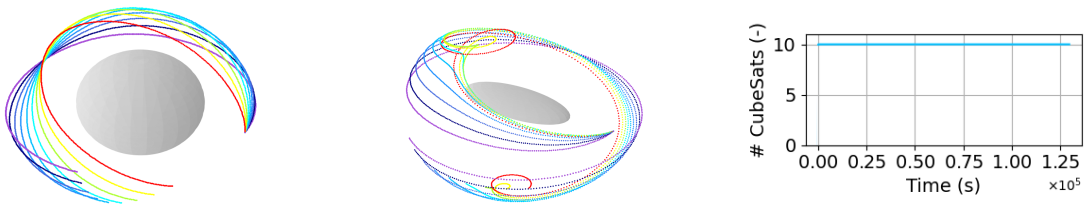

(a) Inertial frame **(b)** Asteroid frame **(c)** CubeSats with LOS

Figure 5.30: COMMS-2 Test: Trajectory plot of the constellation satellites of Scenario 3 and representation of the number of CubeSats with direct LOS with the mothership.

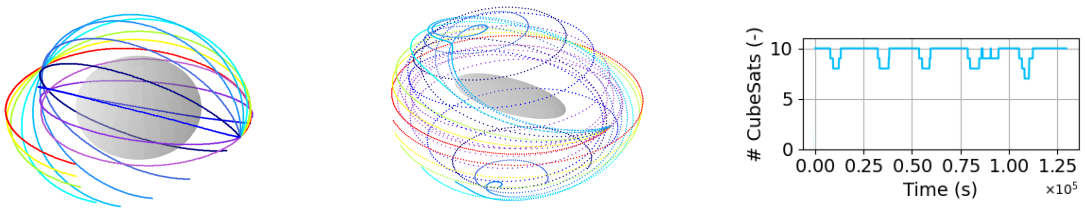

(a) Inertial frame **(b)** Asteroid frame **(c)** CubeSats with LOS

Figure 5.31: COMMS-2 Test: Trajectory plot of the constellation satellites of Scenario 4 and representation of the number of CubeSats with direct LOS with the mothership.

Subsection D.3.2 (Figure D.31). It has been seen that overall, the higher the inclination is, the more interferences there are with the establishment of communications.

Scenario 4 has been analysed by distributing the CubeSats in a wider range of inclinations: 10°, 20°, 40°, 80°, 100°, 120°, 140°, 160°, and 180°. Shown in Figure 5.31, this distribution of satellites has a wider coverage of the satellites and as expected this has a detrimental impact on the communications, having CubeSats at specific points loose LOS with the mothership when crossing the asteroid.

Conclusions

The previous scenarios tested have shown that the communication constraints do not have a considerable effect on the UKF filter. Therefore, no new adaptations are necessary in the design of the constellation filters. Nevertheless, it should be noted that the communication constraint will continue to be considered in the system, and the specific cases where LOS cannot be established between mothership and CubeSats will be treated in the same way as with the visibility constraint.

In the case of configuration CC1, if communications are lost with a satellite that is being used in the position measurements, the filter will be restarted with another available satellite. Moreover, in the case of CC2, if the communications are lost, the filter will consider the last SH coefficients estimated by said CubeSat. Finally, for the CC3 design, CubeSats will not be used during the time steps that it remains without communications.

5.4.3. Analysis of the Satellite Distribution with Restrictions

This section aims to analyse the satellite distribution's impact on the filter estimations when visibility restrictions are considered. This is analysed through a series of tests considering the number of satellites of the constellation, their distribution along the true anomaly and their distribution along the inclination.

Test NUM

The number of satellites used in the constellation has been analysed through several scenarios considering the use of several satellites evenly distributed along the same orbit of 30 km of semi-major axis and 90º of inclination. Further details on the parameters used for the simulation of the scenario can be found in Subsection D.3.3.

As it is depicted in Figure 5.32, the estimation of the gravity-field coefficients improves with the number of satellites in most cases. This can be directly linked to the fact that the more satellites, the more position measurements that are available for each time instant, and the smaller the periods of insufficient measurements are. Nevertheless, as it can be seen, increasing the number of satellites is beneficial up to a point, due to the fact that the estimations are dependent on the satellite's orbit, and

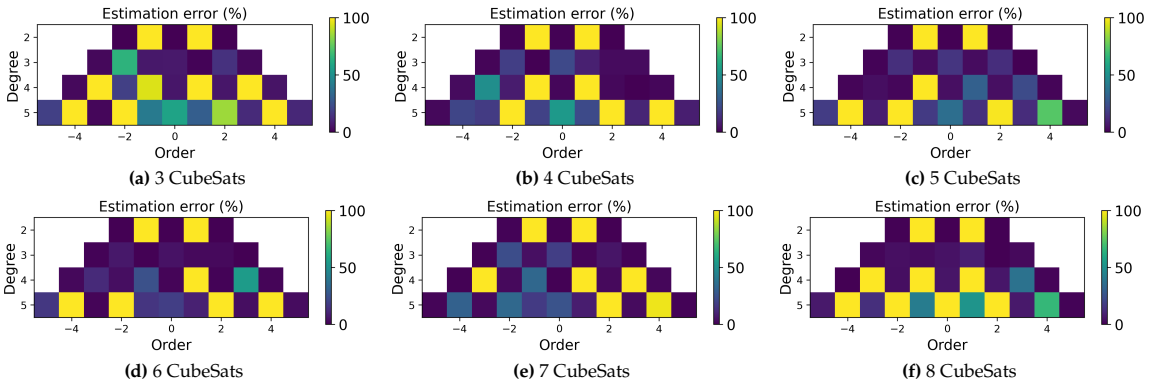

(a) 3 CubeSats **(b)** 4 CubeSats **(c)** 5 CubeSats

(d) 6 CubeSats **(e)** 7 CubeSats **(f)** 8 CubeSats

Figure 5.32: NUM Test: Estimation of the SH coefficients for a number of satellites in the same orbit with evenly distributed true anomaly using two satellites in the position estimation considering visibility and LOS constraints.

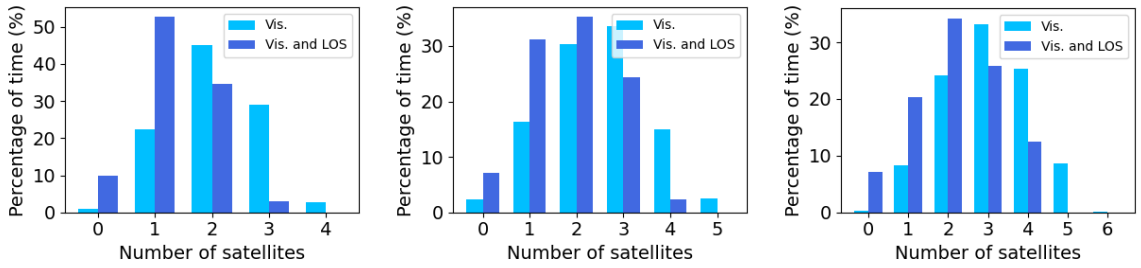

(a) 3 CubeSats **(b)** 4 CubeSats **(c)** 5 CubeSats

Figure 5.33: NUM Test: Time percentages of the number of satellites fulfilling the visibility and both the visibility and communications condition along a 1 million second propagation of the constellation.

thus, even if a large number of CubeSats are available, if the data provided by a satellite following an inefficient orbit is used, the estimates are negatively impacted.

Figure 5.33 presents the percentage of time that a number of satellites of the constellation are available for the constraints considered for constellations of three, four, and five satellites. Additional constellations have been tested and the results can be found in Figure D.33. Note that the difference in the estimates for different constraints considered as a function of the number of satellites in the constellation can be found in Figure D.32. As is depicted, there is a clear difference between the availability time when only visibility conditions are considered versus when communications constraints are added to the model. When adding the LOS constraints, the time percentage is shifted to the left, decreasing the number of satellites and following a similar tendency to when only visibility constraints are considered. The plots present that for a three CubeSat constellation, for approximately 80% of the time, there are two or more satellites available, and this value is reduced to less than 40% when the line-of-sight constraints are added to the model. This percentage of availability increases with the number of satellites in the constellation. For a total of four CubeSats, the availability of two or more satellites is up to more than 80% with visibility constraints and this value is reduced to less than 65% when LOS constraints are added. An additional CubeSat in the constellation increases the availability of the satellites to 90% with LOS and 75% with all the constraints. Therefore, it can be seen that the availability of the satellite improves significantly with the number of satellites. Nevertheless, there is no linear relationship between the improvement of the satellite availability with the accuracy of the estimations. This is due to the fact that the satellites of the constellation orbit with a different asteroid coverage in each case, and the coverage has an extremely relevant effect on the accuracy of the estimations as it has been determined in earlier testing.

The number of filter restarts required for each of the constellations in these cases has been analysed and is presented in Figure 5.34. As can be seen, the number of resets of the filter significantly grows from three to four CubeSats. This is due to the fact that a constellation with three satellites has considerably less time in which two or more satellites of the constellation satellites are available at the same time, and therefore there is a lower amount of time coverage. From four CubeSats and on, the number of resets is similar but variable, highly dependent on the specific orbits followed by the constellation's satellites.

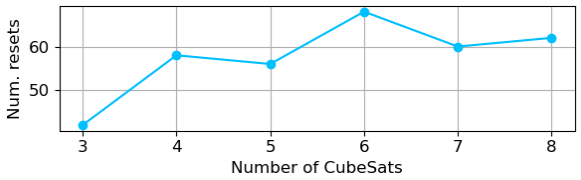

Figure 5.34: NUM Test: Number of filter resets as a function of constellation CubeSat number

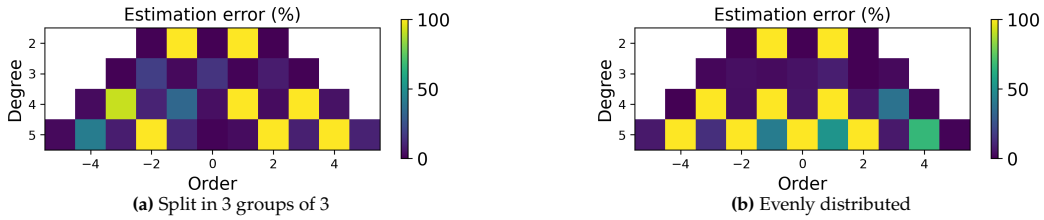

(a) Split in 3 groups of 3 **(b)** Evenly distributed

Figure 5.35: TRU Test: Estimation of the SH coefficients with an eight CubeSat constellation where the satellites distributed along the true anomaly in groups of 3 or evenly. These estimates are computed using two satellites for the estimation considering visibility and LOS constraints.

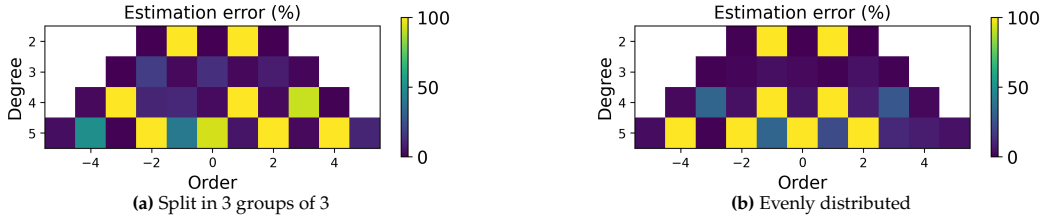

(a) Split in 3 groups of 3 **(b)** Evenly distributed

Figure 5.36: TRU Test: Estimation of the SH coefficients with an eight CubeSat constellation where the satellites distributed along the true anomaly in groups of 3 or evenly. These estimates are computed using three satellites for the estimation considering visibility constraints.

Test TRU

This test aims to analyse how the distribution of the satellites along the true anomaly of the same orbit affects the estimations. Figure 5.35 presents the estimations obtained when testing two different scenarios. Both use constellations with a 30 km semi-major axis and an inclination of 90°. However, the first case uses an even distribution of three groups of satellites along the 360°, and the second considers an even distribution of the satellites. In the estimates obtained, it can be seen that an even spreading of the satellites along the true anomaly has a detrimental effect, presenting significantly larger errors than when the satellites are located more closely together. This can be directly linked to the constraints. Placing the satellites in similar trajectories increases the likelihood that two or more satellites will both be fulfilling the visibility and communications constraints. Furthermore, spreading groups over the 360° of true anomaly also increases the time that visibility constraints are fulfilled, by at least one group of satellites.

Additionally, the same scenario has been tested using the positions of three satellites instead of two in the filter, which would be expected to improve the estimate obtained. The results obtained are presented in Figure 5.36, and show how this filter works correctly when the visibility constraint is considered, but when the communication constraints are added, the filter is unable to get adequate position measurements for three satellites for the UKF to work properly and produce good estimates of the SH coefficients.

Further detail on how the constraints affect the availability of the satellites is presented in Figure 5.37, where the effects of the visibility and communications constraints are shown for each satellite considering an even distribution along the true anomaly. As can be seen, the availability of the satellites is very different depending on their orbit, and this has a direct effect on the estimates. Figure 5.38 represents how the number of available satellites changes over time for the first 30 rotations of the asteroid. This shows how the availability is very variable, thus resulting in a large number of necessary UKF resets. Furthermore, further analysis can be done on the availability of two or more satellites at the same time with Figure 5.39. As expected, by including the communications constraint the plot is shifted to the left, presenting a higher percentage of time for a smaller amount of satellites visible. Moreover, these plots

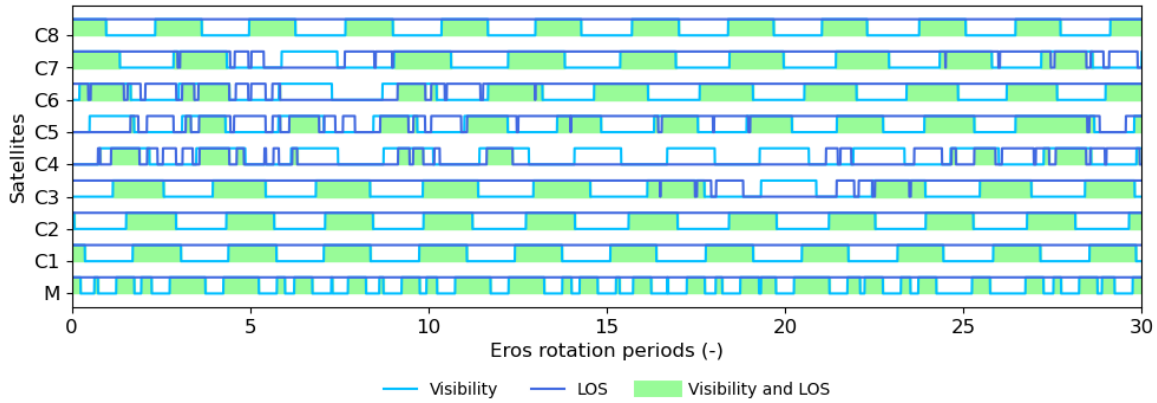

Figure 5.37: TRU Test: Visibility and line-of-sight conditions between the CubeSats and the mothership for the initial 30 rotation periods of Eros for satellites placed in an even distribution.

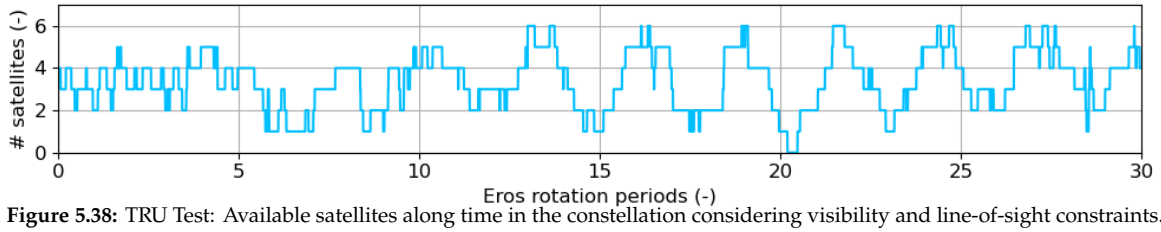

Figure 5.38: TRU Test: Available satellites along time in the constellation considering visibility and line-of-sight constraints.

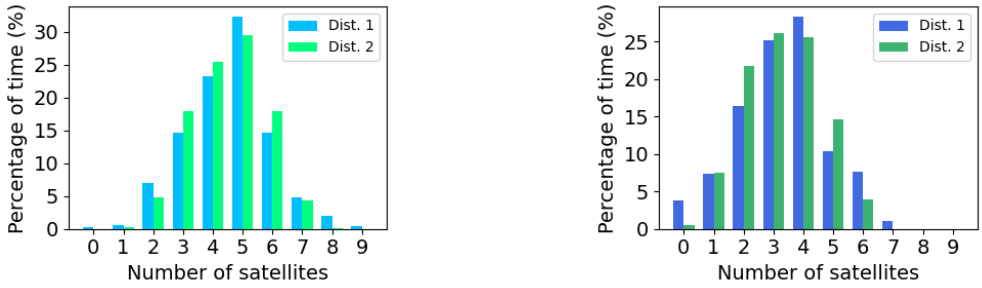

(a) Visibility constraints

(b) Visibility and LOS constraints

Figure 5.39: TRU Test: Time percentages of the number of satellites fulfilling the visibility and both the visibility and communications condition along a 1 million seconds propagation of the constellation. "Dist. 1" references an even distribution of the satellites and "Dist.2" references a distribution of the satellites in groups of three.

also depict a difference in the availability directly linked to the distribution of the satellites along the true anomaly and confirm that an even spreading results in a more limited availability of the satellites of the constellation.

Test INC

This test aims to analyse how the distribution of the satellites along different orbital inclinations affects the estimations when the constraints are considered.

The first scenario considered has been that of the distribution of four satellites into two differently inclined orbits and the second has considered six satellites split into three differently inclined orbits. The results obtained when only visibility constraints are considered demonstrate how the results are governed by the limitations of the orbit and not by those imposed by the constraints. This is due to the fact that not all orbital inclinations are adequate for the estimation of the coefficients. The coefficient estimates can be found in Figure D.35. Nevertheless, the constraints imposed by the communication systems are notable as can be visualised in Figure 5.40, which shows how they present insufficient time periods when two or more satellites are available, therefore being unsuitable for the estimation of the coefficients.

A second scenario has been tested, using six satellites. While the communications constraint has also been quite restrictive for this case, the additional satellites allow the UKF to be able to have enough

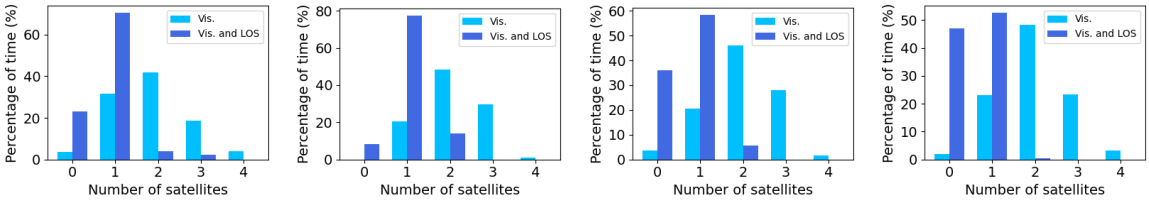

(a) $i = 0^o$ and $i = 90^o$ **(b)** $i = 30^o$ and $i = 90^o$ **(c)** $i = 60^o$ and $i = 90^o$ **(d)** $i = 80^o$ and $i = 90^o$

Figure 5.40: INC Test: Time percentages of the number of satellites fulfilling visibility and both visibility and LOS constraints for a constellation of four satellites split in two different inclination orbits located at the true anomaly of 0^o and 180^o.

measurements to produce the desired estimates. Additionally, it has also been seen that while one would expect orbits with similar inclinations to be less restricted by the LOS constraint, this has not been the case for combinations such as 90° and 80°, which have shown more restrictions than for orbits of 90° and 60°, as well as 90° and 30°. This can be directly related to the disposition of the satellites along the true anomaly and depicts a clear interaction between both parameters.

Conclusions

The constraints of the scenario have been shown to have a considerable effect on the estimates computed, considerably decreasing the availability of the satellites. Several conclusions have been made:

5.4.3.1. The consideration of the constraints has been seen to restrict considerably the availability of the satellites, and therefore lead to more breaks and necessary re-starts of the filter and shorter data time ranges, which has a detrimental effect on the computation. The distribution of the satellites along the constellation has a direct effect on these constraints and is therefore a key factor of an adequate mission design.

5.4.3.2. The number of satellites of the constellation has been shown to affect considerably the percentages of time that satellites's measurements are available to the mothership. The larger the number of satellites, the tendency is that the larger the probability of having two or more satellites available, which can additionally affect the number of restarts of the filter depending on the distribution of said satellites.

5.4.3.3. The distribution of the satellites along the true anomaly and the inclination have a considerable effect on the restrictions. Constellations with closely distributed satellites have been shown to have lower communication restrictions. Nevertheless, this does not directly lead to the estimates being better, since the determining key factor is the adequacy of the trajectory for an appropriate gravity-field determination.

5.5. Summary

1. A sensitivity analysis of the scenario considering a single satellite has highlighted the following trends:

   (a) Coverage and Semi-Major Axis: Effective coverage of the asteroid is crucial for accurate estimation of spherical harmonic (SH) coefficients. Orbits with lower semi-major axes yield better estimates due to stronger gravitational field effects.
   (b) Inclination: Higher orbital inclinations result in improved coverage of the asteroid, leading to better SH coefficient estimates.
   (c) Propagation Time: Increased total propagation time generally enhances coverage and improves SH estimates up to a certain point, beyond which additional time does not significantly improve accuracy.
   (d) Eccentricity: The impact of eccentricity on estimation varies with inclination. Higher eccentricities enhance estimates in polar orbits but degrade them in equatorial orbits.
   (e) Position measurement errors can significantly degrade the accuracy of the coefficient estimations, and the proper adjustment of the uncertainty of the measurements in the filter is significant to obtain an adequate filter performance. In addition, including velocity measurements can improve coefficient estimation by mitigating the impact of measurement errors.

(f) Errors in the gravitational constant and rotation rate estimates of the asteroid used in the filter have a considerable detrimental effect on the estimates of the filter.
(g) Measurement update frequency: Smaller update intervals improve filter performance, although they require longer computation times.
(h) Perturbations in the system: The filter is able to successfully estimate the gravity-field coefficients in the presence of a third-body and SRP perturbations for orbits within the Brillouin Sphere. Moreover, accurate estimation of high-degree and high-order coefficients requires low semi-major axis orbits.

2. A sensitivity analysis of the scenario considering a constellation of satellites has highlighted the following trends:

(a) Three UKF filter designs have been made in an attempt to obtain better estimates of the SH coefficients. It has been seen that no single UKF configuration design performs best in all scenarios. The effectiveness of each design depends on the specific orbital characteristics of the CubeSats and the mothership.
(b) Increasing the number of satellites of the constellation does not guarantee better estimates. The accuracy of the SH coefficient estimates is highly dependent on the quality of the asteroid's coverage.
(c) The frequency update of the measurements has a considerable impact on the estimates, however up to a point, increasing it has no advantages in the estimates. A similar tendency is identified with the propagation time. While larger propagation times improve the estimates, the filter can get saturated if this is too long. Therefore, both settings must be carefully set for optimal results.

3. A sensitivity analysis of the scenario considering a constellation of satellites with constraints has highlighted the following trends:

(a) The addition of visibility and communications has a detrimental effect on filter performance and the accuracy of the estimates.
(b) Orbital parameters such as the inclination and the true anomaly determine the trajectory that is to be followed by the satellites and thus have a considerable effect on the visibility and communications constraints. Therefore, adequate constellations have to be designed considering them.
(c) The number of satellites in the constellation is determinant for the proportion of time where a minimum number of satellites have visibility conditions and can transmit their position to the mothership. The larger the constellation, the larger the portion of time that this proportion is fulfilled.

The next chapter further studies the scenario through the use of ANOVA.

6

Design Exploration using ANOVA for Constellation Optimisation

Optimising the design of a satellite constellation is crucial for accurately and efficiently estimating the spherical harmonic gravity-field coefficients of an irregular asteroid. Key parameters, such as the semi-major axis, inclination, and eccentricity of the satellite orbits, play significant roles in determining the performance of the estimation filter. This chapter presents a systematic analysis of the effects of these design parameters using Analysis of Variance (ANOVA). Additionally, this analysis provides insight into the interactions between the variables, which is data that was not obtained from the analysis conducted in Chapter 5.

The chapter starts with Section 6.1, which introduces the implemented ANOVA methodology. This is followed by its application to the system. The design exploration has been divided into three main testing scenarios to investigate the behaviour and interactions of these parameters. The first scenario, detailed in Section 6.2, analyses the effects of the parameters when the satellites are uniformly distributed with varying true anomalies. The second scenario, discussed in Section 6.3, explores the distribution of satellites along different inclinations. Finally, Section 6.4 presents a scenario with a variable number of satellites and orbital distributions.

It should be considered that in all cases, the tests have been conducted with a fully perturbed environment and modelling the asteroids' gravity field up to degree and order 15. Furthermore, to ensure that only the effects of the distribution are tested, the satellites have all been modelled with the mothership's physical characteristics.

6.1. DoE implementation

As has been presented, the design space for this system is very large, and therefore it is important that the system be explored efficiently. Employing a factorial design method has been considered to explore the effects of the design parameters on the estimations efficiently and using an ANOVA to identify the significant factors and their interactions.

A factorial design is a method that conducts experiments for all combinations of a number of factors (k), which are the design variables of a given scenario. Each factor can be set at different levels (denoted as m), which represent the specific values or conditions under which the factors are studied. For example, a factor can be studied at a minimum, nominal, and maximum value.

The number of levels used defines the type of interactions that can be examined. Note that interactions between factors occur when the effect of one factor is dependent on the level of another factor. The analysis of interactions between factors can provide relevant insight into the functioning of the studied system. For instance, synergistic interactions may be observed, indicating that the combined effect of two variables is larger than that of the sum of their individual effects, as illustrated in Figure 6.1b. On the contrary, antisynergistic interactions might be found, depicting that the combined effect of two factors is smaller than the sum of their individual effects as depicted in Figure 6.1c, thus meaning that one variable reduces the effect of another. The study of these interactions provides relevant insight into the system and the effect of the factors considered.

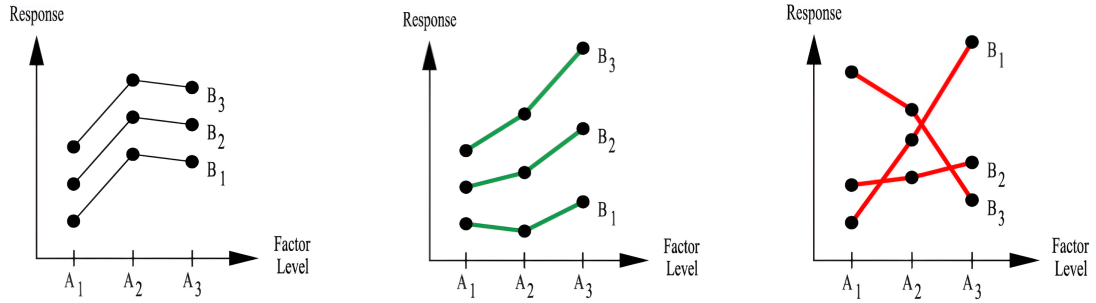

(a) No interaction **(b)** Synergetic interaction **(c)** Antisynergetic interaction

Figure 6.1: Examples of interactions between two factors (A and B) of three levels (1,2,3) each (Mooij, 1998).

To examine the linear interactions between two factors, the settings can be set for a minimum and maximum value, requiring a total of 2^k combinations, which results in information on the main effects due to each factor and their interactions. The following equation presents the response value for any observation (considering the ith level of one factor and the jth level of the other factor in a two-way ANOVA model[1] setup:

$$Y_{ij} = \mu + \alpha_i + \beta_j + (\alpha\beta)_{ij} + E_{ij} \tag{6.1}$$

where μ depicts the overall average value, α_i and β_j represent the main effects of the two factors for the i and j levels respectively. Furthermore, their interaction effect is depicted as $(\alpha\beta)_{ij}$ and E_{ijk} presents the random error for the ith and jth levels. Similarly, the three-way ANOVA primary equation, which considers three factors, is as follows:

$$Y_{ijk} = \mu + \alpha_i + \beta_j + \gamma_k + (\alpha\beta)_{ij} + (\alpha\gamma)_{ik} + (\beta\gamma)_{jk} + (\alpha\beta\gamma)_{ijk} + E_{ijk} \tag{6.2}$$

where it can be seen that the effect of a third factor has been added, with γ_k depicting its main effect for the k level and with $(\alpha\gamma)_{ik}$ and $(\beta\gamma)_{jk}$ depicting the pair-wise interaction between the third factor with the previous two. Moreover, the three-way interaction is depicted with $(\alpha\beta\gamma)_{ijk}$.

To include quadratic effects of the factors, three levels of settings must then be used, varying the parameters for a minimum, nominal, and maximum value, thus requiring a total of 3^k combinations. The response value of an observation for a two-way ANOVA is expressed with the following equation:

$$Y_{ij} = \mu + \alpha_i + \beta_j + \alpha\beta_{ij} + \alpha_i^2 + \beta_j^2 + (\alpha\beta_{ij})^2 + E_{ij} \tag{6.3}$$

where α_i^2 and β_j^2 are the quadratic effects of factors α and β respectively, and $(\alpha\beta_{ij})^2$ the interaction of the quadratic effects.

Including all the factors of the system can add up to a considerable number of simulations. Factorial designs use orthogonal arrays to efficiently explore the effect and interactions between several factors with a reduced number of runs. This array has a balancing property since for any pair of columns, all combinations of the factor levels occur the same number of times. It should be noted that orthogonal arrays assume no interactions between factors and therefore, when designing the test matrix, a factor can be assigned to each column. It should be noted that matrix orthogonality should be considered in a combinatorial sense. An example of the use of the orthogonal array for a fractional factorial design is presented in Table 6.1 for the use of seven factors with two levels. It should be noted that, if interactions are suspected between factors, the factor variances can be confounded with the interaction variances. Therefore, the columns of the matrix associated with the interactions must be left empty to properly analyse the effect of the factors, which results in a restriction of the number of factors that can be considered for a set of experiments. The interactions between the columns are defined by interaction tables, which can be found in many books on design of experiments, including the use of orthogonal arrays. For instance, for a two-factor simulation of two levels, where each of the factors value is represented in the first and second columns of the orthogonal matrix respectively, the third column contains an interaction between columns one and two, and should therefore be kept empty.

[1]GraphPad, "The Ultimate Guide to ANOVA", Available at: https://www.graphpad.com/guides/the-ultimate-guide-to-anova, Accessed on 05-05-2024

The ANOVA has been conducted using a Yates array, which is also an orthogonal array. This full factorial design considers all possible high (+1) and low (-1) combinations of the factors. An example of a full factorial design using the Yates order with three factors is presented in Table 6.2, showing how the same number of experiments are required for a considerably lower number of factors than in the first case. Using this array to set up the experiments, the tests include the same number of experiments for each of the levels for a factor.

ANOVA makes use of the sum of squares (S_i) for factor x_i on the levels $x_{i,k}$. This is computed as the sum of all level variations and is expressed by:

$$S_i = \frac{1}{n_L} \frac{\left(\sum^N y(x_i^+) - \sum^N y(x_i^-)\right)^2}{n_k} \tag{6.4}$$

where each sum adds the responses at level k together, which can be +1 or −1, and n_L represents the number of levels. While the previous formula only shows the computation of a two-level scenario, a three-level scenario would follow the same basis, through the sum of all level variations with the summation of three squared sums: one considering levels -1 and 0, another with levels 0 and +1, and another with levels -1 and +1. Additionally, the total sum of squares (S_T) can be computed as:

$$S_T = \sum_{i=1}^{N} \left(y_i - \bar{y}\right)^2 = \sum_{i=1}^{N} y_i^2 - 2\bar{y} \sum_{i=1}^{N} y_i + N\bar{y}^2 = \sum_{i=1}^{N} y_i^2 - \frac{T^2}{N} \tag{6.5}$$

where T is the total sum and N the number of samples. Moreover, y and $\bar{y}$ represent an individual response and the overall mean of the responses respectively. The variance contribution percentage is then computed with the following equation:

$$P_i = \frac{S_i}{S_T} \cdot 100 \tag{6.6}$$

A full factorial design has been implemented using the Yates algorithm[2], which uses the presented structure to generate the least-squares estimates for the effect of the factors and the interactions in the system. To maximise the efficiency of the analysis, a number of scenarios have been set and studied. These consider a large number of design variables. To obtain a proper insight into the interactions between all the parameters with each other, the FD has been computed considering only two factors and two levels for all the combinations considered in the scenario. This allows the identification of the main effects and interactions of the factors considered. Furthermore, a more complete FD has been computed with all the factors at the same time at the end for each scenario, to get additional information on the contributions between the factors.

Table 6.1: Example of a fractional factorial design considering seven design parameters and two levels

Factor → **Experiment ↓**	**A**	**B**	**C**	**D**	**E**	**F**	**G**
1	−1	−1	−1	−1	−1	−1	−1
2	−1	1	−1	1	1	1	1
3	−1	1	1	−1	−1	1	1
4	−1	−1	1	1	1	−1	−1
5	1	−1	1	−1	1	−1	1
6	1	1	−1	1	−1	1	−1
7	1	1	−1	−1	1	1	−1
8	1	1	−1	1	−1	−1	1

Table 6.2: Example of a full factorial design considering three design parameters and two levels

Factor → **Experiment ↓**	**A**	**B**	**C**
1	−1	−1	−1
2	1	−1	−1
3	−1	1	−1
4	1	1	−1
5	−1	−1	1
6	1	−1	1
7	−1	1	1
8	1	1	1

[2]Engineering Statistics Handbook, "Yates Algorithm", Available at: https://www.itl.nist.gov/div898/handbook/eda/section3/eda35i.htm, Accessed on 05-05-2024

6.2. Scenario 1: Uniform Orbital Parameters with Variable True Anomaly

This section aims to study the effect that the design parameters have on a constellation where the satellites follow the same orbit in the inertial frame, with a range of true anomaly values. This scenario considers a constellation of five CubeSats orbiting the asteroid evenly distributed along the true anomaly using the UKF CC1 design.

The design variables considered are the semi-major axis, the inclination, the eccentricity, and the distribution of the satellites along the true anomaly. The following sections present the analysis of the interactions between these parameters. It should be noted that these variables have initially been considered in pairs to better study their interactions and, finally, a full interaction ANOVA has been carried out.

6.2.1. Semi-Major Axis and Inclination

An analysis focused on the interaction between the semi-major axis and inclination has been conducted, isolating these variables while setting eccentricity to zero and evenly distributing satellites along the true anomaly. The semi-major axis lower value has been set to 30 km, and its maximum value to 40 km. Moreover, the inclination minimum value has been set as 60° and its maximum value to 90°. Further details and results of this analysis are presented in Subsection E.1.1.

The results of the ANOVA, depicted in Figure 6.2, highlight significant findings regarding the impact and interaction of these variables. These depict the contributions that each of the parameters considered have on the estimates of each coefficient, as well as the contribution that the interaction of both has. Notably, the semi-major axis exhibits a predominant influence. Closer orbits to the asteroid experience stronger gravitational effects, leading to more accurate estimations. Reducing the semi-major axis has thus shown improvements in estimation accuracy. However, inclination also plays a crucial role, particularly affecting certain coefficients. This is because inclination is a defining factor in the coverage of the asteroid, and some of the coefficients' contribution to the gravity field might not be accurately estimated if the inclination is insufficient to provide coverage of the field in such locations.

Moreover, it can be noted that the interaction between both variables is also considerable in some cases, which has been confirmed by studying the effect that increasing the inclination for different values of the semi-major axis have slightly diverse tendencies, thus confirming that the effect of the inclination is highly dependent on the semi-major axis.

Additionally, Figure 6.3 illustrates the gradient response of the coefficients in the scenario. This shows the average estimation error produced by the filter for the cosine and sine coefficients. In particular, it depicts the effect that the relative variation of the design variables has on the estimate errors. In this case, it displays the effects of the inclination, by considering a nominal value of 75° and varying it with the same relative value, and thus between 90° and 60°. The same is done for the semi-major axis, which assumes a nominal value of 35 km and is varied 5 km, and thus between the values of 30 and 40 km. It should be noted that only the errors produced by the minimum and maximum values of the variables are presented in the plot. This allows the creation of plots that highlight the effects that a variation in the design variables has, and in particular, how strong the gradient slope is for the relative variation done. This provides interesting information on how strong the effects are for each design parameter, depending on the relative variation depicted. Additionally, it should be considered that the average estimation error of the coefficients is not directly proportional to the decision variables used, since these affect differently each of the coefficients used in the computation of the mean value represented, affected by the trajectory of the satellites and the visibility and communications constraints of each test conducted. Further data on the effects of the variation of the decision parameters on each of the coefficients can be found in Subsection E.1.1.

The gradient response plot reaffirms that lower orbit altitudes and higher inclinations generally reduce estimation errors. It also visually captures parameter interactions, emphasizing that higher inclinations enhance altitude effects due to improved coverage in polar orbits. Notably, the influence of inclination differs between high and low semi-major axis values, resulting in distinct trends for sine and cosine coefficients.

It is important to note that variability in decision variables directly impacts orbit coverage, influenced by satellite trajectory variations due to irregular gravity fields. Furthermore, asteroid rotation complicates system communications and visibility constraints, factors not linearly related to decision variables but

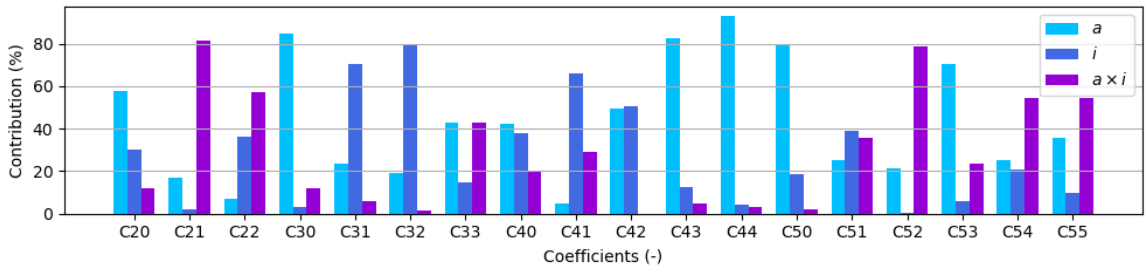

(a) Cosine coefficients

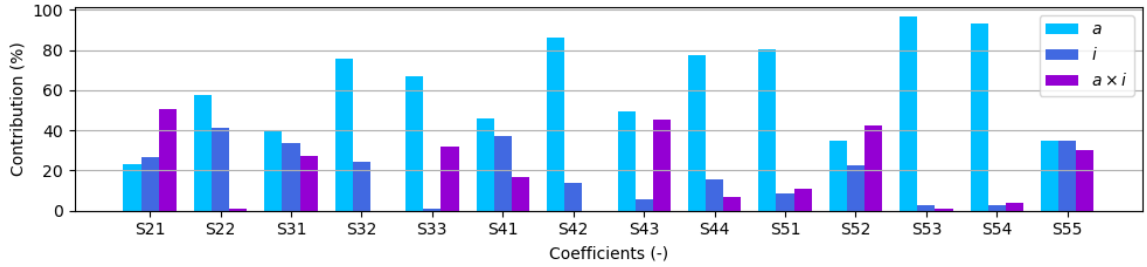

(b) Sine coefficients

Figure 6.2: Results of the ANOVA analysis for Scenario 1 considering the effect of a and i.

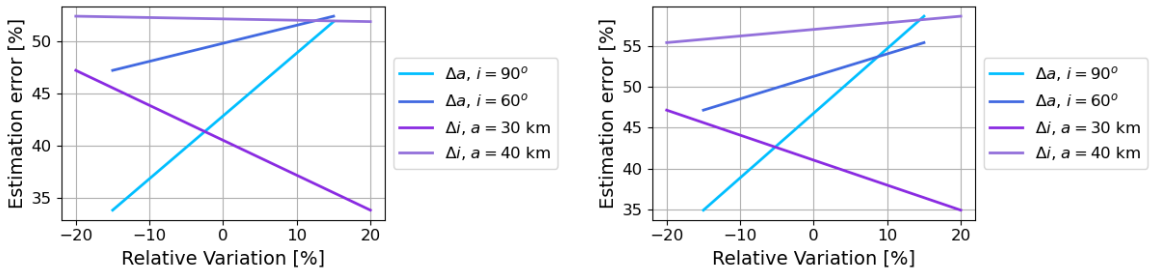

(a) Cosine coefficients

(b) Sine coefficients

Figure 6.3: Estimation error average percentage for the variation of the decision variables a and i.

that play a role in the system results.

6.2.2. Eccentricity and Inclination

Following the previous analysis, the effect of eccentricity and inclination have also been studied within the same scenario, adjusting the decision variables accordingly. For this study, the semi-major axis has been fixed to 40 km to avoid the orbital instability and inconclusive results that arise from combining low altitudes with high eccentricities.

The analysis results, presented in Figure 6.12, illustrate the individual contributions of the variables and their linear interactions. Notably, eccentricity has a dominant effect on the results. This is due to the significant relative variation in eccentricity, ranging from 0 to 0.2, which results in a 100% change and, consequently, a substantial impact on estimations, as shown in Figure 6.5. Increasing eccentricity enhances the overall estimation results because it allows satellites to achieve lower altitudes, improving coverage of the asteroid's gravity field, and leading to lower velocities in certain regions, benefiting the UKF.

In contrast, orbital inclination has a considerably lower impact on the results, with its interaction with eccentricity being more significant than its standalone effect. The gradient of estimation error is more pronounced for higher inclinations, providing better coverage and a stronger gravitational influence at lower satellite altitudes. An unexpected result is the gradient of inclination for circular orbits, which differs between sine and cosine coefficients. This can be attributed to the dependence of coefficient estimation on satellite trajectory and inclination. Additionally, as previously observed, inclination has a more pronounced effect at lower altitudes, explaining the high-altitude circular orbit's

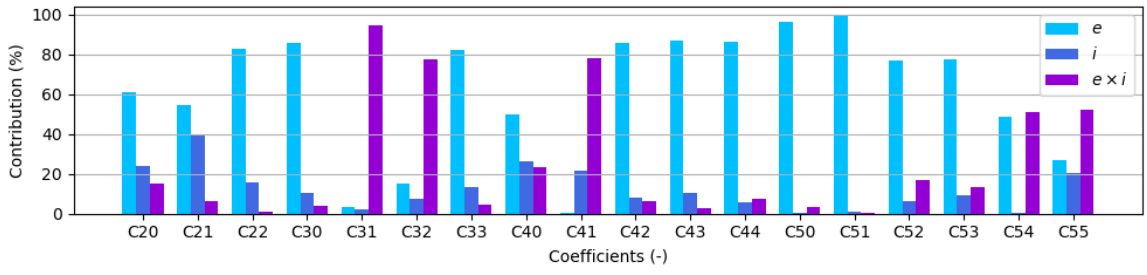

(a) Cosine coefficients

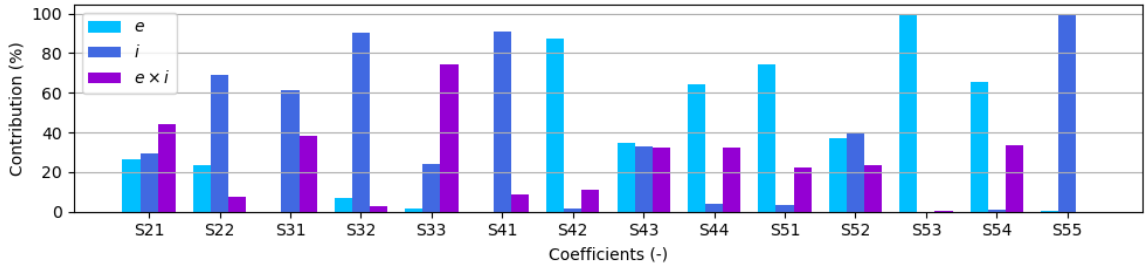

(b) Sine coefficients

Figure 6.4: Results of the ANOVA analysis for Scenario 1 considering the effect of e and i.

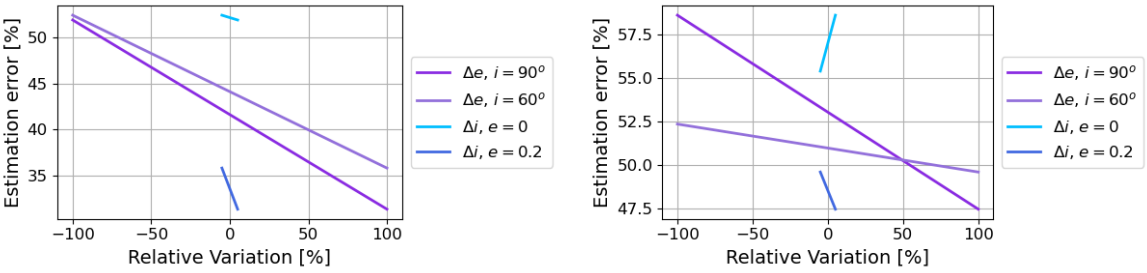

(a) Cosine coefficients

(b) Sine coefficients

Figure 6.5: Estimation error average percentage for the variation of the decision variables e and i.

varied results in this scenario.

Further details on the results obtained by the estimated coefficients can be found in Subsection E.1.2.

6.2.3. Semi-Major Axis and Eccentricity

The effect of the semi-major axis and the eccentricity have been studied within the same scenario. The ANOVA results on the effect of the semi-major axis and the eccentricity on the gravity-field coefficient estimates are presented in Figure 6.6. These figures highlight the variable impact of each factor, showing that eccentricity has a significant effect on most specific coefficients, while the semi-major axis is more relevant for others.

As depicted in Figure E.3, increasing eccentricity directly improves coefficient estimates. This improvement is expected, given the substantial contribution of eccentricity as depicted in the ANOVA results. And, as previously stated, higher eccentricity allows satellites to orbit closer to the asteroid, thereby experiencing a stronger gravitational influence and enabling the filter to produce more accurate estimates.

In addition, a linear interaction between both parameters has been observed, which is specifically illustrated in Figure 6.7. The interaction between the semi-major axis and eccentricity could be attributed to the varying data coverage and density provided by different orbital configurations. A low semi-major axis combined with high eccentricities might allow satellites to gather more precise data points during their periapsis, where they are closer to the asteroid, thus improving the estimates. Conversely, when the semi-major axis is large and the eccentricity is high, the satellite's data collection during the closer passes might be less frequent, reducing the overall accuracy of the gravity-field estimates. Notably, the

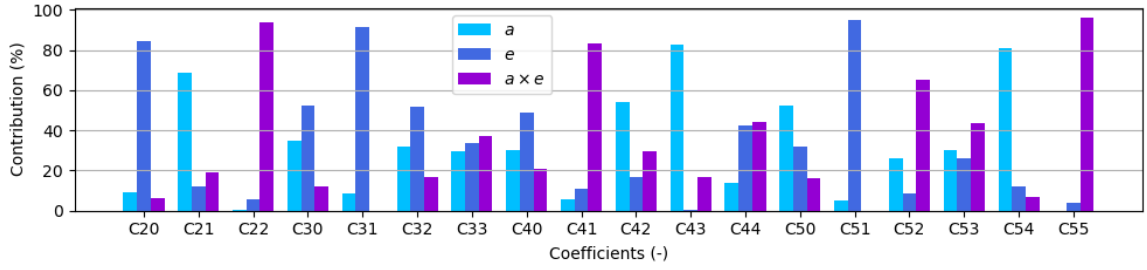

(a) Cosine coefficients

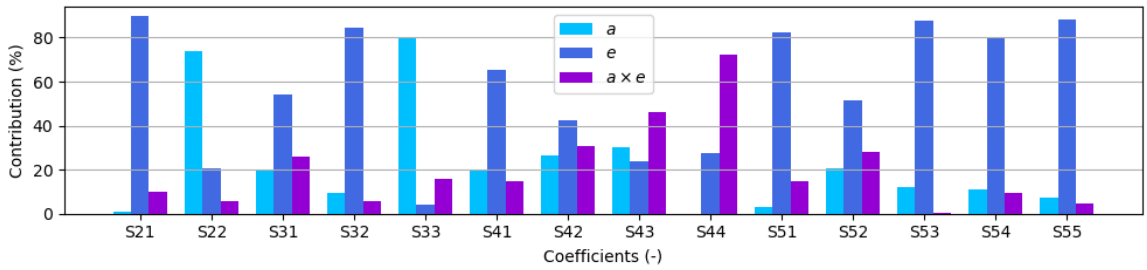

(b) Sine coefficients

Figure 6.6: Results of the ANOVA analysis for Scenario 1 considering the effect of a and e.

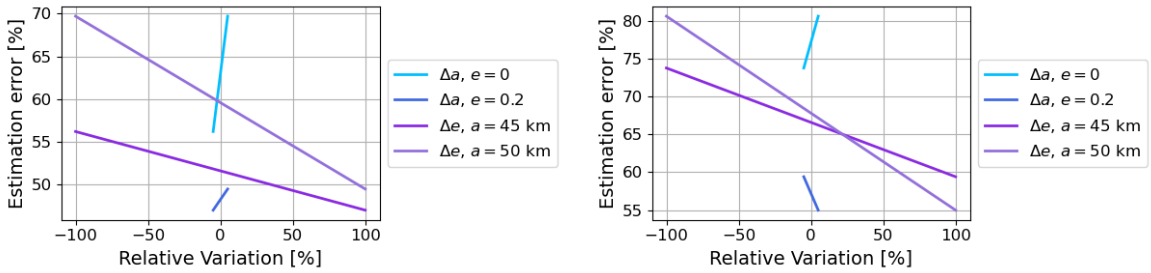

(a) Cosine coefficients **(b)** Sine coefficients

Figure 6.7: Estimation error average percentage for the variation of the decision variables a and e.

sine coefficient estimation shows an opposite trend for high-eccentricity orbits. The gradient indicates a decrease in estimation error with higher altitudes, likely because increased altitude allows for broader coverage and smoother data collection over the asteroid's surface. This broader coverage can compensate for the reduced frequency of close passes, providing a more comprehensive dataset that enhances the estimation of sine coefficients.

Further details on the analysis results obtained by the coefficients estimated can be found in Subsection E.1.3.

6.2.4. Semi-Major Axis and Satellite Distribution along the True Anomaly

The results of the analysis on the effects of the semi-major axis and the distribution of the satellites along the true anomaly are presented in Figure 6.8. Confirming earlier results, this analysis reveals that the semi-major axis has a significant impact on the results, showing improved performance for estimations at lower semi-major axis values. However, it should be noted that several coefficients indicate that the distribution of satellites along the true anomaly is the primary contributing factor to the results.

Figure 6.9 illustrates how the gradient of satellite distribution along the true anomaly is lower compared to that of the semi-major axis. Specifically, it can be observed that increasing the spread of satellites along the true anomaly negatively impacts the overall estimations. This can be attributed to the fact that closer satellites are less restricted by communications constraints. However, an exception is noted for the cosine coefficient estimation at a 30 km semi-major axis. This exception could be due to the specific orbits of the satellites, which may individually lead to better estimations for the cosine coefficients than for the sine coefficients.

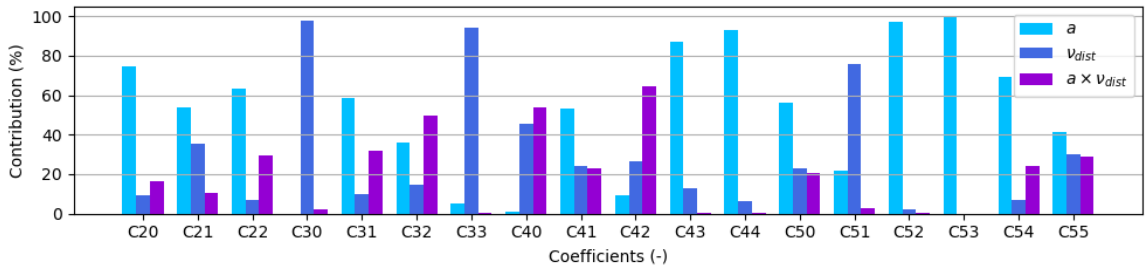

(a) Cosine coefficients

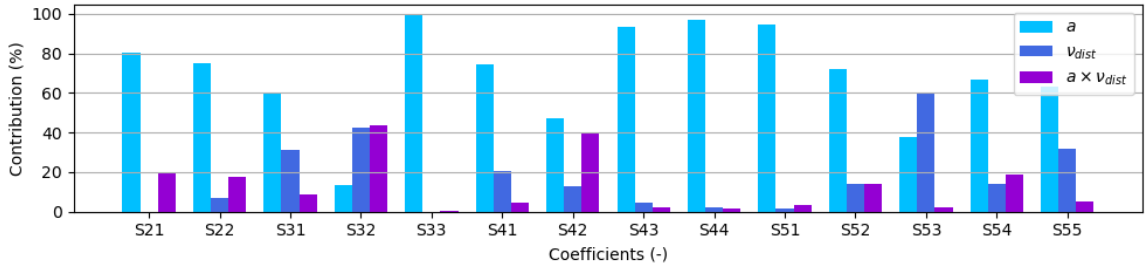

(b) Sine coefficients

Figure 6.8: Results of the ANOVA analysis for Scenario 1 considering the effect of a and ν_{dist}.

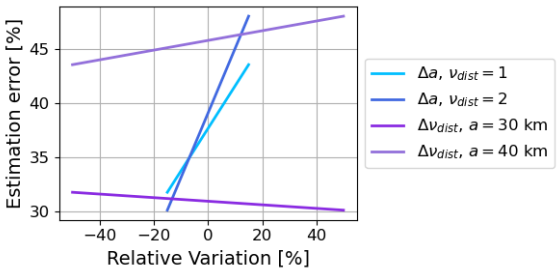

(a) Cosine coefficients

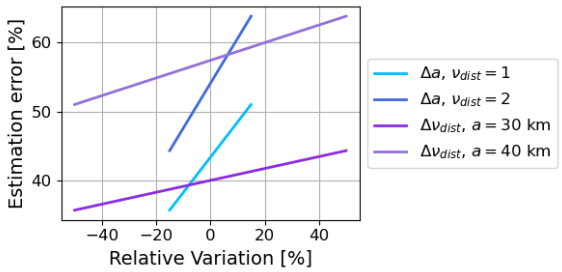

(b) Sine coefficients

Figure 6.9: Results of the ANOVA analysis for Scenario 1 considering the effect of a and ν_{dist}.

Further details on the analysis results obtained by the coefficients estimated can be found in Subsection E.1.4.

6.2.5. Eccentricity and Satellite Distribution along the True Anomaly

The effects of eccentricity and the distribution of satellites along the true anomaly have been analyzed and are presented in Figure 6.10. The analysis shows that the main contribution to the results comes from eccentricity, followed by the linear interaction between eccentricity and satellite distribution. This interaction is further depicted in Figure 6.11 with the gradients of the relative variation of the coefficients.

As shown, increasing the eccentricity leads to a decrease in the estimation error for all cases, as is to be expected. Nevertheless, the variation in the distribution of the satellites along the true anomaly can be seen to be as relevant as the effect of the eccentricity for circular orbits, showing how the coefficient estimates improve considerably when increasing the eccentricity using a larger spreading of the satellites. Conversely, for eccentric orbits, which have more irregular trajectories, the distribution's impact is affected differently by visibility and communication constraints. This results in a variable gradient, showing different effects for cosine and sine estimations.

Further details on the analysis results obtained by the coefficients estimated can be found in Subsection E.1.5.

6.2.6. Inclination and Satellite Distribution along the True Anomaly

The analysis results on the effect of inclination and the distribution of satellites along the true anomaly are presented in Figure 6.12. It can be observed that inclination shows a high linear interaction in

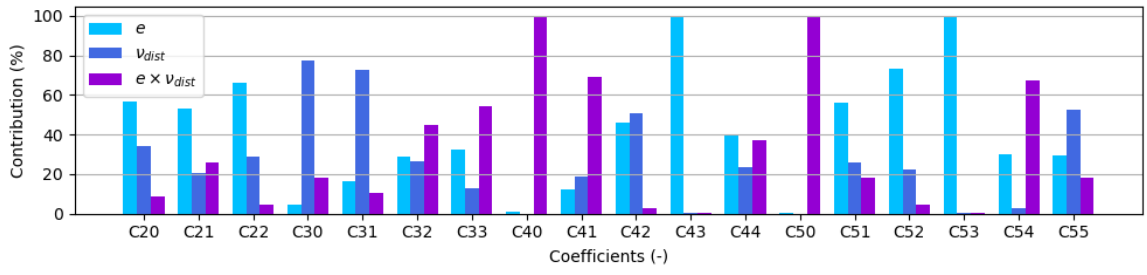

(a) Cosine coefficients

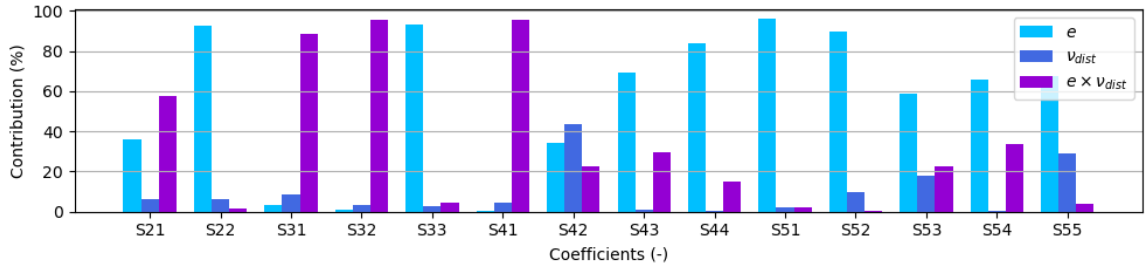

(b) Sine coefficients

Figure 6.10: Results of the ANOVA analysis for Scenario 1 considering the effect of e and ν_{dist}.

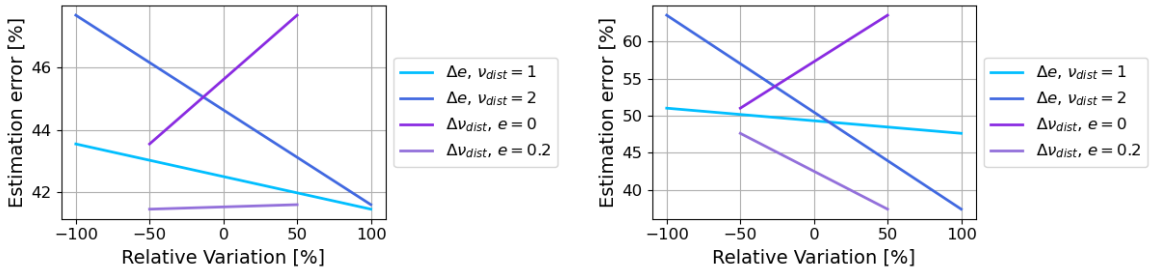

(a) Cosine coefficients **(b)** Sine coefficients

Figure 6.11: Estimation error average percentage for the variation of the decision variables e and ν_{dist}.

some specific coefficients, which can be directly linked to the necessary coverage of certain areas of the asteroid's gravity field. Similarly, the spread of satellites also exhibits a high linear interaction in specific coefficients, indicating that the coverage achieved by such configurations might be either deficient or beneficial for the estimation of these coefficients, demonstrating a significant dependence.

Moreover, a notable level of interaction between inclination and satellite distribution has been observed. Both variables significantly affect orbital coverage and, consequently, interact with each other.

Figure 6.13 further illustrates the effects of these variables on the estimation, depicting a considerable interaction between them. A strong effect is noted when spreading further the coefficients along the true anomaly for a 60° inclination, which improves the estimations. Nevertheless, this effect is less pronounced for a more polar orbit and presents different gradients for sine and cosine coefficients. This can be attributed to the interaction of visibility and communication constraints. Additionally, the effect of inclination is more significant when there is a larger spread of satellites along the true anomaly. This is due to the fact that for polar orbits, the coverage of the asteroid is more complete than for less inclined orbits, therefore, less inclined orbits benefit from having higher satellite distributions that increase their coverage significantly, while the effect on the coverage for polar orbits is much less significant.

Further details on the analysis results obtained by the coefficients estimated can be found in Subsection E.1.6.

6.2.7. Interaction of all the Decision Variables

A comprehensive analysis has been conducted to explore the interactions among all variables within the scenario. In it, the semi-major axis has been varied from 40 km to 50 km, the eccentricity from 0 to 0.2,

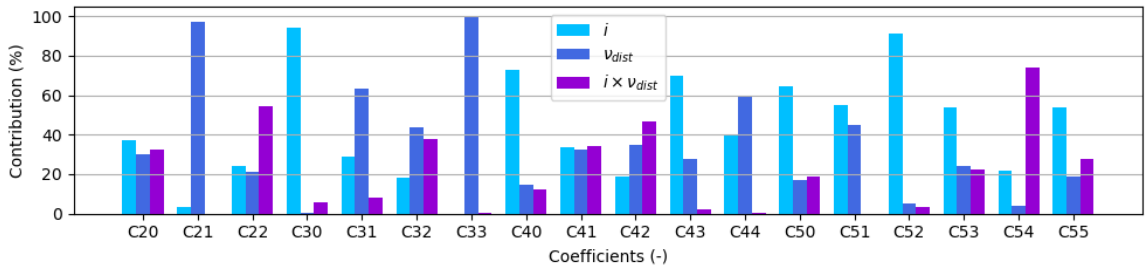

(a) Cosine coefficients

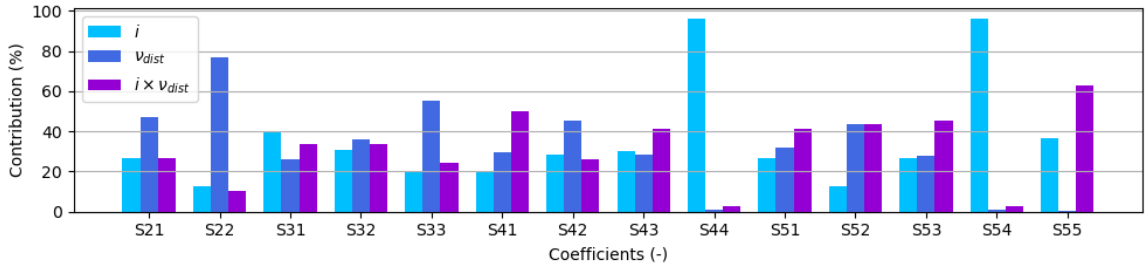

(b) Sine coefficients

Figure 6.12: Results of the ANOVA analysis for Scenario 1 considering the effect of i andν_{dist}.

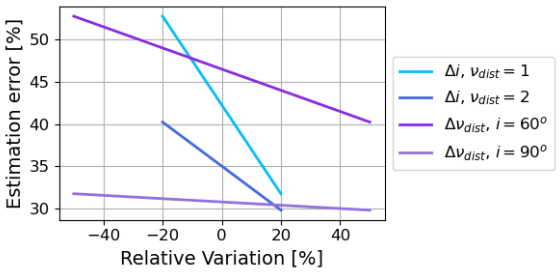

(a) Cosine coefficients

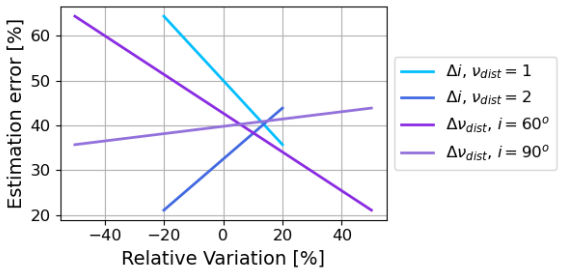

(b) Sine coefficients

Figure 6.13: Estimation error average percentage for the variation of the decision variables e and n.

and the inclination from 30° to 90°.

The individual contributions of the decision variables, detailed in Table 6.3, reveal that the semi-major axis exerts the strongest influence on the estimations. This is expected given the earlier obtained conclusions, which have shown that satellites orbiting closer to the asteroid experience a stronger gravitational influence, leading to more accurate estimations. Following this, eccentricity also plays a significant role. Higher eccentricities enable satellites to orbit nearer to the asteroid at periapsis, thereby amplifying the gravitational impact and improving estimation accuracy.

Additionally, orbital inclination and the distribution of CubeSats along the true anomaly contribute to the estimation process, though to a lesser extent compared to the semi-major axis and eccentricity. Inclination affects the coverage of the asteroid, impacting the accuracy of gravitational field estimations, particularly in specific regions. The distribution of CubeSats along the true anomaly also influences the results, with closer spacing generally improving communication constraints and estimation performance.

The linear interactions between the variables are presented in Table 6.3. The results indicate that the most significant interaction for the cosine coefficients is between the semi-major axis and the satellite distribution. For the sine coefficients, the most notable interaction occurs between the eccentricity and

Table 6.3: Individual contribution of the decision variables for Scenario 1

	a	e	i	ν_{dist}
Cosine coefficients	46.8%	16.3%	1.7%	0.2%
Sine coefficients	30.3%	38.4%	6.2%	1.7%

the inclination. This distinction highlights how different combinations of variables uniquely influence the estimation accuracy of the gravitational field coefficients, underscoring the importance of tailoring orbital parameters to the specific needs of the estimation process.

Table 6.5 presents the contributions of the interactions between three decision variables. Although these contributions are generally minimal, there is a notable impact from the interaction between the semi-major axis, inclination, and satellite distribution. This can be directly linked to the fact that these three parameters are the most determinant of the coverage of the asteroid and therefore have the highest effect on the estimates. The semi-major axis primarily influences the satellite's proximity to the asteroid, with closer orbits enhancing gravitational signal strength. Meanwhile, the inclination and satellite distribution directly shape the satellites' trajectories, influencing the spatial and temporal coverage of the asteroid. This combined effect results in more accurate and comprehensive gravity-field estimations.

6.2.8. Conclusions

From these analyses, several conclusions on the interaction of the variables and how to improve the design of the constellation for a better estimation of the gravity-field coefficients have been derived.

Firstly, the semi-major axis has been confirmed as the most critical factor in the design. The lower the altitude of the satellites, the more intense the gravity field experienced by the satellite, leading to better coefficient estimation by the filter. Therefore, the constellation should be designed with low values of the semi-major axis, ensuring the satellites are close enough to enhance gravitational interactions but far enough to avoid collisions with the asteroid.

Secondly, eccentricity significantly impacts the results. Eccentric orbits allow satellites to approach the asteroid more closely, improving coefficient estimates. However, the eccentricity must be carefully chosen because adding eccentricity to low-altitude satellites can destabilize their trajectories, potentially causing collisions with the asteroid or resulting in escape trajectories if eccentricity is too high.

Thirdly, the inclination of the orbits substantially affects the estimation results. Higher inclination values provide better coverage of the asteroid, improving the estimation of the spherical harmonic coefficients. This effect is more pronounced at lower altitudes, where it influences the cosine and sine coefficients differently due to the varying coverage of the asteroid's latitude and longitude.

Finally, the distribution of the satellites along the true anomaly has a significant effect on the coefficient estimates. Varying the distances between satellites alters how they are influenced by constraints and affects their trajectories. This distribution interacts with all the aforementioned parameters, and no single distribution model works best in all cases. Instead, the optimal distribution depends on the other orbital characteristics considered.

6.3. Scenario 2: Varying Inclinations within the Constellation

This section examines the impact of design parameters on a constellation where satellites are placed in varying orbital inclinations. Building on the previous scenario's foundation, this analysis focuses on the semi-major axis, eccentricity, satellite distribution along the true anomaly, and their distribution across different inclinations.

The effects and interactions of these variables on the spherical harmonic estimates are first explored individually and a comprehensive analysis of variance (ANOVA) is then conducted to assess their combined impact.

Table 6.4: Linear interaction between the decision variables for Scenario 1

	$a \times e$	$a \times i$	$a \times \nu_{dist}$	$e \times i$	$e \times \nu_{dist}$	$i \times \nu_{dist}$
Cosine coefficients	0.6%	2.4%	8.7%	1.0%	1.3%	9.9%
Sine coefficients	0.4%	2.3%	0.3%	10.2%	1.1%	0.1%

Table 6.5: Quadratic contribution of the decision variables for Scenario 1

	$a \times e \times i$	$a \times e \times \nu_{dist}$	$a \times i \times \nu_{dist}$	$e \times i \times \nu_{dist}$
Cosine coefficients	0.7%	1.7%	4.9%	0.2%
Sine coefficients	0.6%	0.0%	5.8%	1.2%

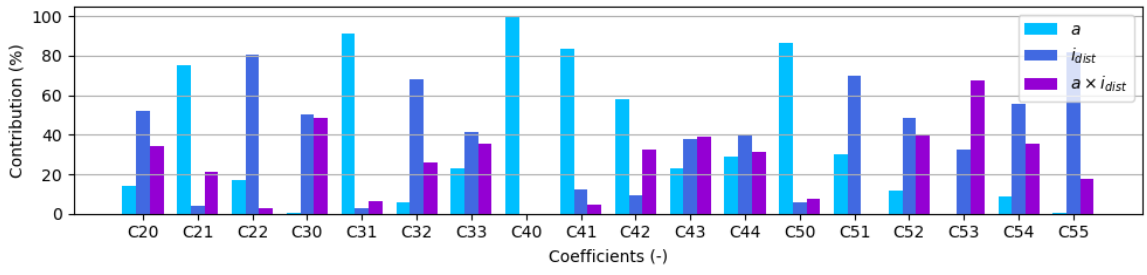

(a) Cosine coefficients

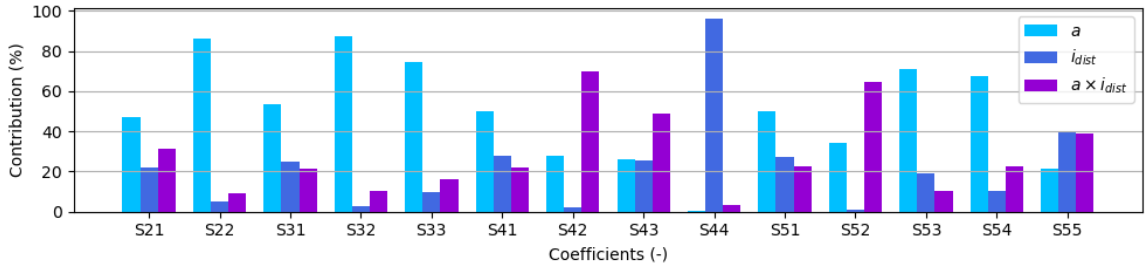

(b) Sine coefficients

Figure 6.14: Results of the ANOVA analysis for Scenario 2 considering the effect of a and i_{dist}.

6.3.1. Semi-Major Axis and Satellite Distribution along the Inclination

The effect of the semi-major axis and the inclination spread of the satellites has been analysed and the results are shown in Figure 6.14. The individual contribution of the semi-major axis is the most significant, confirming earlier results. However, the inclination spread of the satellites also has a considerable impact on some coefficients. This is due to the inclination's role in asteroid coverage; inadequate coverage of specific regions can lead to incorrect coefficient estimations. Additionally, the interaction between these two variables shows lower errors when satellites are at lower altitudes for each inclination distribution.

Furthermore, Figure 6.15 presents a particularly interesting gradient difference in the estimation of cosine and sine coefficients with the inclination distribution used, showing how larger spreads are more beneficial for cosine whereas the inclination does not have a considerable effect for sine coefficients estimations. This can be a result of the way different inclination spreads affect the orbital coverage and data collection patterns over the asteroid's surface. For cosine coefficients, which are often associated with longitudinal variations in the gravity field, a larger inclination spread ensures that satellites cover a wider range of latitudes. This comprehensive latitudinal coverage helps in accurately capturing the variations in the gravity field along different longitudes, leading to improved estimates for cosine coefficients.

In contrast, sine coefficients are typically related to the variations in the gravity field that are more localised or symmetrical about the equator. Since these variations might be less sensitive to changes in inclination, the inclination spread has a negligible effect on the estimation of sine coefficients. The primary factor for sine coefficient estimation remains the altitude, which influences the proximity to the asteroid and the strength of the detected gravitational signal.

Additional analysis has been carried out by testing the effect of setting the constellation satellites with different semi-major axis values. Instead of testing the effect of changing the value from 30 km to 40 km, this analysis compares the difference in the estimates of the coefficient obtained when all the satellites have a 30 km semi-major axis to when each of them is spread along the ranges of 30 km to 40 km. The results are presented in Figure 6.16, and show a different contribution distribution than the previous case, having major contributions of the semi-major axis, the inclination and the interaction of both, depending on the coefficient considered.

Further information can be obtained from Figure 6.17, which shows that spreading the semi-major axis of the satellites is considerably beneficial for the estimates in all cases. This could be attributed to the fact that the filter has estimates that are more affected by the gravity field irregularities at the same time that it has data on more stable trajectories, which might aid the filter in its estimations.

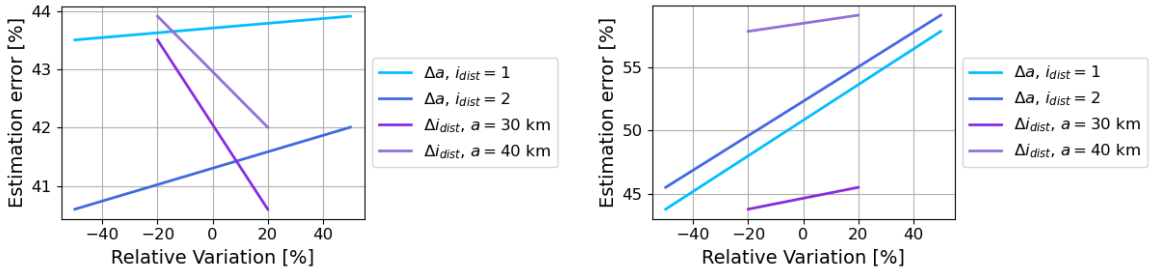

(a) Cosine coefficients **(b)** Sine coefficients

Figure 6.15: Percentage of the average estimation error for the variation of the decision variables a and i_{dist}. It should be noted that $i_{dist} = 1$ represents a satellite spreading along the inclinations of 65° and 90°, and $i_{dist} = 2$ represents a satellite spreading along the inclinations of 40° and 90°.

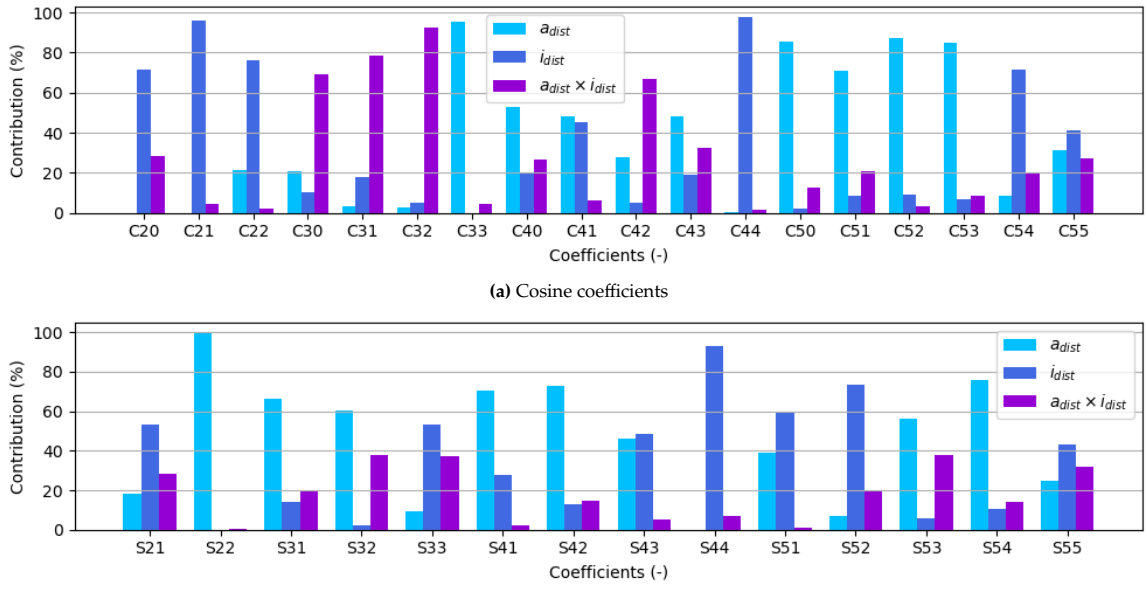

(a) Cosine coefficients

(b) Sine coefficients

Figure 6.16: ANOVA analysis for scenario 2 with satellite spreading along the semi-major axis and the inclination as decision variables

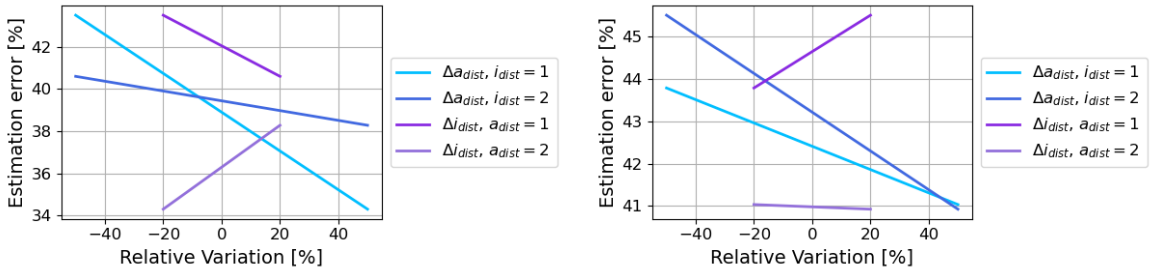

(a) Cosine coefficients **(b)** Sine coefficients

Figure 6.17: Percentage of the average estimation error for the variation of the decision variables a_{dist} and i_{dist}. It should be noted that $i_{dist} = 1$ represents a satellite spreading along the inclinations of 65° and 90°, and $i_{dist} = 2$ represents a satellite spreading along the inclinations of 40° and 90°. Additionally, $a_{dist} = 1$ represents a fixed value of a at 30km, and $a_{dist} = 2$ represents a variation along the range of 30 km to 40 km.

6.3.2. Eccentricity and Satellite Distribution along the Inclination

The analysis of the effects of eccentricity and inclination spread on the constellation's performance is presented in Figure 6.18. As evident, eccentricity has the most significant contribution to the estimation accuracy. Additionally, several coefficients exhibit strong interactions between eccentricity and inclination spread. This interaction arises because eccentricity affects estimations differently

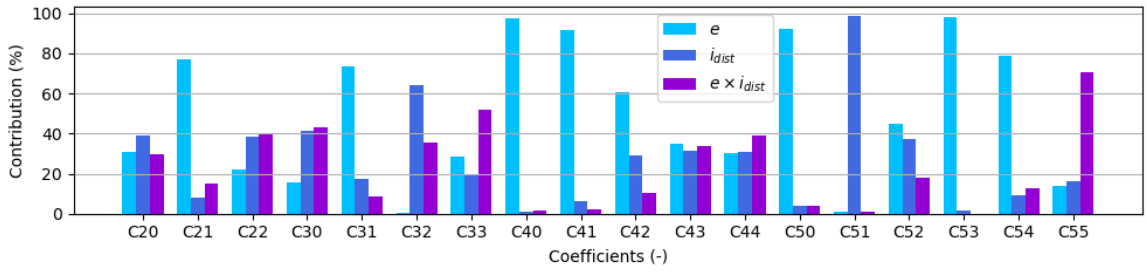

(a) Cosine coefficients

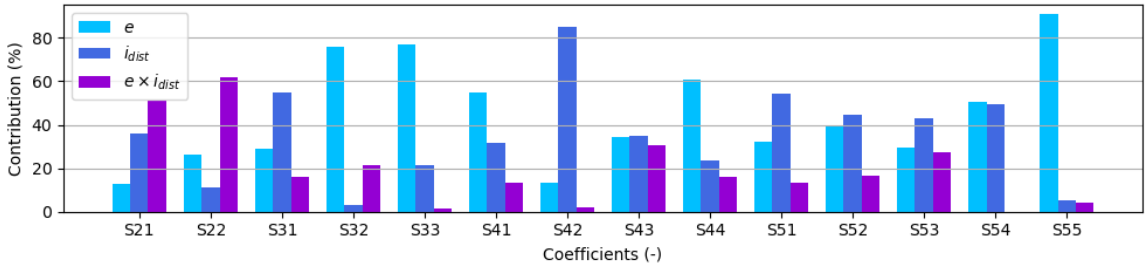

(b) Sine coefficients

Figure 6.18: Results of the ANOVA analysis for Scenario 2 considering the effect of e and i_{dist}.

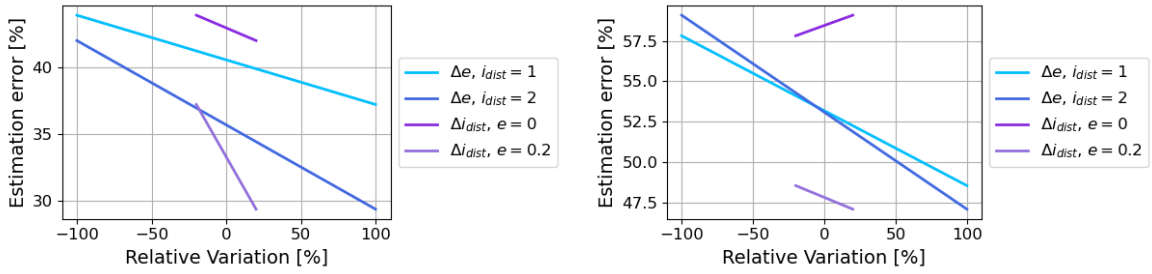

(a) Cosine coefficients **(b)** Sine coefficients

Figure 6.19: Percentage of the average estimation error for the variation of the decision variables e and i_{dist}. It should be noted that $i_{dist} = 1$ represents a satellite spreading along the inclinations of 65° and 90°, and $i_{dist} = 2$ represents a satellite spreading along the inclinations of 40° and 90°.

depending on the orbital inclinations. High eccentricity values lead to closer satellite approaches to the asteroid, and the inclination determines which areas of the asteroid are more closely observed by the satellites.

Figure 6.19 depicts the gradients of the estimation error resulting from the relative variation of the variables. As expected, higher eccentricity values result in lower estimation errors. However, the impact of the satellite distribution along various inclinations is highly dependent on the eccentricity, with different gradients observed for cosine and sine coefficient estimates. This variation underscores the complex interplay between orbital eccentricity and inclination spread in achieving accurate gravitational field estimations.

6.3.3. True Anomaly and Satellite Distribution along the Inclination

This section presents the analysis results concerning the true anomaly of the satellites and their distribution along different orbital inclinations. Two scenarios were evaluated: firstly, comparing satellites placed exclusively on a 90° inclination orbit versus those spread across inclinations ranging from 60° to 110°. Secondly, examining the true anomaly spread of satellites from 0° to 180° versus a full 360° range. The findings are detailed in Figure 6.20.

The impact of true anomaly and inclination spread varies across different coefficients, reflecting their significant influence on asteroid coverage and subsequent estimation accuracy.

Further analysis has been conducted on the effects of these two variables, considering an inclination spread between 65° and 90°, and an increased spread between the values of 40° and 90°. The true

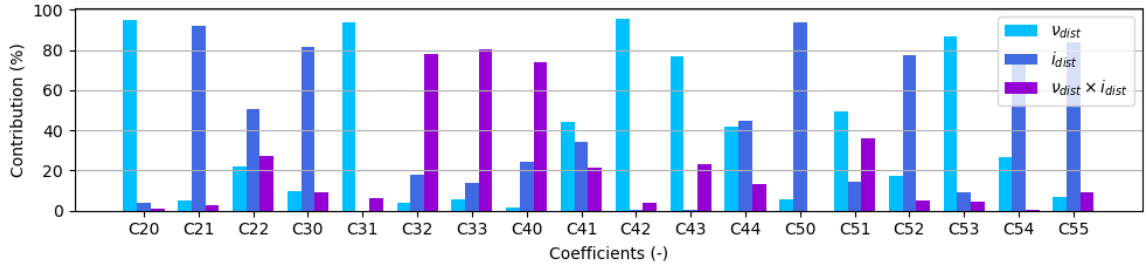

(a) Cosine coefficients

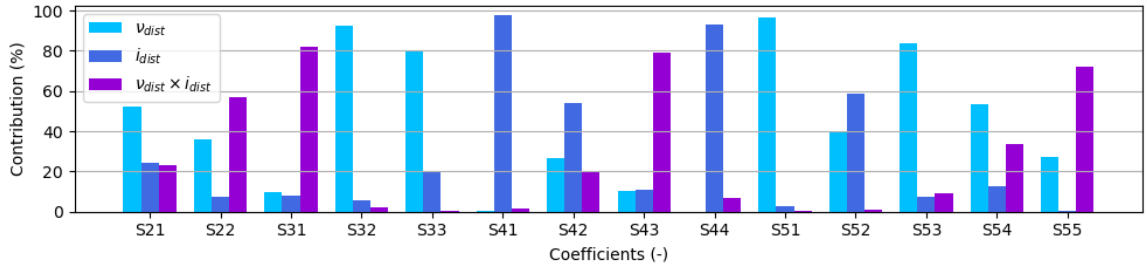

(b) Sine coefficients

Figure 6.20: Results of the ANOVA analysis for Scenario 2 considering the effect of ν_{dist} and i_{dist}.

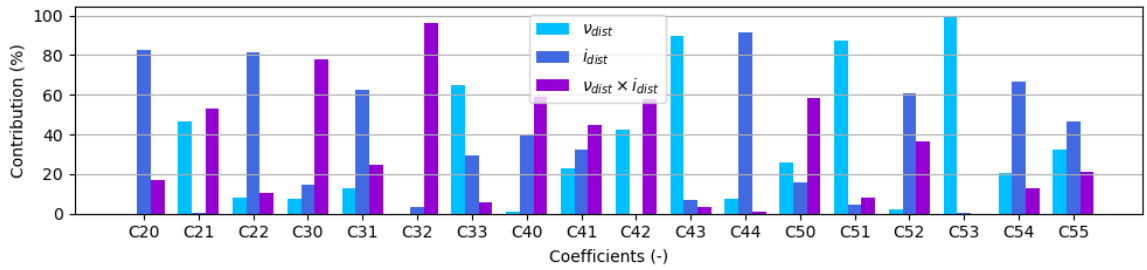

(a) Cosine coefficients

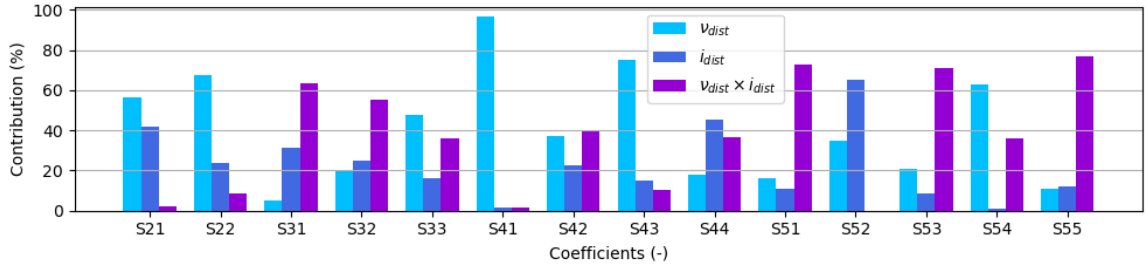

(b) Sine coefficients

Figure 6.21: ANOVA analysis for scenario 2 with an inclination and satellite spreading along the true anomaly as decision variables

anomaly values spreading remains the same as the previously analysed. The results obtained are presented in Figure 6.21, revealing similar overall contributions of both variables but showcasing differential effects on specific coefficients. This confirms the direct influence of true anomaly and inclination spread on individual coefficient estimations.

The gradient responses of the relative variations of these variables are presented in Figure 6.22. These plots illustrate several effects: increasing satellite distribution along the true anomaly positively or negatively affects estimation depending on satellite inclinations, with variable impacts on sine and cosine coefficients. Notably, increasing inclination distribution is detrimental to cosine coefficient estimation but beneficial to sine coefficients, particularly enhancing estimations at lower inclinations due to their favourable impact on sine coefficient calculations.

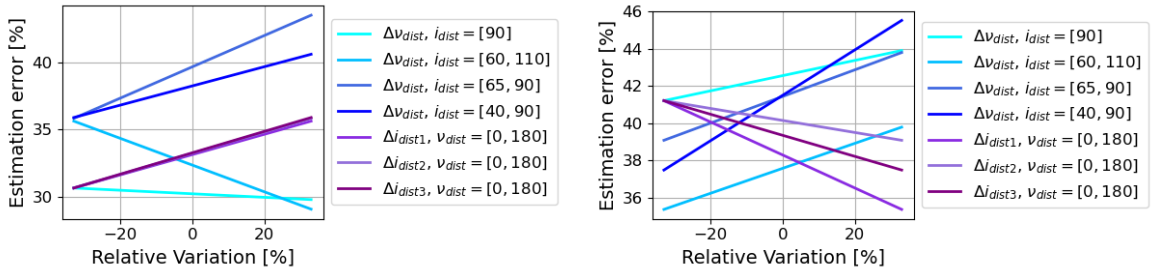

(a) Cosine coefficients

(b) Sine coefficients

Figure 6.22: Percentage of the average estimation error for the variation of the decision variables ν_{dist} and i_{dist}. $\Delta\nu_{dist}$ represents the effect of having the satellites spread from [0°, 180°] to [0°, 360°]. Δi_{dist1} represents the effect of having all the satellites orbit with a 90° i to dispersing them from [60°, 110°], Δi_{dist2} the effect of having the satellites orbit with a 90° i to dispersing them from [65°, 90°], and Δi_{dist1} represents the effect of having all the satellites orbit with a 90° i to dispersing them from [40°, 90°].

6.3.4. Interaction of all the Decision Variables

This section explores the interaction between the decision variables when employing differently inclined orbits for each satellite.

The individual contribution of the semi-major axis, the eccentricity, the true anomaly spread and the inclination spread are presented in Table 6.6. As expected and confirming earlier results, the semi-major axis exhibits the highest contribution, followed by eccentricity. The true anomaly and inclination spread show secondary contributions, varying based on the specific cosine or sine coefficients being evaluated.

The linear interactions between the decision variables are depicted in Table 6.7, where it can be seen that the main interaction is that between the semi-major axis and the inclinations for the sine coefficients estimation. This can be directly linked to having better coverage of particular regions of the gravity field. The lower the altitude is, the better the irregularities of the gravity field that can be detected, and the better suited the inclination is for the coverage, the more significance that some gravity-field effects have on the trajectory of the satellites and therefore the better the estimates can be produced.

Table 6.8 depicts the contributions of the interactions between three decision variables, which have very low effects on the estimates. Nevertheless, for the sine coefficients, the interaction between the semi-major axis, the eccentricity and the inclination has been found to be relevant. This finding underscores the significant impact of inclination on sine coefficient estimation, with the semi-major axis further amplifying this effect. The inclusion of eccentricity enhances these interactions, highlighting its considerable influence on the estimation results.

6.3.5. Conclusions

From these analyses, several conclusions have been derived on the interaction of the variables and how to improve the design of the constellation for a better estimation of the gravity-field coefficients.

Firstly, the semi-major axis consistently demonstrates a beneficial effect regardless of the inclination

Table 6.6: Individual contribution of the decision variables for Scenario 2

	a	e	ν_{dist}	i_{dist}
Cosine coefficients	50.1%	31.5%	0.5%	2.7%
Sine coefficients	35.0%	32.3%	8.4%	1.8%

Table 6.7: Linear interaction between the decision variables for Scenario 2

	$a \times e$	$a \times \nu_{dist}$	$a \times i_{dist}$	$e \times \nu_{dist}$	$e \times i_{dist}$	$\nu \times i_{dist}$
Cosine coefficients	1.2%	2.4%	1.6%	3.1%	0.4%	1.8%
Sine coefficients	0.8%	0.0%	7.5%	2.4%	0.5%	4.4%

Table 6.8: Quadratic contribution of the decision variables for Scenario 2

	$a \times e \times \nu_{dist}$	$a \times e \times i_{dist}$	$a \times \nu_{dist} \times i_{dist}$	$e \times \nu_{dist} \times i_{dist}$
Cosine coefficients	2.5%	0.0%	1.6%	0.7%
Sine coefficients	0.0%	5.9%	0.4%	0.4%

distribution used. Lower altitudes prove advantageous for constellation design, enhancing the filter's performance. Moreover, distributing satellites across orbits with slight variations in semi-major axis further improves estimation accuracy.

Secondly, the effect of the eccentricity of the orbits has been shown to be significant, the larger the eccentricity, the closer the satellites get to the asteroid and the better the estimations are, as long as the semi-major axis is large enough and the eccentricity small enough to ensure a stable orbit. Moreover, it has been shown to have a relevant interaction with the inclination.

Thirdly, the satellite distribution along the true anomaly exhibits considerable effects on estimations, with outcomes varying based on constellation inclinations and the coefficients being estimated (sine or cosine).

Fourthly, the distribution of the satellites along different inclinations has been shown to have a considerable effect on the estimation error. In particular, the cosine estimates have been shown to benefit from a distribution of polar orbits, whereas the sine-coefficient estimates improve when distributing the satellites along a wider range of inclinations having a larger equatorial coverage.

6.4. Scenario 3: Varying Satellite Number and Orbital Distributions

This section aims to study the effect that the orbital distribution and number of satellites have on the estimations of the gravity field.

6.4.1. Number of satellites and orbital distribution

The influence of the number of satellites in the constellation and the variety of orbits used on gravity-field estimates is detailed in Figure 6.23. It is evident that both factors contribute significantly, albeit with varying degrees depending on the specific coefficient under consideration. Notably, the number of CubeSats appears to exert a predominant influence across several coefficients.

Figure 6.24 summarises the effects of these decision variables. The gradients highlight distinct impacts on cosine and sine coefficients. It should be noted that the gradients presented in the plots show considerably different tendencies than in the other cases, having two different gradients for the positive and negative variations. This is due to the fact that the FD has been conducted for three levels using different sets of orbital distributions or the number of satellites. These parameters have a considerable effect on the constellation and therefore on the estimates, thus not presenting a constant trend but a varying one instead.

The plots show that sine coefficients benefit notably from an increased number of satellites and a greater variety of orbits, which enhances their estimation accuracy. This improvement can be attributed to the favourable coverage provided by orbits with lower inclination values for sine coefficient estimation. Conversely, cosine coefficient estimates show a different response. The influence of both the number of orbits and satellites varies, suggesting that certain combinations may not optimise their estimation. This variability could stem from the preference of cosine coefficients for polar orbits, where specific orbital configurations may not align optimally with the asteroid's gravitational characteristics.

6.4.2. Conclusions

Optimising the number of satellites and their orbital distributions is crucial for improving gravity-field coefficient estimations. Sine coefficients benefit from broader orbital diversity and increased satellite counts, whereas cosine coefficients require careful consideration to ensure effective coverage and data collection across various orbital configurations.

6.5. Summary

1. An ANOVA on a constellation of satellites with fixed orbital parameters, spread out along the true anomaly, has revealed the following insights:

   (a) Satellites with lower values of semi-major axis yield improved estimates. Closer orbits around the asteroid amplify gravitational forces, enhancing the accuracy of estimation models.
   (b) Polar orbits generally yield superior estimates due to their comprehensive coverage of the asteroid's surface.
   (c) Eccentric orbits also contribute to better estimates by enabling satellites to reach lower altitudes, crucial for detailed gravity measurements. Notably, there exists a significant

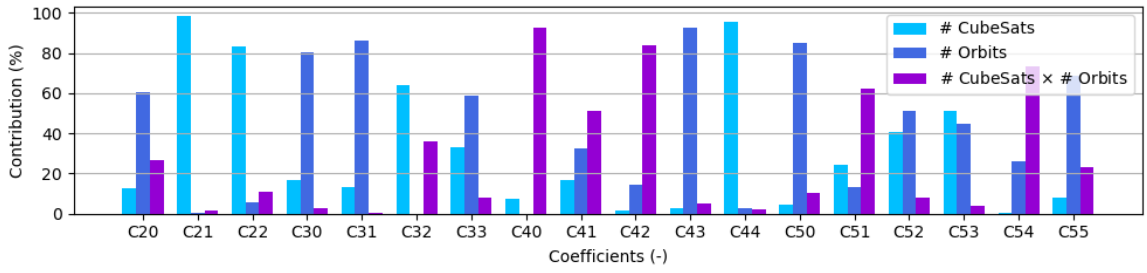

(a) Cosine coefficients

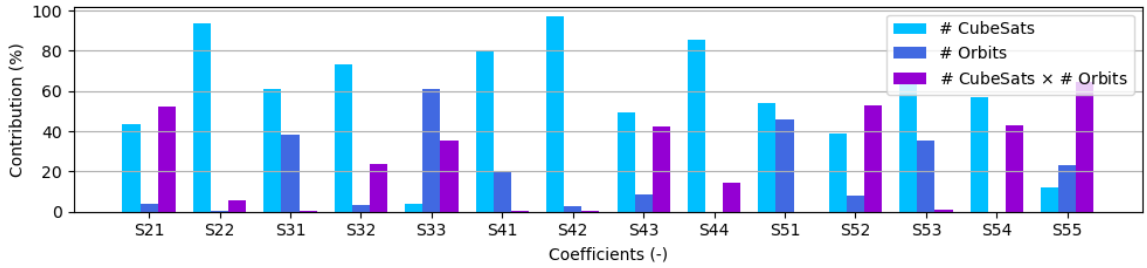

(b) Sine coefficients

Figure 6.23: Results of the ANOVA analysis for Scenario 1 considering the effect of n_{sats} and n_{orb}.

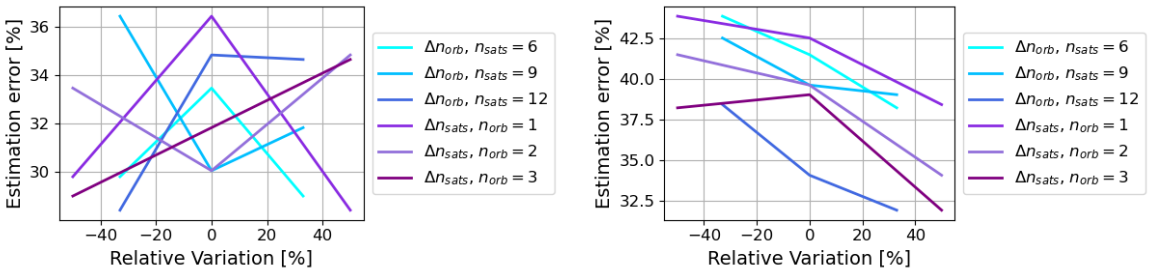

(a) Cosine coefficients **(b)** Sine coefficients

Figure 6.24: Estimation error average percentage for the variation of the decision variables n_{sats} and n_{orb}.

interaction between eccentricity and semi-major axis; stable low-altitude orbits typically require minimal eccentricity.

(d) The distribution of satellites along the true anomaly significantly influences estimation accuracy by affecting the spatial coverage provided by each satellite.

2. An ANOVA on a constellation of satellites with fixed orbital parameters, spread out along various inclinations, has revealed the following insights:

   (a) The inclination spread affects the coverage across the asteroid, thus considerably impacting the SH coefficient estimates. Furthermore, the inclination spread has a clear interaction with the semi-major axis of the satellites, having lower errors the lower the altitude of the satellites.
   (b) The spreading of the satellites along the true anomaly has a considerable impact on the estimates, affecting the sine and cosine estimates differently.
   (c) Optimal inclination distribution crucial: polar orbits enhance cosine coefficient estimation, while broader inclinations improve sine coefficient estimates.

3. An ANOVA on a constellation of satellites with a variable number of CubeSats and different orbital distributions, has revealed the following insights:

   (a) Analysis has revealed significant contributions from both the number of satellites and the diversity of orbital configurations. The number of CubeSats particularly dominates in influencing estimation outcomes, although the impact varies across different coefficients.

(b) Distinct gradients for cosine and sine coefficients. Sine coefficient estimations benefit notably from increased satellite numbers and a greater diversity of orbital inclinations. Conversely, cosine coefficient estimates show nuanced responses where optimal performance depends on specific combinations of satellite counts and orbital configurations.

4. The following chapter presents a design synthesis of the system, applying the results from the analysis to design a constellation for an efficient estimation of the gravity field.

7

Design Synthesis

This chapter contains the synthesis of the design choices and methodologies developed throughout the study to estimate the gravity field of irregular asteroids using a constellation of CubeSats. This analysis culminates in the identification of an "ideal" constellation configuration, optimising factors, such as satellite distribution, orbit parameters, and communication strategies in Section 7.1.

Additionally, the limitations of the filter are critically examined in Section 7.2. Recognising these constraints, innovative adaptations aimed at enhancing filter performance and mitigating identified shortcomings are explored. Through rigorous testing and analysis, the resulting improvements are presented, offering a comprehensive overview of their impact on the accuracy and reliability of the gravity-field estimations.

Furthermore, it should be noted that Appendix F contains additional tests and configurations used in this chapter, acting as support for the presented analysis.

7.1. Design of the constellation

The previous chapter has shown how the design of the constellation is a determinant of the accuracy of the SH coefficient estimates of the filter. This section presents a new constellation design that considers the lessons learnt from the analysis of variables and their interaction aiming to improve the estimates that the system is capable of achieving.

The following considerations have been made for the final design:

1. The number of satellites in the constellation is determinant in the results. A larger number of satellites provides more time instants where two or more satellites are available and therefore, larger time instants where measurement data can be used. This results in the filter having a larger amount of data to produce the coefficient estimates, and thus, being capable of producing better estimates. However, it was observed that if the satellites are not placed correctly, an increase in their number is not beneficial for the estimations. With these considerations, the number of satellites has been set to 12.
2. The semi-major axis of the constellation's satellites has been shown to have the largest effect on the estimates. Lower values have a positive effect on the estimates, nevertheless, a dispersion of the satellites along a range of semi-major axis values has been shown to provide better estimates. Therefore, the satellites have been placed in orbits with values ranging from 30 to 36 km.
3. The eccentricity has been shown to have a positive effect on the estimates. Nevertheless, the interaction between the semi-major axis and the eccentricity is very large, and for low altitudes, eccentric orbits lead to high instability that can result in crashes or escape trajectories. To avoid these undesired effects and ensure stable orbits, this design will use circular orbits.
4. The spreading of the satellites along the true anomaly has been shown to be a highly defining factor of the trajectory, and therefore a correct distribution of the satellites is key. While the most adequate values for trajectories could be determined and studied for the scenario at hand with Eros 433 asteroid, this would be assuming that the data on the asteroid gravity field and shape is already known before starting the mission. Therefore, only a basic definition of the true anomaly

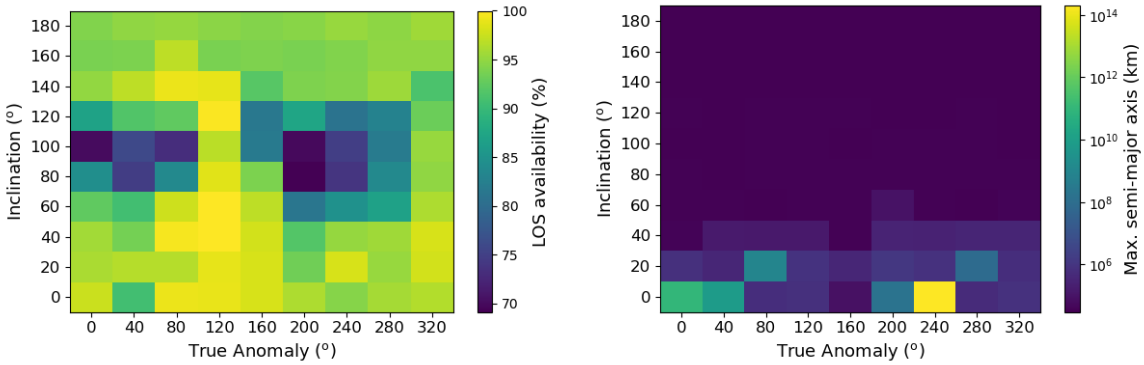

(a) Availability percentage of satellites fulfilling the communications constraints

(b) Maximum distance from the satellite to the centre of the asteroid for different orbital parameters of the mothership.

Figure 7.1: Grid search of the best orbital parameters for the mothership placement in a range of i and ν with a sample constellation of five CubeSats spread out with a=30 km.

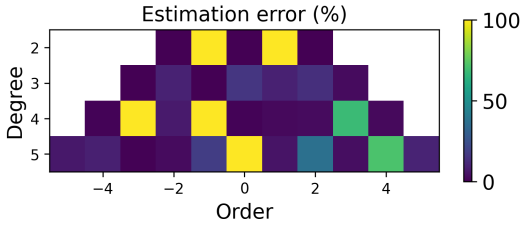

Figure 7.2: Estimates obtained for a one-second time step for a one million second propagation.

parameters is considered in terms of the spreading. The constellation will be designed with its satellites closely spread, with a 30° separation from one another.

In addition, further considerations have been made in the design to improve the estimates of the coefficients. Since communications restrictions have a detrimental effect on the estimates, a study of the orbital parameters of the mothership has been carried out to determine the best trajectory to minimise the restrictions. This has been done by defining a reference constellation with the aforementioned considerations consisting of five CubeSatellites in polar orbits evenly spread along the true anomaly. The line-of-sight availability has been evaluated for this constellation for a mothership in a number of orbits considering a range of inclination and true anomaly values to determine the best-suited orbit to minimise the constraint effect. The results of this analysis are presented in Figure 7.1, where the percentage of visibility of the mothership with the satellites of the constellation is shown using a semi-major axis of 30 km. Note that further results can be found in Section F.1. As can be seen, there are optimal spots in the grid for the orbit placement. In addition, it should be noted that some orbits can be unsuitable if their trajectory escapes the asteroid, which can happen for lower inclination values due to the irregularities of the gravity field. This effect is depicted in Figure 7.1b, which shows the maximum distance from the centre of the asteroid to the mothership. These results confirm the expected and indicate that while the satellite is placed with an orbital inclination of 40° or higher, the satellite will remain in orbit.

With all the previous considerations, the mothership has been placed in an orbit with a 60° inclination and a true anomaly of 120°. Since this trajectory is not ideal for the estimation of the gravity-field coefficients, to ensure that this does not have a detrimental impact on the estimates, the mothership will not use its own measurements for the gravity-field estimation but only those of the CubeSats.

Using the new constellation design, the orbital parameters of which can be found in Table F.1, the filter has been able to provide accurate estimates for most of the coefficients, as depicted in Figure 7.2. The same estimation has been carried out considering velocity parameters as well. Nevertheless, no considerable improvement has resulted from this additional consideration.

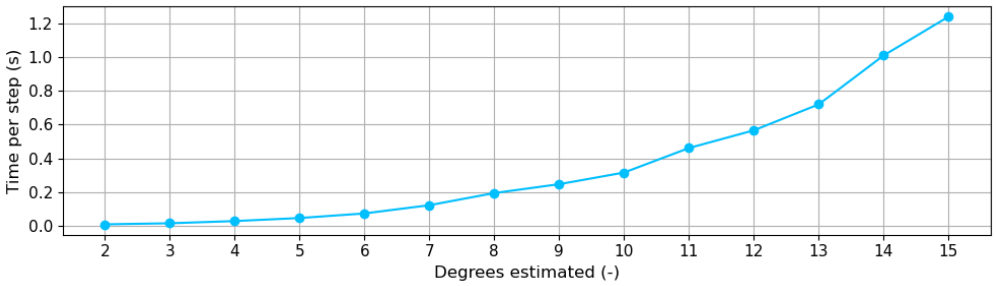

Figure 7.3: Average computation time per time step of the filter for a range of degrees.

7.2. Design of the filter

Although the simulation scenario has been able to estimate most of the gravity-field coefficients accurately, this design has shown two main limitations:

- This filter requires a considerable propagation time of the constellation to produce accurate estimates. Furthermore, it performs better the larger the measurement blocks are and the lower the number of resets experienced by the filter.
- It is very computationally demanding. While the filter is capable of estimating the spherical harmonic coefficients up to fifth degree and order in a reasonable time, the system has been incapable of producing adequate estimates up to degree and order nine in a period smaller than 24 hours. Note that the propagation is conducted for a total of two million seconds with a two-second time step, thus requiring approximately one million state computations. Figure 7.3 depicts how the time step grows exponentially as the degree of the gravity field increases. With this data it can be inferred that the estimation of the states using 15 degrees would require approximately 333 hours, and using nine degrees would require approximately 60 hours, whereas the use of five degrees results in much smaller computational times, that can be computed in approximately 15 h.

To improve the filter estimates and counter the limitations, several considerations have been made to improve the design. These are presented in the following sections.

7.2.1. Step-based approach

A methodical approach to improve the filter estimates by incrementally addressing different gravity-field coefficients is explored in this section. This strategy aims to optimise the estimation process and manage computational resources effectively. Two specific methodologies are considered: estimating coefficients by degrees and partitioning the CubeSat constellation for cosine and sine estimates. Each approach is analysed for its potential benefits and limitations based on experimental results.

By Degrees

In this approach, the system design focuses on sequential estimation to enhance filter performance. Initially, the filter estimates the second-degree coefficients, which are then fixed in the model. This process continues recursively for higher degrees, theoretically reducing computation time and allowing for a better representation of the gravity field.

However, testing revealed a decrease in filter performance, resulting in higher error estimates. The filter struggles to estimate higher-degree effects using a restricted low-degree spherical harmonics model, leading to inaccuracies. Specifically, while the filter accurately estimates the C20, C22, and S22 coefficients initially, it fails with third-degree coefficients. The attempt to model high-order coefficients up to the 15^{th} degree with only a third-degree model results in accumulated errors, highlighting the inadequacy of this design.

By Cosine and Sine Estimates

This approach involves splitting the constellation into two groups, each optimised for either cosine or sine coefficient estimates. However, this method produced inaccurate results. Each constellation's focus on either cosine or sine coefficients increased the difficulty of estimating the opposite set, leading to significant errors.

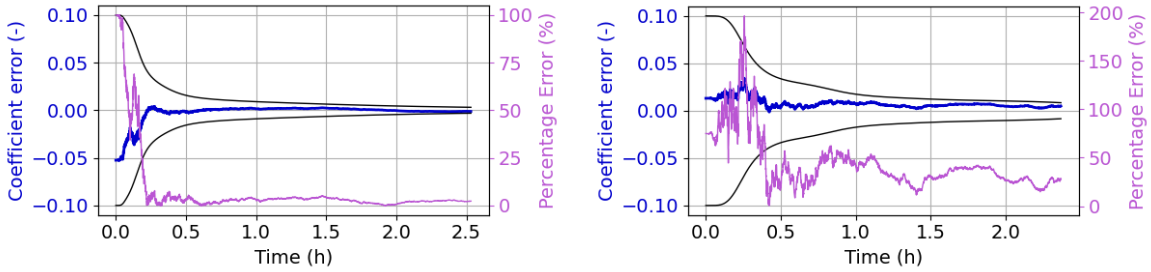

(a) C20 **(b)** C42

Figure 7.4: Converging coefficients estimation.

Initial designs that targeted only sine or cosine coefficients resulted in erroneous values, as the filter could not accurately describe gravity field effects solely on the basis of one set of coefficients. This design has been deemed inadequate. For better outcomes, this approach could be used for fine-tuning results obtained from a comprehensive constellation model, and thus it has not been pursued further.

7.2.2. Tuning of the filter

This section delves into the methodologies aimed at refining the filter's performance to enhance accuracy and efficiency in estimating the gravity-field coefficients.

Covariance Matrices Tuning

An approach to improve filter performance involves optimising the covariance (**P**) and process noise (**Q**) matrices. Observations have revealed a grid-like distribution in the norm of the gravity-field coefficients across the asteroid. By tailoring the covariance and noise matrices to better reflect this distribution, the filter can more accurately model the gravity field dynamics. Details on matrix tuning can be found in Appendix F (Subsection F.2.1), which presents a correlation of the covariance matrix of the filter, and details the tuned initial **P** and **Q** matrices. Moreover, an example of the successful convergence of two given coefficient estimates of the system is depicted in Figure 7.4. These figures highlight the convergence of the estimation from the initial set values of 0 to their correct values. The plots show the percentage error in the right y-axis to better represent the accuracy of their estimations. Note that Figure 7.4a can produce an estimate with an error lower than 5% while, on the other hand, Figure 7.4b shows convergence with a larger percentage error of 30%.

Although this adjustment has shown a significant improvement in estimation accuracy, it does not alleviate the computational burden on the system.

Additionally, the correlation of the covariance matrix after the filter has finalised the estimation of the first measurement block has been analysed in an effort to detect dependencies. The results, which are presented in Figure F.3 have shown only a direct correlation between the position and the velocity coordinates, and the coefficients depict a chaotic distribution of correlations, from which no tendencies can be identified and thus no further improvement can be made on the covariance matrix definition.

Tuning of the filter re-start

The challenge of filter re-starts due to satellite communication and visibility constraints introduces variability in measurements, impacting filter performance and accuracy. To address this challenge, a new design has been proposed.

The main issue with re-starting the filter is that it leads to additional variations in the estimations at the beginning of each re-start, which have a detrimental effect on the estimates. To deal with this issue a new design has been considered where each measurement block is restarted completely with an adapted covariance matrix using the grid-like distribution of the covariance instead of restarting the filter the last computed covariance matrix, this way reducing the initial variations in the estimates. Furthermore, instead of restarting the filter with the last estimated gravity-field coefficients in all cases, the filter now checks for convergence and sets to a null value the coefficients that diverged in the estimation.

Furthermore, to reduce computational load, this design fixes coefficients that have converged at each measurement block. In this manner, the computational load of the filter is reduced considerably, and higher orders can be estimated. This has been shown to provide excellent results in reducing the computational load, providing much faster estimates for the coefficients. This is due to the fact that

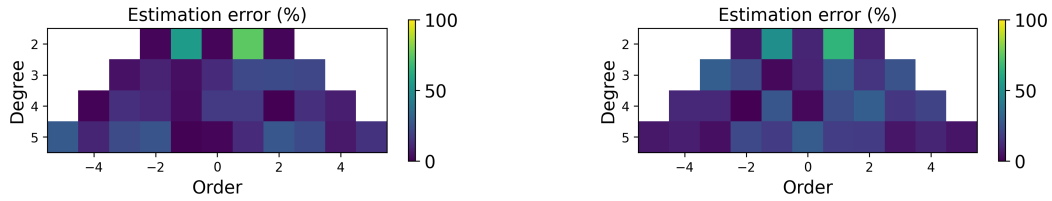

(a) $e_r = 0.1$ m **(b)** $e_r = 10$ m

Figure 7.5: Coefficients estimation up to degree and order five.

there are fewer coefficients to be estimated at each step, the smaller the state vector, and as a result the smaller the sigma points that the filter propagates, which has a very considerable effect on the computational time and thus enhances the filter's efficiency.

7.2.3. Approach combination

While the new design presented with the filter re-start reduces the limitations of the system, it remains insufficient when higher degrees and orders are to be estimated, which leads to considerably computationally expensive estimates that require very large memory. This is due to the fact that the larger the degree, the larger the state vector and therefore the larger the sigma points used in the filter. Additionally, the larger the degree used in the gravity-field model computation, the more computationally expensive each sigma point propagation is, thus resulting in very high computational loads.

To address this challenge, coefficient estimation must be phased. Two different approaches are considered:

Diagonal by diagonal: This approach has been considered due to the grid-like nature of the coefficients norm. The filter has been tested by considering only the coefficients of the outer diagonals up to degree and order nine at the start, and as the number of coefficients to be estimated is reduced, the coefficients from the internal diagonals are included. This approach has not provided the best estimates. This is due to the fact that by modelling the system at the beginning with the effects of the larger order coefficients, the gravity field is not represented with an even distribution and the filter has a hard time producing accurate estimates. Furthermore, this design requires the filter to use the gravity-field model of the highest degree even when most of the coefficients are set to zero, increasing considerably the computational load with no benefits on the estimates.

Degree by degree: This approach has been considered by initially estimating the coefficients of second-degree and adding more degrees as the number of coefficients to be estimated decreases. This filter produces inaccurate results when estimating the initial lower degrees. This is due to the fact that the filter intends to estimate the effects of the gravity field with only a second-order model, which is insufficient for accurate results.

7.2.4. Chosen filter design

Ultimately, an adaptation of the "degree-by-degree" method has been chosen, where the filter starts with a fourth-degree gravity-field model, ensuring robust estimation of system dynamics. As the coefficients converge and the state vector reduces, higher degrees are progressively incorporated until all the coefficients are accurately estimated.

Figure 7.5 illustrates the improved filter performance for an estimation of the first five degrees and orders, demonstrating accuracy within position estimation errors ranging from 10 cm to 10 m. This design is adopted as the final filter design due to its balanced trade-off between computational efficiency and precise estimation. Moreover, the filter design has proven to be capable of adequately estimating larger order coefficients with the computational constraints of the research.

Note that the behaviour of the filter has been studied and it has been verified that the constellation parameters have the same effect on the new filter design that they did in the previous one. An example of this can be found in Subsection F.2.2.

7.3. Limitations of the filter

This section aims to explore the limitations of the system with the improved filter design.

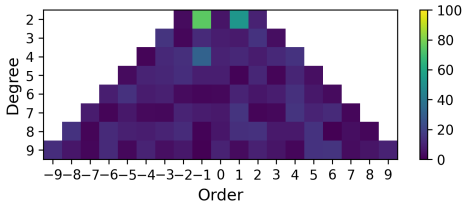

Figure 7.6: Coefficient estimates error percentage for null errors.

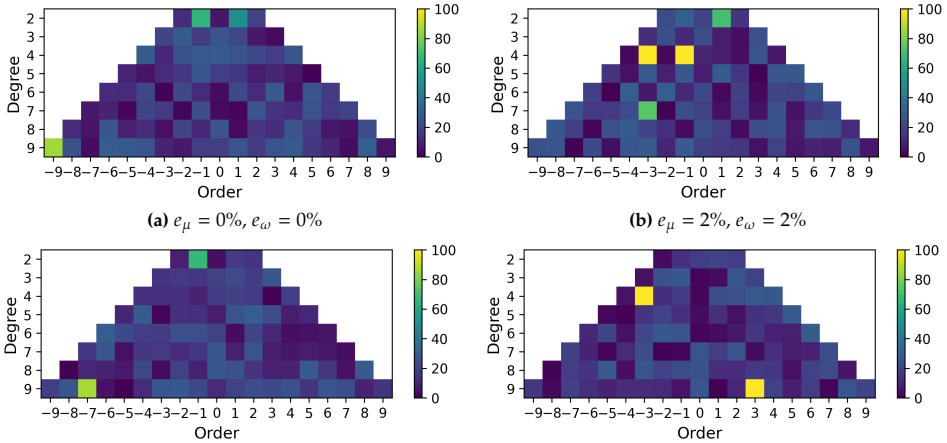

(a) $e_\mu = 0\%, e_\omega = 0\%$ **(b)** $e_\mu = 2\%, e_\omega = 2\%$

(c) $e_\mu = 2\%, e_\omega = 0\%$ **(d)** $e_\mu = 0\%, e_\omega = 2\%$

Figure 7.7: Coefficients estimation for 1 m measurement errors for 2 million seconds for a 30% error threshold.

7.3.1. Filter performance with estimation errors

As has been defined, the system assumes that the gravitational parameter of the asteroid and the rotation rate of the asteroid around its z-axis are initially estimated in the mission and the estimates are used in the gravity-field model of the designed filter.

The system has initially been tested with an ideal-case scenario, where no position measurement errors are considered nor any initial-state errors are present in the model of the filter, and with the true value of the gravitational parameter and asteroid rotation rate. The results, depicted in Figure 7.6, present an excellent estimation with errors generally lower than 15% for all the coefficients.

The addition of a two-percent error in the gravitational parameter and asteroid rotation rate estimates as well as position measurements and initial state errors to the filter has, as expected, a detrimental effect on the estimates. However, the filter remains capable of producing highly accurate estimates for most of the coefficients, clearly showing an improvement with respect to the previous filter design. Furthermore, the results are shown for a nine-degree and order SH coefficient model, further showing the efficiency advantages of using a degree-by-degree estimation method.

In addition, the same test has been conducted with ideal measurement and ideal initial states, which has shown (Figure F.5) the same behaviour, thus further highlighting that the estimation errors have a considerable effect, more relevant than the measurement effect and, thus, it is essential that these estimates are done as accurately as possible to ensure optimal results. Nevertheless, it must be noted that while perfect accuracy cannot be reached for all the coefficient estimates for a 15% threshold, it has been achieved when slightly increasing it to 30%. Moreover, tests conducted with errors of 0.1m, 1m, and 10 m have demonstrated this trend, and shown that as measurement errors are increased, a larger number of coefficients cannot be estimated with the desired accuracy, even for a 30% error threshold.

Figure 7.7 depicts how the addition of the gravitational parameter and the rotation estimation error affects the estimates of the filter. The major errors are produced by the rotational rate error, which can be expected since it has a direct relation to the gravity field felt versus the position in the asteroid reference frame that the satellites estimate. Nevertheless, it should be noted that the rotation error effect remains small due to the polar orbits of the satellites, which minimise the effect, whereas the error is much larger when low inclination orbits are used, as has been demonstrated in Subsection 5.2.2.

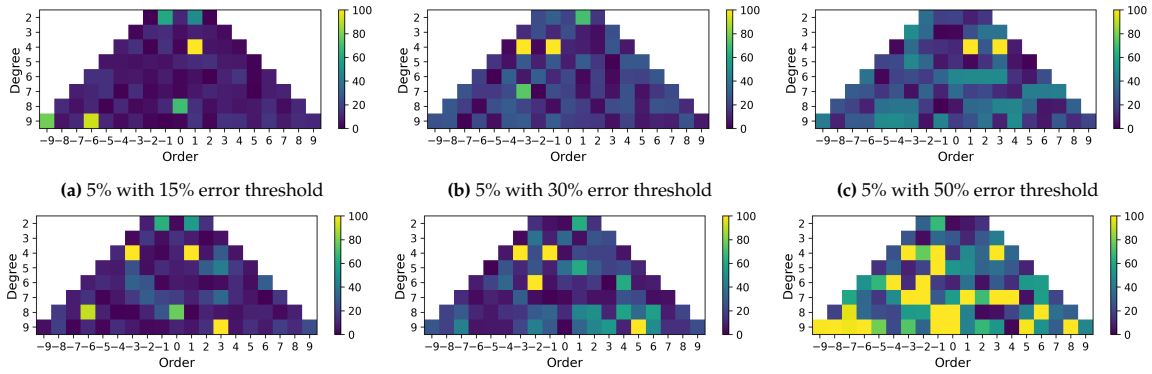

(a) 5% with 15% error threshold **(b)** 5% with 30% error threshold **(c)** 5% with 50% error threshold

(d) 20% with 15% error threshold **(e)** 20% with 30% error threshold **(f)** 20% with 50% error threshold

Figure 7.8: Coefficients estimation for 1m measurement errors.

7.3.2. Convergence filter condition

The filter design undergoes a number of restarts when measurements are lost and a new set is provided. To reduce the computational load of the filter, as introduced previously, the coefficient estimates that have converged are fixed and no longer estimated.

The convergence condition of the filter has a high effect on the resulting estimates. Figure 7.8 presents the differences in the estimates obtained when the convergence is analysed for the last 5% of the estimates for each measurement block versus 20%. As can be seen, the first case provides much better estimates, as is to be expected. Nevertheless, considering a broader spectrum of data such as is done in the second case is a better design for the filter if it has to be applied to other asteroids different to Eros.

In addition, the threshold value has a considerable effect on the estimates. When setting the threshold to approximately an error of 15%, the filter is able to estimate most of the coefficients with very low errors except for a few specific coefficients. As the value increases, the filter is faster in its estimates, but the estimation errors are slightly larger. Finally, it has been seen that setting the value too high as in the case of 50% can have very detrimental consequences, as evidenced in the results. Therefore, it is crucial to tune this value properly.

7.3.3. Spherical Harmonic gravity field degree

While it has been determined that a nine-degree and order gravity-field model is sufficient to fully represent the gravity field felt by the satellites, the scenario has attempted to estimate a model up to 15 degrees. Figure 7.9 presents the results obtained. For the same conditions as in the previous cases, the filter is able to estimate up to degree and order 12. This is a result of two contributions:

1. The estimation of a larger number of coefficients requires longer computational times. From a nine-order estimate to an order 15, there is a difference of 144 coefficients.
2. The estimation of larger-order coefficients increases the computational load of the system since the gravitational field model used to propagate the dynamics of the sigma points is more computationally expensive.

Therefore, the combination of both factors considerably increases the time required for the estimates. The simulation resources are limited and therefore only able to estimate up to degree and order 12, but with more computational time, the system is expected to be able to estimate all the coefficients.

7.3.4. Number of satellite measurements considered

As investigated in the previous chapter, the number of satellites considered in the filter at each block of measurements can have an effect on the results. Figure 7.10 illustrates the difference in the estimates produced when two, three, and four satellites are considered at the same time.

Note that there are key differences in the measurement sets for the estimates. Given that there is a different number of satellites that are required to be available at the same time for the filter to work, for the same constellation of satellites, the measurements used for each case are different:

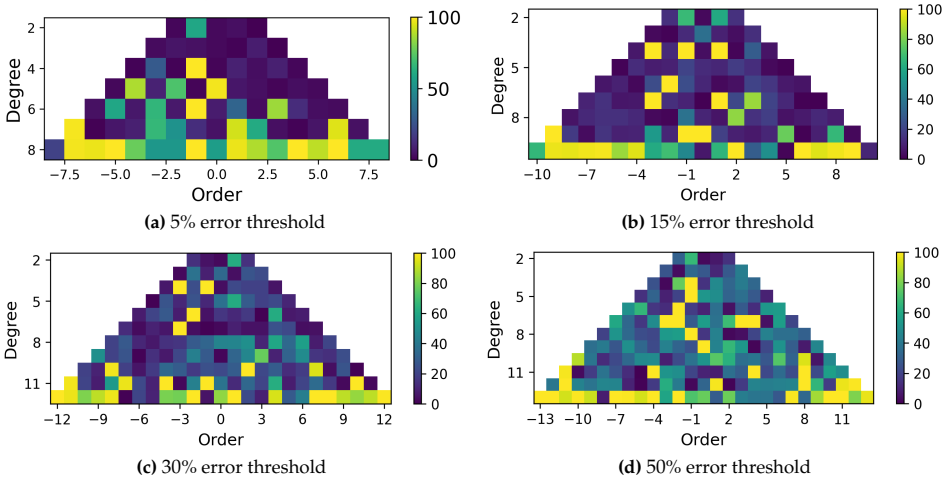

(a) 5% error threshold

(b) 15% error threshold

(c) 30% error threshold

(d) 50% error threshold

Figure 7.9: Coefficients estimation for 1m measurement errors with a 20% convergence average.

- **Two satellites:** The filter is restarted 113 times in which the satellites used for measurements are changed. It can be seen that this filter design is capable of producing good estimates with the majority of the coefficients estimation error lower than 15%.
- **Three satellites:** Requiring an additional satellite to be available at each time instant by the filter, this experiences a total of 170 restarts, which can be expected since the number of times three satellites are available (satellites satisfy adequate visibility and constraint conditions) for the same constellation is lower than that of two satellites. Moreover, as a consequence, the filter operates for shorter lengths of time for a larger amount of restarts. Having both a larger number of estimation blocks of shorter length and additional measurements for better modelling of the filter dynamics aids the filter to obtain better estimates. In addition, it has been observed that only restarting the filter with these measurements 113 times, the same number of restarts presented by the previous case of two satellites, provides worse results than the case of two satellites, thus demonstrating that the additional measurements do not improve the performance of the filter enough to compensate for the use of a shorter propagation time. Furthermore, it should be noted that this configuration comes with an additional CPU load since the state vector is increased, and, in addition, the filter must propagate the dynamics for more satellites.
- **Four satellites:** Requiring four satellites to fulfil the visibility and communications constraints at the same time considerably reduces the times at which the filter can be used. This results in the filter having to be restarted more frequently with shorter periods of estimation. Due to the additional CPU computation load of including four satellites in the filter state vector, the filter is only able to deal with only 89 of the measurement blocks obtained. This has been shown to have considerably detrimental effects on the estimates. The shorter measurement blocks have a damaging effect on the filter since in some cases these are insufficient for coefficient convergence. Moreover, the reduced number of blocks used reduces the measurements and the coverage, thus resulting in worse filter performance.

Overall, these results have shown that increasing the number of satellites used in the filter does not directly lead to an improvement in the estimates. However, this is not a linear relationship and is highly dependent on many factors. The number of satellites used in the filter defines the distribution of the measurements in blocks. Longer measurement blocks have a positive impact on the estimates since they allow for a better convergence of the coefficients. However, the use of more satellites in the dynamics of the filter does present an advantage since a number of measurements are modelled at the same time, which allows for a distribution of the errors of the measurements and since more information on the dynamics is had, the filter's estimates are more accurate, however, this comes at an increased CPU load.

The constellation design has been optimised for two satellites in the previous chapters; therefore, it can be inferred that through a deeper and more thorough optimisation for the three-satelliton case, better results can be obtained, and even in the case of four satellites, by placing the satellites more closely together to maximise the time that four or more are available at the same time.

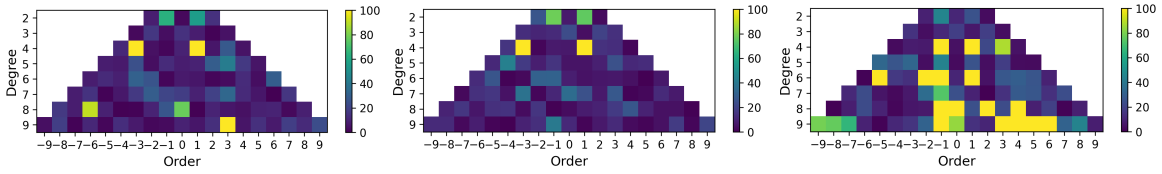

(a) Two satellites **(b)** Three satellites **(c)** Four satellites

Figure 7.10: Coefficients estimation for 1m measurement errors with a 20% convergence average including the states of a different number of satellites in the filter and their respective measurements.

7.3.5. Sensor measurement errors

The sensor measurement errors define the position accuracy estimations of the satellites from which the coefficient estimates are generated. This section presents the effects that the position errors have on the estimates generated for a ninth-degree and order gravity-field model. As illustrated in Figure 7.11, the filter is capable of estimating the position of the satellites with considerable accuracy. For instance, maintaining errors lower to 5 cm for 10 cm error measurements, 0.5 m for 1 m error measurements and 2 m for errors of 10 m.

These results demonstrate that the filter is capable of modelling the gravity field of the asteroid felt by the CubeSats, and therefore these are capable of navigating with accurate estimates of their dynamics, thus considerably improving the safety of asteroid missions.

The measurement errors of the system are directly related to the sensors used in the satellites of the constellation. In regards to the navigation camera (NAVCAM) used to determine the location of the landmarks, as presented in Subsection 4.5.5, the pointing accuracy of the hardware is of the order of 10^{-5} for the mothership and 10^{-4} for the CubeSats, which is the dominant error of the accuracy of the measurements.

The measurement accuracy depends on a number of factors such as the number of detected landmarks in the asteroid. Following the asteroid's data collected in the NEAR mission, a total of 1555 were detected by the spacecraft. With this landmark density, it has been estimated that the position estimation error from the measurements is lower than 100 m for a pointing accuracy of the order of 10^{-4} and lower than 10 meters for the order of 10^{-5}. It should be noted that the position estimation error is done with a basic algorithm and that the position estimation of the CubeSats of the constellation would considerably improve to approximately an error 80% lower if a basic UKF is used in the satellites for position estimation. Additionally, the use of a satellite constellation is an asset for improved position estimation. This is due to the fact that CubeSats can communicate and share data between them to compute their relative positions, which improves the accuracy of position estimates. This relative positioning improvement in the position measurements has however not been included in the simulation. With this in consideration, it can be seen that errors of the order of 100 m are a worst-case scenario.

However, a simulation has been run to determine the filters' efficiency at the gravity-field estimation with these worst-case scenario errors. As depicted in Figure 7.12, the filter performs with high accuracy estimations for a 10 m error in position estimates but is unable to do so for larger orders for the 100 m case. This is indicative that, as expected, such variations in the position estimates difficult the filter performance, making it less prone to converge to adequate coefficient estimates and thus being unable to estimate to the same accuracy all the coefficients for the same propagation time as the 10 m case.

These results confirm that the system is able to perform high-accuracy estimates of the gravity-field coefficients, but that the filter performance and accuracy of these estimates are dependent on the characteristics of the sensors used in the satellites.

7.4. Applicability of the model

To obtain more insights on the applicability of the design presented, the model has been applied to three extreme case asteroids: 216 Kleopatra, 25143 Itokawa, and 4 Vesta, illustrated in Figure 7.13, which challenge the design implemented due to their physical characteristics for which the design is not expected to perform well.

The SH coefficients of these asteroids have been computed through a forward gravitational field model implemented by Root et al. (2016). This method transforms three-dimensional spherical density models through the fast-forward gravitational modelling method into gravitational potential fields

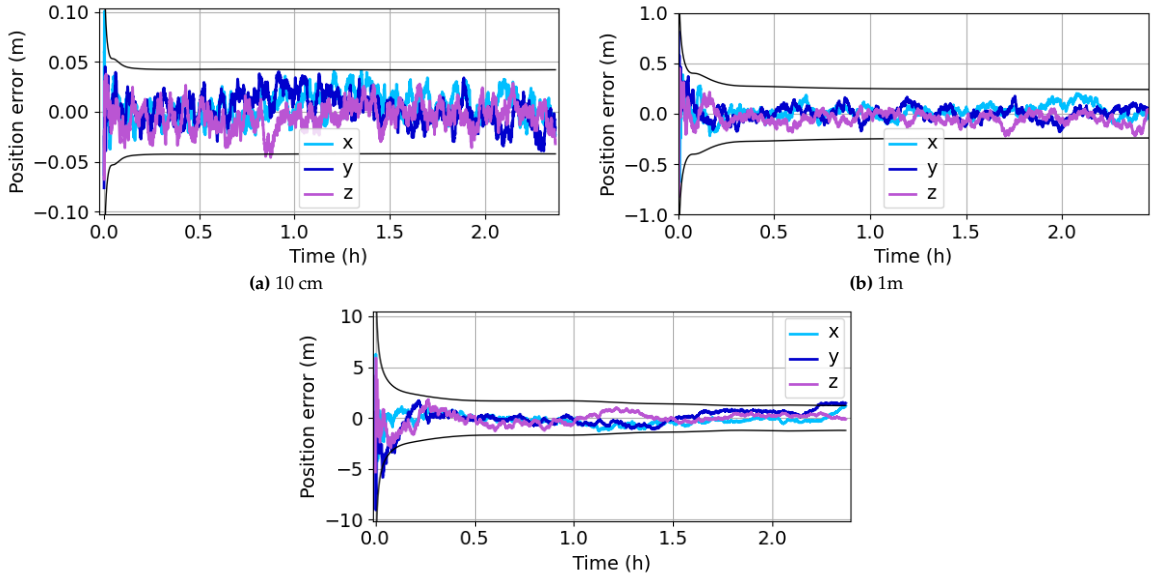

(a) 10 cm **(b)** 1m **(c)** 10m

Figure 7.11: Position estimation error for a set of measurement errors

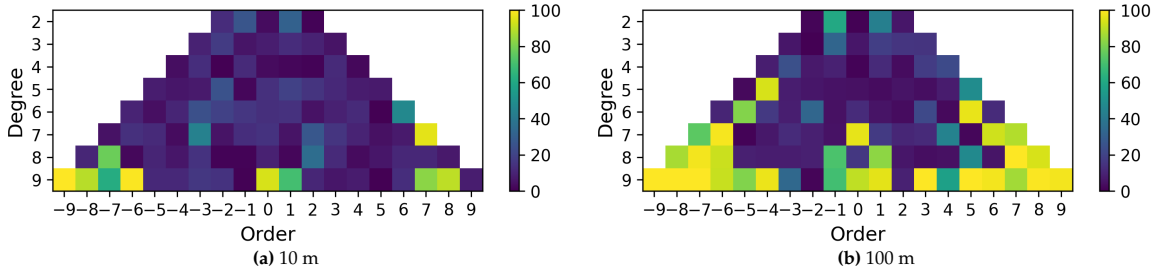

(a) 10 m **(b)** 100 m

Figure 7.12: Gravity field SH coefficient estimation error for a set of measurement errors

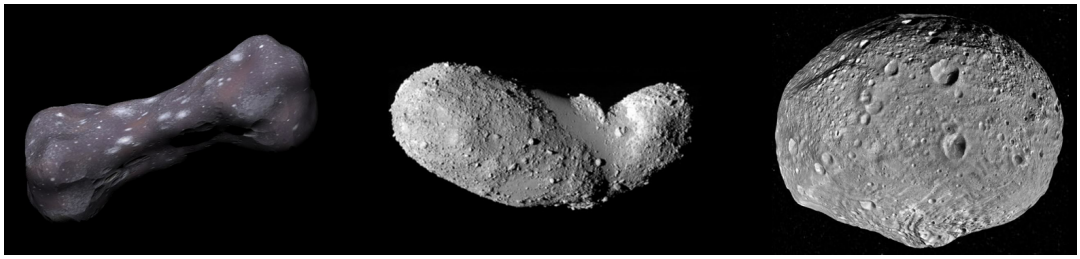

Figure 7.13: Sample asteroids, 216 Kleopatra[1] to the left with a diameter of 122 km, 25143 Itokawa[2] in the centre with a mean diameter of 330 m, and 4 Vesta[3] on the right, with a diameter of 530 km.

using a SH representation. The particular parameters used in the model for the computation of the coefficients can be found in Section F.4.

7.4.1. 216 Kleopatra gravity field estimation

216 Kleopatra[1]is a much larger asteroid than Eros with a mean diameter of 122 km and a considerably more irregular shape, as depicted in Figure 7.13.

To apply the model, it is critical that an adequate altitude is chosen. Following the constellation design of Eros, the same distribution has been maintained and the altitude has been elevated to an average of 160 km radius. This constellation design has nevertheless shown to be highly unstable. This is due to the fact that the asteroid has two prominent bulges that have a very high gravity-field pull, and the very strong irregularities that they induce in the gravity field lead to very strong deviations in the

[1]216 Kleopatra, Available at https://www.flickr.com/photos/mhammergren/2003344861, Accessed on 4-07-2024

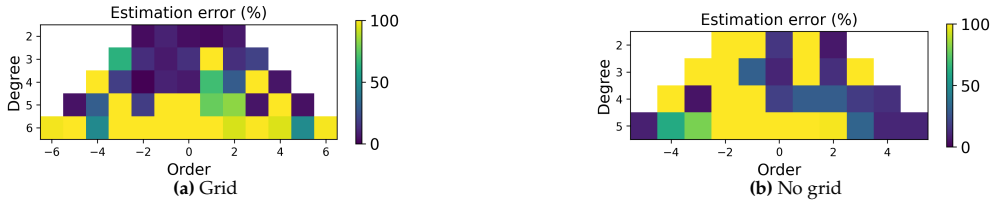

(a) Grid **(b)** No grid

Figure 7.14: Coefficient estimates for Kleopatra's gravity field with the designed constellation for Eros for a $e_r = 10$ m.

(a) Grid **(b)** No grid

Figure 7.15: Coefficient estimates for Kleopatra's gravity field with the updated constellation CubeSat distribution for a $e_r = 10$ m.

trajectory, making most of the CubeSats either crash into the asteroid or escape its orbit.

Applying the filter directly with the inadequacies of the constellation, and with both a null covariance matrix distribution and an accordingly updated grid-like distribution, the filter has produced the results presented in Figure 7.14. As expected, these results are less than ideal. The filter has only been capable of relying on 11 short measurement blocks where all the constraints are fulfilled until the satellites of the constellation escape the orbit or crash into the surface. This is insufficient information for proper modelling of the asteroid. It should be noted that measurement blocks refer to the set of measurements used by the filter, split into a block each time that the filter changes the satellites where the measurements are made due to a loss of communications between the satellite and the mothership or a loss of visibility conditions of the satellites.

In an attempt to further investigate the performance of the system in this exceptionally irregular asteroid, a brief analysis of the better distribution of orbits has been performed and a constellation has been designed to avoid escaping trajectories and crashes. These have been tested under the same conditions and have produced a total of 87 measurement blocks, considerably improving the previously obtained results, note however that for Eros with an adequate orbit around 170 measurement blocks are obtained, therefore the filter performance is expected to be considerably lower in this case.

The new filter coefficient estimates are presented in Figure 7.15 and show a considerable improvement than in the first case. While the filter is still unable to fully estimate the 9th degree and order coefficients, it has shown an adequate performance when sufficient measurements are provided. This issue highlights the need for stable orbits to fully estimate the gravity field, thus showing the need for the proper implementation of a GNC system that is able to maintain the orbits with the use of a thruster. The force of the thruster would have to be additionally considered in the filter state and dynamics, allowing the system to perform adequately even in extremely perturbed environments.

7.4.2. 25143 Itokawa gravity field estimation

25143 Itokawa[2] is a much smaller asteroid than Eros with a mean diameter of 330 m and a similarly irregular shape, as depicted in Figure 7.13. Its reduced shape poses an additional challenge since the gravity field is much lower and therefore the satellites require a much closer orbit to the asteroid to properly estimate its gravity accurately, while at the same time having to maintain a high level of accuracy to ensure the CubeSats are at a safe distance and do not crash into the asteroid.

The constellation design has been tested for an average altitude of 1000 m, 1400 m, and 1800 m. Nevertheless, the CubeSats have been unable to follow adequate trajectories around the asteroid that have not escaped. On the other hand, lower altitudes tested have resulted in crashes. Therefore, no proper trajectory data has been obtained for an adequate performance of the system. This, therefore, highlights the importance again of a GNC system that allows satellites to orbit around asteroids with very low gravitational pull. Attention should be paid to accurately measuring and estimating the effect of the external propulsive accelerations.

[2]25143 Itokawa, Available at https://es.wikipedia.org/wiki/(25143)_Itokawa, Accessed on 4-07-2024

(a) Not considering the first degree and order

(b) Estimating the first degree and order

Figure 7.16: Coefficient estimates for Vesta's gravity field for a $e_r = 10$ m.

7.4.3. 4 Vesta gravity field estimation

4 Vesta[3] is the second asteroid with the largest mass of the asteroid belt, and the third in size, having a rounder shape with its largest diameter being 530 km[4]. The application of the system to this asteroid challenges the design since it evaluates the performance for a very large body. This directly leads to the satellites orbital trajectories having very large semi-major axes and thus to orbit around the asteroid with lower velocities.

The system has been tested with the same satellite constellation design, only raising the semi-major axis to values around 310 km instead of the 30 km used for Eros. The orbits with this system have shown to be stable and therefore adequate for the system implementation. However, it should be noted that when the constellation is applied with the constraints of visibility and communications have a different effect, In this case, the number of measurement blocks is up to 1144, which is much higher with smaller sets for each. This is not the ideal scenario, since having measurement blocks with a low amount of measurements might not be sufficient for the filter to converge adequately. This scenario has been tested with these conditions and the results are depicted in Figure 7.16. In particular, no grid has been defined specifically for the $\boldsymbol{P}$ and $\boldsymbol{Q}$ matrices. Figure 7.16a demonstrates how for a null tuning of the matrices and a non-optimised system, the filter is capable of properly estimating the gravity field with high accuracy. It should be additionally noted that this result has been obtained with the filter design made for Eros, which considered the first-degree coefficients to be null, which is not the case for Vesta. This additional consideration has been taken into account and the filter has been adapted to also estimate the first degree coefficients. The results obtained are shown in Figure 7.16b. As can be observed, the estimates have higher accuracy than in the previous case, which can be directly linked to the fact that the filter was unable to perfectly estimate all the coefficients since it was carrying an error in the model of the three first coefficients representing the first degree of the SH. However, the second case requires a longer propagation time to accurately estimate coefficients up to the ninth degree given the additional efforts that it makes for the initial coefficients estimations. As can be observed, for the same measurements the filter estimates the coefficients accurately up to the seventh degree, and requires a longer propagation time to estimate the remaining higher-degree coefficients.

This highlights the applicability of the system designed for larger asteroids, which has been shown to work effectively even when the filter is not properly tuned to the asteroid model.

7.5. Summary

1. A final optimised design of the satellite constellation has been developed with the lessons learned from the previous chapters aiming to obtain the best measurements for the filter to produce accurate estimates. The constellation has been set with 12 CubeSats in polar orbits with a semi-major axis from 30 to 36 km and null eccentricity. Furthermore, the orbit of the mothership has been optimised to reduce the communications constraints with the satellites.
2. Limitations of the filter have been identified. These consist of the large propagation times required for accurate estimation of coefficients, and the large computational load necessary. A methodical approach has been used to improve the filter's performance. This has been done by:

   (a) Tunning the covariance and process noise matrices to better fit the coefficients to be estimated

[3]Sky & Telescope, "Observe Vesta — and Own a Piece of It, Too", Available at https://skyandtelescope.org/astronomy-news/observe-vesta-and-own-a-piece-of-it-too/, Accessed on 4-07-2024

[4]The Sky Live, "Asteroid 4 Vesta", Available at https://theskylive.com/vesta-info, Accessed on 4-07-2024

(b) Fixing the coefficients that have converged at each filter restart, thus reducing the computational load.
(c) Implementing a "degree-by-degree" approach, starting with a fourth-degree gravity-field model and progressively incorporating higher degrees as coefficients converge, ensuring accurate and efficient estimation.

3. The improved filter design has been tested for performance evaluation in different scenarios:

(a) It has demonstrated that the filter performs adequately when including estimation errors in the gravity field and the rotation rate of the asteroid, only slightly decreasing the accuracy in the estimations of some particular coefficients.
(b) The convergence condition of the filter has demonstrated a relevant impact on the estimates produced. The filter performs better when convergence is evaluated on a smaller sample size of data at the end rather than a larger percentage. Furthermore, it has been seen that the convergence threshold of percentage error in the coefficients estimation has a considerable effect on the estimates and must be tuned adequately. A 15% threshold produces very accurate results but the filter is prone to be unable to estimate a small number of coefficients correctly, on the other hand, a larger threshold of 30% allows the filter to model better in some cases a larger number of coefficients, although with a slightly larger error overall.
(c) Including a larger number of satellite measurements in the filter estimation improves performance at the expense of increasing the computation time as previously demonstrated. However, the number of satellites considered has to be tuned with the constellation design for the filter to perform adequately. For the design done, three satellites have been shown to provide better performance while the addition of more is considerably detrimental to the performance.
(d) The system is able to perform adequately with the defined characteristics of the hardware. However, the more precise the position measurements of the satellites, the faster and better the gravity-field coefficients can be obtained. In particular, the system performs with excellent accuracy for position estimates of the CubeSats with an error of 1 m or lower and has additional difficulties in the estimates as the error increases.

4. The applicability of the model has been tested with three extreme cases that have shown that for extremely irregular asteroids and for very small and low-gravity field asteroids, the model requires the addition of a control system with thrusters to maintain the satellites in the desired orbits without escaping the asteroid or crashing onto it.

8

Conclusions and Recommendations

This chapter reflects on the key objectives of the study by addressing the research questions outlined in the introduction. Drawing on the results of development and simulations, several conclusions are drawn that provide insights into each question.

The implications of the research findings are presented, acknowledging its limitations, and identifying areas for future exploration. In the recommendations section, further investigation is proposed to complete the work initiated in this thesis and suggest potential avenues to expand the study, thereby enhancing the understanding of gravity field estimation using a constellation of satellites.

8.1. Conclusions

This research has conducted an analysis of the orbital design effects on the gravity field spherical harmonics (SH) coefficient estimation, first focusing on a single satellite and then extending the system to a constellation of satellites, followed by the addition of the constraints of the system. Furthermore, it has explored the functioning of the unscented Kalman filter (UKF) exploring different designs for each case in an attempt to find the best model for the system. Additionally, an analysis of variance (ANOVA) has been conducted to gain more insight into the behaviour that the constellation design parameters have on the estimation, allowing to obtain definite conclusions on how an efficient constellation must be designed. Finally, the design of the constellation and of the filter has been revisited and improved to allow for a better estimation of the gravity-field coefficients, which has shown to be able to provide accurate modelling of the dynamics of the system. With the analysis of the previous chapters, the research questions can be answered:

a) What is the influence of the number of satellites in a constellation on the accuracy of gravity field estimation for an asteroid?

This research has demonstrated that the number of satellites in a constellation does not directly determine the accuracy of the gravity field estimation for an asteroid. The primary factor influencing accuracy is the adequacy of each satellite's trajectory, which dictates the coverage and quality of the data obtained. Nevertheless, increasing the number of satellites with appropriate trajectories positively impacts the filter's estimates. When there are one or more satellites with inadequate trajectories, a larger constellation helps mitigate these deficiencies by providing additional data points, thus balancing the overall estimates.

For the chosen UKF design, several key effects of increasing the number of CubeSats have been observed:

- **Measurement Sufficiency and Visibility:**

  A higher number of satellites ensures that the filter receives sufficient measurements, accounting for visibility and communication constraints. With more CubeSats, it is more likely that a minimum number of satellites can provide continuous measurements at any given time.

- **Dynamic Modeling and Computational Demand:**

  Incorporating more CubeSats simultaneously improves the filter's dynamic modelling due to the increased number of measurements. This improves the accuracy of the estimates. However, it also raises the computational demand, as the filter must process a larger volume of data.
- **Measurement Availability and Temporal Coverage:**

  A larger constellation increases the proportion of time during which the necessary satellite measurements are available for the filter. This continuous data stream contributes to improved estimation accuracy. It is important to note that while increasing the number of satellites generally enhances accuracy, this effect plateaus beyond a certain point. Once an optimal number of satellites is reached, further additions do not significantly improve the results.

In summary, the influence of the number of satellites on the accuracy of gravity field estimation is significant but complex. Adequate trajectories and optimal constellation size are critical factors, with more satellites providing diminishing returns beyond a certain threshold. This research underscores the importance of strategic satellite deployment and trajectory planning to maximize the effectiveness of gravity field estimation for asteroids.

b) How does the orbital distribution of the satellites in a constellation impact the accuracy of gravity field estimation for an asteroid?

This research has demonstrated that the orbital distribution of satellites in a constellation is critical to achieving accurate gravity field estimates. The specific trajectories of the satellites significantly influence filter performance and coefficient estimation.

The key findings include:

- **Semi-major Axis**

  The semi-major axis is pivotal for an accurate estimation of the spherical harmonic coefficients. If it is too large, the gravitational effects near the CubeSats are weak, making it difficult for the filter to estimate the SH coefficients accurately. Conversely, if the altitude is too low, the gravity-field irregularities are more pronounced, leading to unstable orbits and potential collisions with the asteroid. This effect is noted in both single satellite estimates and constellations estimations. however, it has been seen that deploying closely located satellites with different semi-major axes leads to a filter coefficients estimates improvement. This approach leverages low-altitude satellites to capture intense gravity-field irregularities, while higher-altitude satellites provide stability and consistent measurements.
- **Inclination**

  Inclination plays a major role in obtaining adequate estimates. Lower inclinations are beneficial for sine-coefficient estimates but in the case of Eros, these can lead to unstable orbits when equatorial paths are used due to the gravity field's irregularities at the equator. Polar orbits, however, provide broader coverage and thus enhance the accuracy of gravity field estimation.

  The distribution of satellites of the constellation along differently inclined orbits has been shown to be detrimental to filter performance. Therefore, it can be concluded that a constellation composed of polar orbits provides better coverage of the asteroid and is better suited for an adequate estimation. Furthermore, polar orbits decrease the effects of errors in the asteroid rotation rate estimate used in the dynamics of the filter.
- **True Anomaly**

  The true anomaly significantly affects the trajectory of the satellites. As the asteroid rotates along its z-axis, the initial area covered by the satellites is determined by their true anomaly, impacting their subsequent paths due to the asteroid's irregular shape.

Having an appropriate orbital distribution is, therefore, crucial for obtaining adequate estimates of the gravity field. This research has explored how the distribution of constellation satellites affects the results and has shown that it is highly dependent on the constraints of the system. Since visibility constraints lead to satellites orbiting close to shadowed areas of the asteroid not being able to produce measurements, having the satellites distributed along the asteroid ensures that

there is at least a satellite with visibility conditions that can produce measurements for the sensor. This would suggest that a distribution of the satellites leads to a good-performing constellation design. Nevertheless, additional considerations have to be made. For instance, communications constraints must be accounted for, and therefore the distribution of the satellites must be able to both ensure adequate trajectories for gravity field estimation and ensure that a number of satellites fulfil both visibility and communications conditions at every time instant. With this consideration in mind, the distribution of the satellites along groups to ensure proper asteroid coverage and maximise the time of conditions fulfilment has been tested; this has led to a smaller number of measurement blocks with larger durations, which has not been shown to produce better estimates with the designed UFK.

Overall, it has been determined that the distribution of the satellites in the constellation is a key factor in obtaining proper estimates.

c) How do the communication constraints of the constellation impact the system?

In an ideal scenario where satellites can take continuous measurements without visibility and communication constraints, the filter for a single satellite can model the gravity field with high accuracy. However, adding constraints significantly impacts the system. Visibility constraints lead to two main issues: loss of asteroid coverage and division of measurement data into blocks, necessitating a robust filter design.

Communication constraints further decrease the number of satellites available for the mothership to use, affecting system performance. This impact is highly dependent on several factors:

- **Number of Constellation Satellites and Their Distribution**
  The number of satellites and their distribution within the constellation significantly affect the system under communication constraints. Without these constraints, the filter performs better as there is a higher chance of multiple satellites being in view of the asteroid simultaneously, allowing for continuous measurement and position estimation. A larger number of satellites increases the likelihood of maintaining line-of-sight LOS with the mothership, thereby enhancing the filter's performance.
- **Mothership Orbit**
  The orbit of the mothership critically influences the filter performance. An inadequately placed orbit can significantly reduce the percentage of the constellation within LOS, limiting the ability to relay information. Optimising the mothership's orbital placement can mitigate communication restrictions, with potential improvements in LOS availability ranging from 70% to 100%, as detailed in Section 7.1.

d) How do the resolution and pointing error of the sensors used affect the position estimation of the satellite system?

The software design reveals that the resolution and pointing error of the sensors used are highly dependent on several system characteristics:

- **Altitude of the Satellites**
  Higher altitude satellites are more affected by the pointing error of the sensors, which impacts position estimation.
- **Number of Landmarks**
  A greater number of detectable landmarks from a given position enhances the precision of position estimation in space. However, testing has demonstrated that increasing the number of landmarks detected by the Shoemaker mission (1555 landmarks) does not have a significant effect on the average position error measurements. Insufficient visible landmarks in specific parts of the asteroid can however lead to very large position measurement errors that can have a detrimental effect on the filter.
- **Distribution of Landmarks**
  A broader distribution of visible landmarks improves position estimation. Conversely, if the same number of landmarks is concentrated in a smaller area, position estimation deteriorates. This specific scenario has been observed when comparing the results obtained for the CubeSat and the mothership NAVCAM. The first has a higher pointing error but a larger coverage,

whereas the second has a smaller pointing error and a smaller coverage. Both have shown to have similar position error estimates, thus compensating the positive effect of a larger landmark distribution with a higher error in the measurements produced.

Tests have shown that the system is able to estimate accurately the gravity field for a range of measurement errors in the position. However, the lower these errors are, the faster and the more accurate that the estimates are obtained.

The tests have been conducted using a randomised set of errors of different magnitudes in the position measurements to represent the variability in the errors obtained in the CubeSats measurements. While these have represented accurately the conditions of the system and are representative of the validation of the system, this method has been used as a bypass to the hardware simulation due to the CPU and time limitations of the system. With these considerations, it is determined that for a more thorough study of the hardware effects, a fully comprehensive test should be conducted estimating the positions at each trajectory from the visualised landmarks and carrying out the gravity field estimation from them. This would allow a better assessment of the direct effect of hardware resolution and landmark availability with the gravity field estimation. This scenario would use UKF filters in the CubeSats to improve position estimates and thus considerably improve the performance of the mothership UKF filter designed in this research.

With these answers to the sub-questions, the main research question can be answered:

How can the integration of autonomous navigation strategies within a satellite constellation enhance the accuracy of gravity field estimation for asteroids?

This research has demonstrated that the UKF converges when using the spherical harmonics gravity-field model to estimate the asteroid's irregular gravity field outside the Brillouin sphere.

The use of a constellation of satellites has been shown to be an asset to an accurate modelling of the gravity field for a number of reasons:

- **Larger coverage of the asteroid and redundancy**

  The research has shown how essential it is for an accurate estimation of the gravity-field coefficients for the satellites to cover a wide area of the asteroid. Insufficient coverage can lead to incorrect modelling of the gravity field, as some irregularities can be missed if full coverage is not achieved. In particular, adequate coverage of areas with large gravity field irregularities has been shown to be more relevant for the estimates than covering areas with a regular gravity field. Results have shown that even for a simplified gravity-field model considering SH up to fifth-degree and order, the coefficient estimates are highly dependent on the coverage of the asteroid. For instance, it has been seen that a change in the inclination of the orbit for a fixed semi-major axis of 50 km from 30° to 60° leads to significant coverage gaps which consequently decreases the accuracy of the coefficient estimates raising the error in five coefficient estimates from lower than 50% to a 100% error. This depicts the unreliability of using a single satellite since its gravity-field estimates will be highly dependent on its orbital parameters. This has further been demonstrated in further tests considering a realistic scenario including visibility restrictions, where the estimates obtained for satellites following orbits with the same inclination and semi-major axis have shown to significantly differ for different true anomaly values from having only three coefficient estimates with 100% errors to having more than seven.

  The use of a constellation (comprised by two satellites or more), increases the density and distribution of measurements. By using a set of satellites, larger coverage of the asteroid is obtained, and the coverage gaps presented by some of the satellites are compensated by the others. This increases the reliability of the estimates produced by the filter.

  Furthermore, having a constellation of satellites allows for the use of various measurement data simultaneously, which improves filter performance by not only compensating for measurement errors (having different sources for each satellite) but also providing a more varied set of measurements. Different positions can enhance the modelling of the dynamics, as has been shown when using the simultaneous measurements of three satellites instead of two, which increases the accuracy of the estimates produced, particularly reducing three coefficients with errors of over 60% to values below 15%.

- **Enhanced temporal resolution**

  Measurements taken by satellites relying on landmark detection are dependent on visibility conditions. Therefore, for a considerable amount of time, satellites in shadow areas of the asteroid cannot obtain measurements and thus cannot produce continuous estimates. The use of a constellation solves this issue by ensuring that the UKF always has a minimum of satellites in adequate visibility conditions and in direct line-of-sight to provide position measurements. This maximises the time when the UKF is able to produce estimates, more than doubling the time that the filter can work for a single satellite, which in consequence significantly reduces the required propagation time for the system to be able to fully accurately estimate the gravity field.
- **Effective Handling of Dynamic Conditions**

  The use of a constellation has been shown to allow for accurate modelling of the dynamics of the system using a UKF. This system has been tested with an open loop and no control system, and even under these conditions, it has shown excellent performance, purely relying on sensor measurements. However, extreme cases have indicated that a control system is required for adequate autonomous navigation, which cannot be achieved otherwise. This demonstrates the constellation's capability to handle dynamic conditions effectively, ensuring continuous and accurate gravity field estimation.
- **Enhanced Precision and Robustness in Estimation**

  The integration of autonomous navigation strategies enables satellites to operate independently, making real-time adjustments and decisions based on onboard sensor data. This capability ensures that the satellites can maintain optimal positioning and adapt to any changes in the asteroid's environment, leading to more precise and robust gravity field estimations.

The integration of autonomous navigation strategies within a satellite constellation significantly enhances the accuracy of gravity field estimation for asteroids. By ensuring comprehensive spatial and temporal coverage, increasing measurement redundancy, and enabling real-time adaptive navigation through the use of a constellation, the system is able to carry out precise gravity field modelling. The research findings underscore the importance of using a constellation approach, demonstrating that even with minimal control systems, the autonomous capabilities of the satellites lead to highly accurate and reliable gravity field estimations, thereby advancing our understanding of asteroid properties and dynamics, and allowing for future asteroid missions to be carried out in an autonomous and safe manner.

The validation of the system with extreme-case scenarios has highlighted the importance of including a control system to maintain orbital stability, improving the gravity field estimation and consequently the safety of autonomous navigation around asteroids.

8.2. Recommendations

This research has identified several areas for improvement, driven primarily by the constraints imposed by computational limitations. To advance the work and derive more comprehensive conclusions, the following recommendations are proposed:

a) Optimisation of the software implementation:

The primary constraint encountered in this research has been computational efficiency. Despite utilising the DelftBlue supercomputer, the extensive computation times significantly limited the number and scope of simulations. The recommendation is made to re-implement the software in C++ to enhance computational efficiency and speed. C++ is known for its performance advantages, particularly in processing-intensive tasks, which will allow for more extensive and detailed simulations.

Additionally, modelling and estimation of the gravity field using Mascon and polyhedron models is also recommended for future work. Both models will allow the estimation of the gravity closer to the surface than the current implementation, which with an efficient software code in C++ could provide more reliable estimations for all mission phases.

b) Polyhedral Model and Spherical Harmonics Coefficients Estimation:

The research initially intended to compare the system's performance using a polyhedral model and the estimation of SH coefficients via the filter. However, this comparison could not be completed due to computational limitations. Future work should focus on this comparison using the more efficient C++ software. Implementing and testing both models will allow for a thorough evaluation of their relative performance, contributing to a better understanding of the strengths and weaknesses of each approach.

In addition, the modelling of the polyhedron gravity field dynamics in the estimation filter is also recommended for future study. This would imply that in addition to the position estimates of the satellites, the filter would estimate the parameters that characterise the shape and mass distribution of the asteroids's polyhedron. While this is expected to be a very complex implementation, its consideration is recommended given that this model would allow more precise modelling of the gravity field, particularly within the Brillouin sphere, where the spherical harmonics model does not converge. This would be a significant improvement since it would be useful for approach phases and landings on the asteroid.

c) Incorporation of Sensor Models:

Due to current computational constraints, the entire system, including sensors, was not fully propagated. Accurately modelling sensor behaviour and errors is crucial for the realistic simulation of measurement inaccuracies and their impact on gravity field estimation. With the optimised C++ implementation, integrating of detailed sensor models is proposed. This will enable a more precise analysis of landmark effects and measurement errors, providing deeper insights into gravity field estimation accuracy.

Furthermore, the research has been carried out considering a scenario where the attitude is controlled and the satellites are always pointing to the centre of mass of the asteroid. For a more accurate representation of the real system, it is recommended that the attitude of the satellites be modelled in the simulation dynamics and controlled.

d) Development of a GNC System:

The time limitations for the research prevented the design and modelling of a complete GNC system. Its implementation is recommended for a proper evaluation of the performance of the filter on a more realistic real mission representation. The addition of the GNC system is expected to improve the results obtained since the orbits will be maintained with time. Furthermore, the addition of this system will allow obtaining an accurate representation of the true applicability and performance of the filter, allowing it to be tested in different phases of the mission such as landing and touch-and-go phases to fully understand the behaviour of the system inside of the Brillouin sphere, which is a limitation that has been present in this research. Note that the spherical harmonics gravity-field model only converges outside of the Brillouin sphere and therefore these tests would require the implementation of recommendation (b) with a polyhedron model.

Adding a GNC system is not only expected to increase the applicability of the filter in terms of further mission phase study, as presented but also is expected to considerably increase the applicability that the system has on asteroid bodies. As presented in the system verification, extraordinarily irregular asteroids or very small bodies can set challenging conditions for stable orbits. Therefore, the addition of a control system with a thruster to correct the trajectory deviations of the satellites is bound to lead to more reliable and safer systems, and most importantly, render the system applicable to a wider range of bodies. It should be noted that this addition would require additional states in the filter and forces in its dynamics for adequate modelling. In particular, any thrusted manoeuvre would induce external accelerations that have to be properly measured by the inertial measurement unit (IMU). Instrument errors, such as bias and scale factor, are examples of the additional states that may have to be estimated.

e) Unscented Kalman Filter Improvement:

The UKF has been shown to be highly dependent on the covariance matrix used. Therefore, it is recommended to explore a method for the initial estimation of an adequate covariance matrix for applicability in different asteroids.

f) Consideration of Other Filter Models:

An initial literature study determined that the UKF was an appropriate option for filter implementation in the system. Nevertheless, after the completion of the simulations it has been seen that the filter has some challenges in the estimation of the SH coefficients. Therefore, it is recommended that other filters are explored in future work and evaluated for better efficiency.

f) Constellation Optimisation:

The effect of constellations on the estimates has been thoroughly studied through various tests and refined with ANOVA. However, the initial consideration of conducting a Monte Carlo analysis has been turned down due to computational and time constraints. With an optimised simulation design and the use of a faster programming language, further optimisation on the satellite constellation should be done for the asteroid intended for study to ensure optimal estimates.

By addressing these recommendations, future research can overcome the current limitations, leading to more robust and comprehensive findings. Implementing these improvements will not only enhance the efficiency and accuracy of simulations but also broaden the scope of potential applications and insights derived from the research.

References

Acciarini, G., Izzo, D., & Mooij, E. (2020). Mhaco: A multi-objective hypervolume-based ant colony optimizer for space trajectory optimization. *2020 IEEE Congress on Evolutionary Computation (CEC)*, 1–8.

Altman, S. (1972). A unified state model of orbital trajectory and attitude dynamics. *Celestial Mechanics*, *5*, 425–446.

Antreasian, P., Chesley, S., Miller, J., Bordi, J., & Williams, B. (2001). The design and navigation of the Near Shoemaker landing on Eros. *Advances in the Astronautical Sciences*, *109*.

Azadmanesh, M., Roshanian, J., & Hassanalian, M. (2023). On the importance of studying asteroids: A comprehensive review. *Progress in Aerospace Sciences*, *142*, 100957.

Bashforth, F., & Adams, J. (1883). *An Attempt to test the Theories of Capillary Action by comparing the theoretical and measured forms of drops of fluid. With an explanation of the method of integration employed in constructing the tables which give the theoretical forms of such drops*. Cambridge University Press.

Berry, M., & Healy, L. (2004). Implementation of Gauss-Jackson Integration for Orbit Propagation. *J of Astronaut Sci*, *52*, 331–357.

Bourgeaux, A. (2020). *Autonomous estimation of the gravity field for asteroid missions* [Master's thesis, University of Bologna].

Bury, G., Sośnica, K., Zajdel, R., & Strugarek, D. (2020). Toward the 1-cm Galileo orbits: challenges in modeling of perturbing forces.

Capannolo, A., Paolini, E., Colagrossi, A., Pesce, V., & Silvestrini, S. (2023). Chapter Three - The space environment. In V. Pesce, A. Colagrossi, & S. Silvestrini (Eds.), *Modern spacecraft guidance, navigation, and control* (pp. 77–129). Elsevier.

Chanut, T., Alijbaae, S., & Carruba, V. (2015). Mascon gravitation model using a shaped polyhedral source. *Monthly Notices of the Royal Astronomical Society*, *450*.

Chanut, T., Winter, O., & Tsuchida, M. (2014). 3D stability orbits close to 433 Eros using an effective polyhedral model method. *Monthly Notices of the Royal Astronomical Society*, *438*, 56–.

Cheng, A. (2002). Near Earth Asteroid Rendezvous: Mission Summary. *Asteroids III*, *1*, 351–366.

Chuanjun, W., Ling, W., & Xuejing, R. (2023). General particle swarm optimization algorithm. *2023 IEEE 2nd International Conference on Electrical Engineering, Big Data and Algorithms (EEBDA)*, 1204–1208.

Clark, B., Barucci, M., Zou, X., Fulchignoni, M., Rivkin, A., Raymond, C., Yoshikawa, M., Elkins-Tanton, L., & Levison, H. (2018). Chapter 1 - A Brief History of Spacecraft Missions to Asteroids and Protoplanets. In N. Abreu (Ed.), *Primitive meteorites and asteroids* (pp. 1–57). Elsevier.

Colagrossi, A., Pesce, V., Silvestrini, S., Gonzalez-Arjona, D., Hermosin, P., & Battilana, M. (2023). Chapter Six - Sensors. In *Modern Spacecraft Guidance, Navigation, and Control* (pp. 253–336). Elsevier.

Diebel, J. (2006). Representing Attitude: Euler Angles, Unit Quaternions, and Rotation Vectors.

Ferrari, F., Franzese, V., Pugliatti, M., Giordano, C., & Topputo, F. (2021). Preliminary mission profile of Hera's Milani CubeSat. *Advances in Space Research*, *67*(6), 2010–2029.

Gad, A. (2022). Particle Swarm Optimization Algorithm and Its Applications: A Systematic Review. *Archives of Computational Methods in Engineering*, *29*, 2531–2561.

Gaskell, R. (2005). Landmark navigation and target characterization in a simulated Itokawa encounter. *AAS/AIAA Astrodynamics Specialists Conference*.

Gebregiorgis, S., & Gonfa, G. (2021). The comparison of Runge-Kutta and Adams-Bashforh-Moulton methods for the first order ordinary differential equations. *International Journal of Current Research*, *8*, 27356–27360.

Geul, J., Mooij, E., & Noomen, R. (2021). Verified regularized interval orbit propagation. *Journal of Guidance, Control, and Dynamics*, *44*, 719–731.

Hayes, A. P. (2011). The Adams-Bashforth-Moulton Integration Methods Generalized to an Adaptive Grid.

Heijden, L. (2022). *Autonomous Navigation around Asteroids using Convolutional Neural Networks* [Master's thesis, TU Delft].

Herfort, U., & Casas, C. (2015). Trajectory preparation for the approach of spacecraft Rosetta to comet 67p/Churyumov-Gerasimenko. *Proceedings 25 th International Symposium on Space Flight Dynamics-25 th ISSFD*.

Hesar, S., Scheeres, D., Mcmahon, J., & Takahashi, Y. (2016). Surface proximity gravitational field analysis of the asteroid 433 Eros.

Hessel, V., Tran, N., Orandi, S., Asrami, M. R., Goodsite, M., & Nguyen, H. (2020). Continuous-Flow Extraction of Adjacent Metals – a Disruptive Economic Window for In-Situ Resource Utilization of Asteroids? *Angewandte Chemie*, *133*.

Hofmann-Wellenhof, B., & Moritz, H. (2005). *Physical Geodesy*. Springer Wien New York.

Hong-de, D., Shao-wu, D., Yuan-cai, C., & Guang-bin, W. (2012). Performance Comparison of EK-F/UKF/CKF for the Tracking of Ballistic Target. *TELKOMNIKA Indonesian Journal of Electrical Engineering*, *10*.

Horváth, K., & Kuslits, M. (2017). Optimization-based parameter tuning of unscented Kalman filter for speed sensorless state estimation of induction machines, 1–7.

Ince, E., Barthelmes, F., Reißland, S., Kirsten, E., Foerste, C., Flechtner, F., & Schuh, H. (2019). ICGEM -15 years of successful collection and distribution of global gravitational models, associated services, and future plans. *Earth System Science Data*, *11*, 647–674.

Izzo, D. (2012). PyGMO and PyKEP: Open Source Tools for Massively Parallel Optimization in Astrodynamics. *Proceedings of the International Conference on Astrodynamics Tools and Techniques*.

Jose, J. (2009). *Performance comparison of Extended and Unscented Kalman Filter implementation in INS-GPS integration* [Master's thesis, Lulea University of Technology].

Julier, S., & Uhlmann, J. (2004). Unscented Filtering and Nonlinear Estimation. *Proceedings of the IEEE*, *92*, 401–422.

Lin, M., Denker, H., & Müller, J. (2014). Regional gravity field modeling using free-positioned point masses. *Stud Geophys Geod*, *58*, 207–226.

Ludwig, S. (2018). Genetic Algorithm Based Kalman Filter Adaptation Algorithm for Magnetic and Inertial Measurement Unit. *2018 IEEE Congress on Evolutionary Computation (CEC)*, 1–7.

March, R. E. (2021). OSIRIS-REx: a NASA Asteroid Space Mission. *International Journal of Mass Spectrometry*, *469*, 116677.

Markley, F., & Crassidis, J. (2014). *Fundamentals of Spacecraft Attitude Determination and Control*. Springer.

Mashiku, A., Garrison, J., & Carpenter, J. (2012). Statistical Orbit Determination using the Particle Filter for incorporating Non-Gaussian Uncertainties. *AIAA Astrodynamics Specialist Conference*.

Mehendale, N., & Neoge, S. (2020). Review on Lidar Technology. *SSRN Electronic Journal*.

Miller, J., Konopliv, A., Antreasian, P., Bordi, J., Chesley, S., Helfrich, C., Owen, W., Wang, T., Williams, B., Yeomans, D., & Scheeres, D. (2002). Determination of Shape, Gravity, and Rotational State of Asteroid 433 Eros. *Icarus*, *155*(1), 3–17.

Mooij, E. (1998). *Aerospace-Plane Flight Dynamics - Analysis of Guidance and Control Concepts* [PhD dissertation]. TU Delft.

Mooij, E., Root, B., & Bourgeaux, A. (2024). Gravity-Field Estimation of Asteroids. *Proceedings of the AIAA SCITECH 2024 Forum*, 1–13.

Moulton, F. R. (1926). New Methods in Exterior Ballistics. *The Mathematical Gazette*, *13*(190), 432–433.

Osada, R., Funkhouser, T., Chazelle, B., & Dobkin, D. (2002). Shape distributions. *ACM Transactions on Graphics*, *21*(4), 807–832.

Pascual, O. (2019). *Analysis of Perturbation incidence in the calculation of trajectories in Ephemeris Model* [Master's thesis, Universitat Politècnica de Catalunya].

Pearl, J. M., & Hitt, D. L. (2022). Cutting Corners: Curvilinear-Surface-Based Gravity Models for Asteroids and Comets. *Journal of Guidance, Control, and Dynamics*, *45*(11).

Peral, E., Im, E., Wye, L., Lee, S., Tanelli, S., Rahmat-Samii, Y., Horst, S., Hoffman, J., Yun, S., Imken, T., & Hawkins, D. (2018). Radar Technologies for Earth Remote Sensing From CubeSat Platforms. *Proceedings of the IEEE*, *106*(3), 404–418.

Prockter, L., Murchie, S., Cheng, A., Krimigis, S., Farquahar, R., Santo, A., & Trombka, J. (2002). The NEAR Shoemaker Mission to Asteroid 433 Eros. *Acta Astronautica*, *51*(1-9), 491–500.

Ramakoti, N., Vinay, A., & Jatoth, R. (2009). Particle Swarm Optimization Aided Kalman Filter for Object Tracking. *2009 International Conference on Advances in Computing, Control, and Telecommunication Technologies*, 531–533.

Ramos, H., & Vigo-Aguiar, J. (2005). A note on step-size selection in the Störmer–Cowell methods [Selected Papers of the International Conference on Computational Methods in Sciences and Engineering]. *Journal of Computational and Applied Mathematics*, *175*(1), 149–159.

Rayman, M. D. (2020). Lessons from the Dawn mission to Ceres and Vesta. *Acta Astronautica*, *176*, 233–237.

Razgus, B. (2017). *Relative Navigation in Asteroid Missions - Dual Quaternion Approach* [Master's thesis, TU Delft].

Rigatos, G. (2012). Nonlinear Kalman Filters and Particle Filters for integrated navigation of unmanned aerial vehicles. *Robotics and Autonomous Systems*, *60*(7), 978–995.

Rollock, K. (1994). *An analysis of orbital propagators for low Earth orbit rendezvous* [Master's thesis, Monterey, California. Naval Postgraduate School].

Root, B., Novák, P., Dirkx, D., Kaban, M., der Wal, W. V., & Vermeersen, L. (2016). On a spectral method for forward gravity field modelling. *Journal of Geodynamics*, *97*, 22–30.

Rosłoniec, S. (2008). Methods for Numerical Integration of Ordinary Differential Equations. In *Fundamental Numerical Methods for Electrical Engineering* (pp. 179–222). Springer Berlin Heidelberg.

Rozman, M. (2017). Multistep methods. *MATH 3510*.

Russell, R., & Arora, N. (2012). Global Point Mascon Models for Simple, Accurate, and Parallel Geopotential Computation. *Journal of Guidance, Control, and Dynamics*, *35*, 1568–1581.

Russell, R., & Wittick, P. (2017). Mascon Models for Small Body Gravity Fields. *Proceedings of the AAS/AIAA Astrodynamics Specialist Conference*, 17–743.

Savitri, T., Kim, Y., Jo, S., & Bang, H. (2017). Satellite Constellation Orbit Design Optimization with Combined Genetic Algorithm and Semianalytical Approach. *International Journal of Aerospace Engineering*, *2017*(Article ID 1235692).

Scardua, L., & Cruz, J. (2017). Complete offline tuning of the unscented Kalman filter. *Automatica*, *80*, 54–61.

Scheeres, D., Williams, B., & Miller, J. (2012). Evaluation of the Dynamic Environment of an Asteroid: Applications to 433 Eros. *Journal of guidance, control and dynamics*, *23*, 2002.

Siddiqi, A. (2018). *Beyond Earth: A Chronicle of Deep Space Exploration* (2nd ed.). National Aeronautics; Space Administration, Office of Communications, NASA History Division.

Spee, S. (2022). *Asteroid gravity field estimation below the Brillouin shpere* [Master's thesis, TU Delft].

Storn, R., & Price, K. (1997). Differential Evolution – A Simple and Efficient Heuristic for global Optimization over Continuous Spaces. *Journal of Global Optimization*, *11*, 341–359.

Vittaldev, V., Mooij, E., & Naeije, M. (2012). Unified State Model theory and application in Astrodynamics. *Celestial Mechanics and Dynamical Astronomy*, *112*, 253–282.

Wakker, K. (2015). *Fundamentals of Astrodynamics*. Institutional Repository Library.

Wan, E., & Merew, R. (2000). The Unscented Kalman Filter for Nonlinear Estimation. *Adaptive Systems for Signal Processing, Communications, and Control Symposium 2000*, *3*, 153–158.

Wan, E., & Merwe, R. (2000). The Unscented Kalman Filter for Nonlinear Estimation. *Proceedings of the IEEE 2000 Adaptive Systems for Signal Processing, Communications, and Control Symposium*, *Cat. No.00EX373*, 153–158.

Wei, W., Gao, S., Zhong, Y., Gu, C., & Hu, G. (2018). Adaptive Square-Root Unscented Particle Filtering Algorithm for Dynamic Navigation. *Sensors*, *18*, 2337.

Welch, G., & Bishop, G. (2006). An Introduction to the Kalman Filter. *University of North Carolina, Department of Computer Science*.

Werner, R., & Scheeres, D. (1996). Exterior Gravitation of a Polyhedron Derived and Compared with Harmonic and Mascon Gravitation Representations of Asteroid 4769 Castalia. *Celestial Mechanics and Dynamical Astronomy*, *65*, 313–344.

Williams, B. (2002). Technical challenges and results for navigation of Near Shoemaker. *Johns Hopkins APL Tech. Dig.*, *23*.

Witze, A. (2023). NASA's Psyche mission is on its way to a huge metal asteroid. *Nature*, *622*.

Woicke, S. (2019). *Hazard Relative Navigation: Towards safe autonomous planetary landings in unknown hazardous terrain* [PhD dissertation]. TU Delft.

Yeomans, D. K., Antreasian, P. G., Barriot, J., Chesley, S. R., & et al. (2000). Radio Science Results During the NEAR-Shoemaker Spacecraft Rendezvous with Eros. *Science*, *289*(5487), 2085–2088.

Yoshikawa, M., Kawaguchi, J., Fujiwara, A., & Tsuchiyama, A. (2021). Chapter 6 - The Hayabusa mission. In A. Longobardo (Ed.), *Sample return missions* (pp. 123–146). Elsevier.

Zarchan, P., & Musoff, H. (2009). *Fundamentals of Kalman Filtering — A Practical Approach* (Third Edition). American Institute of Aeronautics; Astronautics.

A

Development plan

This section presents the development plan for the research, which aims to find how the integration of autonomous navigation strategies within a satellite constellation can enhance the accuracy of gravity field estimation for asteroids. There have been two main plans devised: one at the start of the development after conducting the literature study and another one after a main update during the development. These are presented in the following sections.

A.1. Initial development plan

This is based on 11 main blocks, which are presented below, with the time estimate of each task.

0. Installation of Tudat in the Student Server

Time expected for completion: 2 days
Requirements to start the block: In order to start this first block of tasks access to the student server must be had.
Expected output: After the completion of this block of tasks, the working environment with the Tudat library shall be ready for the start of the development of the thesis simulation in Python. And its operation as well as the proper functioning of PyGMO are verified.

0.1. Installation of Tudat in the server **[0.5 day]**

- **0.1.1.** Access the student server.
- **0.1.2.** Installation of Anaconda or Miniconda following the instructions in website .[1]
- **0.1.3.** Installation of Tudat(py) following the instructions in website [2].
- **0.1.4.** Set up a development environment
- **0.1.5.** Installation of PyGMO following the instructions in website [3].

0.2. Verification of the correct functioning of the environment **[0.5 day]**

- **0.2.1.** Implement the example of "Perturbed satellite orbit" in website [4] and verify the results obtained are correct.
- **0.2.2.** Implement the example of "Asteroid orbit optimisation with PyGMO - Custom Environment" in website [5] and verify the results obtained are correct.

0.3. Buffer **[1 day]**

[1]Miniconda, "Installing Miniconda" Available at: https://docs.conda.io/projects/miniconda/en/latest/miniconda-install.html, Last accessed on: 07-1-2024

[2]Tudat, "Installation" Available at: https://docs.tudat.space/en/latest/_src_getting_started/installation.html, Last accessed on: 07-1-2024

[3]Tudat, "Installing PyGMO" Available at: https://docs.tudat.space/en/stable/_src_advanced_topics/optimization_pygmo.html#installing-pygmo, Last accessed on: 07-1-2024

[4]Tudat, "Perturbed satellite orbit" Available at: https://docs.tudat.space/en/stable/_src_getting_started/_src_examples/notebooks/propagation/perturbed_satellite_orbit.html, Last accessed on: 07-1-2024

[5]Tudat, "Asteroid orbit optimisation with PyGMO - Custom Environment" Available at: https://docs.tudat.space/en/stable/_src_getting_started/_src_examples/notebooks/pygmo/asteroid_orbit_optimisation/aoo_custom_environment.html, Last accessed on: 07-1-2024

1. **Design of the top level simulator architecture**

   Time expected for completion: 4 days
   Requirements to start the block: To start this block of work, the literature study must be completed and contain a description of the scenario, mission hardware (particularly sensors) and physical models.
   Expected output: An architecture design of the simulation where the model is split into different modules and the interaction between them is depicted.

   1.1. Top-level design of the simulation **[1 day]**

      1.1.1. Definition of the main blocks of the system with their respective input and output parameters **[0.5 days]**
      1.1.2. Development of a diagram depicting the connections between the modules and their input and output parameters **[0.5 days]**

   1.2. Revision of the design and changes if needed **[1 day]**
   1.3. Reporting **[1 day]**
   1.4. Buffer **[1 day]**

2. **Definition of the asteroid 433 Eros Environment**

   Time expected for completion: 6 days
   Requirements to start the block: The environment has to be defined with the accelerations acting on the bodies. The accelerations to the model must be known with their respective physical models. Furthermore, the physical characteristics of the orbiting bodies must be known.
   Expected output: The simulation environment, which shall contain all the perturbations and forces considered in the research acting on the orbiting bodies, and those bodies defined accordingly to the research.

   2.1. Architecture of the environment module of the scenario **[1 day]**

      2.1.1. Definition of the architecture **[0.5 day]**
      2.1.2. Reporting **[0.5 day]**

   2.2. Definition and creation of the orbiting bodies and accelerations present in the environment **[1 day]**

      2.2.1. Definition of the mothership in the simulation environment
      2.2.2. Definition of the CubeSat in the simulation environment
      2.2.3. Implementation of the spherical harmonics gravity field of the asteroid
      2.2.4. Implementation of the Solar radiation pressure with the Cannonball model.
      2.2.5. Implementation of the 3rd body perturbation of the Sun.

   2.3. Verification of the model implementation through the visual representation of the propagation of the bodies of the simulation along time and representation of the acceleration present at any point in space **[1 day]**
   2.5. Reporting **[1 day]**
   2.6. Buffer **[1 day]**

3. **Development and simulation of the sensors and constraints for the measurements simulation**

   Time expected for completion: 22 days
   Requirements to start the block: The sensors to implement must have been researched along with their characteristics and physical models.
   Expected output: Verified and tested implementation of the sensors for the CubeSat and mothership bodies.

   3.1. Top-level architecture of the measurement block **[1 day]**

      3.1.1. Architecture design **[0.5 day]**
      3.1.2. Reporting **[0.5 day]**

3.2. Creation of a physical model to represent 433 Eros asteroid with its shape **[4 days]**

3.2.1. Creation of a polyhedron model to represent 433 Eros asteroid **[2 days]**

3.2.1.1. Implement a polyhedron model of the asteroid from the data collected in the NEAR-Shoemaker mission**[0.5 days]**

3.2.1.2. Verification through visual representation of the model and correction if necessary **[0.5 days]**

3.2.1.3. Reporting **[1 day]**

3.2.2. Landmark addition to the asteroid's physical model **[2 days]**

3.2.2.1. Generate landmarks with a random distribution on the asteroid's physical surface represented by a polyhedron **[0.5 days]**

3.2.2.2. Verification through visual representation of the model and correction if necessary**[0.5 day]**

3.2.2.3. Reporting **[1 day]**

3.2.3. Sun-light conditions simulation for visible landmarks determination **[2 days]**

3.2.3.1. Generate an algorithm to determine visible landmarks **[0.5 day]**

3.2.3.2. Verification through visual representation of the model and correction if necessary **[0.5 days]**

3.2.3.3. Reporting **[1 day]**

3.3. Communications constraint **[2 days]**

3.3.1. Design of the communications LOS constraint **[0.25 day]**

3.3.2. Implementation of the communications LOS constraint **[0.25 day]**

3.3.3. Verification of the communications LOS constraint **[0.5 day]**

3.3.4. Reporting **[1 day]**

3.4. NAVCAM sensor **[5 days]**

3.4.1. Design of the NAVCAM sensor algorithm **[0.5 day]**

3.4.2. Implementation of the NAVCAM sensor algorithm **[1.5 days]**

3.4.3. Verification of the correct functioning of the detection algorithm **[1 day]**

3.4.3.1 Verify that the adequate landmarks are detected in several given areas of the asteroid **[0.5 days]**

3.4.3.2. Study how the landmark detection varies along a satellite's orbit **[0.5 days]**

3.4.4. Reporting **[1 day]**

3.4.5. Buffer **[1 day]**

3.5. LiDAR and Altimeter sensors **[5 days]**

3.5.1. Design of an algorithm that when used for LiDAR returns a vector containing the range, and the control angles (azimuth and elevation). **[0.5 days]**

3.5.2. Implementation of the algorithm **[1.5 days]**

3.5.2.1 Implementation of the algorithm **[1 day]**

3.5.2.2 Buffer **[0.5 day]**

3.5.3. Verification of the correct functioning of the algorithm **[1 day]**

3.5.3.2 Test that for a given landmark location, the algorithm is able to measure the range and position adequately **[0.5 days]**

3.5.3.3 Buffer **[0.5 day]**

3.5.4. Reporting **[1 day]**

3.5.5. Buffer **[1 day]**

3.6. Measurement estimation algorithm using the sensors **[4 days]**

3.6.1 Design of the algorithm **[0.5 day]**

3.6.2 Implementation of the algorithm to obtain measurements using the sensors available **[0.5 days]**

3.6.3 Verification tests **[1 day]**

3.6.3.1 Define the tests to be conducted **[0.1 day]**

3.6.3.2 Study the effect of the errors in the NAVCAM sensor on the measurements estimates with the whole system **[0.45 day]**

3.6.3.3 Study the effect of the errors in the altimeter sensor on the measurements estimates with the whole system **[0.45 day]**

3.6.4 Reporting **[1 day]**

3.6.5 Buffer **[1 day]**

3.7. Buffer **[1 day]**

4. Kalman filter implementation

Time expected for completion: 10 days
Requirements to start the block: Theoretical knowledge of the UKF and known input and output parameters. Additionally, the sensor simulation must be completed to determine the measurement outputs, which are used as inputs for this filter.
Expected output: UKF implementation in Python with verified functioning.

4.1. Top-level architecture of the estimation block **[1 days]**

4.1.1 Design of the estimation algorithm **[0.5 day]**
4.1.2 Reporting **[0.5 day]**

4.2. Definition and implementation of the EKF algorithm in Python **[2 days]**

4.2.1 Implementation of the basis of the algorithm in Python from a working Matlab EKF model **[1 day]**
4.2.2 Verification of the basic implementation and correction if necessary using Zarchan's example **[1 day]**

4.3. Definition and implementation of the UKF algorithm in Python **[4 days]**

4.2.1 Implementation of the basis of the algorithm in Python **[2 days]**
4.2.2 Verification of the basic implementation and correction if necessary using a reference example with tuning **[1 day]**
4.2.3 Buffer for issues with code correction **[1 day]**
4.2.4 Reporting **[1 day]**

4.4. Reporting **[2 days]**
4.5. Buffer **[1 day]**

5. Scenario simulation with filter

Time expected for completion: 7 days
Requirements to start the block: Complete implementation of the asteroid model, the UKF, sensors and forces present in the scenario.
Expected output: Verification of the scenario simulation and small sensitivity analysis of the behaviour of the system for different conditions.

5.1. Basic simulation of the scenario **[2 days]**

5.1.1. Simulation of the scenario with a couple of satellites to obtain position measurements **[0.5 days]**
5.1.2. Work on the code to improve the simulation efficiency, addition of configuration files and work on making the code iterable for N satellites chosen **[1.5 days]**

5.2. Implementation of the UKF for the scenario for an individual satellite**[4 days]**

5.2.1. UKF estimation for individual satellites in a set of conditions to analyse the behaviour of the implemented system **[2 days]**
5.2.2. Analyse the efficiency of the estimation process **[1 day]**

5.3. Buffer **[1 day]**

6. Midterm preparation

Time expected for completion: 2 days
Requirements to start the block: Have completed the tasks scheduled before the mid-term review.
Expected output: Reflection on the progress of the project and improvements on details and report in preparation for the mid-term review together with an updated plan.

6.1. Reflection on project status **[1 day]**

6.1.1. Reflection on the status of the project and evaluation of next steps. **[0.5 day]**

6.1.2. Restructuring of the tasks to be followed after the midterm in an updated Gantt Chart. **[0.5 day]**

6.2. Buffer for reporting advances **[1 day]**

7. Post-Midterm work

Time expected for completion: 3 days
Requirements to start the block: Have completed the mid-term review.
Expected output: Reflection on mid-term review and corrections if needed.

7.1. Reflection on mid-term review feed-back **[0.5 day]**
7.2. Buffer for possible changes needed after feedback **[2.5 days]**

8. Sensitivity analysis of the scenario with a satellite constellation

Time expected for completion: 29 days
Requirements to start the block: The simulation of the scenario must be fully working and tested.
Expected output: Detailed analysis of the effects of the constellation and environment on the UKF estimation results.

8.1. Design and test UKF filter **[4 days]**

8.1.1. Design of the UKF filter **[0.25 day]**
8.1.2. Computation and testing of simple scenarios that allow the verification of the correct functioning of the UKF. **[2.75 days]**
8.1.3. Analysis and reporting **[1 day]**

8.2. Analysis of the orbital coverage effect on the estimation **[7 days]**

8.2.1. Design of the analysis procedure and the plots desired **[0.25 day]**
8.2.2. Computation and testing of various scenarios that allow to obtain a comprehensive understanding of the effects that the coverage and constellation design has on the state produced by the UKF. **[4.75 day]**
8.2.3. Analysis and reporting **[2 days]**

8.3. Analysis of the forces considered effect on the estimation **[7 days]**

8.2.1. Design of the analysis procedure and the plots desired **[0.25 day]**
8.2.2. Computation and testing of various scenarios that allow to obtain a comprehensive understanding of the effects that the environment has on the state produced by the UKF. **[4.75 day]**
8.2.3. Analysis and reporting **[2 days]**

8.4. Analysis of the hardware effect on the estimation **[8 days]**

8.2.1. Design of the analysis procedure and the plots desired **[0.25 day]**
8.2.2. Computation and testing of various scenarios that allow to obtain a comprehensive understanding of the effects that the measurement update frequency has on the state produced by the UKF. **[2.25 day]**
8.2.2. Computation and testing of various scenarios that allow to obtain a comprehensive understanding of the effects that the measurement errors have on the state produced by the UKF. **[2.25 day]**
8.2.3. Analysis and reporting **[3.25 days]**

8.4. Buffer **[3 days]**

9. Optimisation of the constellation

Time expected for completion: 35 days
Requirements to start the block: The simulation of the scenario must be fully working and tested.
Expected output: Optimised system, with a proper understanding of the effect of each of the decision variables of the problem and the data on the best characteristics that can be obtained with this mission design.

9.1. Definition of the optimisation problem **[1 day]**

9.1.1. Definition of the problem and objectives to accomplish **[0.25 day]**
9.1.2. Identification of the design variables and their ranges, constraints and any other relevant parameters **[0.5 days]**
9.1.3. Buffer **[0.25 day]**

9.2. Design Space Exploration (DSE) and Design of Experiments (DoE) **[15 days]**

9.2.1. Design of the DSE plan, considering what data to analyse and how to present the information obtained **[1 day]**
9.2.2. Design Space Exploration using a factorial design and ANOVA approach **[10 days]**

9.2.2.1 Implementation of the factorial design for the determined variables **[5 days]**
9.2.2.2 Implementation of the ANOVA approach for the determined variables **[3 days]**
9.2.2.3 Analysis of the obtained results, identification of the best range of design variables and plot creation **[2 days]**

9.2.3. Reporting **[2 days]**
9.2.4. Buffer **[2 days]**

9.3. Global optimisation using PyGMO **[11 days]**

9.3.1 Global optimisation using PyGMO with NSGA2 **[3 days]**

9.3.5.1 Optimisation with the NSGA2 optimiser **[2 days]**
9.3.5.2 Buffer **[1 day]**

6.3.2 Global optimisation using PyGMO with MOEA/D-DE **[3 days]**

9.3.2.1 Optimisation with the MOEA/D-DE optimiser **[2 days]**
9.3.2.2 Buffer **[1 day]**

9.3.3 Evaluation of the performance of the optimisers and determination of the best optimiser for the scenario **[0.5 days]**
9.3.6 Reporting **[4 days]**
9.3.7 Buffer **[1 day]**

9.4 Final optimisation **[5 days]**

9.4.1 Tuning of the chosen optimiser to improve the optimiser performance **[1 day]**
9.4.2 Optimisation with the tuned chosen optimiser **[2 days]**
9.4.3 Reporting **[1 day]**
9.4.4 Buffer **[1 day]**

9.5 Buffer **[3 days]**

10. Conclusion of the research

Time expected for completion: 3 days
Requirements to start the block: All the previous blocks must have been completed.
Expected output: The conclusions and recommendations for future work for the thesis.

10.1. Write the conclusion of the research **[2 days]**
10.2. Buffer **[1 day]**

11. Final reporting

Time expected for completion: 8 days
Requirements to start the block: All the steps of the development plan must have been completed.
Expected output: Full thesis report ready for its delivery.

11.1. Finalise details of the report **[1 day]**

11.1.1. Write abstract
11.1.2. Write preface

11.2. Revision and correction of the report **[5 days]**
11.3. Buffer **[2 days]**

To properly track and organise the development of the research work, a Gantt chart has been created, which is shown in Table A.2. It should be noted that progress starts at week number eight given that the initial seven weeks have been allocated to the literature study.

Table A.1: Gantt chart with progress until the mid-term

	TASK	DAYS EXPECTED	DAYS DONE	TIME USED	START	END	WEEK M	T	W	T	F	
	MILESTONE: LITERATURE REVIEW FINALISATION				**10-Jan**	**10-Jan**			10			*week 8*
0	**Installation of Tudat in the Student Server**	**2**	**1**	**50%**	**11-Jan**	**11-Jan**				11		*week 8*
0.1	Installation of Tudat in the server	0.5	0.5	100%	11-Jan	11-Jan						
0.2	Verification of the environment	0.5	0.5	100%	11-Jan	11-Jan						
0.3	Buffer	1	0		-	-						
1	**Design of the top level simulator architecture**	**4**	**3**	**75%**	**12-Jan**	**16-Jan**					12	*week 8*
1.1	Top-level design of the simulation	1	1	100%	12-Jan	12-Jan	15	16				*week 9*
1.2	Revision of the design and changes if needed	1	1	100%	15-Jan	15-Jan						
1.3	Reporting	1	1	100%	16-Jan	16-Jan						
1.4	Buffer	1										
2	**Definition of the asteroid 433 Eros Environment**	**6**	**5**	**71%**	**17-Jan**	**23-Jan**			17	18	19	*week 9*
2.1	Architecture of the propagation block of the scenario	1	1	100%	17-Jan	17-Jan	22	23				*week 10*
2.2	Environment definition in software	1	1	100%	18-Jan	18-Jan						
2.3	Verification	1	1	100%	19-Jan	19-Jan						
2.4	Reporting	2	2	100%	22-Jan	23-Jan						
2.5	Buffer	1	0		-	-						
3	**Development and simulation of the sensors and constraints for the measurements**	**22**	**19**	**86%**	**24-Jan**	**19-Feb**			24	25	26	*week 10*
3.1	Top-level architecture of the measurement block	1	1	100%	24-Jan	24-Jan	29	30	31	1	2	*week 11*
3.2	Creation of the asteroid's shape model	4	4	100%	25-Jan	30-Jan	5	6	7	8	9	*week 12*
3.3	Communications constraint	2	1.5	75%	31-Jan	01-Feb	12	13	14	15	16	*week 13*
3.4	NAVCAM sensor	5	4.5	90%	01-Feb	07-Feb	19					*week 14*
3.5	LiDAR and Altimeter sensors	5	4	80%	08-Feb	13-Feb						
3.6	Measurement estimation algorithm using the sensors	4	4	100%	14-Feb	19-Feb						
3.7	Buffer	1	0		-	-						
4	**Kalman filter implementation**	**10**	**11**	**110%**	**20-Feb**	**05-Mar**			20	21	22	23	*week 14*
4.1	Top-level architecture of the estimation block	1	1	100%	20-Feb	20-Feb	26	27	28	29	1	*week 15*
4.2	Definition and implementation of the EKF algorithm in Python	2	2	100%	21-Feb	22-Feb	4	5				*week 16*
4.3	Definition and implementation of the UKF algorithm in Python	4	6	150%	23-Feb	01-Mar						
4.4	Reporting	2	2	100%	04-Mar	06-Mar						
3.7	Buffer	1	0		-	-						
5	**Scenario simulation with filter**	**7**	**6**	**86%**	**06-Mar**	**13-Mar**				6	7	8	*week 16*
5.1	Simulation of the scenario	2	2	100%	06-Mar	07-Mar	11	12	13			*week 17*
5.2	Implementation of the UKF for the scenario	4	4	100%	08-Mar	13-Mar						
5.3	Buffer	1	0		-	-						
6	**Midterm preparation**	**2**	**4**	**200%**	**14-Mar**	**19-Mar**					14	15	*week 17*
6.1	Reflection on project status	1	1	100%	14-Mar	14-Mar	18	19				*week 18*
6.2	Buffer for reporting advances	1	3	300%	15-Mar	19-Mar						
	MILESTONE: MIDTERM REVIEW				**20-Mar**	**20-Mar**			20			*week 18*
7	**Post-Midterm work**	**3**	**0**	**0%**	**21-Mar**	**02-Apr**				21	22	*week 18*
7.1	Reflection on mid-term review feed-back	0.5	0	0%	21-Mar	21-Mar	25	26	27	28	29	*holiday*
7.2	Buffer for possible changes needed after feedback	2.5	0	0%	22-Mar	21-Mar	1	2				*week 19*
8	**Sensitivity analysis of the scenario with a constellation of satellites**	**29**	**0**	**0%**	**03-Apr**	**13-May**			3	4	5	*week 19*
8.1	Design and test of UKF filter	4	0	0%	03-Apr	08-Apr	8	9	10	11	12	*week 20*
8.2	Analysis of orbital coverage effects	7	0	0%	09-Apr	17-Apr	15	16	17	18	19	*week 21*
8.3	Analysis of environment effect	7	0	0%	18-Apr	26-Apr	22	23	24	25	26	*week 22*
8.4	Analysis of the hardware effect	8	0	0%	29-Apr	08-May	29	30	1	2	3	*week 23*
8.5	Buffer	3	0	0%	-	-	6	7	8	9	10	*week 24*
							13					
9	**Optimisation of the constellation**	**35**	**0**	**0%**	**14-May**	**01-Jul**		14	15	16	17	*week 25*
9.1	Definition of the optimization problem	1	0	0%	14-May	14-May	20	21	22	23	24	*week 26*
9.2	Design Space Exploration (DSE) and Design of Experiments (DoE)	15	0	0%	15-May	04-Jun	27	28	29	30	31	*week 27*
9.3	Global optimization using PyGMO	11	0	0%	05-Jun	19-Jun	3	4	5	6	7	*week 28*
9.3.1	Global optimization with NSGA2						10	11	12	13	14	*week 29*
9.3.2	Global optimization with MOEA/D-DE						17	18	19	20	21	*week 30*
9.4	Final optimisation design and results analysis	5	0	0%	20-Jun	26-Jun	24	25	26	27	28	*week 31*
9.5	Buffer	3	0		-	-	1					
13	**Conclusion on the research questions and recommendations**	**3**	**0**	**0%**	**02-Jul**	**04-Jul**		2	3	4		*week 32*
13.1	Write the conclusion of the research and answer the research questions	2	0	0%	02-Jul	03-Jul						
13.2	Buffer	1	0		-	-						
14	**Final reporting**	**8**	**0**	**0%**	**05-Jul**	**16-Jul**					5	*week 32*
14.1	Finalize details of the report	1	0	0%	05-Jul	05-Jul	8	9	10	11	12	*week 33*
14.2	Revision and correction of the report	5	0	0%	08-Jul	12-Jul	15	16				*week 34*
14.3	Buffer	2	0		-	-						
	MILESTONE: FINAL REPORT				**17-Jul**	**17-Jul**			17			*week 34*
	MILESTONE: GREEN LIGHT MEETING				**24-Jul**	**24-Jul**			24			*week 35*

A.2. Updated development plan

As has been presented, as a part of the development plan, a block of time was allocated for re-planning future tasks in preparation for the mid-term review. This time block was well allocated, and considerable changes were considered there for better continuation of the research.

After the first part of software development and before the mid-term work, having implemented and tested simple scenario simulations, the limitations of the system were analysed. It was determined that the system was considerably limited by the high requirements of CPU load and computation time required by each simulation, which would render the planned development of the optimisation plan unfeasible in the amount of time allocated for the research, even with access to the student server and DelftBlue supercomputer.

With these considerations, the development plan for the sensitivity analysis was updated. Furthermore, the latter part of the project, which intended to optimise the design constellation using the NSGA2 and MOEAD/D-DE optimisation algorithms was then re-designed and transformed into an in-depth analysis of the effects that the design parameters had on the results of the simulation, followed by an analysis of variance (ANOVA) and a final design synthesis with the results obtained from the previous.

It should be noted that to carry out these changes, the development was extended an additional week from the initial plan, maintaining however the duration of the research within the available time frame.

The updated development plan after the mid-term is as follows:

7. Post-Midterm work

Time expected for completion: 3 days
Requirements to start the block: Have completed the mid-term review.
Expected output: Reflection on mid-term review and corrections if needed.

7.1. Reflection on mid-term review feed-back **[0.5 day]**
7.2. Buffer for possible changes needed after feedback **[2.5 days]**

8. Sensitivity analysis of the scenario with a single satellite

Time expected for completion: 11 days
Requirements to start the block: The simulation of the scenario must be fully working and tested.
Expected output: Detailed analysis of the effects of the trajectory, hardware and environment conditions on the UKF estimations when only one satellite is considered.

8.1. Analysis of the orbital coverage effect on the estimation **[3 days]**

8.1.1. Design of the analysis procedure and the plots desired **[0.25 day]**
8.1.2. Computation and testing of various scenarios that allow to obtain a comprehensive understanding of the effects that the coverage has on the state produced by the UKF. **[1.75 day]**
8.1.3. Analysis and reporting **[1 day]**

8.2. Analysis of the hardware effect on the estimation **[4 days]**

8.2.1. Design of the analysis procedure and the plots desired **[0.5 day]**
8.2.2. Computation and testing of various scenarios that allow to obtain a comprehensive understanding of the effects that measurement errors have on the state produced by the UKF. **[1.5 day]**
8.3.2. Computation and testing of various scenarios that allow to obtain a comprehensive understanding of the effects that the update frequency of the measurements has on the state produced by the UKF. **[1.5 day]**
8.4.3. Analysis and reporting **[1 day]**

8.3. Analysis of the environment effect on the estimation **[3 days]**

8.3.1. Design of the analysis procedure and the plots desired **[0.25 day]**
8.3.2. Computation and testing of various scenarios that allow for obtaining a comprehensive understanding of the effects that the environmental forces have on the state produced by the UKF. **[1.75 day]**
8.3.3. Analysis and reporting **[1 day]**

8.4. Buffer **[2 days]**

9. Sensitivity analysis of the scenario with a satellite constellation

Time expected for completion: 15 days
Requirements to start the block: The sensitivity analysis of the scenario for a single satellite must be done to properly tune the tests in this scenario.
Expected output: Detailed analysis of the effects of the satellite constellation on the estimates produced and an appropriate filter design must be found considering the constellation system conditions.

9.1. Design several UKF filters **[1 day]**

9.1.1. Design of different filters for testing and later analysis. **[0.5 day]**
8.1.2. Reporting **[0.5 day]**

9.2. Analysis of the satellite distribution effect on the estimation **[4 days]**

9.2.1. Design of the analysis procedure and the plots desired **[0.25 day]**
9.2.2. Computation and testing of various scenarios that allow to obtain a comprehensive understanding of the effects that the satellite distribution in the constellation has on the state produced by the UKF for all the designed filters. **[2.75 day]**
9.2.3. Analysis and reporting **[1 day]**

9.3. Analysis of the number of satellites in the constellation effect on the estimation **[4 days]**

9.3.1. Design of the analysis procedure and the plots desired **[0.25 day]**
9.3.2. Computation and testing of various scenarios that allow to obtain a comprehensive understanding of the effects that the number of satellites within a constellation has on the state produced by the UKF for all the designed filters. **[2.75 day]**
9.3.3. Analysis and reporting **[1 day]**

9.4. Analysis of the constellation satellite's hardware effect on the estimation **[4 days]**

9.4.1. Design of the analysis procedure and the plots desired **[0.25 day]**
9.4.2. Computation and testing of various scenarios that allow to obtain a comprehensive understanding of the effects that the hardware of the constellation satellites has on the state produced by the UKF for all the designed filters. **[2.75 day]**
9.4.3. Analysis and reporting **[1 day]**

9.5. Buffer **[2 day]**

10. Sensitivity analysis of the scenario with a satellite constellation with constraints

Time expected for completion: 15 days
Requirements to start the block: The sensitivity analysis of the scenario for a satellite constellation must be done to properly tune the tests in this scenario and the constraints of the hardware must be implemented in the software.
Expected output: Detailed analysis of the effects of the satellite constellation with constraints has on the estimates produced and an appropriate filter design must be found considering the constellation system conditions.

10.1. Analysis of the effect of the visibility constraints on the systems estimates **[3 days]**

10.1.1. Design of the analysis procedure and the plots desired **[0.25 day]**
10.1.2. Computation and testing of various scenarios that allow to obtain a comprehensive understanding of the effects that the visibility constraints have on the system. **[1.75 day]**
10.1.3. Reporting **[1 day]**

10.2. Analysis of the effect of the communications constraints on the systems estimates **[3 days]**

10.2.1. Design of the analysis procedure and the plots desired **[0.25 day]**
10.2.2. Computation and testing of various scenarios that allow to obtain a comprehensive understanding of the effects that the communications constraints have on the system. **[1.75 day]**
10.2.3. Reporting **[1 day]**

10.3. Analysis of the filer performance **[3 day]**

10.3.1. Analysis and comparison of the results obtained with the considered filter designs **[0.25 day]**
10.3.2. Determination of the best filter design for the system **[0.25 day]**
10.3.3. Buffer: Redesign of the filter and testing if needed for performance improvement if results are unsuitable **[2 days]**
10.3.4. Reporting **[0.5 day]**

10.4. Analysis of the system behaviour with all constraints considered **[3 days]**

10.4.1. Design of the analysis procedure and the plots desired **[0.25 day]**
10.4.2. Computation and testing of various scenarios that allow us to obtain a comprehensive understanding of the effects that both constraints have on the system. **[1.75 day]**
10.4.3. Reporting **[0.5 day]**

10.5. Buffer **[1 day]**

11. Design Exploration of the system

Time expected for completion: 7 days
Requirements to start the block: All the previous blocks must have been completed.
Expected output: The conclusions and recommendations for future work for the thesis.

11.1. Definition of the design exploration **[0.5 days]**

11.1.1. Definition of the objectives of the design exploration **[0.25 day]**
11.1.2. Identification of the design variables, their ranges and constraints. **[0.25 day]**

11.2. Design Space Exploration with ANOVA **[5.5 days]**

11.2.1. Definitions of the ANOVA scenarios and tests to be conducted **[0.5 day]**
11.2.2. Implementation of the ANOVA for the defined scenarios **[3 days]**
11.2.3. Analysis of the obtained results and reporting **[2 days]**

11.3. Buffer **[1 day]**

12. Final design synthesis

Time expected for completion: 19 days
Requirements to start the block: All the previous blocks must have been completed.
Expected output: The final optimal constellation and filter design for the scenario are presented and their results and applicability to the scenario are analysed.

12.1. Design of an ideal constellation and analysis of the results **[3 days]**

12.1.1. Constellation design with the lessons learned from ANOVA and previous sensitivity analysis. **[0.5 day]**
12.1.2. System testing with the defined constellation **[1 days]**
12.1.3. Detailed analysis of the obtained results, applicability and limitations, and reporting **[1.5 days]**

12.2. Improve the design with the observed results **[10 days]**

12.2.1. Improve the design of the constellation or the filter design if needed **[2 days]**
12.2.2. Test the behaviour of the final design **[6 day]**
12.2.3. Analysis and reporting **[2 day]**

12.3. Test the design's applicability with the use of the model for extreme-case asteroids **[5 days]**

12.3.1. Apply the design to Kleopatra asteroid **[2 day]**
12.3.2. Apply the design to Itokawa asteroid **[2 day]**
12.3.3. Analysis and reporting **[1 day]**

12.4. Buffer **[1 day]**

13. Conclusion of the research

Time expected for completion: 3 days
Requirements to start the block: All the previous blocks must have been completed.
Expected output: The conclusions and recommendations for future work for the thesis.

13.1. Write the conclusion of the research **[2 days]**
13.2. Buffer **[1 day]**

14. Final reporting

Time expected for completion: 8 days
Requirements to start the block: All the steps of the development plan must have been completed.
Expected output: Full thesis report ready for its delivery.

14.1. Finalise details of the report **[1 day]**

14.1.1. Write abstract
14.1.2. Write preface

14.2. Revision and correction of the report **[5 days]**
14.3. Buffer **[2 days]**

The Gantt chart with the post-midterm tasks is depicted in Table A.2.

As can be seen by the progress shown in the Gantt chart, the development plan has been followed quite accurately. Thanks to the addition of buffers to the planning, the completion of the tasks has remained within the bounds of the expected time frame, even if some of the tasks done have required a larger amount of time than estimated initially.

Overall, given the difficulty in estimating the completion time for the tasks before starting the software implementation, the importance of buffers has been highlighted. Moreover, the successful completion of the research in the given time has been possible due to the access to the supercomputer DelftBlue, which has allowed the parallel computation of a number of tasks that from a personal computer could not have been carried out in the desired time frame.

Table A.2: Updated Gantt chart with progress

	TASK	DAYS EXPECTED	DAYS DONE	TIME USED	START	END	WEEK M	T	W	T	F	
	MILESTONE: LITERATURE REVIEW FINALISATION				**10-Jan**	**10-Jan**			10			*week 8*
0	**Installation of Tudat in the Student Server**	**2**	**1**	**50%**	**11-Jan**	**11-Jan**				11		*week 8*
0.1	Installation of Tudat in the server	0.5	0.5	100%	11-Jan	11-Jan						
0.2	Verification of the environment	0.5	0.5	100%	11-Jan	11-Jan						
0.3	Buffer	1	0		-	-						
1	**Design of the top level simulator architecture**	**4**	**3**	**75%**	**12-Jan**	**16-Jan**					12	*week 8*
1.1	Top-level design of the simulation	1	1	100%	12-Jan	12-Jan	15	16				*week 9*
1.2	Revision of the design and changes if needed	1	1	100%	15-Jan	15-Jan						
1.3	Reporting	1	1	100%	16-Jan	16-Jan						
1.4	Buffer	1										
2	**Definition of the asteroid 433 Eros Environment**	**6**	**5**	**71%**	**17-Jan**	**23-Jan**			17	18	19	*week 9*
2.1	Architecture of the propagation block of the scenario	1	1	100%	17-Jan	17-Jan	22	23				*week 10*
2.2	Environment definition in software	1	1	100%	18-Jan	18-Jan						
2.3	Verification	1	1	100%	19-Jan	19-Jan						
2.4	Reporting	2	2	100%	22-Jan	23-Jan						
2.5	Buffer	1	0		-	-						
3	**Development and simulation of the sensors and constraints for the measurements**	**22**	**19**	**86%**	**24-Jan**	**19-Feb**			24	25	26	*week 10*
3.1	Top-level architecture of the measurement block	1	1	100%	24-Jan	24-Jan	29	30	31	1	2	*week 11*
3.2	Creation of the asteroid's shape model	4	4	100%	25-Jan	30-Jan	5	6	7	8	9	*week 12*
3.3	Communications constraint	2	1.5	75%	31-Jan	01-Feb	12	13	14	15	16	*week 13*
3.4	NAVCAM sensor	5	4.5	90%	01-Feb	07-Feb	19					*week 14*
3.5	LiDAR and Altimeter sensors	5	4	80%	08-Feb	13-Feb						
3.6	Measurement estimation algorithm using the sensors	4	4	100%	14-Feb	19-Feb						
3.7	Buffer	1	0		-	-						
4	**Kalman filter implementation**	**10**	**11**	**110%**	**20-Feb**	**05-Mar**		20	21	22	23	*week 14*
4.1	Top-level architecture of the estimation block	1	1	100%	20-Feb	20-Feb	26	27	28	29	1	*week 15*
4.2	Definition and implementation of the EKF algorithm in Python	2	2	100%	21-Feb	22-Feb	4	5				*week 16*
4.3	Definition and implementation of the UKF algorithm in Python	4	6	150%	23-Feb	01-Mar						
4.4	Reporting	2	2	100%	04-Mar	06-Mar						
3.7	Buffer	1	0		-	-						
5	**Scenario simulation with filter**	**7**	**6**	**86%**	**06-Mar**	**13-Mar**			6	7	8	*week 16*
5.1	Simulation of the scenario	2	2	100%	06-Mar	07-Mar	11	12	13			*week 17*
5.2	Implementation of the UKF for the scenario	4	4	100%	08-Mar	13-Mar						
5.3	Buffer	1	0		-	-						
6	**Midterm preparation**	**2**	**4**	**200%**	**14-Mar**	**19-Mar**				14	15	*week 17*
6.1	Reflection on project status	1	1	100%	14-Mar	14-Mar	18	19				*week 18*
6.2	Buffer for reporting advances	1	3	300%	15-Mar	19-Mar						
	MILESTONE: MIDTERM REVIEW				**20-Mar**	**20-Mar**			20			*week 18*
7	**Post-Midterm work**	**3**	**2**	**67%**	**21-Mar**	**22-Mar**				21	22	*week 18*
7.1	Reflection on mid-term review feed-back	0.5	0.5	100%	21-Mar	21-Mar	25	26	27	28	29	*holiday*
7.2	Buffer for possible changes needed after feedback	2.5	1.5	60%	22-Mar	22-Mar	1					
8	**Sensitivity analysis of the scenario with a single satellite**	**12**	**11**	**92%**	**02-Apr**	**16-Apr**		2	3	4	5	*week 19*
8.1	Orbital coverage analysis	3	4	133%	02-Apr	05-Apr	8	9	10	11	12	*week 20*
8.2	Analysis of hardware effects	4	4	100%	08-Apr	11-Apr	15	16				*week 21*
8.3	Analysis of environment effect	3	3	100%	12-Apr	16-Apr						
8.4	Buffer	2	0		-	-						
9	**Sensitivity analysis of the scenario with a constellation of satellites**	**15**	**16**	**107%**	**17-Apr**	**08-May**			17	18	19	*week 21*
9.1	Design several UKF filters for the constellation	1	1	100%	17-Apr	17-Apr	22	23	24	25	26	*week 22*
9.2	Analysis of the effect of the satellite distribution	4	5	125%	18-Apr	24-Apr	29	30	1	2	3	*week 23*
9.3	Analysis of the effect of the number of satellites	4	5	125%	25-Apr	01-May	6	7	8			*week 24*
9.4	Analysis of the hardware effects	4	5	125%	02-May	08-May						
9.5	Buffer	2	0		-	-						
10	**Analysis of the scenario constellation with constraints**	**13**	**12**	**92%**	**09-May**	**24-May**				9	10	*week 24*
10	Analysis of the effect of the visibility constraints	3	3	100%	09-May	13-May	13	14	15	16	17	*week 25*
10	Analysis of the effect of the communications constraints	3	2	67%	14-May	15-May	20	21	22	23	24	*week 26*
10	Analysis of the filer performance	3	3	100%	16-May	20-May						
10	Analysis of the system behaviour with all constraints considered	3	4	133%	21-May	24-May						
11	Buffer	1	0	0%	-	-						
11	**Design Exploration of the system**	**7**	**9**	**129%**	**27-May**	**06-Jun**	27	28	29	30	31	*week 27*
11	Definition of the optimization problem	0.5	1	200%	27-May	27-May	3	4	5	6		*week 28*
11	Design Space Exploration with ANOVA	5.5	8	145%	28-May	06-Jun						
11	Buffer	1	0		-	-						
12	**Final design synthesis**	**19**	**19**	**100%**	**07-Jun**	**03-Jul**					7	*week 28*
12	Ideal constellation results analysis	3	3	100%	07-Jun	11-Jun	10	11	12	13	14	*week 29*
12	Improve the design with the observed results and test	10	10	100%	12-Jun	25-Jun	17	18	19	20	21	*week 30*
12	Verify the design with other asteroids	5	6	120%	26-Jun	03-Jul	24	25	26	27	28	*week 31*
12	Buffer	1	0		-	-	1	2	3			*week 32*
13	**Conclusion on the research questions and recommendations**	**3**	**2**	**100%**	**04-Jul**	**05-Jul**				4	5	*week 32*
13	Write the conclusion of the research and answer the research questions	2	2	100%	04-Jul	05-Jul						
13	Buffer	1	0		-	-						
14	**Final reporting**	**8**	**12**	**100%**	**08-Jul**	**23-Jul**	8	9	10	11	12	*week 33*
14	Finalize details of the report	1	1	100%	08-Jul	08-Jul	15	16	17	18	19	*week 34*
14	Revision and correction of the report	5	11	220%	09-Jul	23-Jul	22	23				*week 35*
14	Buffer	2	0		-	-						
	MILESTONE: FINAL REPORT				**24-Jul**	**24-Jul**			24			*week 35*
	MILESTONE: GREEN LIGHT MEETING				**31-Jul**	**31-Jul**			31			*week 36*

B

Software Architecture

This chapter presents further detail on the software designed for the research presented in Chapter 4. The code is divided in the following modules:

Configuration Module : This module has been coded for ease in the computation of different scenarios for the research. It contains the following:

- **Configuration class**: This class is able to read from a configuration file all the necessary data for the proper configuration of the parameters required in the software simulation.
- **Configuration files**: A number of configuration files in YAML format can be used to determine the parameters to be used in the simulation.

Asteroid Module : This module contains all the software used for the definition and modelling of the asteroid. It includes the following:

- **Asteroid class**: This class holds all the defining parameters of the asteroid and the functions required to create the gravity field model and define the polyhedron model and the landmarks.
- **Eros 433 files**: The asteroid Class makes use of a number of files containing the spherical harmonics gravity-field coefficients, the polyhedral shape facets and vertices and the landmarks amongst others.

Further detail on the implementation of this module is presented in Section 4.3.

Dynamics Module : This module includes all the software used for the definition of the scenario and the propagation of the satellites in the system. It contains the following:

- **Scenario class**: This class requires the Configuration and Asteroid classes as inputs to define the scenario to be propagated and to save the results adequately.

Hardware Module : This module encloses a number of classes required for the simulation of the hardware components of the system. These are the following:

- **NAVCAM class**: This class contains the attributes defining the NAVCAM instrument in use as well as the functions used for its simulation.
- **Altimeter class**: This class holds the attributes defining the altimeter instrument in use as well as the functions used for its simulation.
- **Sensors class**: This class requires the Altimeter and NAVCAM classes as inputs and contains functions to obtain the position estimation of a satellite from the sensors in use.
- **Visibility class**: This class contains the functions to compute the visibility constraints of the satellites to determine if a given landmark is visible or not considering light conditions.
- **Communications class**: This class contains the functions to determine if communications can be established between two satellites.

Its implementation is presented in Section 4.5.

Estimation Module : This module deals with the estimation functionalities of the software. These are the following:

- **Estimators class**: This class contains the programmed unscented Kalman filter for a number of different states.

Utils Module : This module contains functionalities that are used along with the software. These are as follows:

- **files_utils.py**: This python file includes the functions to save and read data from files.
- **frames_utils.py**: This python file holds the functions to rotate and translate position and velocity coordinates from one coordinate frame to another.
- **coordinate_utils.py**: This Python file has the functions to transform position and velocity coordinates from one coordinate frame to another.
- **plots_utils.py**: This python file contains the functions to generate plots from given data.
- **logger.py**: This python file includes the logger definition for its use along the software.

Additionally, it contains four Python files that require the use of the previous modules. These are as follows:

main: This is the file used to run the software making use of all the modules and blocks.

propagation_block.py: This file includes the functions necessary for the propagation of the system using the configuration, asteroid and scenario classes. This block results in the creation of a dictionary with all the resulting data and or files as chosen by the user.

measurements_block.py: This file comprises the functions necessary for the simulation of the hardware of the satellites. It takes as input the propagated states of the satellites in the scenario and makes use of the hardware module to compute the states of the satellites from the measurements in the asteroid reference frame.

estimation_block.py: This file holds the functions necessary for the Unscented Kalman Filter for the estimation of the spherical harmonic coefficients.

Figure B.1 presents the code architecture depicting a clear summary of the code distribution within module folders.

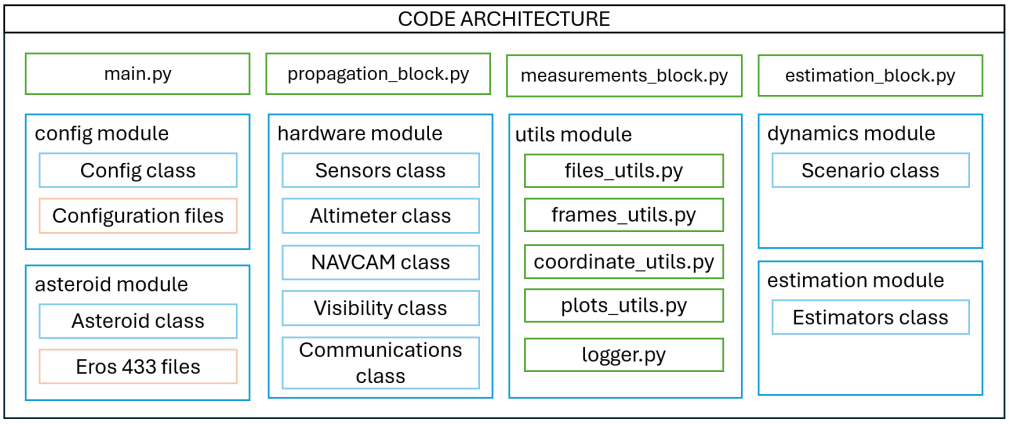

Figure B.1: Top level architecture

C

Spherical Harmonic Coefficients

Having a proper understanding of the spherical harmonic coefficients and their effects on the gravity field of the asteroid is essential for accurately characterising its gravitational environment. These coefficients encapsulate the effects that the asteroid's shape, and density distribution amongst others have on its gravity field. These coefficients not only allow safe navigation outside of the Brillouin sphere of an asteroid, but their analysis can additionally provide information about the asteroid's internal structure.

This appendix first presents the spherical harmonic coefficients used for the simulation of the true gravity field of the asteroid as obtained in the NEAR mission in Section C.1. This is then followed by an analysis of their individual contribution to the gravity field in Section C.2.

C.1. Coefficients used in the model

The following table presents the coefficients used for this study as the true coefficients of the gravity field of Eros. It should be noted that these coefficients have been obtained from the data collected by the NEAR mission.

Table C.1: Spherical harmonic normalised coefficients from m=0 to m=5

m	n	$C_{m,n}$	$S_{m,n}$
0	0	$1.000000000000 \cdot 10^{1}$	$0.000000000000 \cdot 10^{0}$
1	0	$0.000000000000 \cdot 10^{0}$	$0.000000000000 \cdot 10^{0}$
1	1	$0.000000000000 \cdot 10^{0}$	$0.000000000000 \cdot 10^{0}$
2	0	$-5.24618393097 \cdot 10^{-2}$	$0.000000000000 \cdot 10^{0}$
2	1	$-1.63791296116 \cdot 10^{-6}$	$-1.40003806164 \cdot 10^{-7}$
2	2	$8.23993879858 \cdot 10^{-2}$	$-2.81095559016 \cdot 10^{-2}$
3	0	$-1.41446537045 \cdot 10^{-3}$	$0.000000000000 \cdot 10^{0}$
3	1	$4.06016475596 \cdot 10^{-3}$	$3.36846899323 \cdot 10^{-3}$
3	2	$1.77591409489 \cdot 10^{-3}$	$-7.03803181478 \cdot 10^{-4}$
3	3	$-1.04163999496 \cdot 10^{-2}$	$-1.20714404820 \cdot 10^{-2}$
4	0	$1.29314819962 \cdot 10^{-2}$	$0.000000000000 \cdot 10^{0}$
4	1	$-1.00350933584 \cdot 10^{-4}$	$1.36939929063 \cdot 10^{-4}$
4	2	$-1.74688018325 \cdot 10^{-2}$	$4.62909953071 \cdot 10^{-3}$
4	3	$-3.00201192046 \cdot 10^{-4}$	$-1.19207164256 \cdot 10^{-4}$
4	4	$1.74551668902 \cdot 10^{-2}$	$-9.10529276948 \cdot 10^{-3}$
5	0	$6.58933858013 \cdot 10^{-4}$	$0.000000000000 \cdot 10^{0}$
5	1	$-2.76507316000 \cdot 10^{-3}$	$-1.21764377610 \cdot 10^{-3}$
5	2	$-7.83400083663 \cdot 10^{-4}$	$3.81291649798 \cdot 10^{-4}$
5	3	$4.57612464839 \cdot 10^{-3}$	$3.53948354414 \cdot 10^{-3}$
5	4	$4.96909573768 \cdot 10^{-4}$	$-6.98062572977 \cdot 10^{-4}$
5	5	$-1.02064314816 \cdot 10^{-2}$	$-5.83950568922 \cdot 10^{-3}$

Table C.2: Spherical harmonic normalised coefficients from m=6 to m=10

m	n	$C_{m,n}$	$S_{m,n}$
6	0	-4.97836830437·10^{-3}	0.000000000000·10^{0}
6	1	-2.43584360884·10^{-5}	-1.23806736405·10^{-4}
6	2	6.54236012916·10^{-3}	-1.19068956912·10^{-3}
6	3	2.87760856777·10^{-4}	7.54297057642·10^{-5}
6	4	-5.64696275765·10^{-3}	1.76871415479·10^{-3}
6	5	-4.87912268921·10^{-4}	4.79265798636·10^{-5}
6	6	5.08559874845·10^{-3}	-1.60218963559·10^{-3}
7	0	-4.56465554646·10^{-4}	0.00000000000·10^{0}
7	1	1.72212842068·10^{-3}	7.04232300006·10^{-4}
7	2	3.83562866553·10^{-4}	-1.98217150641·10^{-4}
7	3	-2.47156882972·10^{-3}	-1.43634284583·10^{-3}
7	4	-2.42836745686·10^{-4}	3.26817153996·10^{-4}
7	5	3.77380680782·10^{-3}	1.90051572734·10^{-3}
7	6	3.24908737435·10^{-5}	-4.95855917059·10^{-4}
7	7	-6.76682521427·10^{-3}	-2.19813817734·10^{-3}
8	0	2.63212620638·10^{-3}	0.00000000000·10^{0}
8	1	-5.00251571436·10^{-5}	-1.80509056174·10^{-5}
8	2	-3.13715054851·10^{-3}	2.80086999721·10^{-5}
8	3	-3.08700030069·10^{-4}	-3.19178761046·10^{-5}
8	4	2.76703659050·10^{-3}	-4.80859248402·10^{-4}
8	5	4.82584868144·10^{-4}	-1.02494392443·10^{-4}
8	6	-2.54134608560·10^{-3}	2.38751937165·10^{-5}
8	7	-1.90465417509·10^{-4}	-7.00412168746·10^{-5}
8	8	2.26721252014·10^{-3}	1.37112588975·10^{-3}
9	0	1.82381470524·10^{-4}	0.00000000000·10^{0}
9	1	-7.65841810598·10^{-4}	-1.25828763205·10^{-4}
9	2	-3.72214732495·10^{-4}	-1.89464220843·10^{-4}
9	3	1.41592298982·10^{-3}	9.98616252456·10^{-4}
9	4	-4.84244343546·10^{-4}	-2.74835674258·10^{-4}
9	5	-1.71645413405·10^{-3}	-9.79868420897·10^{-4}
9	6	-2.35947224651·10^{-4}	8.48626690994·10^{-5}
9	7	3.06274643906·10^{-3}	8.67524523741·10^{-4}
9	8	4.39923903761·10^{-4}	-7.12609459189·10^{-5}
9	9	-3.27339319759·10^{-3}	-7.22599450487·10^{-4}
10	0	-3.45521920962·10^{-4}	0.00000000000·10^{0}
10	1	-5.92277322251·10^{-4}	1.12359538868·10^{-3}
10	2	1.44591662224·10^{-3}	-7.67662656405·10^{-4}
10	3	4.19639934209·10^{-4}	4.50322622142·10^{-4}
10	4	-3.61489944481·10^{-5}	-7.04604805314·10^{-4}
10	5	-6.30688268739·10^{-4}	-9.24904765129·10^{-4}
10	6	1.52741535971·10^{-3}	9.30333438975·10^{-4}
10	7	7.93390540000·10^{-4}	-8.88264880037·10^{-4}
10	8	-9.02608748543·10^{-4}	-4.35810565051·10^{-5}
10	9	-1.57701659895·10^{-3}	5.24710138002·10^{-5}
10	10	1.18741936384·10^{-3}	1.34677342074·10^{-3}

Table C.3: Spherical harmonic normalised coefficients from m=11 to m=13

m	n	$C_{m,n}$	$S_{m,n}$
11	0	$1.54321499636 \cdot 10^{-3}$	$0.00000000000 \cdot 10^{0}$
11	1	$6.31823976559 \cdot 10^{-4}$	$-1.38549197046 \cdot 10^{-3}$
11	2	$6.52217158913 \cdot 10^{-5}$	$-1.33669393867 \cdot 10^{-3}$
11	3	$3.91040151923 \cdot 10^{-4}$	$-2.46897362404 \cdot 10^{-4}$
11	4	$-1.31539212495 \cdot 10^{-3}$	$-1.15109019804 \cdot 10^{-3}$
11	5	$1.90294627348 \cdot 10^{-3}$	$2.10454519084 \cdot 10^{-3}$
11	6	$5.57377510804 \cdot 10^{-4}$	$-2.77861735189 \cdot 10^{-4}$
11	7	$1.25179860134 \cdot 10^{-4}$	$-5.92684806889 \cdot 10^{-4}$
11	8	$7.87549613803 \cdot 10^{-4}$	$-5.86284007252 \cdot 10^{-4}$
11	9	$2.83000268299 \cdot 10^{-3}$	$1.46807373946 \cdot 10^{-3}$
11	10	$-2.91654518345 \cdot 10^{-4}$	$1.38914799790 \cdot 10^{-4}$
11	11	$-1.27519001987 \cdot 10^{-3}$	$-9.61764869853 \cdot 10^{-4}$
12	0	$2.43134157484 \cdot 10^{-4}$	$0.00000000000 \cdot 10^{0}$
12	1	$6.70401782514 \cdot 10^{-4}$	$2.66147634246 \cdot 10^{-3}$
12	2	$3.40969412508 \cdot 10^{-3}$	$2.11338208433 \cdot 10^{-3}$
12	3	$1.84391298394 \cdot 10^{-3}$	$7.34714719855 \cdot 10^{-4}$
12	4	$9.63450375044 \cdot 10^{-4}$	$-7.72272424542 \cdot 10^{-4}$
12	5	$-3.15066714240 \cdot 10^{-3}$	$-1.16078999537 \cdot 10^{-3}$
12	6	$1.71647635011 \cdot 10^{-3}$	$3.87423072086 \cdot 10^{-3}$
12	7	$-7.23789657114 \cdot 10^{-4}$	$-2.50460154900 \cdot 10^{-3}$
12	8	$8.40481692621 \cdot 10^{-4}$	$2.69378638905 \cdot 10^{-4}$
12	9	$-1.90707458776 \cdot 10^{-3}$	$5.07736951940 \cdot 10^{-5}$
12	10	$-1.91918703901 \cdot 10^{-3}$	$-2.43039244069 \cdot 10^{-3}$
12	11	$4.60884803403 \cdot 10^{-4}$	$3.86783323510 \cdot 10^{-4}$
12	12	$9.05145838127 \cdot 10^{-4}$	$1.82571845934 \cdot 10^{-3}$
13	0	$3.74969536769 \cdot 10^{-3}$	$0.00000000000 \cdot 10^{0}$
13	1	$-5.36052072597 \cdot 10^{-3}$	$-2.28682416648 \cdot 10^{-3}$
13	2	$-4.98998549861 \cdot 10^{-5}$	$3.80868752898 \cdot 10^{-4}$
13	3	$2.23512532397 \cdot 10^{-3}$	$-2.20238723327 \cdot 10^{-4}$
13	4	$1.37906981479 \cdot 10^{-3}$	$-5.09578367346 \cdot 10^{-3}$
13	5	$-1.92452690984 \cdot 10^{-3}$	$3.39499155225 \cdot 10^{-4}$
13	6	$1.73487606396 \cdot 10^{-4}$	$-8.46971792025 \cdot 10^{-5}$
13	7	$3.19135579685 \cdot 10^{-4}$	$-5.94688927422 \cdot 10^{-6}$
13	8	$-1.21894358345 \cdot 10^{-3}$	$-1.42819782954 \cdot 10^{-3}$
13	9	$-6.81071160852 \cdot 10^{-4}$	$-8.47832375960 \cdot 10^{-5}$
13	10	$-6.49816193754 \cdot 10^{-4}$	$-6.42847066547 \cdot 10^{-5}$
13	11	$1.74913637253 \cdot 10^{-3}$	$-3.94413809614 \cdot 10^{-4}$
13	12	$1.38380937672 \cdot 10^{-4}$	$-5.45616670715 \cdot 10^{-5}$
13	13	$-5.97579634119 \cdot 10^{-4}$	$-1.15278788997 \cdot 10^{-3}$

Table C.4: Spherical harmonic normalised coefficients m=14 and m=15

m	n	$C_{m,n}$	$S_{m,n}$
14	0	-2.01393711520·10^{-3}	0.00000000000·10^{0}
14	1	1.45768176334·10^{-3}	1.64601483248·10^{-3}
14	2	8.13105097980·10^{-3}	4.15927949676·10^{-3}
14	3	2.08863476619·10^{-3}	1.69122756650·10^{-4}
14	4	-3.24155693382·10^{-3}	9.77509184922·10^{-4}
14	5	-4.04295596616·10^{-3}	-1.33873699236·10^{-4}
14	6	2.34691045354·10^{-3}	4.38662705205·10^{-3}
14	7	-1.03991731686·10^{-3}	-3.21882909571·10^{-3}
14	8	-1.24639437483·10^{-3}	-2.33084229489·10^{-3}
14	9	-1.96446240979·10^{-4}	7.96888143637·10^{-4}
14	10	1.11844183007·10^{-3}	1.75934930818·10^{-4}
14	11	1.56599539616·10^{-3}	1.45582269663·10^{-4}
14	12	-1.72346255183·10^{-3}	-7.25244770370·10^{-4}
14	13	-3.14428656512·10^{-4}	5.09677479318·10^{-5}
14	14	1.31686078722·10^{-3}	1.50964825342·10^{-3}
15	0	2.62133242363·10^{-3}	0.00000000000·10^{0}
15	1	-5.21704851641·10^{-3}	-1.29515020754·10^{-4}
15	2	2.87383690816·10^{-4}	2.92573028489·10^{-3}
15	3	-1.71536162683·10^{-3}	4.59751597254·10^{-4}
15	4	2.23477484628·10^{-3}	-5.30279430715·10^{-3}
15	5	-2.95431731160·10^{-3}	-3.17673017227·10^{-3}
15	6	-2.86890570331·10^{-4}	-3.70050559030·10^{-4}
15	7	-1.32413967143·10^{-3}	-2.37854024479·10^{-4}
15	8	-3.07665938142·10^{-3}	7.65686758400·10^{-4}
15	9	-9.74823782750·10^{-4}	-8.24779017027·10^{-5}
15	10	2.53802474287·10^{-5}	-3.50261528320·10^{-4}
15	11	-8.58760760673·10^{-4}	-1.08402315089·10^{-3}
15	12	2.60303051879·10^{-4}	2.28290714369·10^{-4}
15	13	1.26707170902·10^{-3}	6.00423407607·10^{-4}
15	14	2.11776693300·10^{-4}	-1.47864314643·10^{-4}
15	15	-1.13644926646·10^{-3}	-1.02266014805·10^{-3}

C.2. Analysis on the contribution of each coefficient to the gravity field

This section presents the gravity-field norm contribution of the spherical harmonic coefficients presented previously on the asteroid's gravity field.

Figure C.1 represents the differences in the distribution effect of the gravity-field coefficients effect along a sphere representing the asteroid. As it can be seen, this plot depicts very clear and different patterns between each other as is expected from the spherical harmonics model.

Further detail on the contributions for each degree and order coefficients on the gravity field can be found in the following figures, depicting the detailed effects in longitude and latitude that a satellite would feel at an orbit of 30 km of semi-major axis.

As expected, zero-order coefficients, known as zonals, have a latitudinal contribution to the gravity field while coefficients with equal degree and order, or sectorials, have a longitudinal effect. Moreover, the rest of the coefficient combinations, known as tesserals, present a grid-like contribution to the field.

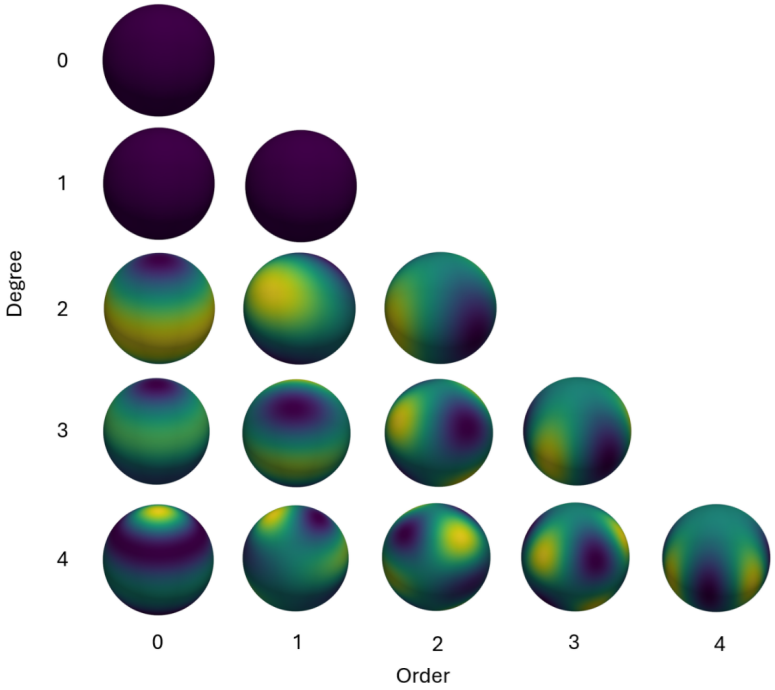

Figure C.1: Spherical harmonics gravity field coefficient contribution.

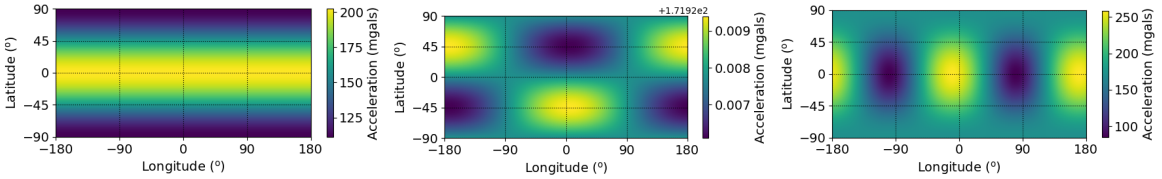

(a) $m = 2, n = 0$ **(b)** $m = 2, n = 1$ **(c)** $m = 2, n = 2$

Figure C.2: Gravity-field norm contribution of the spherical harmonic coefficients of degree two.

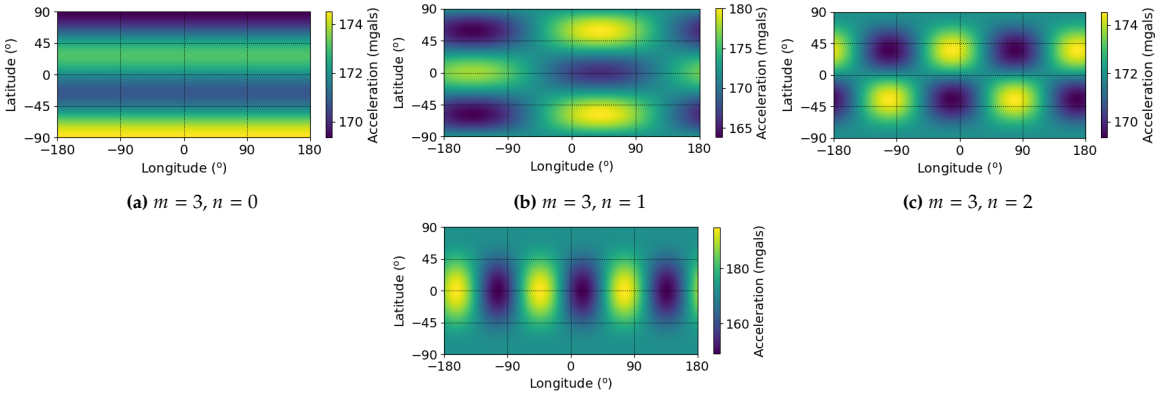

(a) $m = 3, n = 0$ **(b)** $m = 3, n = 1$ **(c)** $m = 3, n = 2$

(d) $m = 3, n = 3$

Figure C.3: Gravity-field norm contribution of the spherical harmonic coefficients of degree three.

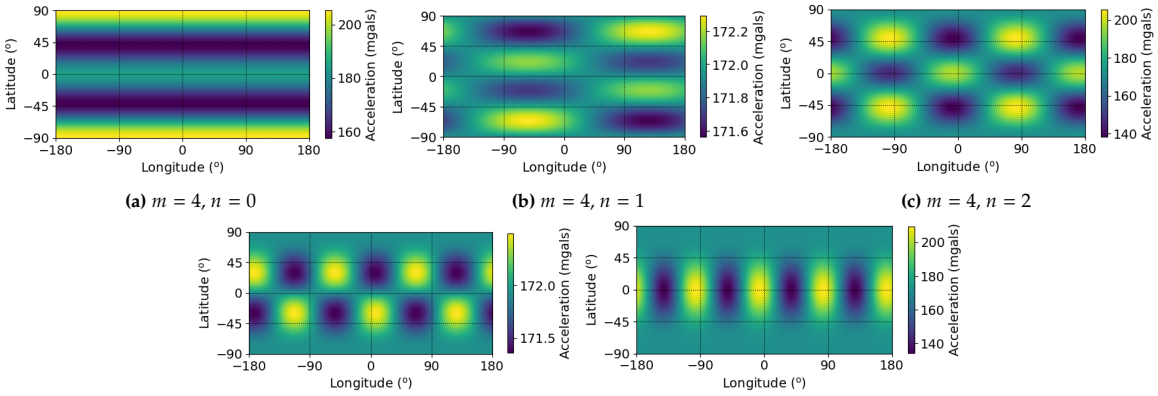

(a) $m = 4, n = 0$ **(b)** $m = 4, n = 1$ **(c)** $m = 4, n = 2$

(d) $m = 4, n = 3$ **(e)** $m = 4, n = 4$

Figure C.4: Gravity-field norm contribution of the spherical harmonic coefficients of degree four.

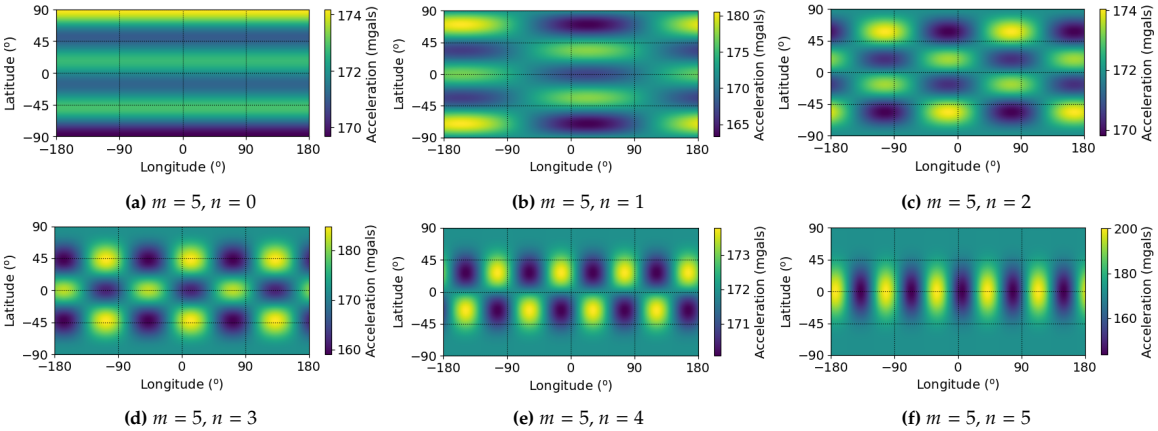

(a) $m = 5, n = 0$ **(b)** $m = 5, n = 1$ **(c)** $m = 5, n = 2$

(d) $m = 5, n = 3$ **(e)** $m = 5, n = 4$ **(f)** $m = 5, n = 5$

Figure C.5: Gravity-field norm contribution of the spherical harmonic coefficients of degree five.

D

Sensitivity Analysis Settings and Supporting Results

This appendix acts as a support to Chapter 5, which presents an in-depth analysis of the effects of the parameters affecting the spherical harmonic coefficient estimates obtained by the unscented Kalman filter. This chapter presents further details on the tests conducted and the results obtained.

Section D.1 presents the tests conducted for the sensitivity analysis of the scenario when a single satellite is considered, including a detailed description of the UKF used. This is followed by the tests and filters implemented for a constellation of satellites in Section D.2 and finally Section D.3 considering constraints in the satellite constellation.

D.1. Sensitivity Analysis: Single Satellite

This section presents the analysis done for a scenario considering a single satellite orbiting Eros. Subsection D.1.1 presents the details of the UKF design used. Moreover, an orbital coverage analysis is depicted in Subsection D.1.2, followed by an analysis of the state and measurements errors in Subsection D.1.3 and the frequency update of the measurements effect in the system is analysed in Subsection D.1.4. Additionally, Subsection D.1.5 presents an analysis of the forces considered in the scenario.

D.1.1. UKF Design For a Single Satellite

The Unscented Kalman filter used for the coefficient estimation for a single data presents the following characteristics, where the state contains the position, velocity, cosine and sine coefficients, and the measurements are the position of the satellite. It should be noted that this filter has been designed to be adaptable to the desired coefficients to be estimated depending on the degree of the filter's SH selected by the user. Therefore, the state vector, measurement vector and matrices are of variable size. This is represented with n_C and n_S which represent the number of cosine and sine coefficients to be estimated respectively. For instance, when a nine-degree SH model is used, $n_C = 52$ and $n_S = 44$, and when a four-degree model is used the values are reduced to $n_C = 18$ and $n_S = 14$. In addition, note that σ_p depicts the measurement error.

$$\mathbf{x}_k = \begin{pmatrix} \mathbf{x}_A \\ \dot{\mathbf{x}}_A \\ \mathbf{c_{nm}} \\ \mathbf{s_{nm}} \end{pmatrix} \tag{D.1}$$

$$\mathbf{z}_k = \begin{pmatrix} \mathbf{x}_A \end{pmatrix} + \begin{pmatrix} \sigma_p \\ \sigma_p \\ \sigma_p \end{pmatrix} \tag{D.2}$$

$$\mathbf{P} = \begin{bmatrix} \mathbf{I}_{3\times3} \cdot p_{pos} & \mathbf{0}_{3\times3} & \mathbf{0}_{3\times n_C} & \mathbf{0}_{3\times n_S} \\ \mathbf{0}_{3\times3} & \mathbf{I}_{3\times3} \cdot p_{vel} & \mathbf{0}_{3\times n_C} & \mathbf{0}_{3\times n_S} \\ \mathbf{0}_{n_C\times3} & \mathbf{0}_{n_C\times3} & \mathbf{I}_{n_C\times n_C} \cdot p_{Cmn} & \mathbf{0}_{n_C\times n_S} \\ \mathbf{0}_{n_S\times3} & \mathbf{0}_{n_S\times3} & \mathbf{0}_{n_S\times n_C} & \mathbf{I}_{n_S\times n_S} \cdot p_{Smn} \end{bmatrix} \tag{D.3}$$

$$\mathbf{Q} = \begin{bmatrix} \mathbf{I}_{3\times3} \cdot q_{pos} & \mathbf{0}_{3\times3} & \mathbf{0}_{3\times n_C} & \mathbf{0}_{n_S\times n_S} \\ \mathbf{0}_{3\times3} & \mathbf{I}_{3\times3} \cdot q_{vel} & \mathbf{0}_{3\times n_C} & \mathbf{0}_{n_S\times n_S} \\ \mathbf{0}_{n_C\times3} & \mathbf{0}_{n_C\times3} & \mathbf{I}_{n_C\times n_C} \cdot q_{Cmn} & \mathbf{0}_{n_C\times n_S} \\ \mathbf{0}_{n_S\times3} & \mathbf{0}_{n_S\times3} & \mathbf{0}_{n_S\times n_C} & \mathbf{I}_{n_S\times n_S} \cdot q_{Smn} \end{bmatrix} \tag{D.4}$$

$$\mathbf{R} = \begin{bmatrix} \sigma_p^2 & 0 & 0 \\ 0 & \sigma_p^2 & 0 \\ 0 & 0 & \sigma_p^2 \end{bmatrix} \tag{D.5}$$

D.1.2. Orbit Coverage Analysis

This section presents the details of four orbital coverage analyses conducted, presenting the parameters used in the simulation and the results obtained for the spherical harmonics coefficient estimations. Table D.1 presents the configuration parameters used in the tests for this scenario.

Test ORB-1

This test aims to analyse the effect that the orbital semi-major axis and inclination have on the coverage of the asteroid and how that has an effect on the spherical harmonic coefficient estimation. The parameters used for the simulation are presented in Table D.2.

The orbital settings are determinants of the coverage of the asteroid. The coverage obtained for a propagation time of 2.5 million seconds is illustrated in Figure D.1. In addition Figure D.2 presents the coefficient estimates obtained for the scenarios tested with the given settings for the 30° inclination orbits. It should be noted that the other scenarios have shown very similar coefficient estimates to those obtained for a propagation time of 1 million seconds. As can be seen, the larger the semi-major axis, the worse estimates that the filter produces. On the other hand, the effect of the inclination is less notable, and dependent on the particular semi-major axis used, since the combination of both has a considerable effect on the coverage of the asteroid.

Test ORB-2

This test aims to analyse the effect that the eccentricity of the orbit has on the estimation of the spherical harmonic coefficients. The scenario has been tested for the parameters depicted in Table D.3 for a polar and a low-inclination orbit.

Table D.1: ORB general test configuration parameters

Propagation	Δt **(s)**		t_{prop} **(s)**	
	1		$1 \cdot 10^6, 2.5 \cdot 10^6$	
Forces	**Eros SH**		**3rd BP**	**SRP**
	$m = 5, n = 5$		None	None
Error	e_r (m)		e_v (m/s)	z_r (m)
	0		0.0	10.0
UKF	**Q**			**R**
	$\mathbf{q_{pos}}$	$\mathbf{q_{vel}}$	$\mathbf{q_{Cmn}}$	$\mathbf{q_{Smn}}$	$\sigma_\mathbf{p}$
	$1.0 \cdot 10^{-10}$	$1.0 \cdot 10^{-9}$	$1.0 \cdot 10^{-35}$	$1.0 \cdot 10^{-35}$	10.0

Table D.2: ORB-1 test configuration parameters

Orbit	a (km)	i (deg)	e (deg)	ν (deg)
	30, 50, 100	30, 60, 90	0	0

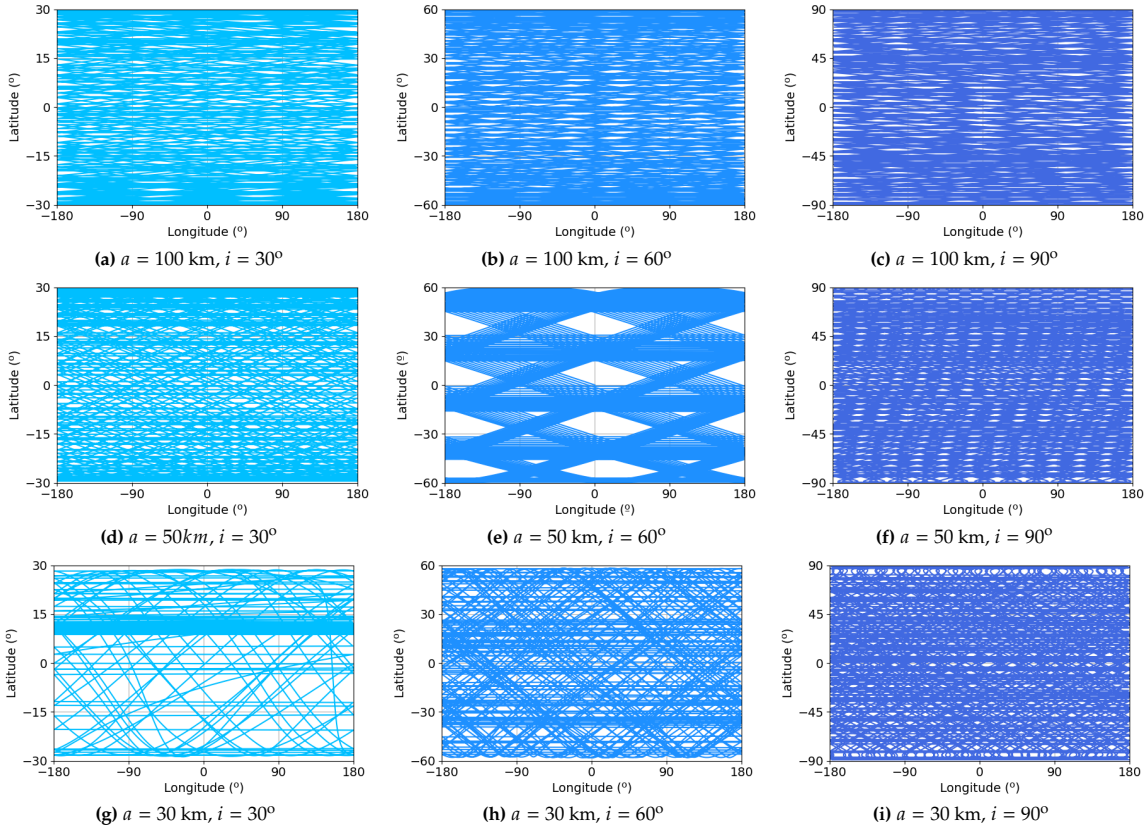

(a) $a = 100$ km, $i = 30^o$ **(b)** $a = 100$ km, $i = 60^o$ **(c)** $a = 100$ km, $i = 90^o$

(d) $a = 50km$, $i = 30^o$ **(e)** $a = 50$ km, $i = 60^o$ **(f)** $a = 50$ km, $i = 90^o$

(g) $a = 30$ km, $i = 30^o$ **(h)** $a = 30$ km, $i = 60^o$ **(i)** $a = 30$ km, $i = 90^o$

Figure D.1: ORB-1 Test: Coverage for a total propagation time of 2.5 million seconds

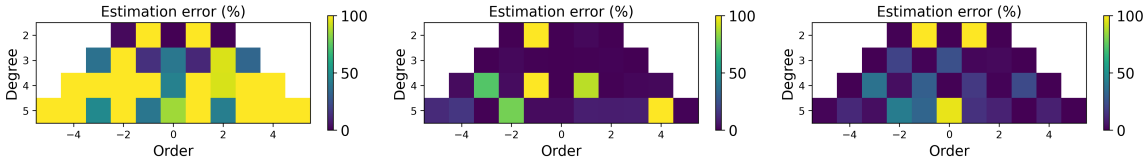

(a) $a = 100$ km, $i = 30^o$ **(b)** $a = 50$ km, $i = 30^o$ **(c)** $a = 30$ km, $i = 30^o$

Figure D.2: ORB-1 Test: Estimation error of the SH coefficients degree and order 5 for 2.5 million seconds

The SH coefficient estimates for the polar orbit are illustrated in Figure D.3, where it can be seen that there is a general trend where the estimates improve with eccentricity, which can be related to the effect of the altitude of the satellites with the asteroid (presented in Subsection 5.2.1). Additionally, Figure D.5 shows the estimation errors for SH coefficients in the low-inclination scenario. Unlike the highly inclined orbit, higher eccentricities result in worse estimations due to significant coverage gaps, thus denoting the interaction between the inclination and the eccentricity in the asteroids' coverage and filter's estimates. An equatorial orbit makes the satellite orbit more closely to Eros's main gravity field concentrations, which if coupled with higher eccentricities can lead to divering orbits that have high altitudes and thus lead to a decrease of accuracy in the estimations produced by the filter. Not that the coverage obtained for the low-inclination scenario is depicted in Figure D.4, presenting the aforementioned gaps for eccentricities over 0.3.

Table D.3: ORB-2 test configuration parameters

	a (km)	i (deg)	e (deg)	ν (deg)
Orbit	50	30, 90	0 - 0.5	0

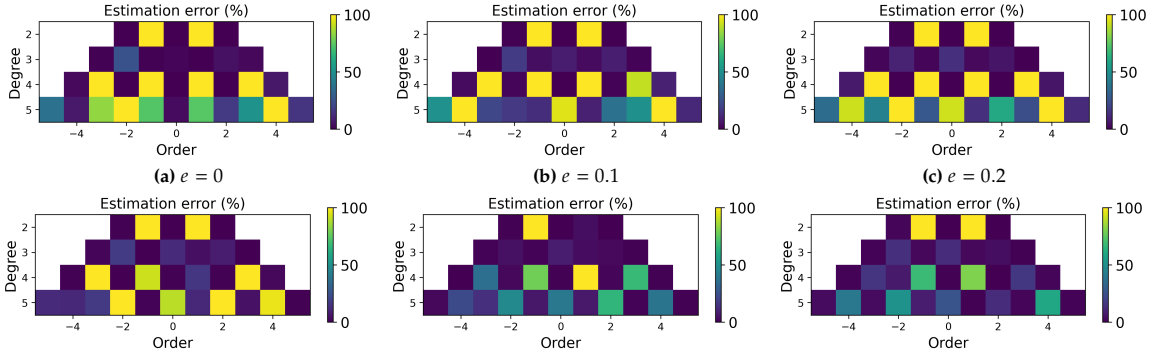

(a) $e = 0$ **(b)** $e = 0.1$ **(c)** $e = 0.2$

(d) $e = 0.3$ **(e)** $e = 0.4$ **(f)** $e = 0.5$

Figure D.3: ORB-2 Test: Estimation error of the SH coefficients degree and order 5 for a propagation time of 1 million seconds with a high inclination orbit of $i = 90^{o}$

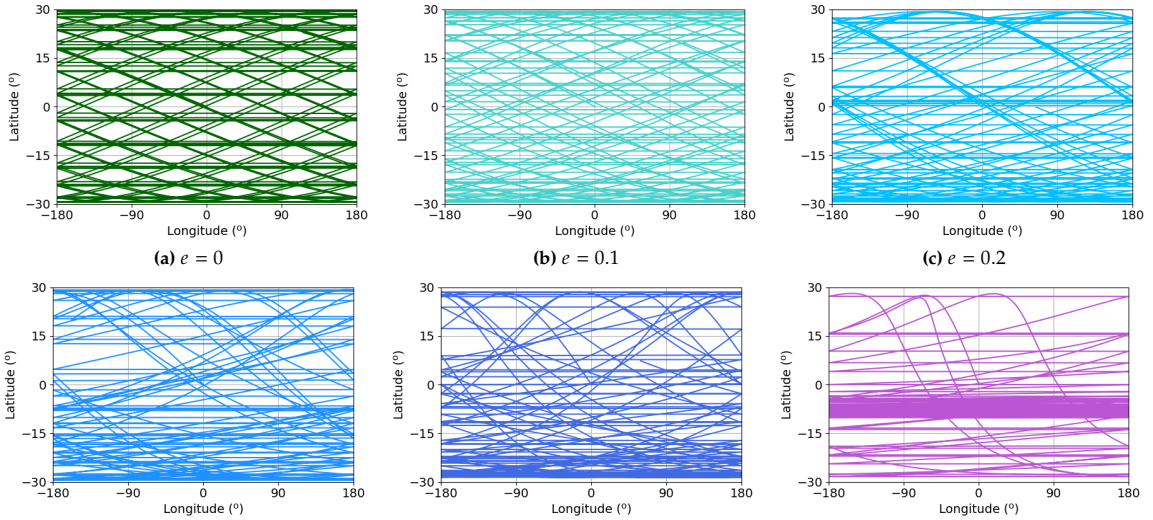

(a) $e = 0$ **(b)** $e = 0.1$ **(c)** $e = 0.2$

(d) $e = 0.3$ **(e)** $e = 0.4$ **(f)** $e = 0.5$

Figure D.4: ORB-2 Test: Coverage for a total propagation time of 1 million seconds for an orbit with $a = 50$ km and $i = 30^{o}$

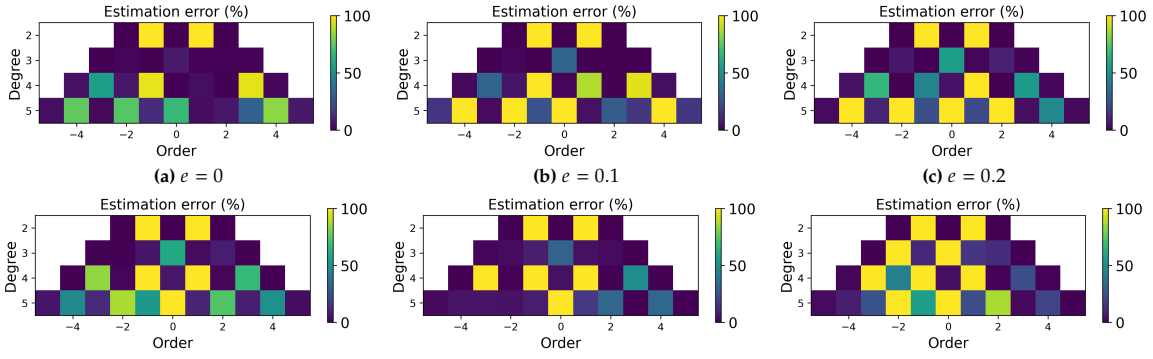

(a) $e = 0$ **(b)** $e = 0.1$ **(c)** $e = 0.2$

(d) $e = 0.3$ **(e)** $e = 0.4$ **(f)** $e = 0.5$

Figure D.5: ORB-2 Test: Estimation error of the SH coefficients degree and order 5 for a propagation time of 1 million seconds for an orbit with $a = 50\ km$ and $i = 30^{o}$

Conclusions

An in-depth analysis conducted with the obtained results is presented in Subsection 5.2.1. This has reached a number of conclusions which can be summarised into the following:

- The accurate estimation of the coefficients with the same degree and order requires orbits to cover the equatorial regions of the asteroid, the precise estimation of null order coefficients requires coverage of its polar regions, and the estimation of the rest of the coefficients requires coverage of the mid-latitude regions. The fulfilment of these requirements can be best accomplished with the

use of polar orbits.

- Orbits with lower semi-major axes experience the effects of the gravity field more strongly and can therefore provide better estimations of the SH coefficients.
- The effect of the eccentricity is highly dependent on the orbital inclination. Higher eccentricities have shown improvement in the estimations for polar orbits, but negative effects in the case of equatorial orbits.

D.1.3. Analysis of the State and Measurements Errors

This subsection presents a set of tests that aim to analyse the effect that measurement and state errors have on the spherical harmonic estimates produced by the UKF. These tests are analysed in Subsection 5.2.2 and this section presents their specifications. Table D.4 illustrates the configuration parameters used in the tests conducted.

Test ERR-1

This test aims to analyse the effect that the errors have on the SH coefficient estimations by including several sets of errors for a fixed orbital trajectory. The settings used in the simulation are presented in Table D.5.

Additionally, velocity measurements have been added to the filter measurement for further analysis. Table D.6 presents the parameters used for that simulation.

Test ERR-2

This test aims to analyse the effect that errors in the gravitational parameter and rotational rate estimation of the asteroid can have on the gravity-field coefficient estimates. The parameters used for the simulation are presented in Table D.7.

Conclusions

These tests and their results have been analysed in Subsection 5.2.2. This has reached a number of conclusions which can be summarised into the following:

- Larger errors in position measurements significantly degrade the accuracy of the coefficient estimates. This particularly affects higher-order coefficients, leading to errors of up to 100%.

Table D.4: ERR test configuration parameters

Propagation	Δt **(s)**	t_{prop} **(s)**		
	1	$1 \cdot 10^6$		
Orbit	a (km)	i (deg)	e (deg)	ν (deg)
	30	90	0	0

Table D.5: ERR1 test configuration parameters

Error	e_r (m)		e_v (m/s)		z_r (m)
	0, 1, 10, 100		0.0, 0.1, 1.0		1, 10, 100
UKF	**Q**				**R**
	$\mathbf{q_{pos}}$	$\mathbf{q_{vel}}$	$\mathbf{q_{Cmn}}$	$\mathbf{q_{Smn}}$	$\sigma_{\mathbf{p}}$
	$1.0 \cdot 10^{-10}$	$1.0 \cdot 10^{-9}$	$1.0 \cdot 10^{-35}$	$1.0 \cdot 10^{-35}$	1.0, 10.0, 100.0

Table D.6: ERR1 test configuration parameters for position and velocity measurements

Error	e_r (m)		e_v (m/s)		z_r (m)	
	0, 1, 10, 100		0.0, 0.1, 1.0		1, 10, 100	
UKF	**Q**				**R**	
	$\mathbf{q_{pos}}$	$\mathbf{q_{vel}}$	$\mathbf{q_{Cmn}}$	$\mathbf{q_{Smn}}$	$\sigma_{\mathbf{z}}$	$\sigma_{\mathbf{v}}$
	$1.0 \cdot 10^{-10}$	$1.0 \cdot 10^{-9}$	$1.0 \cdot 10^{-35}$	$1.0 \cdot 10^{-35}$	1.0, 10.0, 100.0	1.0, 10.0

Furthermore, the incorporation of velocity measurements in the filter has been seen to be beneficial, considerably decreasing the errors in the estimates by having additional information with a different error source.

- A proper uncertainty adjustment considering the errors in the measurements is essential for optimal filter performance.
- Errors in the initial state, when of the same magnitude as the measurement errors, do not significantly affect the estimation of the coefficients.
- Accurate estimation of the asteroid's rotation rate is essential to obtain accurate coefficient estimates. The effect caused by an incorrect rotation rate is reduced with polar orbits having the orbital plane parallel to the rotation axis of the asteroid, resulting in a smaller impact from the rotational rate error.

D.1.4. Analysis of the Frequency Update of the Measurements

This section aims to analyse the effect that the frequency update of the measurements has on the coefficient estimates through the test STEP-1. The configuration parameters of the test are depicted in Table D.8.

Test STEP-1

This test studies the effect of the propagation time step used in the simulation to obtain the measurements of the satellites. Two scenarios have been simulated for different altitudes of satellites. The parameters used in the simulation for a low-altitude orbit are presented in Table D.9 and the coefficient estimates obtained are depicted in Figure 5.12. Additionally, the higher altitude scenario simulation parameters are presented in Table D.10, the results of which can be found in Figure D.6, which present the coefficient estimates for the same orbit computed for a range of time steps. These figures illustrate how the estimation errors increase with the time step used. As can be seen, the filter is able to produce estimates with around 20 coefficients with accuracy for the time steps of one, two and five seconds, while accurate coefficient estimates are reduced to a total of approximately nine for a 30-second time step, four for a minute time step and only three for a two minute time step. This therefore highlights the importance of using a high update frequency of the measurements in the UKF.

Conclusions

This test and its results have been analysed in Subsection 5.2.3. This has reached a number of conclusions which can be summarised into the following:

Table D.7: ERR2 test configuration parameters

Error	e_r (m)		e_v (m/s)		z_r (m)
	0		0.0		10
UKF	**Q**				**R**
	$\mathbf{q_{pos}}$	$\mathbf{q_{vel}}$	$\mathbf{q_{Cmn}}$	$\mathbf{q_{Smn}}$	$\sigma_\mathbf{p}$
	$1.0 \cdot 10^{-10}$	$1.0 \cdot 10^{-9}$	$1.0 \cdot 10^{-35}$	$1.0 \cdot 10^{-35}$	10.0

Table D.8: STEP-1 Test configuration parameters

Propagation	Δt **(s)**			t_{prop} **(s)**	
	1, 5, 60, 120			2,500,000	
Forces	**Eros SH**		**3rd BP**		**SRP**
	$m = 5, n = 5$		None		None
Error	e_r (m)		e_v (m/s)		z_r (m)
	0		0.0		10
UKF	**Q**				**R**
	$\mathbf{q_{pos}}$	$\mathbf{q_{vel}}$	$\mathbf{q_{Cmn}}$	$\mathbf{q_{Smn}}$	$\sigma_\mathbf{p}$
	$1.0 \cdot 10^{-10}$	$1.0 \cdot 10^{-9}$	$1.0 \cdot 10^{-35}$	$1.0 \cdot 10^{-35}$	10.0

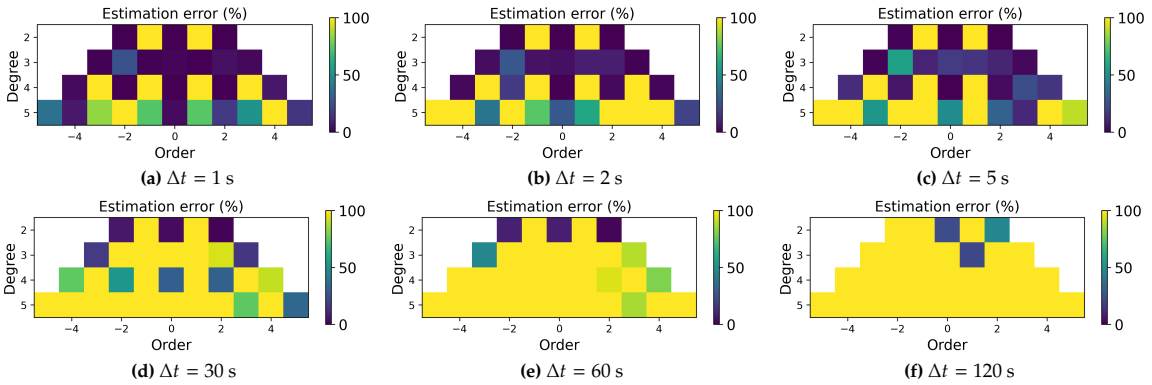

(a) $\Delta t = 1$ s **(b)** $\Delta t = 2$ s **(c)** $\Delta t = 5$ s

(d) $\Delta t = 30$ s **(e)** $\Delta t = 60$ s **(f)** $\Delta t = 120$ s

Figure D.6: STEP-1 Test: Estimation error of the SH coefficients degree and order 5 for 1 million seconds with an a=50 km for a range of time steps

- The measurement update frequency significantly affects the estimation of spherical harmonic coefficients. Smaller update intervals improve filter performance, although they increase the computational load.
- The ideal time step for the filter depends on the satellite's orbit semi-major axis, with smaller steps providing better accuracy by capturing the system's nonlinearities and enhancing filter stability.

D.1.5. Analysis of the Real Scenario Forces

This section presents a set of tests that aim to analyse the effect that the forces considered in the model have on the estimations of the SH coefficients produced by the filter. The configuration parameters used for the tests are depicted in Table D.11.

Test FOR-1

This test analyses the effect that including the point mass gravity of the Sun and the solar radiation pressure. The parameters of the test are presented in Table D.12.

Figure D.7 illustrates the coefficient estimates produced by the filter for a range of semi-major axis considering only the Eros's gravity field, its gravity field, and the point mass perturbations of the Sun, and its gravity field and solar radiation pressure. These show how the filter is able to produce the same

Table D.9: STEP-1.1 Test configuration parameters

Orbit	a (km)	i (deg)	e (deg)	ν (deg)
	30	90	0	0

Table D.10: STEP-1.2 Test configuration parameters

Orbit	a (km)	i (deg)	e (deg)	ν (deg)
	50	90	0	0

Table D.11: FOR-1 Test configuration parameters

Propagation	Δt **(s)**		t_{prop} **(s)**	
	1		$1 \cdot 10^6$	
Orbit	a (km)	i (deg)	e (deg)	ν (deg)
	30	90	0 - 0.5	0
Error	e_r (m)	e_v (m/s)	z_r (m)	
	0	0.0	10	
UKF	**Q**			**R**
	$\mathbf{q_{pos}}$	$\mathbf{q_{vel}}$	$\mathbf{q_{Cmn}}$	$\mathbf{q_{Smn}}$	$\sigma_\mathbf{p}$
	$1.0 \cdot 10^{-10}$	$1.0 \cdot 10^{-9}$	$1.0 \cdot 10^{-35}$	$1.0 \cdot 10^{-35}$	10.0

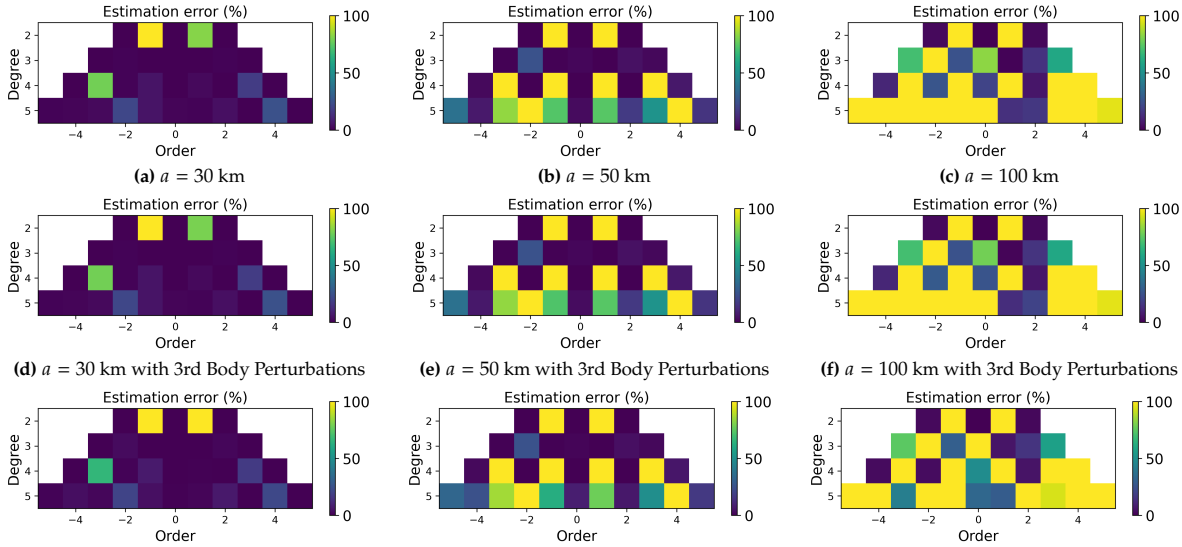

(a) $a = 30$ km **(b)** $a = 50$ km **(c)** $a = 100$ km

(d) $a = 30$ km with 3rd Body Perturbations **(e)** $a = 50$ km with 3rd Body Perturbations **(f)** $a = 100$ km with 3rd Body Perturbations

(g) $a = 30$ km with SRP **(h)** $a = 50$ km with SRP **(i)** $a = 100$ km with SRP

Figure D.7: FOR-1 Test: Estimation error of degree and order 5 for 1 million seconds considering the 3rd body perturbation of the Sun and Solar Radiation Pressure

estimates independently of the forces considered for the case of a 30 km semi-major axis. Furthermore, it can be observed that the 3rd body perturbation does not have a relevant effect in either of the orbital configurations. However, the SRP effect, while being very low given that these tests are inside of the Bruillin sphere, it is noticeable and increases with the semi-major axis.

Test FOR-2

This test analyses the effect that the degree of the spherical harmonic coefficients used for the simulation of the real gravity field has on the coefficients estimates produced by the filer. The parameters of the test are presented in Table D.13.

The estimates of the SH coefficients are illustrated in Figure D.8. The plots depict how the larger the degree and order used to model the true gravity field of the asteroid, the larger errors in the coefficient estimates produced by the UKF. This effect is particularly noticeable for a low semi-major axis orbit (30 km) when increasing from a 5-degree to a 9-degree model, which introduces considerable errors in 5 coefficient estimates. As the semi-major axis of the orbit increases, the effect is lower, which is to be expected given that larger altitudes have more difficulty in producing accurate estimates of the gravity field. Furthermore, it can be observed that an increase from a 9-degree to a 15-degree SH model has a lower effect on the estimates.

Conclusions

This test and its results have been analysed in Subsection 5.2.4. This has reached a number of conclusions which can be summarised into the following:

- Having considered orbits inside of the Brillouin sphere, the dominant force is that of the asteroid. Consequently, it has been seen that the third-body perturbation of the Sun has no effect on coefficient estimation. Moreover, this is also the case for the Solar Radiation Pressure, which does

Table D.12: FOR-1 Test configuration parameters

Forces	Eros SH	3rd BP	SRP
	$m = 5, n = 5$	True	True

Table D.13: FOR-2 Test configuration parameters

Forces	Eros SH	3rd BP	SRP
	$m = 5, 9, 15, n = 5, 9, 15$	True	True

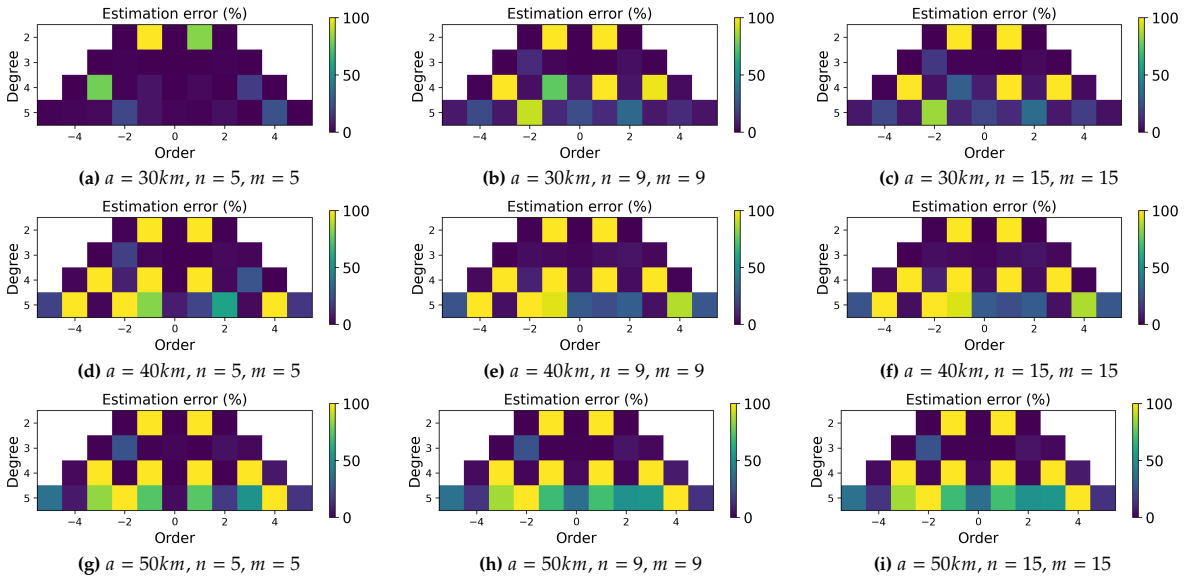

(a) $a = 30km, n = 5, m = 5$ **(b)** $a = 30km, n = 9, m = 9$ **(c)** $a = 30km, n = 15, m = 15$

(d) $a = 40km, n = 5, m = 5$ **(e)** $a = 40km, n = 9, m = 9$ **(f)** $a = 40km, n = 15, m = 15$

(g) $a = 50km, n = 5, m = 5$ **(h)** $a = 50km, n = 9, m = 9$ **(i)** $a = 50km, n = 15, m = 15$

Figure D.8: FOR-2 Test: Estimation error of the degree and order 5 for 1 million seconds considering different degrees and order of spherical harmonics for the simulation of the true gravity field.

not present a significant contribution in the coefficient estimation for orbits with semi-major axis smaller than 100 km.

- It has been confirmed that as concluded in previous tests, accurate estimation of high degree and order coefficients requires low semi-major axis orbits.

D.2. Sensitivity Analysis: Satellite Constellation

This section presents the analysis done for a scenario considering a constellation of satellites orbiting Eros. Subsection D.2.1 details the design of three filter configurations to be tested and analysed with the different constellation sensitivity analysis. In addition, an analysis of the effect of the satellite distribution along the constellation is shown in Subsection D.2.2, followed by an analysis of the number of satellites present in the constellation in Subsection D.2.3. Additionally, Subsection D.2.4 presents an analysis of the effects that the measurement frequency and the orbital propagation have on the UKF estimation.

D.2.1. Design of the Filter

This section presents the design of three different filter configurations. It should be noted that the equations presented are made for a constellation composed of a mothership and two CubeSats. However, the filter algorithms have been implemented for a variable number of CubeSats selected by the user.

Configuration 1

This design consists of the transmission of the position of each of the satellites at each time step to the mothership. Then the mothership would use a UKF algorithm with the states of the satellites and its own to estimate the spherical harmonics coefficients.

The Unscented Kalman filter used for the coefficient estimation for a single data presents the following characteristics, where the state contains the position, velocity, C and S coefficients, and the measurements are the position of the satellite.

The state vector of the filter is as follows:

$$\mathbf{x}_k = \begin{pmatrix} \mathbf{x_M}_A \\ \dot{\mathbf{x}}_{\mathbf{M}A} \\ \mathbf{x_{C1}}_A \\ \dot{\mathbf{x}}_{\mathbf{C1}A} \\ \mathbf{x_{C2}}_A \\ \dot{\mathbf{x}}_{\mathbf{C2}A} \\ \mathbf{c_{nm}} \\ \mathbf{s_{nm}} \end{pmatrix} \tag{D.6}$$

where it can be seen that the filter propagates the states of the mothership and the CubeSats, as well as the SH coefficients. Furthermore, the measurements vector is presented by the following equation:

$$\mathbf{z}_k = \begin{pmatrix} \mathbf{x_M}_A \\ \mathbf{x_{C1}}_A \\ \mathbf{x_{C2}}_A \end{pmatrix} + \begin{pmatrix} \boldsymbol{\sigma_{p_M}} \\ \boldsymbol{\sigma_{p_{C1}}} \\ \boldsymbol{\sigma_{p_{C2}}} \end{pmatrix} \tag{D.7}$$

where the measurement noise of the mothership is defined as $\boldsymbol{\sigma_{p_M}} = (\sigma_{p_M}\ \sigma_{p_M}\ \sigma_{p_M})^T$, and the measurement noise of the CubeSats are defined as $\boldsymbol{\sigma_{p_{C1}}} = (\sigma_{p_{C1}}\ \sigma_{p_{C1}}\ \sigma_{p_{C1}})^T$ and $\boldsymbol{\sigma_{p_{C2}}} = (\sigma_{p_{C2}}\ \sigma_{p_{C2}}\ \sigma_{p_{C2}})^T$ respectively. Moreover, the **P**, **Q**, and **R** matrices are defined as follows:

$$\mathbf{P} = \begin{bmatrix} \mathbf{I}_{3\times3}\cdot p_{pos} & \mathbf{0}_{3\times3} & \mathbf{0}_{3\times3} & \mathbf{0}_{3\times3} & \mathbf{0}_{3\times3} & \mathbf{0}_{3\times3} & \mathbf{0}_{3\times n_C} & \mathbf{0}_{3\times n_S} \\ \mathbf{0}_{3\times3} & \mathbf{I}_{3\times3}\cdot p_{vel} & \mathbf{0}_{3\times3} & \mathbf{0}_{3\times3} & \mathbf{0}_{3\times3} & \mathbf{0}_{3\times3} & \mathbf{0}_{3\times n_C} & \mathbf{0}_{3\times n_S} \\ \mathbf{0}_{3\times3} & \mathbf{0}_{3\times3} & \mathbf{I}_{3\times3}\cdot p_{vel} & \mathbf{0}_{3\times3} & \mathbf{0}_{3\times3} & \mathbf{0}_{3\times3} & \mathbf{0}_{3\times n_C} & \mathbf{0}_{3\times n_S} \\ \mathbf{0}_{3\times3} & \mathbf{0}_{3\times3} & \mathbf{0}_{3\times3} & \mathbf{I}_{3\times3}\cdot p_{vel} & \mathbf{0}_{3\times3} & \mathbf{0}_{3\times3} & \mathbf{0}_{3\times n_C} & \mathbf{0}_{3\times n_S} \\ \mathbf{0}_{3\times3} & \mathbf{0}_{3\times3} & \mathbf{0}_{3\times3} & \mathbf{0}_{3\times3} & \mathbf{I}_{3\times3}\cdot p_{vel} & \mathbf{0}_{3\times3} & \mathbf{0}_{3\times n_C} & \mathbf{0}_{3\times n_S} \\ \mathbf{0}_{3\times3} & \mathbf{0}_{3\times3} & \mathbf{0}_{3\times3} & \mathbf{0}_{3\times3} & \mathbf{0}_{3\times3} & \mathbf{I}_{3\times3}\cdot p_{vel} & \mathbf{0}_{3\times n_C} & \mathbf{0}_{3\times n_S} \\ \mathbf{0}_{n_C\times3} & \mathbf{0}_{n_C\times3} & \mathbf{0}_{n_C\times3} & \mathbf{0}_{n_C\times3} & \mathbf{0}_{n_C\times3} & \mathbf{0}_{n_C\times3} & \mathbf{I}_{n_C\times n_C}\cdot p_{Cmn} & \mathbf{0}_{n_C\times n_S} \\ \mathbf{0}_{n_S\times3} & \mathbf{0}_{n_S\times3} & \mathbf{0}_{n_S\times3} & \mathbf{0}_{n_S\times3} & \mathbf{0}_{n_S\times3} & \mathbf{0}_{n_S\times3} & \mathbf{0}_{n_S\times n_C} & \mathbf{I}_{n_S\times n_S}\cdot p_{Smn} \end{bmatrix} \tag{D.8}$$

$$\mathbf{Q} = \begin{bmatrix} \mathbf{I}_{3\times3}\cdot q_{pos} & \mathbf{0}_{3\times3} & \mathbf{0}_{3\times3} & \mathbf{0}_{3\times3} & \mathbf{0}_{3\times3} & \mathbf{0}_{3\times3} & \mathbf{0}_{3\times n_C} & \mathbf{0}_{3\times n_S} \\ \mathbf{0}_{3\times3} & \mathbf{I}_{3\times3}\cdot q_{vel} & \mathbf{0}_{3\times3} & \mathbf{0}_{3\times3} & \mathbf{0}_{3\times3} & \mathbf{0}_{3\times3} & \mathbf{0}_{3\times n_C} & \mathbf{0}_{3\times n_S} \\ \mathbf{0}_{3\times3} & \mathbf{0}_{3\times3} & \mathbf{I}_{3\times3}\cdot q_{vel} & \mathbf{0}_{3\times3} & \mathbf{0}_{3\times3} & \mathbf{0}_{3\times3} & \mathbf{0}_{3\times n_C} & \mathbf{0}_{3\times n_S} \\ \mathbf{0}_{3\times3} & \mathbf{0}_{3\times3} & \mathbf{0}_{3\times3} & \mathbf{I}_{3\times3}\cdot q_{vel} & \mathbf{0}_{3\times3} & \mathbf{0}_{3\times3} & \mathbf{0}_{3\times n_C} & \mathbf{0}_{3\times n_S} \\ \mathbf{0}_{3\times3} & \mathbf{0}_{3\times3} & \mathbf{0}_{3\times3} & \mathbf{0}_{3\times3} & \mathbf{I}_{3\times3}\cdot q_{vel} & \mathbf{0}_{3\times3} & \mathbf{0}_{3\times n_C} & \mathbf{0}_{3\times n_S} \\ \mathbf{0}_{3\times3} & \mathbf{0}_{3\times3} & \mathbf{0}_{3\times3} & \mathbf{0}_{3\times3} & \mathbf{0}_{3\times3} & \mathbf{I}_{3\times3}\cdot q_{vel} & \mathbf{0}_{3\times n_C} & \mathbf{0}_{3\times n_S} \\ \mathbf{0}_{n_C\times3} & \mathbf{0}_{n_C\times3} & \mathbf{0}_{n_C\times3} & \mathbf{0}_{n_C\times3} & \mathbf{0}_{n_C\times3} & \mathbf{0}_{n_C\times3} & \mathbf{I}_{n_C\times n_C}\cdot q_{Cmn} & \mathbf{0}_{n_C\times n_S} \\ \mathbf{0}_{n_S\times3} & \mathbf{0}_{n_S\times3} & \mathbf{0}_{n_S\times3} & \mathbf{0}_{n_S\times3} & \mathbf{0}_{n_S\times3} & \mathbf{0}_{n_S\times3} & \mathbf{0}_{n_S\times n_C} & \mathbf{I}_{n_S\times n_S}\cdot q_{Smn} \end{bmatrix} \tag{D.9}$$

$$\mathbf{R} = \begin{bmatrix} \mathbf{I}_{3\times3}\cdot\sigma^2_{p_M} & \mathbf{0}_{3\times3} & \mathbf{0}_{3\times3} \\ \mathbf{0}_{3\times3} & \mathbf{I}_{3\times3}\cdot\sigma^2_{p_{C1}} & \mathbf{0}_{3\times3} \\ \mathbf{0}_{3\times3} & \mathbf{0}_{3\times3} & \mathbf{I}_{3\times3}\cdot\sigma^2_{p_{C2}} \end{bmatrix} \tag{D.10}$$

Configuration 2

This design considers using the UKF algorithm for each satellite to estimate the spherical harmonic coefficients and transmit the estimations to the mothership. Then apply a new UKF algorithm using the mean value of the SH coefficient estimations received from the CubeSats and the state of the mothership to refine the estimation and obtain the final SH coefficient estimates.

The state vector of the filter is as follows:

$$\mathbf{x}_k = \begin{pmatrix} \mathbf{x_M}_A \\ \dot{\mathbf{x}}_{\mathbf{M}A} \\ \mathbf{c_{nm}} \\ \mathbf{s_{nm}} \end{pmatrix} \tag{D.11}$$

where it can be seen that the filter propagates the states of the mothership as well as the SH coefficients. Furthermore, the measurements vector is presented by the following equation:

$$\mathbf{z}_k = \begin{pmatrix} \mathbf{x_M}_A \\ \mathbf{c_{nm}} \\ \mathbf{s_{nm}} \end{pmatrix} + \begin{pmatrix} \boldsymbol{\sigma_p} \\ \boldsymbol{\sigma_c} \\ \boldsymbol{\sigma_s} \end{pmatrix} \tag{D.12}$$

where the measurement noise of the mothership is defined as $\boldsymbol{\sigma_{p_M}} = (\sigma_{p_M}\ \sigma_{p_M}\ \sigma_{p_M})^T$, and the measurement noise of the SH average coefficients estimated by the Cubesats are presented by the vectors $\boldsymbol{\sigma_{p_c}}$ and $\boldsymbol{\sigma_{p_s}}$. Moreover, the **P**, **Q**, and **R** matrices are defined as follows:

$$\mathbf{P} = \begin{bmatrix} \mathbf{I}_{3\times3} \cdot p_{pos} & \mathbf{0}_{3\times3} & \mathbf{0}_{3\times n_C} & \mathbf{0}_{3\times n_S} \\ \mathbf{0}_{3\times3} & \mathbf{I}_{3\times3} \cdot p_{vel} & \mathbf{0}_{3\times n_C} & \mathbf{0}_{3\times n_S} \\ \mathbf{0}_{n_C\times3} & \mathbf{0}_{n_C\times3} & \mathbf{I}_{n_C\times n_C} \cdot p_{Cmn} & \mathbf{0}_{n_C\times n_S} \\ \mathbf{0}_{n_S\times3} & \mathbf{0}_{n_S\times3} & \mathbf{0}_{n_S\times n_C} & \mathbf{I}_{n_S\times n_S} \cdot p_{Smn} \end{bmatrix} \tag{D.13}$$

$$\mathbf{Q} = \begin{bmatrix} \mathbf{I}_{3\times3} \cdot q_{pos} & \mathbf{0}_{3\times3} & \mathbf{0}_{3\times n_C} & \mathbf{0}_{3\times n_S} \\ \mathbf{0}_{3\times3} & \mathbf{I}_{3\times3} \cdot q_{vel} & \mathbf{0}_{3\times n_C} & \mathbf{0}_{3\times n_S} \\ \mathbf{0}_{n_C\times3} & \mathbf{0}_{n_C\times3} & \mathbf{I}_{n_C\times n_C} \cdot q_{Cmn} & \mathbf{0}_{n_C\times n_S} \\ \mathbf{0}_{n_S\times3} & \mathbf{0}_{n_S\times3} & \mathbf{0}_{n_S\times n_C} & \mathbf{I}_{n_S\times n_S} \cdot q_{Smn} \end{bmatrix} \tag{D.14}$$

$$\mathbf{R} = \begin{bmatrix} \mathbf{I}_{3\times3} \cdot \sigma_p^2 & \mathbf{0}_{3\times n_C} & \mathbf{0}_{3\times n_S} \\ \mathbf{0}_{n_C\times3} & \mathbf{I}_{n_C\times n_C} \cdot \sigma_c^2 & \mathbf{0}_{n_C\times n_S} \\ \mathbf{0}_{n_S\times3} & \mathbf{0}_{n_S\times n_C} & \mathbf{I}_{n_S\times n_S} \cdot \sigma_s^2 \end{bmatrix} \tag{D.15}$$

Configuration 3

This design considers using the UKF algorithm for each satellite to estimate the spherical harmonic coefficients and transmit the estimations to the mothership after the final estimation is done. Then apply a new UKF algorithm using the coefficients estimations and the state of the mothership to refine the estimation.

The state vector of the filter is as follows:

$$\mathbf{x}_k = \begin{pmatrix} \mathbf{x_M}_A \\ \dot{\mathbf{x}}_{\mathbf{M}A} \\ \mathbf{c_{nm}} \\ \mathbf{s_{nm}} \end{pmatrix} \tag{D.16}$$

where it can be seen that the filter propagates the states of the mothership as well as the SH coefficients. Furthermore, the measurements vector is presented by the following equation:

$$\mathbf{z}_k = \begin{pmatrix} \mathbf{x_M}_A \\ \mathbf{c_{nm}}_{C1} \\ \mathbf{s_{nm}}_{C1} \\ \mathbf{c_{nm}}_{C2} \\ \mathbf{s_{nm}}_{C2} \end{pmatrix} + \begin{pmatrix} \boldsymbol{\sigma_p} \\ \boldsymbol{\sigma_c} \\ \boldsymbol{\sigma_s} \\ \boldsymbol{\sigma_c} \\ \boldsymbol{\sigma_s} \end{pmatrix} \tag{D.17}$$

where the measurement noise of the mothership is defined as $\boldsymbol{\sigma_{p_M}} = (\sigma_{p_M}\ \sigma_{p_M}\ \sigma_{p_M})^T$, and the measurement noise of the SH coefficients estimated by the Cubesats are presented by the vectors $\boldsymbol{\sigma_{p_c}}$ and $\boldsymbol{\sigma_{p_s}}$. Moreover, the **P**, **Q**, and **R** matrices are defined as follows:

$$\mathbf{P} = \begin{bmatrix} \mathbf{I}_{3\times3} \cdot p_{pos} & \mathbf{0}_{3\times3} & \mathbf{0}_{3\times n_C} & \mathbf{0}_{3\times n_S} \\ \mathbf{0}_{3\times3} & \mathbf{I}_{3\times3} \cdot p_{vel} & \mathbf{0}_{3\times n_C} & \mathbf{0}_{3\times n_S} \\ \mathbf{0}_{n_C\times3} & \mathbf{0}_{n_C\times3} & \mathbf{I}_{n_C\times n_C} \cdot p_{Cmn} & \mathbf{0}_{n_C\times n_S} \\ \mathbf{0}_{n_S\times3} & \mathbf{0}_{n_S\times3} & \mathbf{0}_{n_S\times n_C} & \mathbf{I}_{n_S\times n_S} \cdot p_{Smn} \end{bmatrix} \tag{D.18}$$

$$\mathbf{Q} = \begin{bmatrix} \mathbf{I}_{3\times3} \cdot q_{pos} & \mathbf{0}_{3\times3} & \mathbf{0}_{3\times n_C} & \mathbf{0}_{3\times n_S} \\ \mathbf{0}_{3\times3} & \mathbf{I}_{3\times3} \cdot q_{vel} & \mathbf{0}_{3\times n_C} & \mathbf{0}_{3\times n_S} \\ \mathbf{0}_{n_C\times3} & \mathbf{0}_{n_C\times3} & \mathbf{I}_{n_C\times n_C} \cdot q_{Cmn} & \mathbf{0}_{n_C\times n_S} \\ \mathbf{0}_{n_S\times3} & \mathbf{0}_{n_S\times3} & \mathbf{0}_{n_S\times n_C} & \mathbf{I}_{n_S\times n_S} \cdot q_{Smn} \end{bmatrix} \tag{D.19}$$

$$\mathbf{R} = \begin{bmatrix} \mathbf{I}_{3\times3}\cdot\sigma_p^2 & \mathbf{0}_{3\times n_C} & \mathbf{0}_{3\times n_S} & \mathbf{0}_{3\times n_C} & \mathbf{0}_{3\times n_S} \\ \mathbf{0}_{n_C\times3} & \mathbf{I}_{n_C\times n_C}\cdot\sigma_c^2 & \mathbf{0}_{n_C\times n_S} & \mathbf{0}_{n_C\times n_C} & \mathbf{0}_{n_C\times n_S} \\ \mathbf{0}_{n_S\times3} & \mathbf{0}_{n_S\times n_C} & \mathbf{I}_{n_S\times n_S}\cdot\sigma_s^2 & \mathbf{0}_{n_S\times n_C} & \mathbf{0}_{n_S\times n_S} \\ \mathbf{0}_{n_C\times3} & \mathbf{0}_{n_C\times n_C} & \mathbf{0}_{n_C\times n_S} & \mathbf{I}_{n_C\times n_C}\cdot\sigma_c^2 & \mathbf{0}_{n_C\times n_S} \\ \mathbf{0}_{n_S\times3} & \mathbf{0}_{n_S\times n_C} & \mathbf{0}_{n_S\times n_S} & \mathbf{0}_{n_S\times n_C} & \mathbf{I}_{n_S\times n_S}\cdot\sigma_s^2 \end{bmatrix} \tag{D.20}$$

D.2.2. Analysis of the Distribution of the Satellites

This section aims to analyse the effect that the distribution of the satellites in the constellation orbiting Eros has on the coefficient estimates. Table D.14 presents the configuration parameters used for this scenario testing.

Test DIST-1

This test has been designed to analyse the effect that the distribution of the satellites of the constellation has along the true anomaly for the three UKF designs. It has been split into two scenarios: the first has the satellites spread out evenly along the 360° and the second places the satellites of the constellation closely together.

The first scenario places the satellites at ν 0, 120 and 240°. The specific parameters of the test are presented in Table D.15. In particular, this test has considered three cases, by placing the mothership in each of the presented orbits and the other two CubeSats in the rest. The first scenario places the satellites at ν 0, 10 and 20°. The parameters of the test are presented in Table D.16.

Figure D.11 presents the coefficient estimates produced by each of the satellites of the constellation individually, where it can be observed how each satellite trajectory leads to different errors in the estimates produced by the filter, being $\nu = 240°$ the best performing. Furthermore, the resulting coefficient estimates for all the scenario cases are presented in Figure D.12. The results show how, as expected, when the C1 filter is used the mothership orbit within the constellation is irrelevant. However, this is not the case in the C2 and C3 filters, since their designs rely on the trajectory of the mothership and the coefficient estimates produced by the CubeSats in the constellation. For instance, this can be observed in Figure D.10h, which shows better estimates for a mothership in $\nu = 240°$, which is the orbit that when used as a single satellite has provided the most accurate estimates. Furthermore, C3 shows a better performance than C2, which is indicative that using all the cosine and sine coefficient estimates produced by both CubeSats leads to better results than using their mean value, as is done in C2.

Table D.14: DIST test general configuration parameters

Propagation	Δt **(s)**			t_{prop} **(s)**		
	1			$1\cdot10^6$		
Forces	**Eros SH**		**3rd BP**		**SRP**	
	$m = 15, n = 15$		True		True	
Error	e_r (m)		e_v (m/s)		z_r (m)	
	0		0.0		10.0	
UKF Const. 1	**Q**				**R**	
	$\mathbf{q_{pos}}$	$\mathbf{q_{vel}}$	$\mathbf{q_{Cmn}}$	$\mathbf{q_{Smn}}$	$\sigma_\mathbf{p}$	
	$1.0\cdot10^{-10}$	$1.0\cdot10^{-9}$	$1.0\cdot10^{-35}$	$1.0\cdot10^{-35}$	10.0	
UKF Const. 2	**Q**				**R**	
	$\mathbf{q_{pos}}$	$\mathbf{q_{vel}}$	$\mathbf{q_{Cmn}}$	$\mathbf{q_{Smn}}$	$\sigma_\mathbf{p}$	$\sigma_\mathbf{C}$, $\sigma_\mathbf{S}$
	$1.0\cdot10^{-10}$	$1.0\cdot10^{-9}$	$1.0\cdot10^{-35}$	$1.0\cdot10^{-35}$	10.0	0.01
UKF Const. 3	**Q**				**R**	
	$\mathbf{q_{pos}}$	$\mathbf{q_{vel}}$	$\mathbf{q_{Cmn}}$	$\mathbf{q_{Smn}}$	$\sigma_\mathbf{p}$	$\sigma_\mathbf{C}$, $\sigma_\mathbf{S}$
	$1.0\cdot10^{-10}$	$1.0\cdot10^{-9}$	$1.0\cdot10^{-35}$	$1.0\cdot10^{-35}$	10.0	0.01

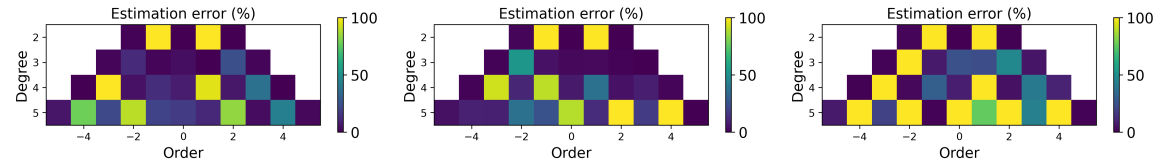

(a) $\nu = 0^o$ **(b)** $\nu = 10^o$ **(c)** $\nu = 20^o$

Figure D.11: DIST-1.2 Test: Estimation error of the SH coefficients degree and order 5 for 1 million seconds for single satellites.

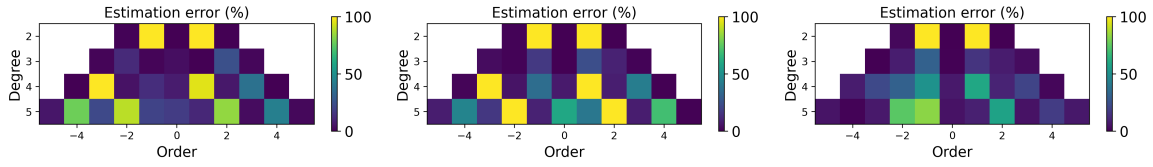

(a) $\nu = 0^o$ **(b)** $\nu = 120^o$ **(c)** $\nu = 240^o$

Figure D.9: DIST-1.1 Test: Estimation error of the SH coefficients degree and order 5 for 1 million seconds for single satellites.

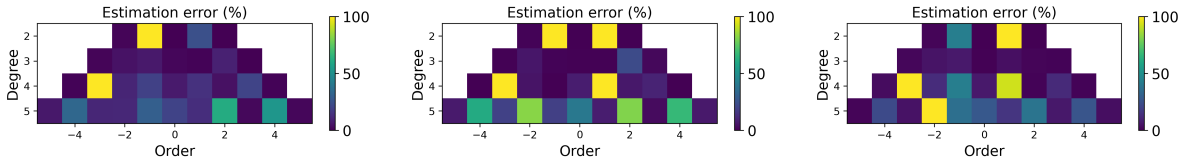

(a) C1, mothership with $\nu = 0^o$ **(b)** C2, mothership with $\nu = 0^o$ **(c)** C3, mothership with $\nu = 0^o$

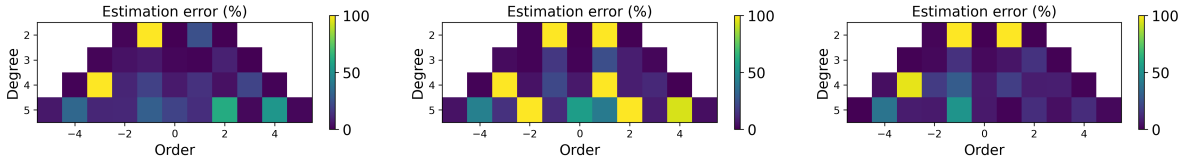

(d) C1, mothership with $\nu = 120^o$ **(e)** C2, mothership with $\nu = 120^o$ **(f)** C3, mothership with $\nu = 120^o$

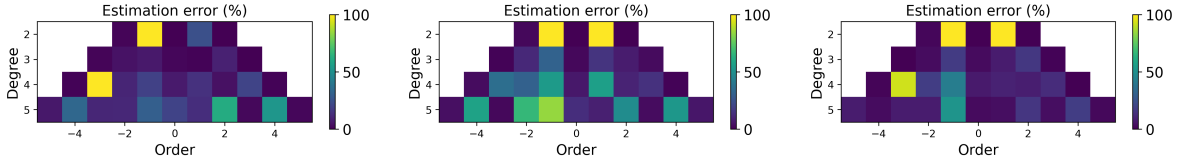

(g) C1, mothership with $\nu = 240^o$ **(h)** C2, mothership with $\nu = 240^o$ **(i)** C3, mothership with $\nu = 240^o$

Figure D.10: DIST-1.1 Test: Estimation error of the SH coefficients degree and order 5 for 1 million seconds for the constellation.

Test DIST-2

This test has been designed to analyse the effect that the distribution of the satellites of the constellation has along the inclination for the three UKF designs. The parameters of the test scenario are presented in Table D.17.

Figure D.13 presents the coefficient estimates produced by each of the satellites of the constellation individually, which shows that the filter produces highly inaccurate coefficient estimates for the satellite orbiting with 30° inclination. This has a considerable effect on the coefficient estimates for all the

Table D.15: DIST-1.1 test configuration parameters

	a (km)	i (deg)	e (deg)	ν (deg)
Orbit	30	90	0	0, 120, 240

Table D.16: DIST-1.2 test configuration parameters

	a (km)	i (deg)	e (deg)	ν (deg)
Orbit	30	90	0	0, 10, 20

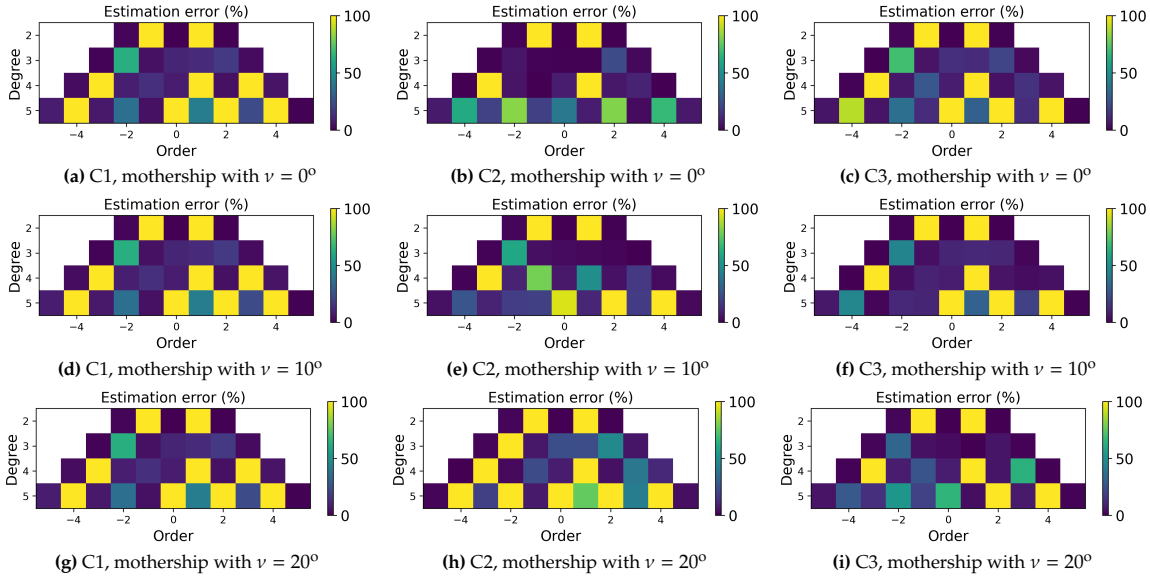

(a) C1, mothership with $\nu = 0^o$ **(b)** C2, mothership with $\nu = 0^o$ **(c)** C3, mothership with $\nu = 0^o$

(d) C1, mothership with $\nu = 10^o$ **(e)** C2, mothership with $\nu = 10^o$ **(f)** C3, mothership with $\nu = 10^o$

(g) C1, mothership with $\nu = 20^o$ **(h)** C2, mothership with $\nu = 20^o$ **(i)** C3, mothership with $\nu = 20^o$

Figure D.12: DIST-1.2 Test: Estimation error of the SH coefficients degree and order 5 for 1 million seconds for the constellation.

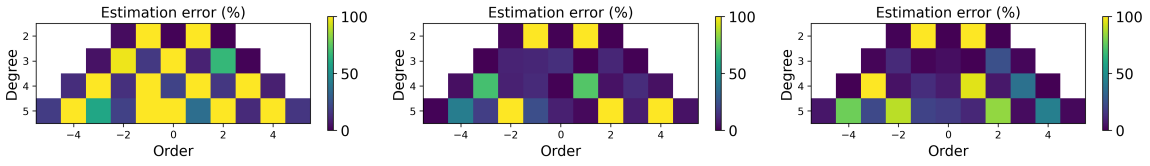

(a) $i = 30^o$ **(b)** $i = 60^o$ **(c)** $i = 90^o$

Figure D.13: DIST-2 Test: Estimation error of the SH coefficients degree and order 5 for 1 million seconds for single satellites.

scenario cases with the constellation that are presented in Figure D.14. As can be observed, the C2 filter with the mothership with $i = 30°$ presents very poor estimates since it relies heavily on the mothership's orbit, whereas the same design presents much better estimates using the mothership in the remaining orbits. The opposite can be observed for the C3 filter, which shows how the filter relies more on the SH coefficients estimated by the CubeSats, thus presenting only high-error estimates when one of the CubeSats orbits with an inclination of 30°. In addition, the results show how the C1 design is able to obtain adequate estimates in all cases, which demonstrates that the use of the position of the three satellites at the same time makes the filter more dependable than the other designs.

Test DIST-3

This test has been designed to analyse the effect that the distribution of the satellites of the constellation has along the semi-major axis for the three UKF designs. The parameters of the test scenario are presented in Table D.18.

It should be noted that Figure D.15 presents the coefficient estimates produced by each of the satellites of the constellation individually. Furthermore, the resulting coefficient estimates for all the scenario cases are presented in Figure D.16.

Table D.17: DIST-2 test configuration parameters

	a (km)	i (deg)	e (deg)	ν (deg)
Orbit	30	30, 60, 90	0	0

Table D.18: DIST-3 test configuration parameters

	a (km)	i (deg)	e (deg)	ν (deg)
Orbit	30, 35, 40	90	0	0

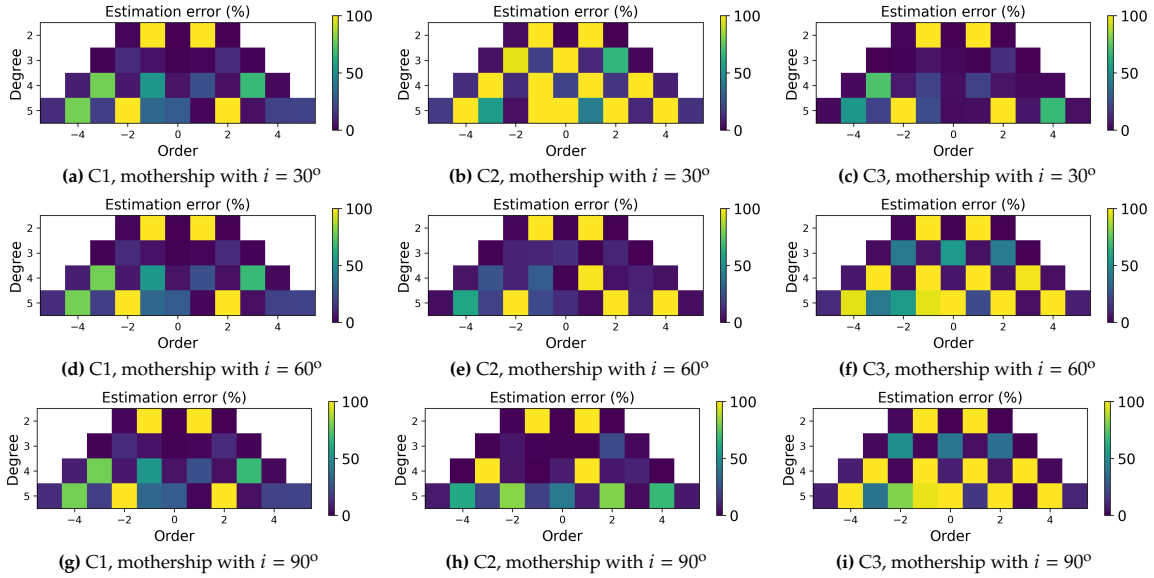

(a) C1, mothership with $i = 30^o$ **(b)** C2, mothership with $i = 30^o$ **(c)** C3, mothership with $i = 30^o$

(d) C1, mothership with $i = 60^o$ **(e)** C2, mothership with $i = 60^o$ **(f)** C3, mothership with $i = 60^o$

(g) C1, mothership with $i = 90^o$ **(h)** C2, mothership with $i = 90^o$ **(i)** C3, mothership with $i = 90^o$

Figure D.14: DIST-2 Test: Estimation error of the SH coefficients degree and order 5 for 1 million seconds for the constellation for satellites distributed along different inclinations.

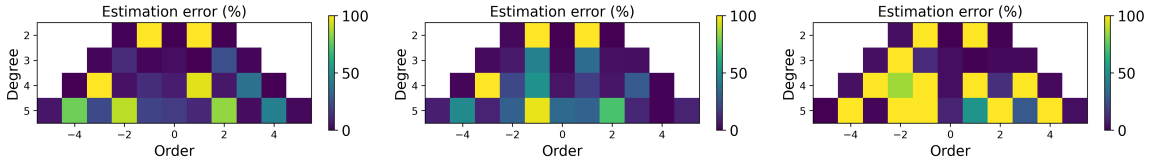

(a) 30 km **(b)** 35 km **(c)** 40 km

Figure D.15: DIST-3 Test: Estimation error of the SH coefficients degree and order 5 for 1 million seconds for single satellites.

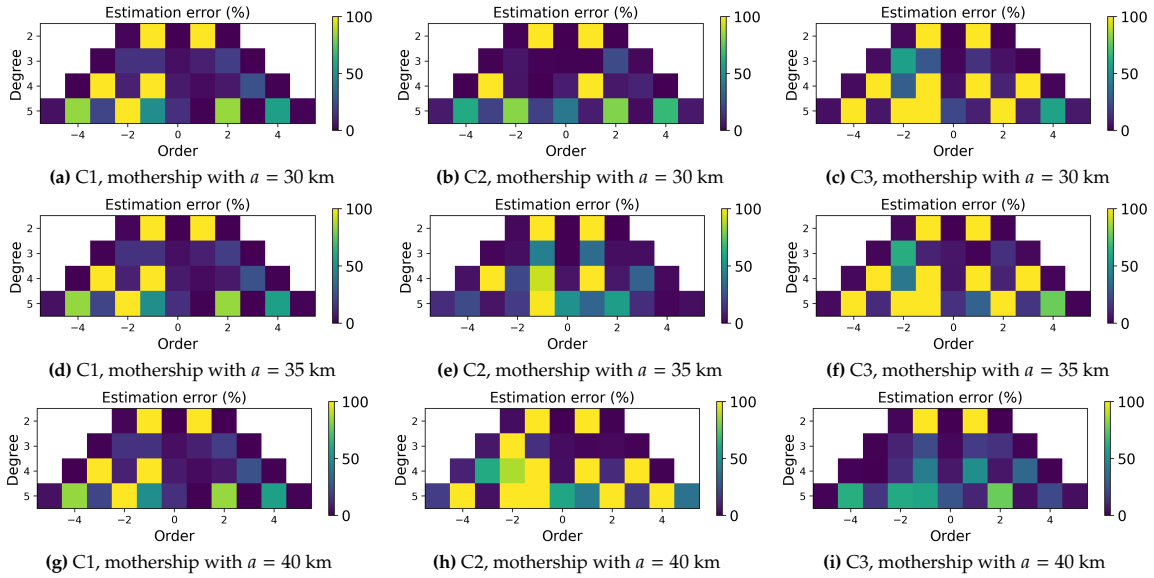

(a) C1, mothership with $a = 30$ km **(b)** C2, mothership with $a = 30$ km **(c)** C3, mothership with $a = 30$ km

(d) C1, mothership with $a = 35$ km **(e)** C2, mothership with $a = 35$ km **(f)** C3, mothership with $a = 35$ km

(g) C1, mothership with $a = 40$ km **(h)** C2, mothership with $a = 40$ km **(i)** C3, mothership with $a = 40$ km

Figure D.16: DIST-3 Test: Estimation error of the SH coefficients degree and order 5 for 1 million seconds for the constellation.

Conclusions

An in-depth analysis conducted with the obtained results is presented in Subsection 5.3.2, where the following conclusions have been reached:

- No single UKF configuration design performs best in all scenarios. The effectiveness of each design depends on the specific orbital characteristics of the CubeSats and the mothership.
- The C1 configuration is reliable, being able to combine the position measurements of all the

satellites equally. This leads to very accurate estimates when all the orbits are adequate. However, if one or more of the orbits have poor coverage, the overall estimation accuracy suffers. Furthermore, the orbit of the mothership does not affect the performance when using this UKF design.

- Configuration C2 is highly dependent on the mothership's orbit. This UFK design performs well when the orbit of the mothership has good coverage, leading to accurate estimates. The SH coefficient estimates of the other orbits improve the estimations of the filter. However, if these estimates are inaccurate, the overall estimation quality decreases slightly. Conversely, if the SH estimates are accurate but the mothership's orbit is inadequate, the final constellation estimation becomes unreliable. This is because the filter relies more on the mothership's position measurements than on SH coefficient estimates from other satellites.
- Configuration C3 excels when the spherical harmonic measurements from the CubeSats have low error rates. In such cases, even if the mothership's position measurements are inadequate, the filter can still produce good estimates by relying on data from other satellites. Therefore, this design is highly dependent on the accuracy of the CubeSats' SH estimates.

D.2.3. Analysis of the Number of Satellites

This section aims to analyse the effect that the number of satellites has on the estimates produced by each filter design. The main configuration parameters of the test are depicted in Table D.19.

Test NUM-1

This test contains the computations of a number of scenarios considering different numbers of satellites in the constellation. The details on the orbital parameters of each test are presented in Table D.20 for the case of 2 CubeSats, Table D.21 for the case of 4 CubeSats, Table D.22 for the case of 6 CubeSats, and Table D.23 for the case of 8 CubeSats.

Figure D.17 presents the SH coefficient estimates produced by the filters in the different configurations.

Table D.19: NUM test configuration parameters

Propagation	Δt **(s)**			t_{prop} **(s)**		
	1			$1 \cdot 10^6$		
Forces	**Eros SH**		**3rd BP**		**SRP**	
	$m = 15, n = 15$		True		True	
Error	e_r (m)		e_v (m/s)		z_r (m)	
	0		0.0		10.0	
UKF Const. 1	**Q**				**R**	
	$\mathbf{q_{pos}}$	$\mathbf{q_{vel}}$	$\mathbf{q_{Cmn}}$	$\mathbf{q_{Smn}}$	$\sigma_{\mathbf{p}}$	
	$1.0 \cdot 10^{-10}$	$1.0 \cdot 10^{-9}$	$1.0 \cdot 10^{-35}$	$1.0 \cdot 10^{-35}$	10.0	
UKF Const. 2	**Q**				**R**	
	$\mathbf{q_{pos}}$	$\mathbf{q_{vel}}$	$\mathbf{q_{Cmn}}$	$\mathbf{q_{Smn}}$	$\sigma_{\mathbf{p}}$	$\sigma_{\mathbf{C}}, \sigma_{\mathbf{S}}$
	$1.0 \cdot 10^{-10}$	$1.0 \cdot 10^{-9}$	$1.0 \cdot 10^{-35}$	$1.0 \cdot 10^{-35}$	10.0	0.01
UKF Const. 3	**Q**				**R**	
	$\mathbf{q_{pos}}$	$\mathbf{q_{vel}}$	$\mathbf{q_{Cmn}}$	$\mathbf{q_{Smn}}$	$\sigma_{\mathbf{p}}$	$\sigma_{\mathbf{C}}, \sigma_{\mathbf{S}}$
	$1.0 \cdot 10^{-10}$	$1.0 \cdot 10^{-9}$	$1.0 \cdot 10^{-35}$	$1.0 \cdot 10^{-35}$	10.0	0.01

Table D.20: NUM-1.1 test configuration parameters for the case of 2 CubeSats

Orbit	a (km)	i (deg)	e (deg)	ν (deg)
	30	90	0	0, 120, 240

Table D.21: NUM-1.2 test configuration parameters for the case of 4 CubeSats

Orbit	a (km)	i (deg)	e (deg)	ν (deg)
	30	90	0	0, 72, 144, 216, 288

Table D.22: NUM-1.3 test configuration parameters for the case of 6 CubeSats

	a (km)	i (deg)	e (deg)	ν (deg)
Orbit	30	90	0	0, 52, 104, 156, 208, 260, 312

Table D.23: NUM-1.4 test configuration parameters for the case of 8 CubeSats

	a (km)	i (deg)	e (deg)	ν (deg)
Orbit	30	90	0	0, 40, 80, 120, 160, 200, 240, 280, 320

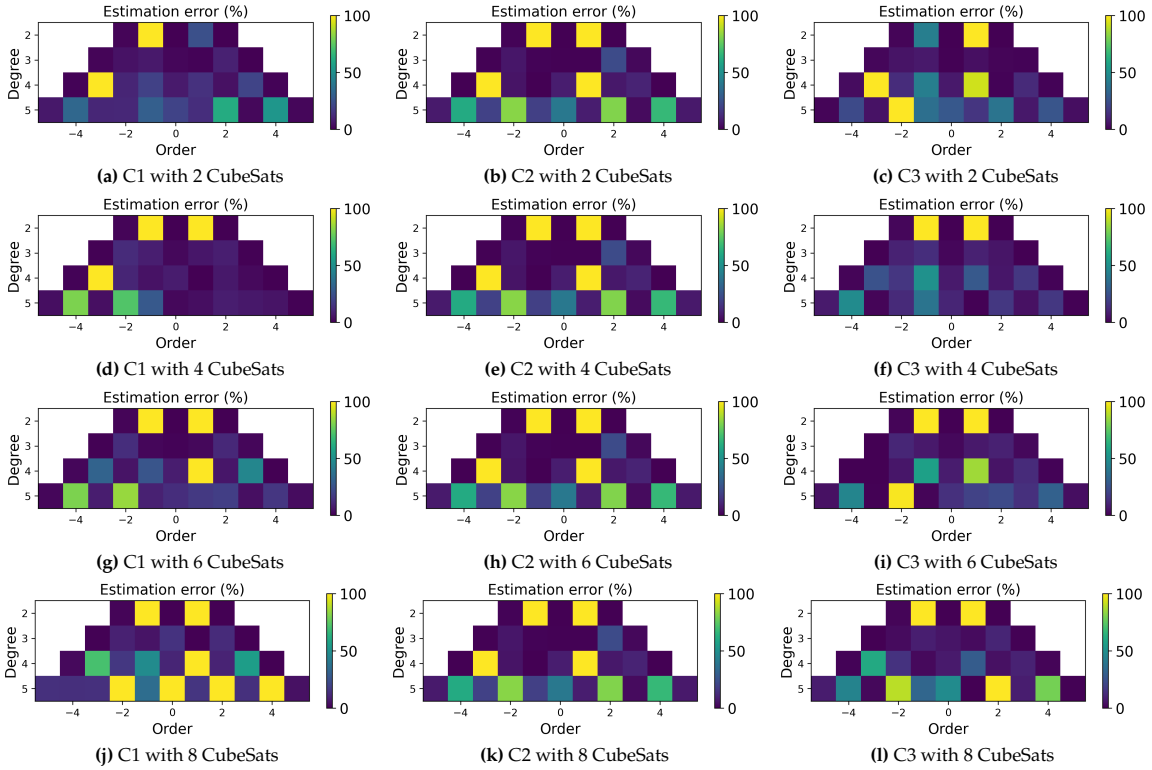

(a) C1 with 2 CubeSats **(b)** C2 with 2 CubeSats **(c)** C3 with 2 CubeSats

(d) C1 with 4 CubeSats **(e)** C2 with 4 CubeSats **(f)** C3 with 4 CubeSats

(g) C1 with 6 CubeSats **(h)** C2 with 6 CubeSats **(i)** C3 with 6 CubeSats

(j) C1 with 8 CubeSats **(k)** C2 with 8 CubeSats **(l)** C3 with 8 CubeSats

Figure D.17: NUM-1 Test: Estimation error of the SH coefficients degree and order 5 for 1 million seconds for a constellation of a mothership and several CubeSats.

It can be seen that the increase in the number of CubeSats considered in the C1 design leads to a higher number of inaccurate coefficient estimations, which can be related directly to the orbits followed by the CubeSats. On the other hand, this effect is less prominent in the C2 and C3 filters. In particular, the C2 filter results show very similar estimates since it mainly relies on all cases in the mothership's orbit and the average of the SH produced by the CubeSats. The C3 filter is also highly affected by the mothership's orbit, but is more affected by the SH estimates, and thus shows a larger variance of the results accuracy as more CubeSats are used.

Test NUM-2

This test contains the computations of a number of scenarios considering different numbers of satellites in the constellation. The parameters used for this test scenario are presented in Table D.24 for the case of 2 CubeSats, Table D.25 for the case of 3 CubeSats, and Table D.26 for the case of 4 CubeSats.

The coefficient estimates obtained by the single satellites used in the constellation are depicted in Figure D.18, and the constellation SH coefficient estimates are presented in Figure D.19. As can be seen, the orbits selected in this test are better suited for the gravity-field estimation. With these, the constellation estimates have shown much better accuracies than for Test NUM-1. It can be seen that when all trajectories are adequate, the C1 filter performance improves with the number of satellites used. The same can be said for the C3 filter. However, this is not the case for the C2 design, that by using the average of the SH coefficients estimated by the CubeSats, the filter does not benefit from the

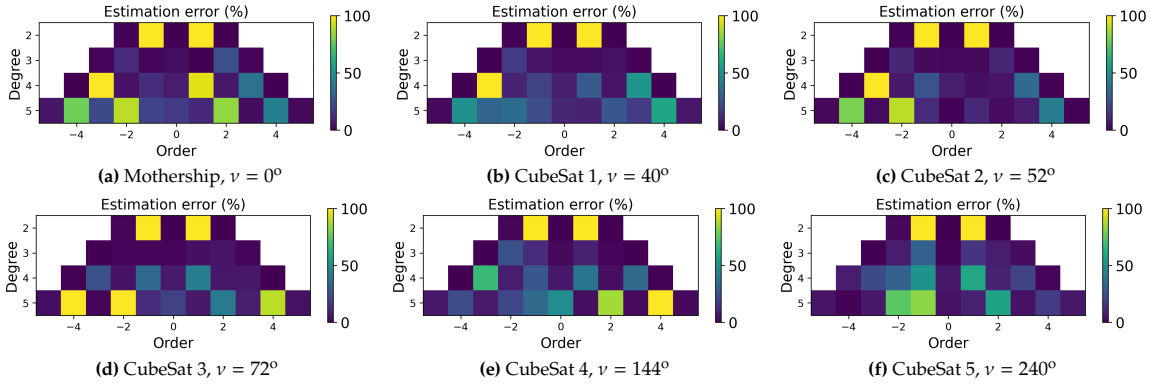

(a) Mothership, $\nu = 0^o$ **(b)** CubeSat 1, $\nu = 40^o$ **(c)** CubeSat 2, $\nu = 52^o$

(d) CubeSat 3, $\nu = 72^o$ **(e)** CubeSat 4, $\nu = 144^o$ **(f)** CubeSat 5, $\nu = 240^o$

Figure D.18: NUM-2 Test: Estimation error of the SH coefficients degree and order 5 for 1 million seconds for a single CubeSat.

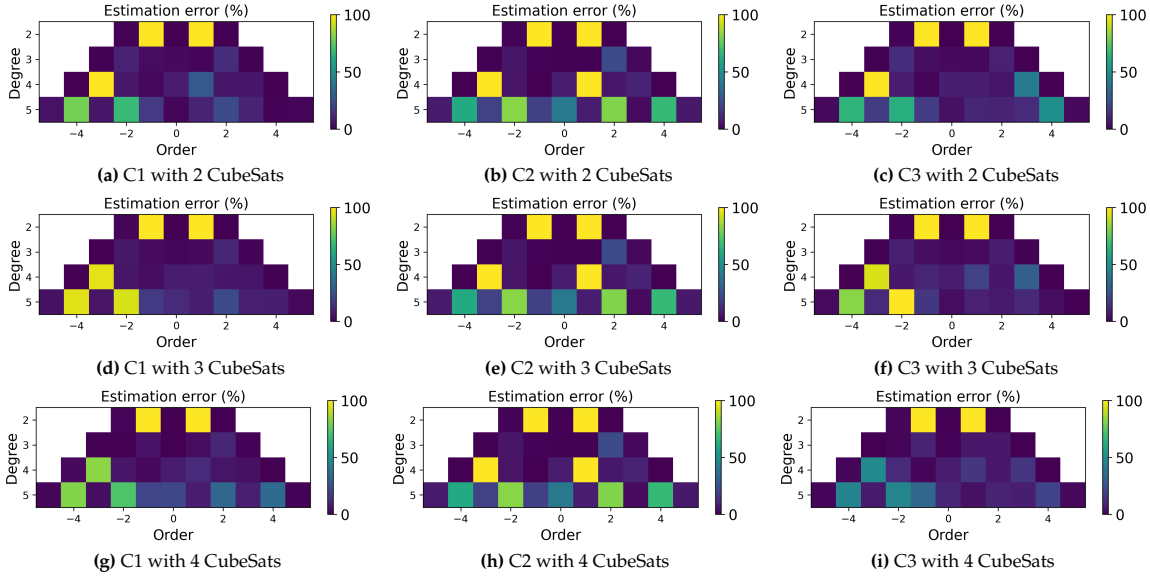

(a) C1 with 2 CubeSats **(b)** C2 with 2 CubeSats **(c)** C3 with 2 CubeSats

(d) C1 with 3 CubeSats **(e)** C2 with 3 CubeSats **(f)** C3 with 3 CubeSats

(g) C1 with 4 CubeSats **(h)** C2 with 4 CubeSats **(i)** C3 with 4 CubeSats

Figure D.19: NUM-2 Test: Estimation error of the SH coefficients degree and order 5 for 1 million seconds for a constellation of a mothership and several CubeSats.

addition of SH estimates.

Conclusions

An in-depth analysis performed with the obtained results is presented in Subsection 5.3.2, where the following conclusions have been reached:

- Simply increasing the number of CubeSats in the constellation does not guarantee better estimates.

Table D.24: NUM-2.1 test configuration parameters for the case of 2 CubeSats

Orbit	a (km)	i (deg)	e (deg)	ν (deg)
	30	90	0	0, 40

Table D.25: NUM-2.2 test configuration parameters for the case of 3 CubeSats

Orbit	a (km)	i (deg)	e (deg)	ν (deg)
	30	90	0	0, 40, 52

Table D.26: NUM-2.3 test configuration parameters for the case of 4 CubeSats

Orbit	a (km)	i (deg)	e (deg)	ν (deg)
	30	90	0	0, 40, 52, 72

The accuracy of the estimates heavily depends on the quality of the CubeSats' trajectories. When a constellation includes satellites with inadequate trajectories, having more satellites can improve the overall estimates by reducing the reliance on any single poor-quality trajectory.

- Configuration C1 performs well across various numbers of constellation satellites. However, as the number of satellites increases, the state of the filter grows, since each satellite adds three position values and three velocity values to the state. Consequently, the computational time required for coefficient estimation also increases, which can become a limiting factor for this filter.
- Configuration C2 has shown minimal improvement with additional satellites. It relies primarily on the mothership's orbit and uses the average coefficient estimates from other satellites. Adjustments to the **R** matrix could potentially optimize this, but relying on average estimates is not ideal. If even one CubeSat has an inadequate trajectory, it significantly impacts the average and degrades the estimates. However, this design does not require additional computational time with more satellites, which is an advantage.
- Configuration C3 has shown to perform well. Similarly to C1, this filter design provides improved estimates as the number of satellites in the constellation increases when they have adequate trajectories. When some trajectories are inadequate, the filter still maintains acceptable error levels by leveraging estimates from other CubeSats. The computational time for this filter increases with the number of CubeSats due to the additional measurements for each satellite's coefficients, but it remains lower than the computational time required by the C1 design.

D.2.4. Analysis of the Measurements Frequency and Orbital Propagation Duration

This section analyses the measurement update frequency and orbital propagation time on the UKF coefficients estimation. The configuration parameters used in the scenario for this analysis are presented in Table D.27.

Test CSTEP-1

This test aims to analyse the effect that frequency measurement update rate has on the constellation filter design. The parameters used for this simulation are shown in Table D.28. Furthermore, Figure D.20 presents the results obtained for the SH coefficient estimates for the three filter designs with different sets of time steps ranging from two seconds to ten seconds. The results show how in general increasing the time step from two seconds to five does not have a significant negative effect, even presenting results of similar accuracy in the C1 filter. However, raising the time step to ten seconds does lead to a considerable increase in the coefficient estimate errors. Thus indicating that the chosen time step for the

Table D.27: CSTEP and CPROP test configuration parameters

Orbit	a (km)		i (deg)		e (deg)	ν (deg)
	30		90		0	0, 120, 240
Forces	**Eros SH**		**3rd BP**		**SRP**	
	$m = 15, n = 15$		True		True	
Error	e_r (m)		e_v (m/s)		z_r (m)	
	0		0.0		10.0	
UKF Const. 1	**Q**				**R**	
	$\mathbf{q_{pos}}$	$\mathbf{q_{vel}}$	$\mathbf{q_{Cmn}}$	$\mathbf{q_{Smn}}$	$\sigma_\mathbf{p}$	
	$1.0 \cdot 10^{-10}$	$1.0 \cdot 10^{-9}$	$1.0 \cdot 10^{-35}$	$1.0 \cdot 10^{-35}$	10.0	
UKF Const. 2	**Q**				**R**	
	$\mathbf{q_{pos}}$	$\mathbf{q_{vel}}$	$\mathbf{q_{Cmn}}$	$\mathbf{q_{Smn}}$	$\sigma_\mathbf{p}$	$\sigma_\mathbf{C}$, $\sigma_\mathbf{S}$
	$1.0 \cdot 10^{-10}$	$1.0 \cdot 10^{-9}$	$1.0 \cdot 10^{-35}$	$1.0 \cdot 10^{-35}$	10.0	0.01
UKF Const. 3	**Q**				**R**	
	$\mathbf{q_{pos}}$	$\mathbf{q_{vel}}$	$\mathbf{q_{Cmn}}$	$\mathbf{q_{Smn}}$	$\sigma_\mathbf{p}$	$\sigma_\mathbf{C}$, $\sigma_\mathbf{S}$
	$1.0 \cdot 10^{-10}$	$1.0 \cdot 10^{-9}$	$1.0 \cdot 10^{-35}$	$1.0 \cdot 10^{-35}$	10.0	0.01

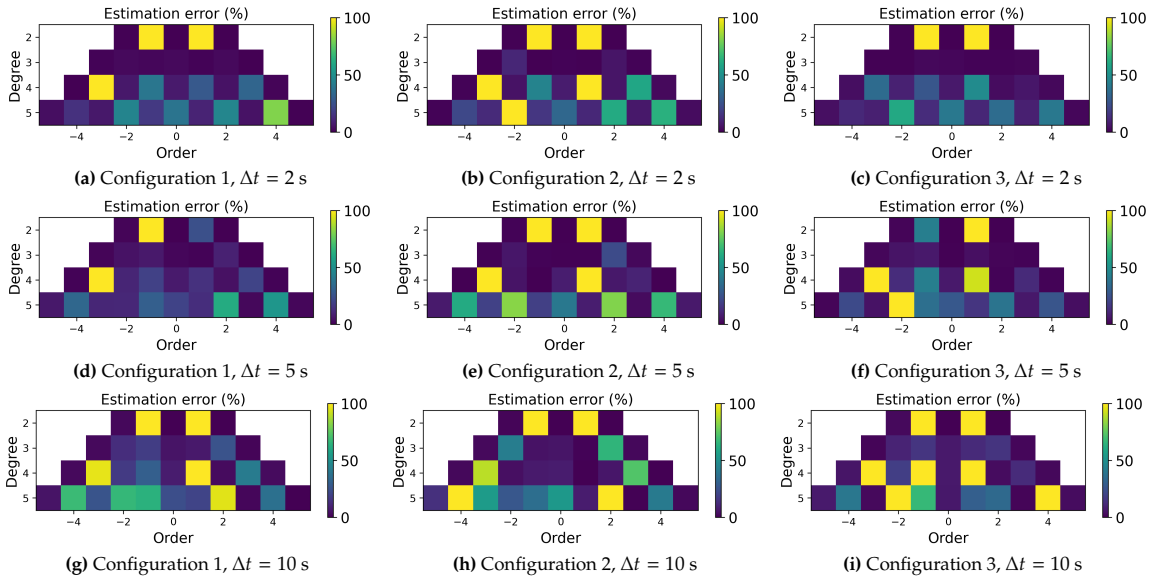

(a) Configuration 1, $\Delta t = 2$ s **(b)** Configuration 2, $\Delta t = 2$ s **(c)** Configuration 3, $\Delta t = 2$ s

(d) Configuration 1, $\Delta t = 5$ s **(e)** Configuration 2, $\Delta t = 5$ s **(f)** Configuration 3, $\Delta t = 5$ s

(g) Configuration 1, $\Delta t = 10$ s **(h)** Configuration 2, $\Delta t = 10$ s **(i)** Configuration 3, $\Delta t = 10$ s

Figure D.20: CSTEP-1 Test: Estimation error of the SH coefficients degree and order 5 for 1 million seconds for the constellation for different measurement frequencies.

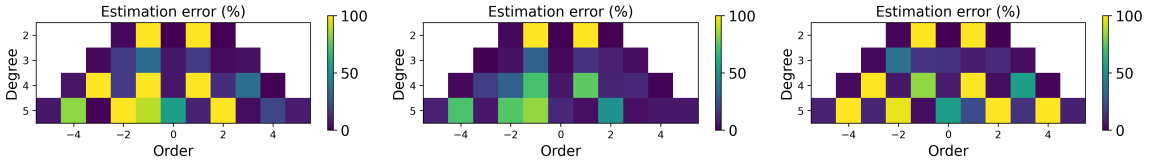

(a) $t_{prop} = 5 \cdot 10^5$ s **(b)** $t_{prop} = 1 \cdot 10^6$ s **(c)** $t_{prop} = 2 \cdot 10^6$ s

Figure D.21: CPROP-1 Test: Estimation error of the SH coefficients degree and order 5 for 1 million seconds for a single satellite.

filter has a considerable effect on the estimates and indicating that the values used should not surpass five to ensure the best filter performance.

Test CPROP-1

This test aims to analyse the effect that the propagation time has on the constellation filter design. The parameters used for this simulation are shown in Table D.29.

The estimates produced by a single satellite for a different range of propagation times have been computed as a reference for the results obtained for the constellation. The results are presented in Figure D.21, showing how the best estimates are obtained for a $t_{prop} = 1 \cdot 10^6$ s. This is indicative of the fact that the filter benefits from having a large set of measurement values with time for the coefficient estimates to converge, but that after a given point, too many measurements might saturate the filter. Additionally, the SH estimates using the constellations are presented in Figure D.22. As can be seen, the same tendency is followed, where in general $t_{prop} = 1 \cdot 10^6$ s provides the best estimates.

Conclusions

An in-depth analysis conducted with the obtained results is presented in Subsection 5.3.3, where the following conclusions have been reached:

Table D.28: CSTEP-1 test configuration parameters

Propagation	Δt **(s)**	t_{prop} **(s)**
	2, 5, 10	$1 \cdot 10^6$

Table D.29: CPROP-1 test configuration parameters

Propagation	Δt **(s)**	t_{prop} **(s)**
	5	$5 \cdot 10^5, 1 \cdot 10^6, 2 \cdot 10^6$

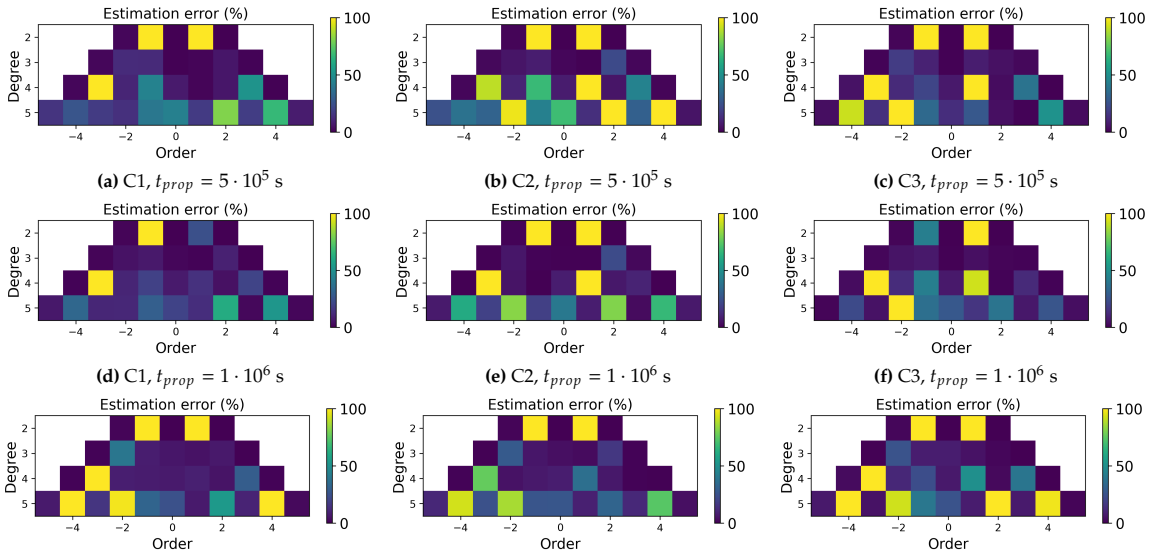

(a) C1, $t_{prop} = 5 \cdot 10^5$ s **(b)** C2, $t_{prop} = 5 \cdot 10^5$ s **(c)** C3, $t_{prop} = 5 \cdot 10^5$ s

(d) C1, $t_{prop} = 1 \cdot 10^6$ s **(e)** C2, $t_{prop} = 1 \cdot 10^6$ s **(f)** C3, $t_{prop} = 1 \cdot 10^6$ s

(g) C1, $t_{prop} = 2 \cdot 10^6$ s **(h)** C2, $t_{prop} = 2 \cdot 10^6$ s **(i)** C3, $t_{prop} = 2 \cdot 10^6$ s

Figure D.22: CPROP-1 Test: Estimation error of the SH coefficients degree and order 5 for the constellation for different simulation durations.

- The frequency measurement update has a considerable impact on the estimations. While one might expect the higher the frequency update, the better the results, this has been shown not to be the case. In particular, the use of a five-second time step has been shown to provide overall the best results.
- The propagation time of the satellites in the constellation has been shown to have a relevant impact on the estimations. However, this has been directly linked to the orbits adequate for coefficient estimation. Low values of propagation time can lead to insufficient coverage and therefore worse estimations, whereas propagation values that are too large might lead to orbital instabilities and be detrimental to the SH coefficient estimations.

D.3. Sensitivity Analysis: Satellite Constellation with Constraints

This section presents the test's characteristics and some of the results obtained in the analysis of the design of the constellation and filter when visibility and communication constraints are considered.

Subsection D.3.1 conducts an analysis on the visibility constraints effects, followed by Subsection D.3.2 which considers only the communications constraints. Moreover, the satellite distribution effects within the constellation are analysed considering all the constraints in Subsection D.3.3.

D.3.1. Analysis of the Visibility Restrictions between the Satellites

This section aims to analyse the effect that visibility restrictions have on the coefficient estimations. This is done considering an example scenario where half of the three-dimensional space in inertial coordinates is considered to be in the shade and the other part is considered to be sun-lit. This simplified scenario considers all satellites located in negative X coordinates of the inertial reference frame, and then the measurements are considered null for those positions.

The tests performed for this analysis have been set with the configuration presented in Table D.30.

Test VIS-SAT-1

An initial test has been carried out for a range of satellites with trajectories following orbits with diverse true anomalies considering visibility restrictions.

Test VIS-SAT-2

A new design of the UKF has been made. This stops the filter when the measurements are lost and restarts the filter when the satellite fulfils again the visibility requirements. This test aims to analyse the behaviour of the new filter when visibility constraints are taken into account with different propagation times and measurement update frequencies.

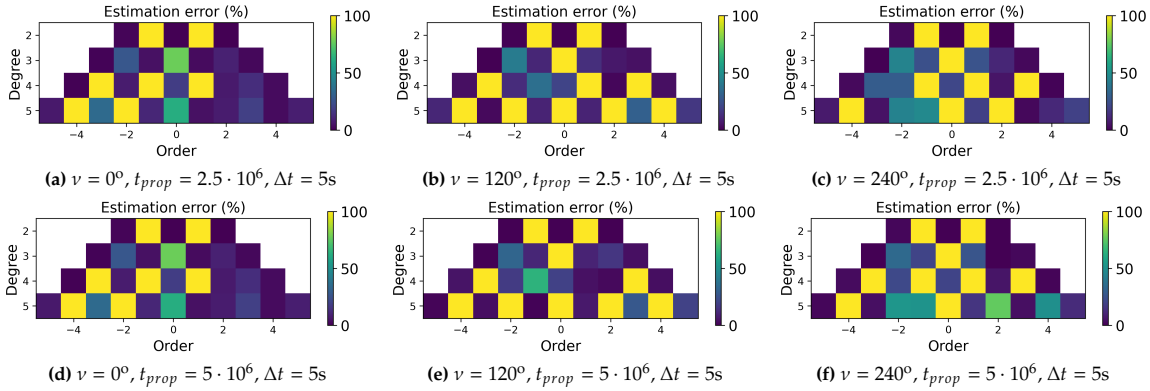

(a) $\nu = 0^{o}$, $t_{prop} = 2.5 \cdot 10^{6}$, $\Delta t = 5$s **(b)** $\nu = 120^{o}$, $t_{prop} = 2.5 \cdot 10^{6}$, $\Delta t = 5$s **(c)** $\nu = 240^{o}$, $t_{prop} = 2.5 \cdot 10^{6}$, $\Delta t = 5$s

(d) $\nu = 0^{o}$, $t_{prop} = 5 \cdot 10^{6}$, $\Delta t = 5$s **(e)** $\nu = 120^{o}$, $t_{prop} = 5 \cdot 10^{6}$, $\Delta t = 5$s **(f)** $\nu = 240^{o}$, $t_{prop} = 5 \cdot 10^{6}$, $\Delta t = 5$s

Figure D.23: VIS-SAT-2 Test: Estimation error of the SH coefficients degree and order 5 for single satellites with a five-second time step.

Figure D.23 presents the coefficient estimates obtained for an update frequency of five seconds for different propagation times for a single satellite. It can be observed that the estimates obtained are considerably inaccurate, and the bad performance is similar for both propagation times simulated. Furthermore, it can be observed that the satellite orbiting with a null true anomaly provides better estimates than the others, particularly in the cosine SH coefficients.

Similarly, the same test results are depicted in Figure D.24 for a one-second time step. These results in a considerable improvement for the orbits with $\nu = 0°$ and $\nu = 240°$. Moreover, the same tendency is observed where the propagation length does not have a significant effect in the estimates accuracy for this scenario. Additionally, the filter has been tested adding velocity measurements, and the estimates produced are depicted in Figure D.25. These show no major improvements with respect to the previous test.

Test VIS-CONST-1

A basic test is carried out to analyse the behaviour of the refined filters with a constellation of satellites considering visibility restrictions.

This test considers a constellation with six satellites in total: the mothership located at $\nu = 0^{o}$, and five CubeSats spread out along the true anomaly. The parameters used for the simulation can be found in Table D.31.

To fully analyse the behaviour of the filters, estimations have been produced for each satellite of the constellation. The errors in the estimates are depicted in Figure D.26, showing a varied estimation accuracy. In particular, it can be seen that the satellite orbiting with $\nu = 180°$ leads to extremely inaccurate coefficient estimates, whereas satellites orbiting with $\nu = 60°$ and $\nu = 300°$ produce much more accurate coefficient estimates.

The estimates produced by the redesigned constellation filters are presented in Figure D.27, showing

Table D.30: VIS-SAT-1 Test configuration parameters

Propagation	Δt **(s)**		t_{prop} **(s)**	
	1, 5		$1 \cdot 10^{6}$	
Orbit	a (km)	i (deg)	e (deg)	ν (deg)
	30	90	0	0, 120, 240
Forces	**Eros SH**	**3rd BP**	**SRP**	
	$m = 16, n = 16$	True	True	
Error	e_r (m)	e_v (m/s)	z_r (m)	
	0	0.0	10	
UKF	**Q**			**R**
	$\mathbf{q_{pos}}$	$\mathbf{q_{vel}}$	$\mathbf{q_{Cmn}}$	$\mathbf{q_{Smn}}$	$\sigma_{\mathbf{p}}$
	$1.0 \cdot 10^{-10}$	$1.0 \cdot 10^{-9}$	$1.0 \cdot 10^{-35}$	$1.0 \cdot 10^{-35}$	10.0

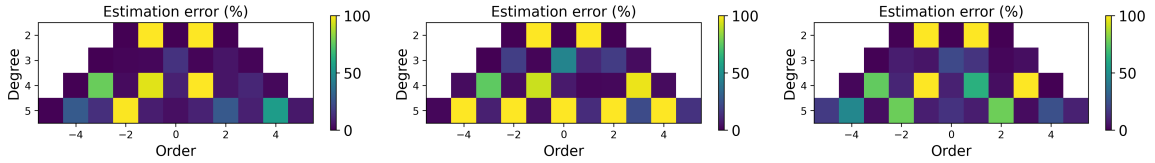

(a) $\nu = 0^o$, $t_{prop} = 2.5 \cdot 10^6$, $\Delta t = 1$s **(b)** $\nu = 120^o$, $t_{prop} = 2.5 \cdot 10^6$, $\Delta t = 1$s **(c)** $\nu = 240^o$, $t_{prop} = 2.5 \cdot 10^6$, $\Delta t = 1$s

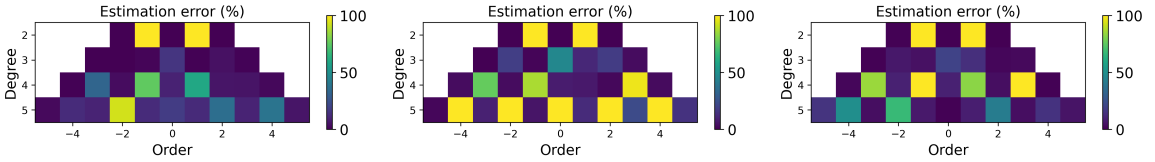

(d) $\nu = 0^o$, $t_{prop} = 5 \cdot 10^6$, $\Delta t = 1$s **(e)** $\nu = 120^o$, $t_{prop} = 5 \cdot 10^6$, $\Delta t = 1$s **(f)** $\nu = 240^o$, $t_{prop} = 5 \cdot 10^6$, $\Delta t = 1$s

Figure D.24: VIS-SAT-2 Test: Estimation error of the SH coefficients degree and order 5 for single satellites with a 1 second time step.

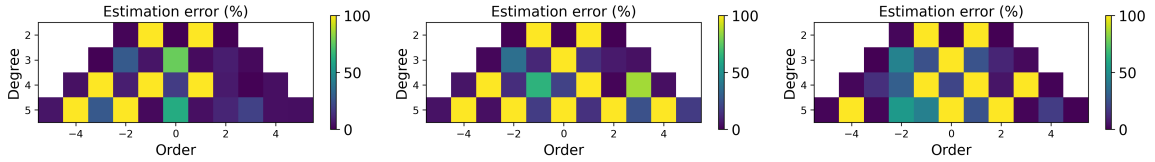

(a) $\nu = 0^o$, $t_{prop} = 2.5 \cdot 10^6$, $\Delta t = 5$s **(b)** $\nu = 120^o$, $t_{prop} = 2.5 \cdot 10^6$, $\Delta t = 5$s **(c)** $\nu = 240^o$, $t_{prop} = 2.5 \cdot 10^6$, $\Delta t = 5$s

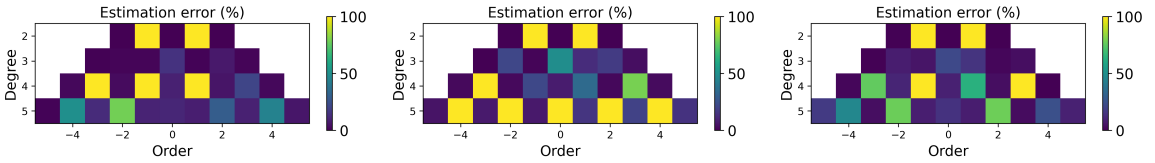

(d) $\nu = 0^o$, $t_{prop} = 2.5 \cdot 10^6$, $\Delta t = 1$s **(e)** $\nu = 120^o$, $t_{prop} = 2.5 \cdot 10^6$, $\Delta t = 1$s **(f)** $\nu = 240^o$, $t_{prop} = 2.5 \cdot 10^6$, $\Delta t = 1$s

Figure D.25: VIS-SAT-2 Test: Estimation error of the SH coefficients degree and order 5 for single satellites with a 1-second time step with velocity measurements.

the results for a variety of propagation and frequency updates. As expected, the estimates contain considerable estimation errors, which can be directly linked to the single satellite coefficient estimates

Table D.31: VIS-CONST-1 test configuration parameters

Propagation	Δt **(s)**			t_{prop} **(s)**	
	5			$2.5 \cdot 10^6$	
Orbit	a (km)	i (deg)		e (deg)	ν (deg)
	30	90		0	0, 60, 120, 180, 240, 300
Forces	**Eros SH**	**3rd BP**		**SRP**	
	$m = 15, n = 15$	True		True	
Error	e_r (m)	e_v (m/s)		z_r (m)	
	0	0.0		10.0	
UKF Const. 1	**Q**			**R**	
	$\mathbf{q_{pos}}$	$\mathbf{q_{vel}}$	$\mathbf{q_{Cmn}}$	$\mathbf{q_{Smn}}$	$\sigma_\mathbf{p}$
	$1.0 \cdot 10^{-10}$	$1.0 \cdot 10^{-9}$	$1.0 \cdot 10^{-35}$	$1.0 \cdot 10^{-35}$	10.0
UKF Const. 2	**Q**				**R**
	$\mathbf{q_{pos}}$	$\mathbf{q_{vel}}$	$\mathbf{q_{Cmn}}$	$\mathbf{q_{Smn}}$	$\sigma_\mathbf{p}$ / $\sigma_\mathbf{C}, \sigma_\mathbf{S}$
	$1.0 \cdot 10^{-10}$	$1.0 \cdot 10^{-9}$	$1.0 \cdot 10^{-35}$	$1.0 \cdot 10^{-35}$	10.0 / 0.1
UKF Const. 3	**Q**				**R**
	$\mathbf{q_{pos}}$	$\mathbf{q_{vel}}$	$\mathbf{q_{Cmn}}$	$\mathbf{q_{Smn}}$	$\sigma_\mathbf{p}$ / $\sigma_\mathbf{C}, \sigma_\mathbf{S}$
	$1.0 \cdot 10^{-10}$	$1.0 \cdot 10^{-9}$	$1.0 \cdot 10^{-35}$	$1.0 \cdot 10^{-35}$	10.0 / 10.0

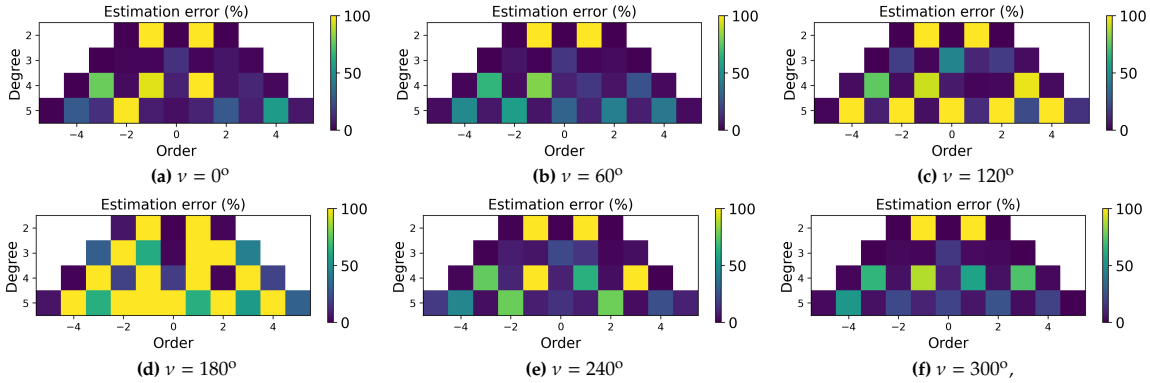

(a) $\nu = 0^o$ **(b)** $\nu = 60^o$ **(c)** $\nu = 120^o$

(d) $\nu = 180^o$ **(e)** $\nu = 240^o$ **(f)** $\nu = 300^o$,

Figure D.26: VIS-CONST-1 Test: Estimation error of the SH coefficients degree and order 5 for single satellites for a 1 second time step and a propagation time of $2.5 \cdot 10^6$ s.

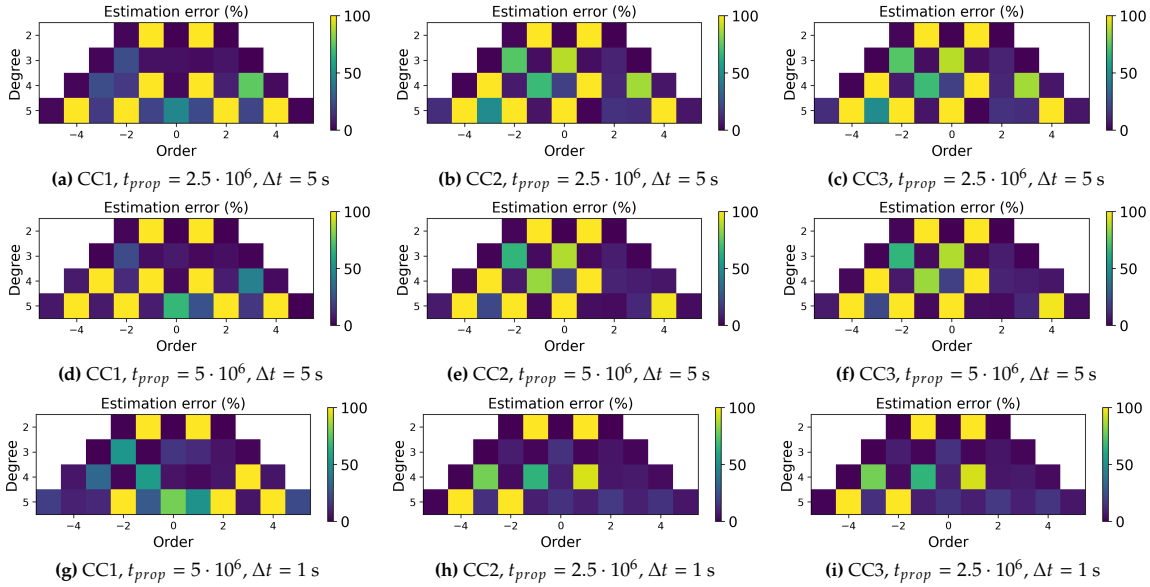

(a) CC1, $t_{prop} = 2.5 \cdot 10^6$, $\Delta t = 5$ s **(b)** CC2, $t_{prop} = 2.5 \cdot 10^6$, $\Delta t = 5$ s **(c)** CC3, $t_{prop} = 2.5 \cdot 10^6$, $\Delta t = 5$ s

(d) CC1, $t_{prop} = 5 \cdot 10^6$, $\Delta t = 5$ s **(e)** CC2, $t_{prop} = 5 \cdot 10^6$, $\Delta t = 5$ s **(f)** CC3, $t_{prop} = 5 \cdot 10^6$, $\Delta t = 5$ s

(g) CC1, $t_{prop} = 5 \cdot 10^6$, $\Delta t = 1$ s **(h)** CC2, $t_{prop} = 2.5 \cdot 10^6$, $\Delta t = 1$ s **(i)** CC3, $t_{prop} = 2.5 \cdot 10^6$, $\Delta t = 1$ s

Figure D.27: VIS-CONST-1 Test: Estimation error of the SH coefficients degree and order 5 for the new constellation designs for a time step of 5 seconds.

obtained in the previous test. Moreover, the figures illustrate a considerable improvement in estimation when increasing the propagation time to $5.0 \cdot 10^6$ s, which can be linked to the fact that with the new UKF designs considering visibility constraints, there are less measurements that can be used for the same propagation time and, therefore, the filters do not experience saturation.

Figure D.28 illustrates the effects of the uncertainty parameter of the coefficient measurements for the CC2 and CC3 filters. The results obtained illustrate the same tendency for both filters, showing an increase on the estimates error as the uncertainty parameter is reduced.

Additionally, Figure D.29 presents the estimates obtained for the filters when the mothership is placed in an orbit with $\nu = 120°$. This shows the same results for the CC1 filter, as expected, but negatively impacts the estimates produced by the CC2 and CC3 filters, since they are more reliant on the mothership trajectory.

Conclusions

An in-depth analysis conducted with the obtained results is presented in Subsection 5.4.1, which analyses the effect that visibility constraints have on the system and has presented an improved filter design to better estimate these conditions. In it, the following conclusions have been reached:

- The CC1 design uses the desired number of CubeSats that are visible in the constellation, which for this testing purpose has been set to two. This has the advantage that the filter uses measurements from all the satellites with time. This is an advantage since in the case that some of the trajectories

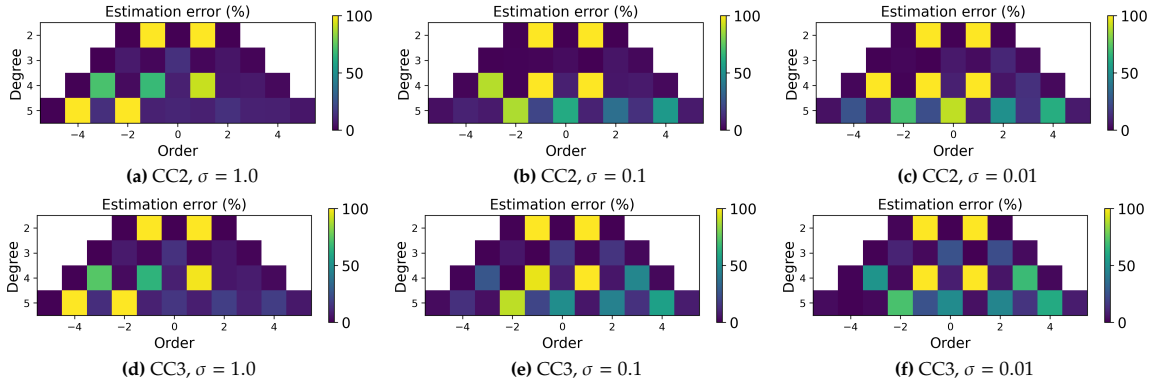

(a) CC2, $\sigma = 1.0$ **(b)** CC2, $\sigma = 0.1$ **(c)** CC2, $\sigma = 0.01$

(d) CC3, $\sigma = 1.0$ **(e)** CC3, $\sigma = 0.1$ **(f)** CC3, $\sigma = 0.01$

Figure D.28: VIS-CONST-1 Test: Estimation error of the SH coefficients degree and order 5 for the new constellation designs for a time step of 1 second.

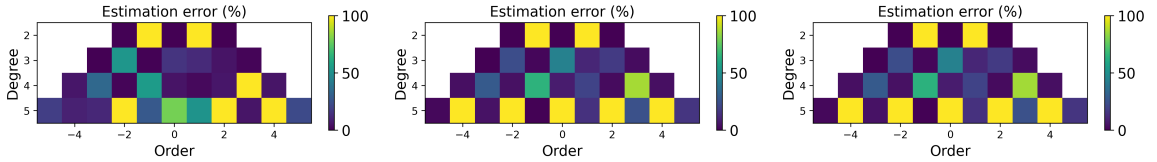

(a) CC1 **(b)** CC2 **(c)** CC3

Figure D.29: VIS-CONST-1 Test: Estimation error of the SH coefficients degree and order 5 for the new constellation designs for a time step of one-second setting the mothership in the orbit $\nu = 120^{o}$.

of the CubeSats are inadequate, the filter can rely on the others, and therefore it ensures that the estimates will not be overpowered by incorrect trajectories. Nevertheless, this design is also the most computationally expensive, in particular the more satellite measurements that are considered at the same time.

- The CC2 design has been shown to perform adequately using the weighted average of the coefficients estimations produced by the CubeSats. However, the accuracy obtained is highly dependent on the mothership trajectory id a high value is given to the R matrix, so it is crucial that this matrix is adjusted adequately for the scenario.
- The CC3 design has shown similar results to the CC2 design, producing slightly worse results and requiring larger computation times.

D.3.2. Analysis of the Communications Restrictions between the Satellites

An analysis has been conducted on the LOS constraints on the system, which constrain the transmission of data between the CubeSats and the mothership. This section presents the LOS establishment between the mothership and a number of CubeSats with a range of true anomalies in Figure D.30 and Figure D.31 aiming to highlight the significance that the orbital distribution has on the communications restrictions and confirm that the similar the orbits followed by mothership and CubeSat are, the smaller the times when they lose LOS.

Conclusions

An in-depth analysis conducted with the obtained results is presented in Subsection 5.4.2, which analyses the effect that communications constraints have on the system. In it, the conclusion is reached that the communications constraints do not have a considerable effect on the UKF filter and no adaptations to the filter design are necessary.

D.3.3. Analysis of the Satellite Distribution with Restrictions

This section analyses the satellite distribution's impact on the filter estimations when visibility restrictions are considered by varying the number of satellites considered in the constellation, the distribution of the satellites along the true anomaly and the distribution of the satellites in several inclinations.

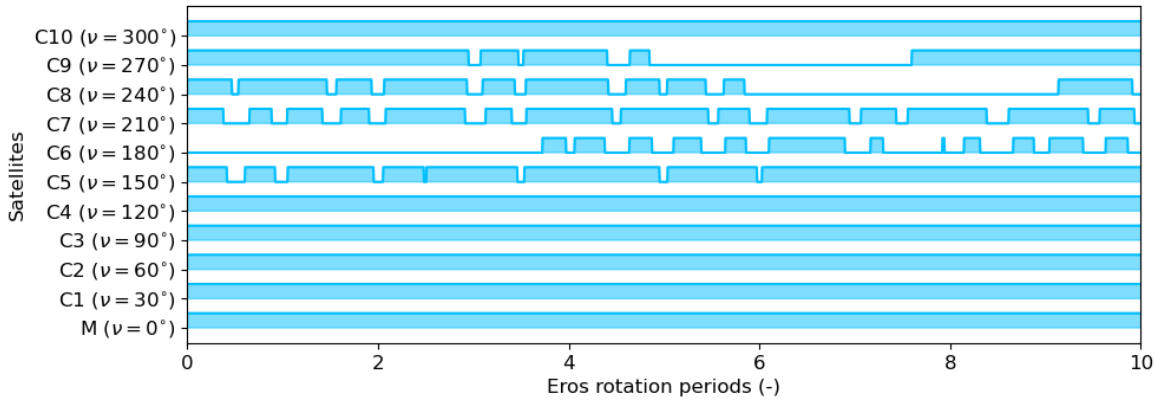

Figure D.30: Line-of-sight establishment between the CubeSats and the Mothership for the initial 10 rotation periods of Eros.

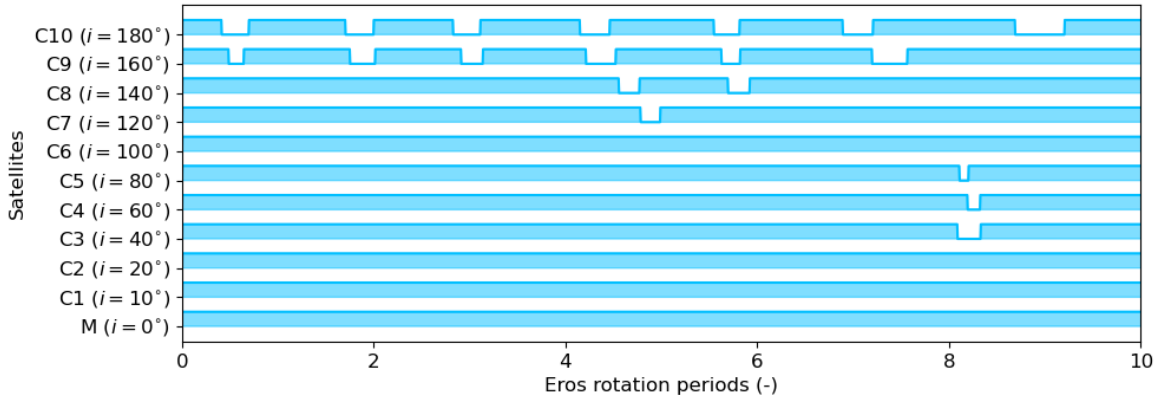

Figure D.31: Line-of-sight establishment between the CubeSats and the Mothership for the initial 10 rotation periods of Eros.

Test NUM

The number of satellites used in the constellation has been analysed through several scenarios considering a different number of satellites evenly distributed along the true anomaly. The parameters used for the simulation of the scenario are presented in Table D.32.

Figure D.32 presents the coefficient estimates obtained when only visibility constraints and both visibility and LOS constraints. The results obtained show an improvement in the estimates as the number of satellites in the constellation is increased. Furthermore, as shown, the addition of the communications constraint has a higher effect the lower the number of CubeSats. Therefore, the more satellites in the constellation, the less constraining the communications are to the system, which is to be expected given that the availability of the satellites required for the filter estimation increases. The

Table D.32: NUM test configuration parameters

Propagation	Δt **(s)**			t_{prop} **(s)**	
	5			$2.5 \cdot 10^6$	
Orbit	a (km)		i (deg)	e (deg)	ν (deg)
	30		90	0	[0, 360]
Forces	**Eros SH**		**3rd BP**	**SRP**	
	$m = 15, n = 15$		True	True	
Error	e_r (m)		e_v (m/s)	z_r (m)	
	0		0.0	10.0	
UKF Const. 1	**Q**				**R**
	$\mathbf{q_{pos}}$	$\mathbf{q_{vel}}$	$\mathbf{q_{Cmn}}$	$\mathbf{q_{Smn}}$	$\sigma_{\mathbf{p}}$
	$1.0 \cdot 10^{-10}$	$1.0 \cdot 10^{-9}$	$1.0 \cdot 10^{-35}$	$1.0 \cdot 10^{-35}$	10.0

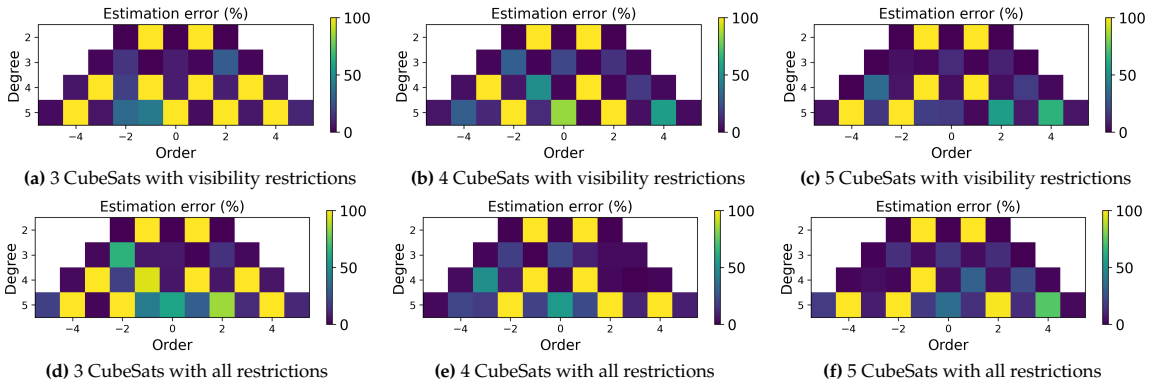

(a) 3 CubeSats with visibility restrictions **(b)** 4 CubeSats with visibility restrictions **(c)** 5 CubeSats with visibility restrictions

(d) 3 CubeSats with all restrictions **(e)** 4 CubeSats with all restrictions **(f)** 5 CubeSats with all restrictions

Figure D.32: NUM Test: Estimation of the SH coefficients for a number of satellites in the same orbit with evenly distributed true anomaly using two satellites in the position estimation considering different constraints.

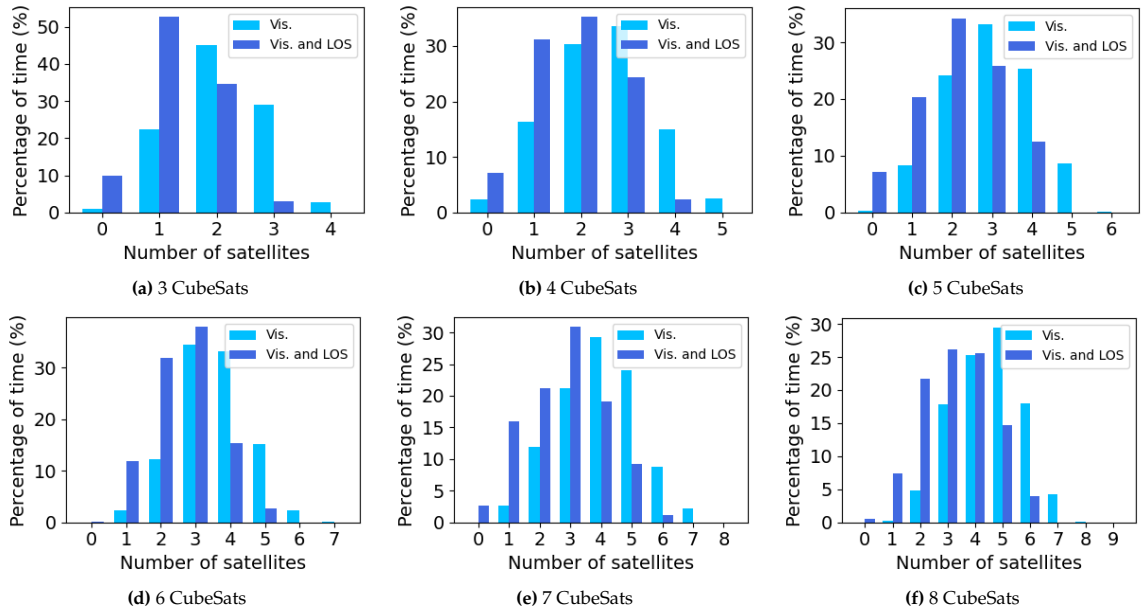

(a) 3 CubeSats **(b)** 4 CubeSats **(c)** 5 CubeSats

(d) 6 CubeSats **(e)** 7 CubeSats **(f)** 8 CubeSats

Figure D.33: Time percentages of the number of satellites fulfilling the visibility and both the visibility and communications condition along a 1 million second propagation of the constellation.

availabilities for a varied number of satellites in the constellation are depicted in Figure D.33, where it can be seen that as the number of satellites increases, the lower the availabilities of only one or two satellites at the same time decreases and the number of satellites available at the same time increases. Furthermore, the figures depict a negative effect of the communications constraint, that further reduces the availability.

Test INC

This test aims to analyse how the distribution of the satellites along different orbital inclinations affects the estimations. As can be seen, the inclination has a considerable effect on the estimations.

In particular, the use of equatorial orbits has been seen to be detrimental for the system. This is directly related to the fact that equatorial orbits are more affected by the perturbations in the asteroid's gravity field (considering the two bulges of Eros's shape) and this makes the orbit unstable, leading to scape trajectories and therefore to an inadequate performance of the system as depicted in Figure D.34a and Figure D.35a. Moreover, while non-equatorial orbits provide adequate results, the more polar the orbit is, the better the estimates obtained, which can be directly linked to the coverage obtained of the asteroid.

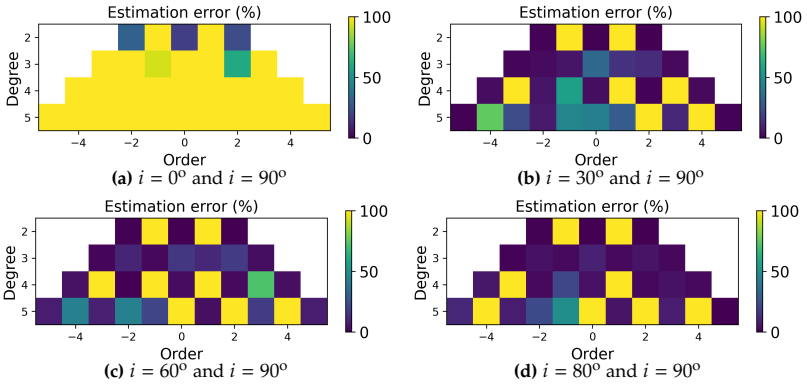

(a) $i = 0^o$ and $i = 90^o$ **(b)** $i = 30^o$ and $i = 90^o$

(c) $i = 60^o$ and $i = 90^o$ **(d)** $i = 80^o$ and $i = 90^o$

Figure D.34: INC Test: Estimation with 4 satellites split in two different inclination orbits located at the true anomaly of 0° and 180° considering visibility constraints.

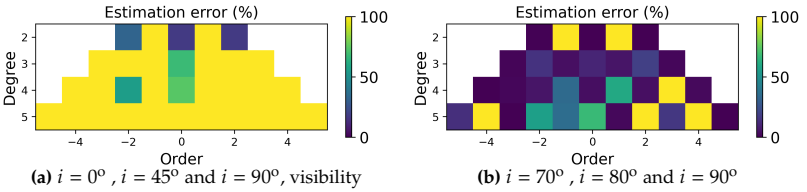

(a) $i = 0^o$, $i = 45^o$ and $i = 90^o$, visibility **(b)** $i = 70^o$, $i = 80^o$ and $i = 90^o$

Figure D.35: INC Test: Estimation with 6 satellites split in three different inclination orbits located at the true anomaly of 0° and 180° considering visibility constraints.

Conclusions

An in-depth analysis conducted with the obtained results is presented in Subsection 5.4.3. This has presented the following conclusions:

- The consideration of the constraints has been seen to restrict considerably the availability of the satellites, and therefore lead to more breaks and necessary re-starts of the filter and shorter data time ranges, which has a detrimental effect on the computation. The distribution of the satellites along the constellation has a direct effect on these constraints and is therefore a key factor of an adequate mission design.
- The number of satellites of the constellation has been shown to affect considerably the percentages of time that satellites's measurements are available to the mothership. The larger the number of satellites, the tendency is that the larger the probability of having two or more satellites available, which can additionally affect the number of restarts of the filter depending on the distribution of said satellites.
- The distribution of the satellites along the true anomaly and the inclination have a considerable effect on the restrictions. Constellations with closely distributed satellites have been shown to have lower communication restrictions. Nevertheless, this does not directly lead to the estimates being better, since the determining key factor is the adequacy of the trajectory for an appropriate gravity field determination.

E

Design exploration settings and results

This chapter acts as a support for the ANOVA optimisation presented in Chapter 6, depicting in detail the settings used for the tests conducted and containing further results to better analyse the effects of the parameters studied on the estimates produced by the filter.

E.1. Scenario 1: Uniform Orbital Parameters with Variable True Anomaly

This scenario has been designed with the aim of studying the effect that the design parameters have on a constellation where the satellites follow the same orbit in the inertial frame, with a range of true anomaly values. This scenario considers a constellation of five CubeSats orbiting the asteroid evenly distributed along the true anomaly using the UKF CC1 design. The design variables considered are the semi-major axis, the inclination, the eccentricity and the distribution of the satellites along the true anomaly. The following sections present the analysis of the interactions between these parameters. It should be noted that these variables have been initially considered in pairs to more adequately study their interactions and finally a full interaction ANOVA has been carried out.

E.1.1. Semi-major Axis and Inclination

An analysis of the effect and interaction between the semi-major axis and the inclination has been done only considering these decision variables, setting the eccentricity to zero and distributing the satellites evenly along the true anomaly. The bounds used for the analysis are presented in Table E.1.

Further detail on the effects of these variables are shown in Figure E.1. These plots depict how variations in these variables affect the estimations of the coefficients individually.

As can be seen, increasing the inclination of the orbit improves the estimates of the majority of the SH coefficients for the 30 km semi-major axis orbit while doing the same for the 40 km orbit improves some of the coefficients but has a negative effect on others. This can be directly related to the coverage of the asteroid derived from the combination of both parameters. Furthermore, for a fixed inclination orbit, decreasing the altitude of the orbit has a positive effect in all cases, which can be directly related to the fact that the closer the orbit is from the asteroid, the more disturbed the environment is and therefore, the better the estimates produced can be.

Table E.1: Bounds of the decision variables

	a [km]	i [°]
Upper bound	40	90
Lower bound	30	60

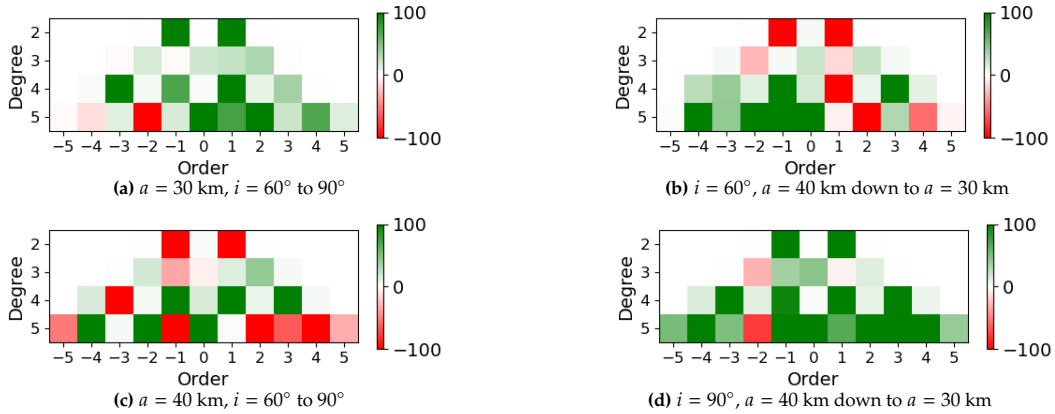

(a) $a = 30$ km, $i = 60°$ to $90°$

(b) $i = 60°$, $a = 40$ km down to $a = 30$ km

(c) $a = 40$ km, $i = 60°$ to $90°$

(d) $i = 90°$, $a = 40$ km down to $a = 30$ km

Figure E.1: Estimation percentage improvement from the variation of the decision variables a and i.

E.1.2. Eccentricity and Inclination

The analysis of the effect and interaction of e and i is carried out with the bounds presented in Table E.2.

Figure E.2 presents how these variables affect the estimations of the coefficients individually. In particular, it can be clearly seen how for a fixed inclination value, increasing the eccentricity has a positive effect on the filter estimates, thus demonstrating how higher eccentricities can improve the filter behaviour. This can be directly linked to the fact that eccentric orbits have a trajectory where the satellites get closer to the asteroid, thus being more affected by the irregular gravity field environment and therefore being better suited to model it accurately. Furthermore, the combination of lower altitude trajectory blocks with higher altitude blocks enables the filter to perform better, since higher altitudes lead to lower orbital velocity and therefore can improve the filter stability.

Additionally, an increase in the orbital inclination provides a slightly better total estimation of the coefficients, nevertheless, the effect on the coefficients is variable, improving some estimates and degrading others. This can be directly linked to the fact that the inclination is highly determinant of the asteroid coverage and therefore determines the areas covered, and consequently, the areas covered determine the specific coefficients that can be properly estimated. Moreover, it is important to note that this scenario considers a 40 km orbital semi-major axis to ensure orbital stability, and at this altitude, the effect of the inclination is much lower than that for a lower altitude.

Table E.2: Bounds of the decision variables

	e [-]	i [°]
Upper bound	0.2	90
Lower bound	0.0	60

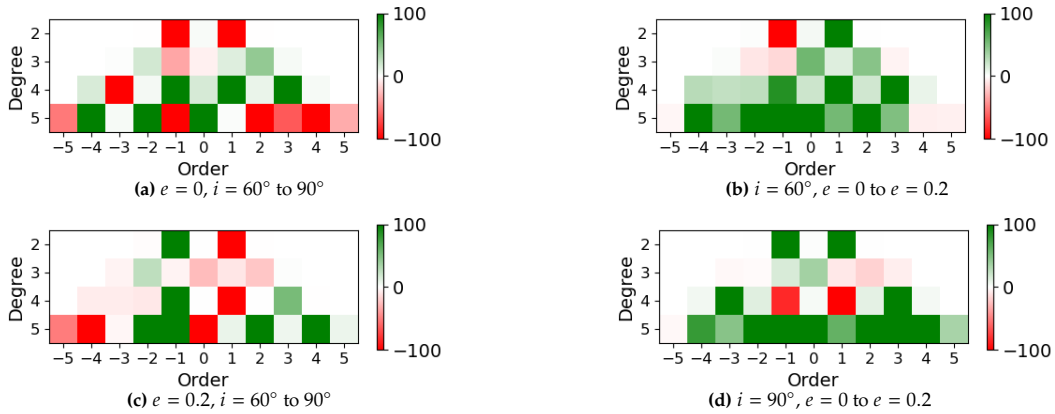

(a) $e = 0$, $i = 60°$ to $90°$

(b) $i = 60°$, $e = 0$ to $e = 0.2$

(c) $e = 0.2$, $i = 60°$ to $90°$

(d) $i = 90°$, $e = 0$ to $e = 0.2$

Figure E.2: Estimation percentage improvement from the variation of the decision variables e and i.

E.1.3. Semi-major Axis and Eccentricity

The analysis of the effect and interaction of a and e is carried out with the bounds presented in Table E.3.

Figure E.3 presents how these variables affect the estimations of the coefficients individually. The estimates computed verify how for a fixed semi-major axis, the filter is able to more accurately estimate the SH coefficients for eccentric orbits. It should be noted that this is the case for sufficiently large values of semi-major axis and that lower values of altitude can lead to orbital instability causing the satellites to crash onto the asteroid or escape its orbit. This is also the case when larger values of eccentricity are considered. Note that the positive effect of the eccentricity is the same that has been noted in the previous analysis test.

Table E.3: Bounds of the decision variables

	a [km]	e [-]
Upper bound	50	90
Lower bound	45	60

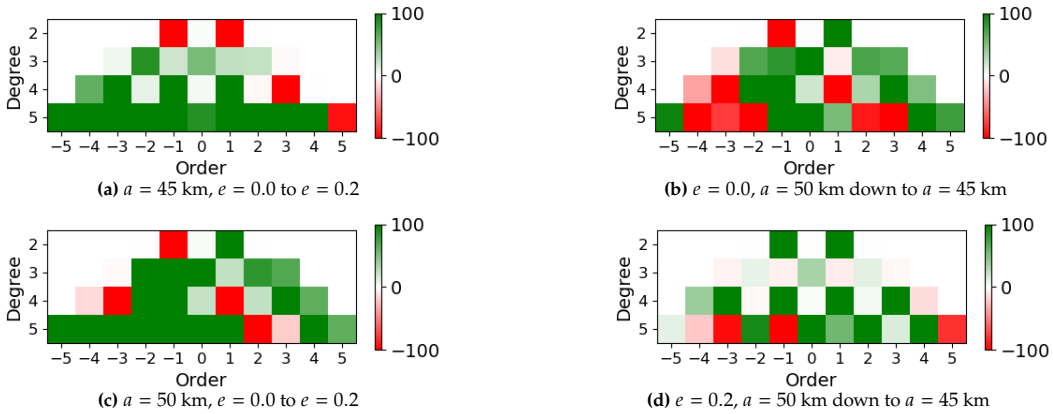

(a) $a = 45$ km, $e = 0.0$ to $e = 0.2$

(b) $e = 0.0$, $a = 50$ km down to $a = 45$ km

(c) $a = 50$ km, $e = 0.0$ to $e = 0.2$

(d) $e = 0.2$, $a = 50$ km down to $a = 45$ km

Figure E.3: Estimation percentage improvement from the variation of the decision variables a and e.

E.1.4. Semi-major Axis and Satellite Distribution along the True Anomaly

The analysis of the effect and interaction of a and $v_{distribution}$ is carried out with the limits presented in Table E.4. Consider that a $v_{dist} = 2$ means that the satellites are evenly spread along 360°, and that $v_{dist} = 1$ shows that the satellites are evenly spread along 240°.

Figure E.4 presents how these variables affect the estimations of the coefficients individually. In particular, as is to be expected, the results illustrate how for any spreading settings of the satellites, a decrease in the semi-major axis has a positive effect on the estimates since as presented beforehand, the lower the altitude, the higher the perturbations effect and the better the filter is able to model their dynamics. Changing the distribution of the satellites along the true anomaly affects the coefficients differently since the true anomaly of each satellite determines the trajectory followed, and the perturbations experienced by the satellite. Therefore, the better performing true anomaly value for a satellite is dependent on the irregularity of the asteroid and cannot be determined, and its value will determine the coverage obtained and thus the SH estimates accuracy. However, it should be noted that the distribution of the asteroids within an adequate range of true anomaly values is also dependent on visibility and communications constraints.

Table E.4: Bounds of the decision variables

	a [km]	v_{dist} [-]
Upper bound	40	2
Lower bound	30	1

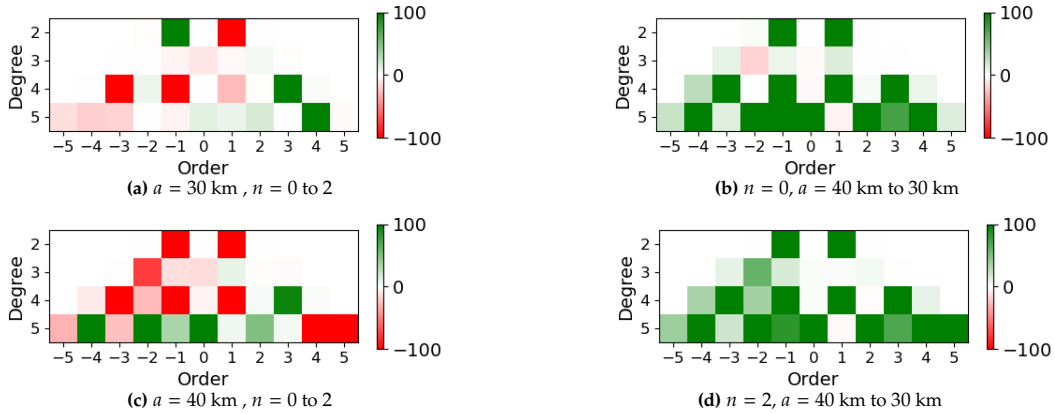

(a) $a = 30$ km , $n = 0$ to 2 **(b)** $n = 0$, $a = 40$ km to 30 km

(c) $a = 40$ km , $n = 0$ to 2 **(d)** $n = 2$, $a = 40$ km to 30 km

Figure E.4: Estimation percentage improvement from the variation of the decision variables a and n.

E.1.5. Eccentricity and Satellite Distribution along the True Anomaly

The analysis of the effect and interaction of e and v_{dist} is carried out with the bounds presented in Table E.5. Consider that a $v_{dist} = 2$ means that the satellites are evenly spread along 360° and that $v_{dist} = 1$ shows that the satellites are evenly spread along 240°.

Further detail on the effects of these variables are shown in Figure E.5. These plots depict how variations in these variables affect the estimations of the coefficients individually. As expected, the positive effect of the eccentricity of the estimates is maintained and shown in the results. However, there is a visible variability in the effects of the individual coefficients. While the improvement for a largely distributed scenario is widespread across the majority of the coefficients, this is not the case for a closer satellite distribution. This can be directly linked to the fact that the true anomaly determines the initial perturbations experienced by the satellites and higher eccentricities increase the effect of the perturbations by reducing the altitude of the satellite trajectories in some areas and increasing it in others. Therefore, the effects of the true anomaly are highlighted and thus the coverage of some areas is better modelled while some others are not, thus resulting in this coefficient improvement distribution. Moreover, the variability in the results is further accentuated by the visibility and communications constraints within the constellation.

Table E.5: Bounds of the decision variables

	e [-]	v_{dist} [-]
Upper bound	0.2	2
Lower bound	0.0	1

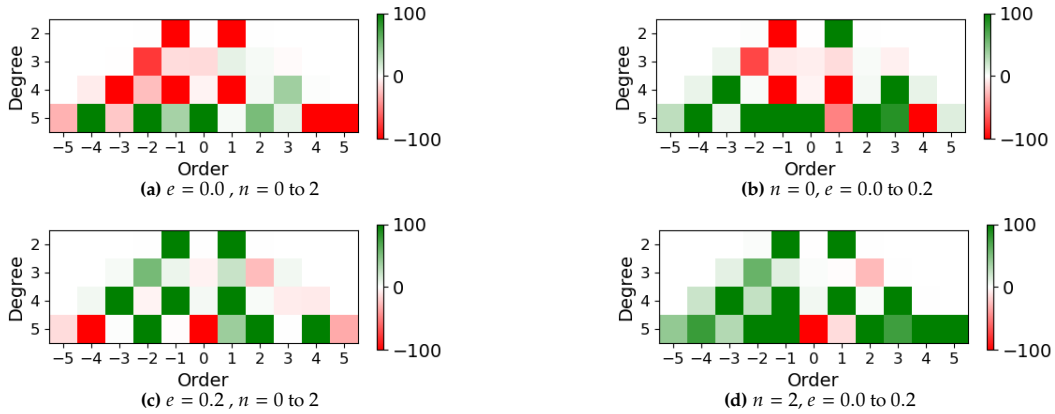

(a) $e = 0.0$, $n = 0$ to 2 **(b)** $n = 0$, $e = 0.0$ to 0.2

(c) $e = 0.2$, $n = 0$ to 2 **(d)** $n = 2$, $e = 0.0$ to 0.2

Figure E.5: Estimation percentage improvement from the variation of the decision variables e and n.

E.1.6. Inclination and Satellite Distribution along the True Anomaly

The analysis of the effect and interaction of i and n is carried out with the bounds presented in Table E.6. Consider that a $\nu_{dist} = 2$ means that the satellites are evenly spread along 360°, and that $\nu_{dist} = 1$ shows that the satellites are evenly spread along 240°.

Further detail on the effects of these variables are shown in Figure E.6. These plots depict how variations in these variables affect the estimations of the coefficients individually. An increase in the orbital inclination has been shown to present a consistent improvement in the SH coefficients estimates for a reduced satellite distribution, which can be directly linked to the fact that polar orbits have a larger coverage of the asteroid and thus, the filter has more data on the dynamics to more accurately estimate the coefficients. This, however, is not the case for a larger distribution of the satellites across the true anomaly, showing how sine coefficients benefit from less polar orbits but cosine coefficients do benefit from more polar orbits, as noted in the system sensitivity analysis. The variability of the inclination effect based on the satellite distribution shows a clear interaction between both variables, being asteroid coverage significantly dependent on both. Additionally, for a fixed orbital inclination, the satellite distribution has a higher effect for lower inclinations. This is due to the fact that a 60° inclination performs worse than a more polar orbit and thus, benefits significantly from a larger distribution since it provides additional coverage of the asteroid. This is however not the case for a polar orbit, since the system already has a large coverage of the asteroid and thus a larger distribution of the satellites does not offer significant coverage improvement thus not resulting in significant change in the coefficient estimates.

Table E.6: Bounds of the decision variables

	i [°]	ν_{dist} [-]
Upper bound	90	2
Lower bound	60	1

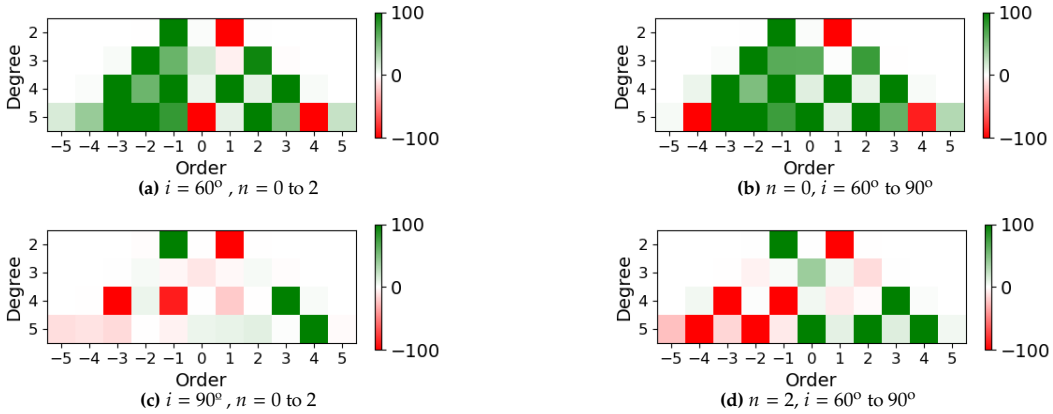

(a) $i = 60^o$, $n = 0$ to 2 **(b)** $n = 0$, $i = 60^o$ to 90^o

(c) $i = 90^o$, $n = 0$ to 2 **(d)** $n = 2$, $i = 60^o$ to 90^o

Figure E.6: Estimation percentage improvement from the variation of the decision variables i and n.

E.2. Scenario 2: Varying Inclinations within the Constellation

This scenario has been designed to study the effect that the design parameters have on a constellation where the satellites are placed in different orbital inclinations. The same basis as the previous scenario analysed is used, with a focus on the analysis of the semi-major axis, the eccentricity, the distribution of the satellites along the true anomaly, and their distribution along different inclination orbits. This section presents the effects and interactions of these variables on the SH estimates individually first, and then considering them all with a complete ANOVA.

E.2.1. Semi-Major Axis and Satellite Distribution along the Inclination

The analysis of the effect and interaction of a and i_{dist} is carried out with the bounds presented in Table E.7. Consider that a $i_{dist} = 2$ depicts that the satellites are spread along the inclinations of 90°, 80°, 70°, 60°, 50°, and 40°. Moreover, $i_{dist} = 1$ shows that the satellites are spread out along closer inclinations of 90°, 85°, 80°, 75°, 70°, and 65°.

Figure E.7 illustrates the positive effect that decreasing the semi-major axis of the orbits has on the SH coefficients estimates, as expected given the results obtained previously. It should be noted that the effect of the inclinations used is maintained independently of the semi-major axis, which is to be expected since the main difference between both cases is then that the larger semi-major axis satellites will orbit more slowly and with slightly fewer perturbations, following similar trajectory distributions.

Table E.7: Bounds of the decision variables

	a [km]	i_{dist} [-]
Upper bound	40	2
Lower bound	30	1

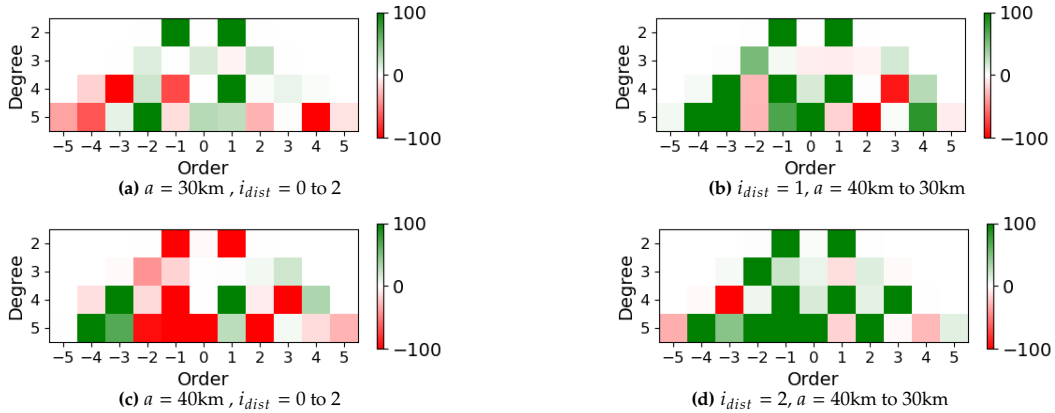

(a) a = 30km , i_{dist} = 0 to 2 **(b)** i_{dist} = 1, a = 40km to 30km

(c) a = 40km , i_{dist} = 0 to 2 **(d)** i_{dist} = 2, a = 40km to 30km

Figure E.7: Estimation percentage improvement from the variation of the decision variables a and i_{dist}.

E.2.2. Eccentricity and Satellite Distribution along the Inclination

The analysis of the effect and interaction of e and i_{dist} is carried out with the bounds presented in Table E.8. Consider that a i_{dist} = 2 depicts that the satellites are spread along the inclinations of 90°, 80°, 70°, 60°, 50°, and 40°. Moreover, i_{dist} = 1 shows that the satellites are spread out along closer inclinations of 90°, 85°, 80°, 75°, 70°, and 65°.

Further detail on the effects of these variables is shown in Figure E.8. These plots depict how variations in these parameters affect the estimations of the coefficients individually. In particular, the effect of the eccentricity is as expected positively for the majority of the coefficients independently of the inclination orbital distribution. This is to be expected since adding eccentricity to the orbit allows for better estimation of the dynamics as it has been determined in the previous analysis, independently of the inclination followed by the trajectory as long as the orbit is stable. Considering that larger eccentricities provide better estimates than for circular orbits, the effect of the distribution of the satellites along the inclination is different in both cases. While larger distributions appear to be more beneficial for eccentric orbits this is not the case for circular ones. This can be directly attributed to the larger perturbations effect that eccentric orbits have on the satellite's trajectory and thus the coverage obtained. Furthermore, it is also affected by visibility and communications constraints. Therefore, when considering the definition of these parameters, further analysis should be conducted to determine the best combination of both depending on the system characteristics.

Table E.8: Bounds of the decision variables

	e [-]	i_{dist} [-]
Upper bound	0.2	2
Lower bound	0.0	1

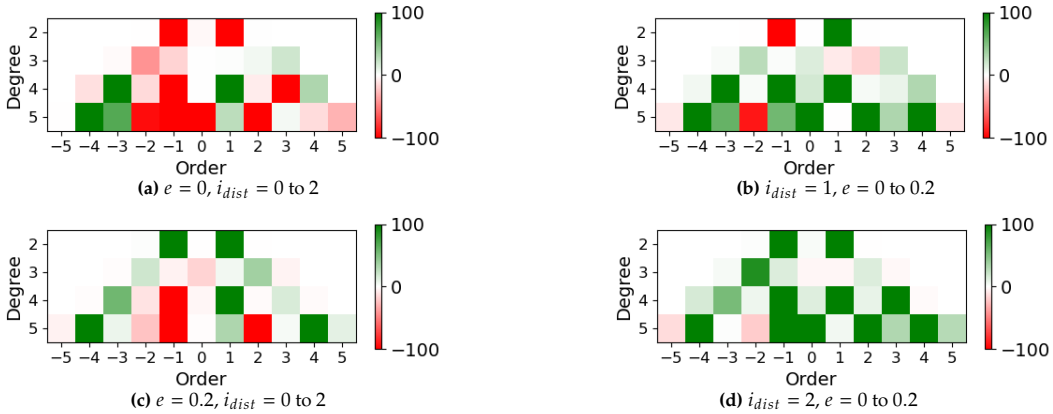

(a) $e = 0$, $i_{dist} = 0$ to 2 **(b)** $i_{dist} = 1$, $e = 0$ to 0.2

(c) $e = 0.2$, $i_{dist} = 0$ to 2 **(d)** $i_{dist} = 2$, $e = 0$ to 0.2

Figure E.8: Estimation percentage improvement from the variation of the decision variables e and i_{dist}.

E.2.3. True Anomaly and Satellite Distribution along the Inclination

The analysis of the effect and interaction of v_{dist} and i_{dist} is carried out with the bounds presented in Table E.9. Consider that a $i_{dist} = 2$ depicts that the satellites are spread along the inclinations of 90°, 80°, 70°, 60°, 50°, and 40°. Moreover, $i_{dist} = 1$ shows that the satellites are spread out along closer inclinations of 90°, 85°, 80°, 75°, 70°, and 65°. Furthermore, a $v_{dist} = 2$ means that the satellites are evenly spread along 360° and that $v_{dist} = 1$ shows that the satellites are evenly spread along 240°.

Further detail on the effects of these variables is shown in Figure E.9. These plots depict how variations in these parameters affect the estimations of the coefficients individually. As can be seen, for a fixed distribution of the satellites along the true anomaly, the inclination has a considerable effect on the results. In particular, the main tendency that can be identified is that when distributing the satellites with lower inclinations (Figure E.9c), the cosine coefficients experience a detrimental effect while the sine coefficients estimation accuracy improves. When this distribution is done more conservatively, the satellites show an improvement for higher degrees but a detrimental effect on lower ones, thus overall performing better. Additionally, distributing the inclination along a wider range of polar orbits has shown a very similar tendency. These results are particularly affected by the systems constraints, which have a considerable effect on the dispersion of satellites along a range of orbits. Overall, it can be concluded that a slight inclination dispersion in the asteroids is beneficial to the system.

Table E.9: Bounds of the decision variables

	v_{dist} [-]	i_{dist} [-]
Upper bound	2	2
Lower bound	1	1

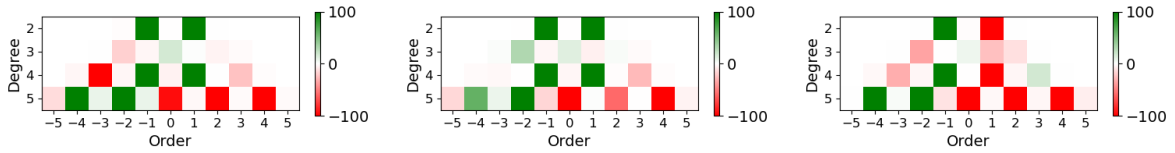

(a) v_{dist} along 180°, $i_{dist} = [90]^{\circ}$ to $[60, 110]$ **(b)** v_{dist} along 180°, $i_{dist} = [90°]$ to $[90°, 65°]$ **(c)** v_{dist} along 180°, $i_{dist} = [90°]$ to $[90°, 40°]$

Figure E.9: Estimation percentage improvement from the variation of the decision variables v_{dist} and i_{dist}.

E.3. Scenario 3: Varying Satellite Number and Orbital Distributions

This section aims to study the effect that the orbital distribution and number of satellites have on the estimations of the gravity field. The effect that the number of satellites of the constellation and the number of different orbits used on the estimates produced are presented in Figure E.10. These illustrate that the addition of satellites does not directly result in improved coefficient estimates, as can be illustrated by Figure E.10a. This is due to the fact that having appropriate satellite trajectories within the orbit is more important than having a higher number of satellites, therefore, satellites shall

not be included blindly unless they have adequate trajectories that can benefit the filter and improve its estimation. As has been analysed in Chapter 5, satellites with inadequate trajectories can have a detrimental effect on the system.

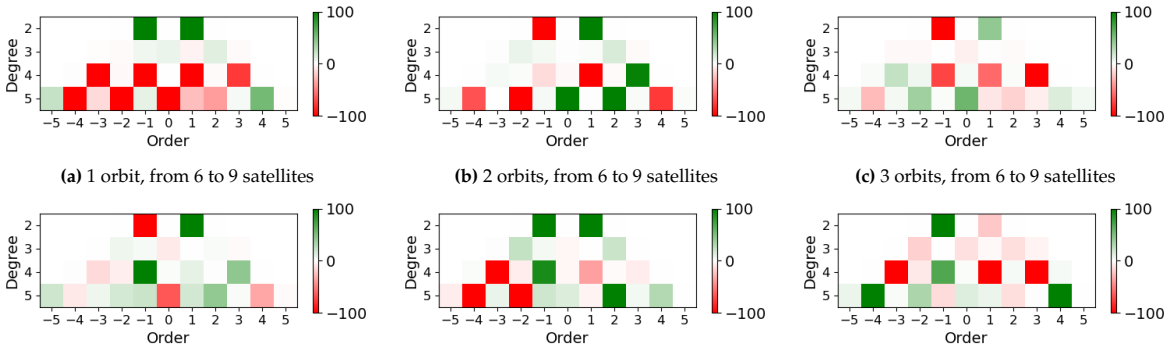

(a) 1 orbit, from 6 to 9 satellites

(b) 2 orbits, from 6 to 9 satellites

(c) 3 orbits, from 6 to 9 satellites

(d) 1 orbit, from 6 to 12 satellites

(e) 2 orbits, from 6 to 12 satellites

(f) 3 orbits, from 6 to 12 satellites

Figure E.10: Estimation percentage improvement from the variation of the decision variables number of satellites in the constellation for a fixed number of orbits.

F

Design synthesis

This chapter presents in more detail the settings and tests used in the design approach presented in Chapter 7. Section F.1 presents the design of the constellation depicting the specific configuration of the satellites used. This is followed by Section F.2, which details the specific parameters used in the filter tunning. Furthermore, Section F.3 presents tests conducted to assess the limitations of the filter, and Section F.4 the settings used for the computation of the SH coefficients used for studying the applicability of the system for three additional asteroids.

F.1. Design of the constellation

To define the best constellation for this scenario, the location of the mothership has been optimised to minimise the communications constraints with the CubeSats. An initial grid search of the best inclination and true anomaly over the values of 180° and 360° respectively has been conducted to determine the combination of both variables which results in a higher percentage of LOS availability between the mothership and the satellites. The results for a semi-major axis of 30 and 40 km are depicted in Figure F.1.

Following the lessons learned in the sensitivity analysis of the constellation and the ANOVA, a constellation has been designed to optimise the estimates, as detailed in Section 7.1. The final constellation design orbital parameters are presented in Table F.1.

Figure F.2 presents the estimates obtained when the velocity and position measurements are considered. These have been compared to the ones with only measurement errors and it has been determined that the addition of velocity measurements to the filter does not have a significant effect on the estimates and therefore is not considered, this way reducing further the computational load of the filter by not including the additional measurement values.

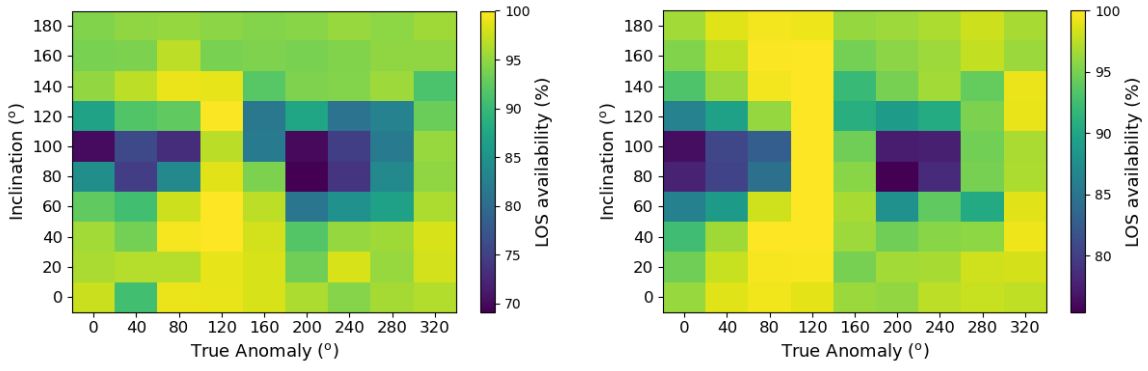

(a) $a = 30$ km **(b)** $a = 40$ km

Figure F.1: Percentage of the availability of satellites fulfilling the communications constraints between a mothership in a range of i and ν with a sample constellation of five CubeSats spread out.

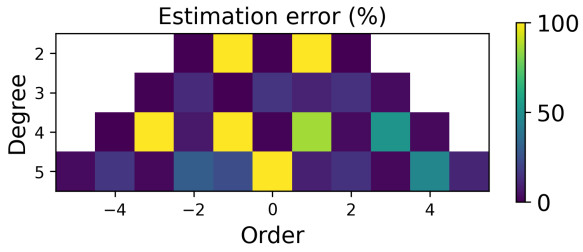

Figure F.2: Estimates obtained for a one-second time step for a 1 million second propagation using position and velocity measurements.

F.2. Design of the filter

In an effort to improve the filter estimates, several considerations have been made, as presented in Section 7.2. One of the main improvements subjected to the filter is its tunning, as presented in the following section.

F.2.1. Tuning of the filter

To redesign the filter, the characteristics of the covariance matrix have been closely analysed to identify relations between coefficients. The correlation of the covariance matrix after a simple estimation up to degree and order four is depicted in Figure F.3. This has shown only a direct correlation between the position and the velocity coordinates, and the coefficients depict a chaotic distribution of correlations, from which no tendencies can be identified and thus no further improvement can be made to the covariance matrix definition.

Table F.1: Orbital parameters of the CubeSats of the final constellation design

Satellite	a (km)	i (deg)	e (deg)	ν (deg)
Mothership	30	60	0	120
CubeSat 1	30	90	0	0
CubeSat 2	32	90	0	30
CubeSat 3	34	90	0	60
CubeSat 4	36	90	0	89
CubeSat 5	30	90	0	120
CubeSat 6	32	90	0	150
CubeSat 7	34	90	0	179
CubeSat 8	36	90	0	210
CubeSat 9	30	90	0	240
CubeSat 10	32	90	0	270
CubeSat 11	34	90	0	300
CubeSat 12	36	90	0	330

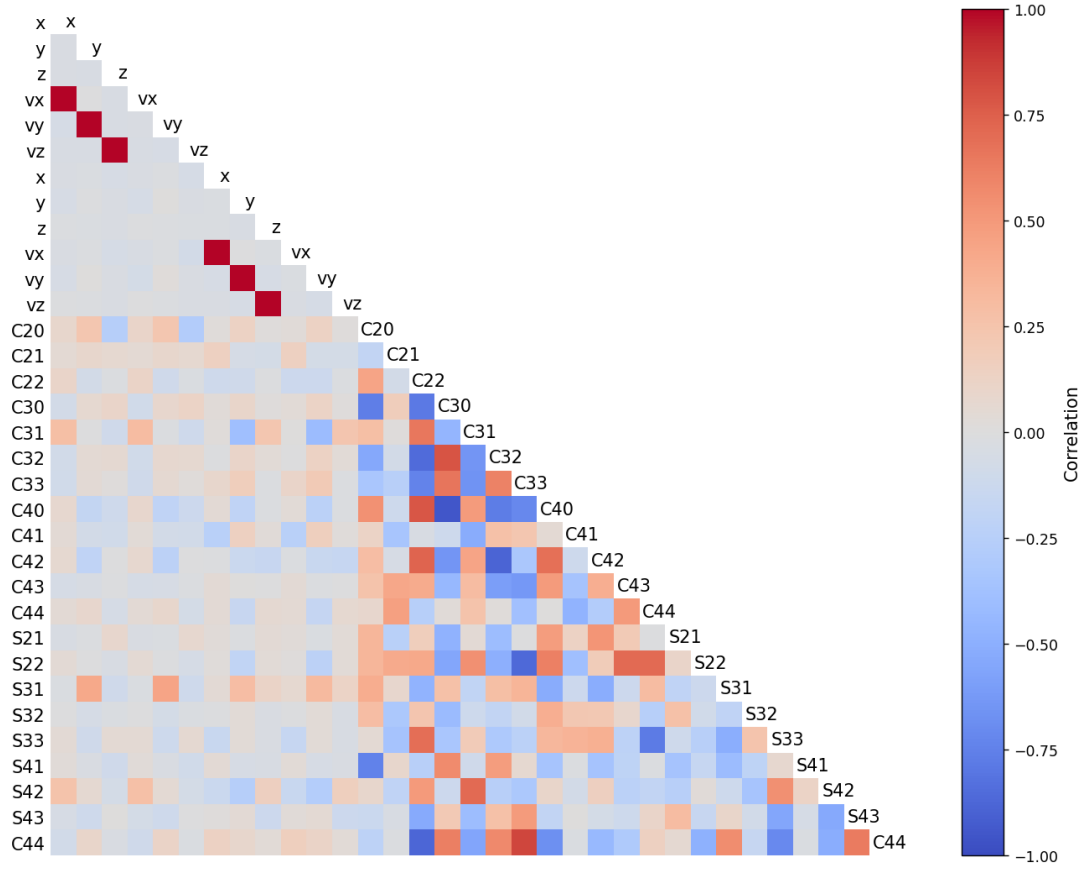

Figure F.3: Correlation of the covariance matrix for 4$^{\text{th}}$ degree and order coefficients of the SH gravity field.

After careful testing of appropriate initial covariance matrices for efficient tuning of the filter, the following matrices have been fixed:

$$\mathbf{P} = \begin{bmatrix} \mathbf{I}_{3\times3} \cdot p_{pos,1} & \mathbf{0}_{3\times3} & \mathbf{0}_{3\times n_C} & \mathbf{0}_{3\times n_S} \\ \mathbf{0}_{3\times3} & \mathbf{I}_{3\times3} \cdot p_{pos,2} & \mathbf{0}_{3\times n_C} & \mathbf{0}_{3\times n_S} \\ \mathbf{0}_{n_C\times3} & \mathbf{0}_{n_C\times3} & \mathbf{I}_{n_C\times n_C} \cdot p_{Cmn} & \mathbf{0}_{n_C\times n_S} \\ \mathbf{0}_{n_S\times3} & \mathbf{0}_{n_S\times3} & \mathbf{0}_{n_S\times n_C} & \mathbf{I}_{n_S\times n_S} \cdot p_{Smn} \end{bmatrix} \tag{F.1}$$

where $p_{pos} = 10^3$, $p_{vel} = 10^2$, and the p_{Cmn} and the p_{Smn} values are as follows for the first five degrees and order:

$$\begin{aligned} p_{C20-C22} &= \begin{bmatrix} 1 & 10^{-7} & 1 \end{bmatrix} \\ p_{C30-C33} &= \begin{bmatrix} 10^{-2} & 10^{-2} & 10^{-2} & 1 \end{bmatrix} \\ p_{C40-C44} &= \begin{bmatrix} 1 & 10^{-4} & 1 & 10^{-4} & 1 \end{bmatrix} \\ p_{C50-C55} &= \begin{bmatrix} 10^{-4} & 10^{-2} & 10^{-4} & 10^{-2} & 10^{-4} & 1 \end{bmatrix} \end{aligned} \tag{F.2}$$

$$\begin{aligned} p_{S21-S22} &= \begin{bmatrix} 10^{-7} & 1 \end{bmatrix} \\ p_{S31-S33} &= \begin{bmatrix} 10^{-2} & 10^{-4} & 1 \end{bmatrix} \\ p_{S41-S44} &= \begin{bmatrix} 10^{-4} & 10^{-2} & 10^{-4} & 10^{-2} \end{bmatrix} \\ p_{S51-S55} &= \begin{bmatrix} 10^{-2} & 10^{-4} & 10^{-2} & 10^{-4} & 10^{-2} \end{bmatrix} \end{aligned} \tag{F.3}$$

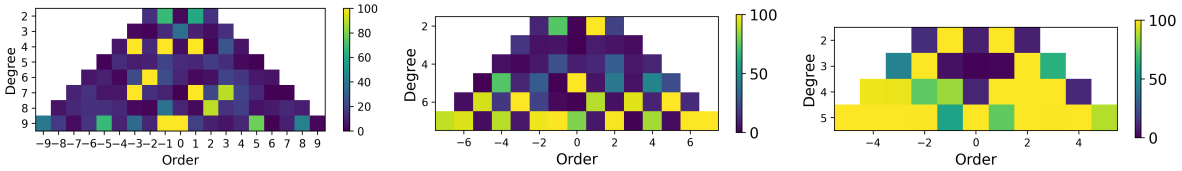

(a) 30 km **(b)** 50 km **(c)** 100 km

Figure F.4: Coeffcients estimation for 1 m position error with μ and ω estimation errors for a range of semi-major axis.

Furthermore, the process noise covariance matrix is as follows;

$$\mathbf{Q} = \begin{bmatrix} \mathbf{I}_{3\times3} \cdot q_{pos} & \mathbf{0}_{3\times3} & \mathbf{0}_{3\times n_C} & \mathbf{0}_{3\times n_S} \\ \mathbf{0}_{3\times3} & \mathbf{I}_{3\times3} \cdot q_{vel} & \mathbf{0}_{3\times n_C} & \mathbf{0}_{3\times n_S} \\ \mathbf{0}_{n_C\times3} & \mathbf{0}_{n_C\times3} & \mathbf{I}_{n_C\times42} \cdot q_{Cmn} & \mathbf{0}_{n_C\times n_S} \\ \mathbf{0}_{n_S\times3} & \mathbf{0}_{n_S\times3} & \mathbf{0}_{n_S\times42} & \mathbf{I}_{n_S\times n_S} \cdot q_{Smn} \end{bmatrix} \tag{F.4}$$

where $q_{pos} = 10^{-10}$, $q_{vel} = 10^{-9}$, and the q_{Cmn} and the q_{Smn} values are as follows for the first five degrees and order:

$$\begin{aligned} q_{C20-C22} &= \begin{bmatrix} 10^{-32} & 10^{-37} & 10^{-32} \end{bmatrix} \\ q_{C30-C33} &= \begin{bmatrix} 10^{-33} & 10^{-33} & 10^{-33} & 10^{-32} \end{bmatrix} \\ q_{C40-C44} &= \begin{bmatrix} 10^{-32} & 10^{-34} & 10^{-32} & 10^{-34} & 10^{-32} \end{bmatrix} \\ q_{C50-C55} &= \begin{bmatrix} 10^{-34} & 10^{-33} & 10^{-34} & 10^{-33} & 10^{-34} & 10^{-32} \end{bmatrix} \end{aligned} \tag{F.5}$$

$$\begin{aligned} q_{S21-S22} &= \begin{bmatrix} 10^{-38} & 10^{-32} \end{bmatrix} \\ q_{S31-S33} &= \begin{bmatrix} 10^{-33} & 10^{-34} & 10^{-32} \end{bmatrix} \\ q_{S41-S44} &= \begin{bmatrix} 10^{-34} & 10^{-33} & 10^{-34} & 10^{-33} \end{bmatrix} \\ q_{S51-S55} &= \begin{bmatrix} 10^{-33} & 10^{-34} & 10^{-33} & 10^{-34} & 10^{-33} \end{bmatrix} \end{aligned} \tag{F.6}$$

F.2.2. Verification of filter performance

A verification test has been conducted to confirm that the new filter design while having improved efficiency, continues to behave in the same manner as the previous filter. Figure F.4 shows how the altitude of the satellites in the constellation has a large effect on the estimates obtained. As presented in initial tests, the semi-major axis is a key determinant of the estimation of the coefficients, and as expected, the system is unable to estimate the gravity field for the 100 km case since at such large values, the irregularities have barely any effect and therefore, the asteroid's gravity field's irregularities cannot be estimated. As altitude is reduced, the effects of the higher degree and order coefficients are larger and the filter is able to estimate them.

F.3. Filter limitations

Several tests have been conducted to determine the limitations of the filter and in particular the effect that the estimation errors in the gravitational parameter and the rotation rate of the asteroid have on the estimation of the coefficients. Figure F.5 depicts the estimates obtained considering a 2% error in the estimates with ideal measurements for a set of error thresholds. As can be seen, the filter is unable to perfectly estimate with very high accuracy the coefficients when the estimation contains errors, but does so for a relatively low error.

Figure F.6 to Figure F.8 depict how the errors slightly increase as the measurement errors increase in value, thus showing that the filter performance is dependent on the accuracy of the measurements, as expected, as well as verifying the filter performance with a wide range of measurement errors.

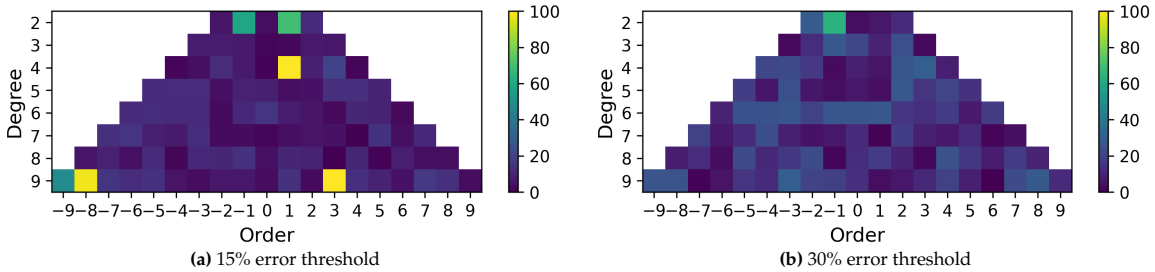

(a) 15% error threshold **(b)** 30% error threshold

Figure F.5: Coefficients estimation for null position error with μ and ω estimation errors

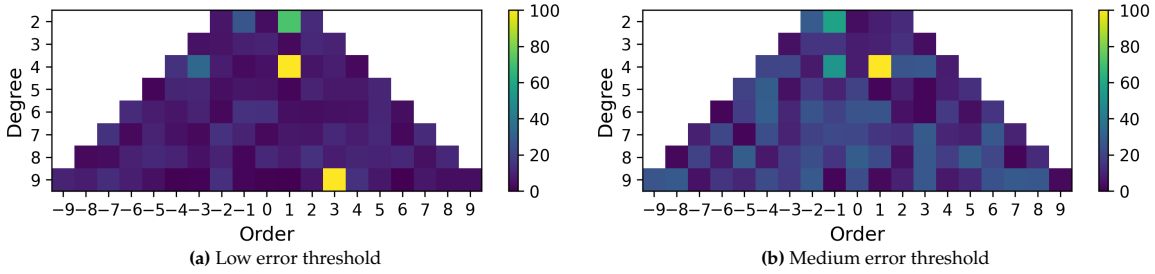

(a) Low error threshold **(b)** Medium error threshold

Figure F.6: Coefficients estimation for 0.1 m position error with μ and ω estimation errors

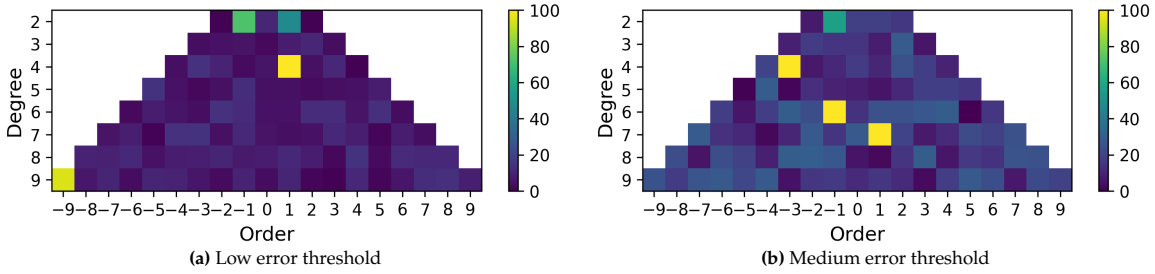

(a) Low error threshold **(b)** Medium error threshold

Figure F.7: Coefficients estimation for 1 m position error with μ and ω estimation errors

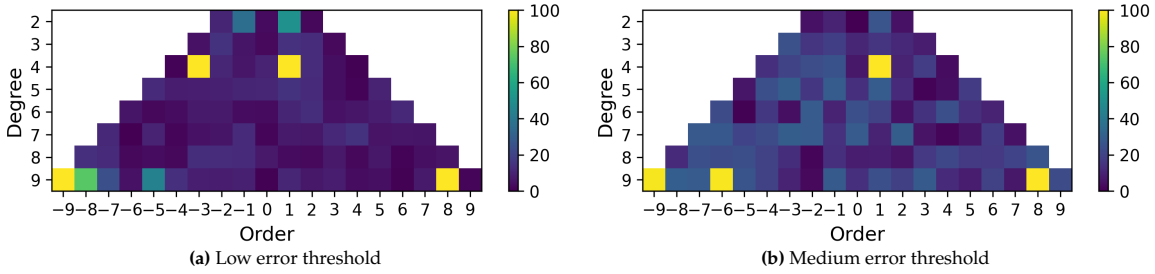

(a) Low error threshold **(b)** Medium error threshold

Figure F.8: Coefficients estimation for 10 m position error with μ and ω estimation errors

F.4. Applicability of the model

As presented in Section 7.4, the system performance has been tested with three extreme case asteroids: 216 Kleopatra[1], 25143 Itokawa[2], and 4 Vesta[3]. The SH coefficients of these asteroids have been computed through a forward gravitational field model implemented by Root et al. (2016). The parameters used for the application of this model are presented in Table F.2. The results obtained for the estimations are presented in Section 7.4.

[1] "216 Kleopatra", Available at: https://en.wikipedia.org/wiki/216_Kleopatra, Accessed on 05-07-2024
[2] "25143 Itokawa", Available at: https://en.wikipedia.org/wiki/25143_Itokawa, Accessed on 05-07-2024
[3] "4 Vesta", Available at: https://en.wikipedia.org/wiki/4_Vesta, Accessed on 05-07-2024

Table F.2: Parameters used for the SH computation of 216 Kleopatra, 25143 Itokawa, and 4 Vesta

Parameter	216 Kleopatra	25143 Itokawa	4 Vesta
Mass [kg]	$2.62 \cdot 10^{18}$	$3.51 \cdot 10^{10}$	$2.59 \cdot 10^{20}$
Radius [m]	$118 \cdot 10^{3}$	$267.5 \cdot 10^{0}$	$286.3 \cdot 10^{3}$
Density [kg/m^3]	$3.45 \cdot 10^{3}$	$1.90 \cdot 10^{3}$	$3.46 \cdot 10^{3}$
Degree and order	200	200	16
Layer height [m]	1000	100	1000